TECHNISCHE UNIVERSITÄT WIEN
Vienna | Austria

DISSERTATION

Stability Analysis of Incompressible Boundary-Driven Flows in Rectangular Cavities

ausgeführt zum Zwecke der Erlangung des akademischen Grades eines Doktors der technischen Wissenschaften (Dr. techn.), eingereicht an der TU Wien, Fakultät für Maschinenwesen und Betriebswissenschaften, von

Pierre-Emmanuel des Boscs

Mat. Num.: 1649639

unter der Leitung von
Univ.-Prof. Hendrik C. Kuhlmann
Institut für Strömungsmechanik und Wärmeübertragung

Wien, August 2020

Begutachtet von

Univ.-Prof. M. Kaltenbacher
Technische Universität Graz

Univ.-Prof. A. Gelfgat
Tel-Aviv University

I confirm, that going to press of this thesis needs the confirmation of the examination committee.

Affidavit

I declare in lieu of oath, that I wrote this thesis and performed the associated research myself, using only literature cited in this volume. If text passages from sources are used literally, they are marked as such.
I confirm that this work is original and has not been submitted elsewhere for any examination, nor is it currently under consideration for a thesis elsewhere.

Vienna, August 2020

Pierre-Emmanuel des Boscs

Zusammenfassung

Die Stabilität Strömung eines inkompressiblen Fluids, das in einem Rechteckbehälter eingeschlossen ist, wird untersucht. In jeder der drei untersuchten Konfigurationen wird die Strömung durch eine sich bewegende Grenzfläche angetrieben.

Zuerst betrachten wir einen in Spannweitenrichtung unendlich ausgedehnten Behälter, in dem die Strömung durch eine tangentiale, aber schräge Bewegung eines Deckels angetrieben wird. Wir erhalten die kritische Reynoldszahle für den Einsatz einer drei-dimensionen Strömung für den gesamten Bereich der Gierwinkel. Für alle untersuchten Aspektverhältnisse ist die Strömung im Vergleich zu den beiden Grenzfällen stark destabilisiert. Die Vielzahl der instabilen Moden wird beschrieben und der Hauptmechanismus der Destabilisierung analysiert.

Danach wird die lineare Stabilität einer thermokapillar-angetriebenen Strömung in einem unendlich ausgedehnten Behälter betrachtet. Bei Erhöhung der Stärke des Antriebs kann die Strömung aufgrund einer linearen Instabilität oszillieren. Interesse gilt der Sensitivität der Instabilität in Bezug auf den Wärmestrom, der an der Grenzfläche aufgeprägt wird. Eine auf Sensitivität basierende Strategie zur effizienten Stabilisierung oder Destabilisierung der stationären Strömung unter Verwendung eines konstruierten Wärmeflusses wird als nichtlineares Optimierungsproblem formuliert.

Schließlich wird die Stabilitätsgrenze der Strömung in einem kubischen Behälter untersucht, der durch eine konstante Scherspannung angetrieben wird. Im Gegensatz zu der von einem Deckel angetriebenen Behälterströmung verliert die Strömung zunächst ihre räumliche Symmetrie, bevor sie zeitabhängig wird. Die aufeinanderfolgenden Bifurkationen sind alle überkritisch. Mit zunehmender Stärke des Antriebs kann eine komplexe Dynamik zwischen zwei Grenzzyklen beobachtet werden.

Abstract

The stability of an incompressible fluid flow in a cavity is investigated. In each of the three setups examined the flow is driven by a moving boundary.

First, we consider a cavity infinitely extended in the spanwise direction in which the flow is driven by a tangential but oblique motion of a lid. We obtain the critical Reynods number for the onset of three-dimensional flow for the whole range of yaw angles. For all aspect ratios studied, the flow is strongly destabilized in comparison with the two limiting cases. The wide variety of unstable modes is detailed and the main destabilization mechanism is analyzed.

Then, the linear stability of a thermocapillary-driven flow in an infinitely extended cavity is considered. Upon increasing the strength of the driving force, the flow can become oscillatory due to a linear instability. Attention is paid to the sensitivity of the onset of three-dimensional flow with respect to the heat flux imposed at the interface. A sensitivity-based strategy to efficiently stabilize or destabilize the flow using a designed heat flux is formulated as a non-linear optimization problem.

Finally, the stability boundary of the flow in a cubic cavity driven by a constant shear stress is investigated. Unlike its lid-driven counterpart the flow first loses its spatial symmetry before becoming time dependent. Successive bifurcations are all supercritical. As the strength of the driving increases a complex dynamics between two limit cycles is observed. Although the destabilization mechanisms are similar for the cubic lid-driven and shear-driven cavities, the transition to the turbulence does not follow the same path.

Acknowledgments

Honor where honor is due, I shall start by thanking Prof. Hendrik C. Kuhlmann for his guidance, encouragement and particularly for the patience he demonstrated during my doctoral studies. All along, he gave me an absolute freedom in the choices I made, and valuable advice to improve the quality of my work. I appreciated your demand for precision, and the precision of your demands.

I would like to thank Prof. Alexander Gelfgat and Prof. Manfred Kaltenbacher for immediately accepting to review this thesis, as well as Prof. Alfredo Soldati for being the head of the jury.

A special mention goes to Francesco Romanò, who is to me a sort of scientific older brother. I should point out your numerous helpful suggestions at the beginning of my stay and the never ending conversations about our legitimate partitions of Europe and unorthodox hierarchies among Latin languages.

For having contributed to a nice and relaxed working atmosphere, I would like to thanks my colleagues (in order of appearance) the Dominiks, Michael, Behnaz, Mario and Ivo, Lukas, Ilya and Ariane, and of course Kathi who took care of all of us.

To old and new friends, I am thankful for the support and for the fun. I thank my family for always pushing me forward and for their communicative joys. Finally, I want to thank Beate for sharing the path and I wish her good luck in her own works.

Mais alors à quoi bon chercher d'autres planètes si ne nous pouvons pas nous y rendre ? Pourquoi chercher d'autres formes de vie si nous ne pouvons pas communiquer avec elles ? Si vous avez déjà regardé les anneaux de Saturne dans un télescope vous connaissez une partie de la réponse.

Nous cherchons pour comprendre la réalité qui nous entoure, nous cherchons pour connaître notre place au sein de l'univers, et enfin nous cherchons pour nous émerveiller. En combinant ces trois pilliers, comme les télescopes de Paranal ou l'antenne d'ALMA, on obtient le plus puissant des moteurs.

C'était déjà celui qui guidait l'humanité à l'époque d'Épicure, et aujourd'hui encore, c'est celui qui anime les chasseurs de mondes.

Patrick Baud, *Les chasseurs de mondes.*

Contents

1

General introduction

In this chapter, we will present the background of this dissertation. We will present the family of flows that will be investigated, namely incompressible boundary-driven cavity flows.

1.1 Boundary-Driven Cavity Flows

Boundary-driven flows are flows where the considered fluid is set in motion by a moving surface, at a boundary of the considered domain. This boundary can represent, for instance, an interface between the fluid and a solid non-deformable body (for example at a wall), or an interface between two fluids, in one of which the motion is not taken into account or simplified (for example at a liquid/gas interface). In both cases, the flow at the boundary is modeled by applying different boundary conditions.

In the following, we shall give some examples of incompressible flows driven by a moving solid body or by moving interface between two fluids. In fluid dynamics, a solid body driving a flow is often interchangeably called a *moving wall*, a *moving plate* or a *moving lid* when it moves tangentially to itself. At the boundary, the velocity of the fluid is the same as the velocity of the moving wall.

One of the simplest configuration with a moving plate is the Couette flow [18]. It is the flow of a fluid between two infinite parallel plates, one of which (upper plate in fig. 1.1(a)) moves tangentially to the other. Due to the viscous forces, the fluid between the plates is set in motion. The velocity profile in the fluid is linearly increasing in the wall normal direction y from 0 at the lower wall to $\boldsymbol{U}$ at the upper wall, as shown in fig. 1.1(a). This flow is, however, not recirculating, as a fluid element would indefinitely travel in the same direction.

Another fundamental configuration is the lid-driven cavity [87]. A square container is filled with a liquid, whose flow is driven by a lid moving tangentially to itself. As sketched in fig. 1.1(b), the flow velocity at the lid $\boldsymbol{U}$ is given. The flow is confined between the four walls and the fluid recirculates within the cavity. In particular, if the flow is incompressible, two-dimensional and steady, a fluid particle would travel along a closed trajectory. Although in these two examples, the flows are set in motion by a

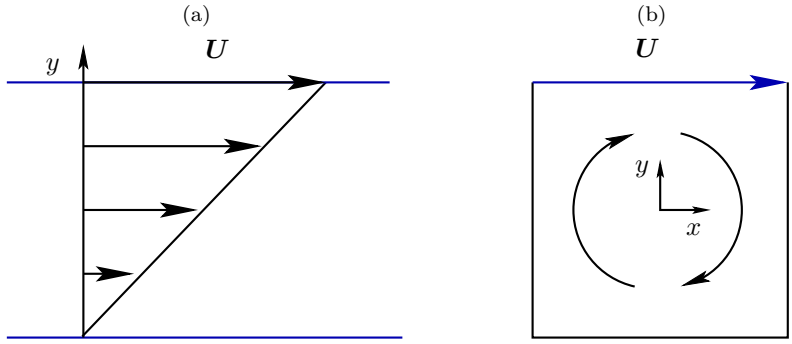

FIGURE 1.1 – (a) Sketch of a Couette flow. The upper wall is moving with a velocity $\boldsymbol{U}$, while the lower wall is stationnary. (b) Sketch of a two-dimensional lid-driven cavity flow. The upper wall is moving with a velocity $\boldsymbol{U}$, while the lower wall is stationary.

surface moving at a *given* velocity, this is not always the case.

At the surface between a liquid and a gas, the molecules of the fluid are more attracted to each other, due to cohesion forces, than attracted by the molecules of the gas, due to adhesion forces. This force imbalance results in a force normal to the surface, directed toward the liquid. Surface tension is a force per unit of length at the surface. It depends on the fluid properties like the composition, temperature, the presence of impurities at the surface, among many others.

A spatial variation of these properties along the surface induces a spatial variation of the surface tension $\Delta\Sigma$. Provided that the variation of surface tension is very small in comparison to the total surface tension, this variation of surface tension results in a local shear stress τ tangential to the surface, setting the fluid in motion [76]. In contrast to wall-driven flows, the tangential flow velocity is not given, but the shear stress at the surface is imposed. A flow driven by surface tension variations coming from variations of the temperature along the free surface is called a thermocapillary-

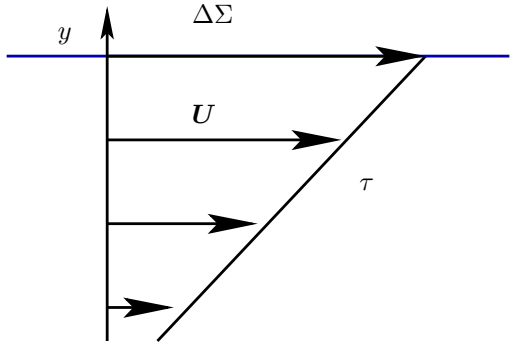

FIGURE 1.2 – Sketch illustrating the tangential shear stress τ stemming from a surface tension variation $\Delta\Sigma$, and the flow velocity $\boldsymbol{U}$ close to the surface.

driven flow.

In this thesis, we are focusing on flows in rectangular containers, driven by the tangential motion of one of its boundaries, where either the velocity or the shear stress is imposed. These type of flows are of interest: In addition to their minimalistic geometries, they often serve as simplifications of more complex systems. For example, the lid-driven cavity can be thought as a restriction of the flow over a cavity, or a confined fluid flow driven by the motion of a piston. Therefore, they are still widely investigated. For instance, there are research efforts concerning the flow topology [21, 137], or exotic particle accumulation structures [138]. Here, we are particularly interested in the stability of such flows.

1.2 Hydrodynamic Stability

Hydrodynamic stability theory is the field of fluid mechanics dealing with the stability or the onset of instability of a fluid flow. In more than 150 years, hydrodynamic stability received a lot of attention. As a proof of this, the names of many great scientists are associated to classical hydrodynamic instabilities. To cite a few, a wake instability is named after Theodore von Kármán and is illustrated in fig. 1.3(a). Lord Kelvin and Herman Ludwig von Helmholtz gave their names to the Kelvin–Helmholtz instability depicted in fig. 1.3(b), and painted in fig. 1.3(c).

The concept of stability of a state of a system was understood already in the nineteenth century. As quoted by Drazin [46], James Clerk Maxwell clearly expressed the qualitative concept:

> When ... an infinitely small variation of the present state will alter only by an infinitely small quantity the state at some future time, the condition of the system, whether at rest or in motion, is said to be stable; but when an infinitely small variation in the present state may bring about a finite difference in the state of the system in a finite time, the condition of the system is said to be unstable.

This is the backbone of the linear stability theory. This theory allows, for instance, to successfully predict the onset of instability of flow around cylinder like in fig. 1.3(a) or the destabilization of the two-dimensional flow in a lid-driven cavity (fig. 1.1(b)). However, it fails by predicting that Couette flow (fig. 1.1(a)) is stable for all plate velocity magnitudes.

Although this theory has some clear limitations, it is nonetheless a powerful tool. As we shall see in this thesis, it enables us to understand the different mechanisms at play in the destabilization of the flow.

(a)

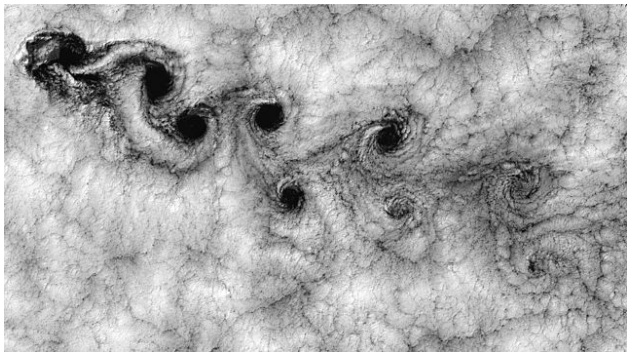

(b)

(c)

FIGURE 1.3 – (a) This photography from Landsat 7 satellite on September 15, 1999 shows the von Kármán vortex street visualized by the clouds, near the Juan Fernandez Islands in Chile. In (b) and (c), the shape of the clouds reveal Kelvin–Helmholz instabilities in a photography taken by Beverly Shannon in 1999 of the mount Mount Shasta in California, and in *La nuit étoilée* painted in 1889 by Vincent van Gogh, respectively.

1.3 Organization of the Dissertation

The present dissertation deals with the stability of flows in cavities driven either by the motion of a lid, thermocapillary stresses or a constant shear stress. It is organized in the following order.

In Chapter 2, we will introduce the theoretical background necessary for the linear stability analysis, and perturbation energy analysis.

In Chapter 3, the numerical tools that will be used throughout this dissertation will be presented. First, the spatial and time discretization techniques employed for two-dimensional and three-dimensional problems. Then, diverse methods used to solve steady problems and large eigenvalue problems will be recalled. Finally, algorithms more specific to infinitely extended setups will be introduced.

In Chapter 4, we will study the onset of the linear instability of a flow in a rectangular container infinitely extended in its spanwise direction, driven at the top surface by the motion of a lid. The lid velocity has a non-zero spanwise component, and therefore the lid motion is not aligned with the cross section of the cavity: there is a so-called yaw angle. The onset of instability is investigated for a wide range of angles, and for square, shallow and deep cavities. The aim of this chapter is to explore the different destabilization mechanisms, and provide data lacking in the literature.

In Chapter 5, the focus will be on shallow thermocapillary-driven cavities for a low- and a high-Prandtl-number fluids. In particular, we will investigate the changes of the onset of linear instability induced by variations of the spatial distribution the heat flux through the free surface. The aim of this chapter is to clarify the role of external heat flux on the stability of the system and to show how to efficiently stabilize or destabilize the system by designing optimal fluxes.

In Chapter 6, we will study the progressive destabilization of the flow contained in a cubic cavity driven by a constant shear stress at its top surface. Particular attention will be paid to the destabilization mechanisms and the evolution of the temporal and spatial symmetries exhibited by the system. The aim of this chapter is to probe whether this system follows the same destabilization scenario as the cubic lid-driven cavity.

2

Theoretical Basics

2.1 Equations of Fluid Dynamics

The equations describing the motion of an incompressible viscous fluid have been derived in the XIX century in their definitive form and with the correct interpretation by Saint-Venant in 1843. Unfortunately for him, they are named after Navier who derived the correct equations in 1822 but attributed the dissipative term not to shear stresses but to intermolecular repulsive forces, and after Stokes who independently derived them two year later in 1845 [11]. The Navier–Stokes equations read

$$\rho\left(\frac{\partial}{\partial t}+\boldsymbol{U}\cdot\nabla\right)\boldsymbol{U}=-\nabla P+\mu\Delta\boldsymbol{U}, \tag{2.1a}$$

$$\nabla\cdot\boldsymbol{U}=0, \tag{2.1b}$$

where t denotes time, ρ the fluid density, μ the dynamic viscosity, $\boldsymbol{U}$ the flow velocity and P the pressure. Later the kinematic viscosity $\nu=\mu/\rho$ will be used as well. $\boldsymbol{U}$ is a vector field with d components, and P is a scalar field.

The first equation is the momentum conservation equation, that is nothing else than the second law of Newton. The second equation is the mass conservation, also called the incompressibility constraint.

All along this chapter, we consider the lid-driven cavity setup which is sketched in fig. 2.1. The flow is bounded by walls forming a cuboid. All walls are at rest, except for one which moves tangentially to itself and drives the flow. More details concerning this fundamental setup will be given in Chapters 4 & 6. The boundary conditions are

$$\boldsymbol{U}=(U_{\text{lid}},0,0)^{\mathrm{T}}\text{ at the moving wall, and}\quad \boldsymbol{U}=(0,0,0)^{\mathrm{T}}\text{ at the walls,}$$

where U_{lid} is the velocity imposed at the moving wall, also called lid.

The Navier–Stokes equations are non-linear due to the convective term $(\boldsymbol{U}\cdot\nabla)\boldsymbol{U}$ in the left-hand side of the momentum equations, and unfortunately no universal solution can be found. Already the proof of existence and smoothness of solutions in three dimension and whether their energy remains bounded in time is one of the unsolved

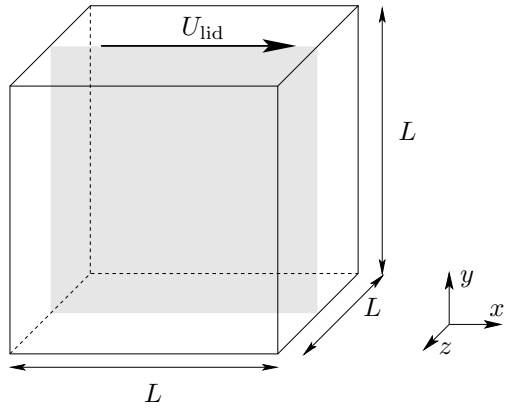

FIGURE 2.1 – Sketch of a cubic cavity of side length L, driven by a top lid with a velocity $\boldsymbol{U} = (U_{\text{lid}}, 0, 0)^{\mathrm{T}}$.

millennium problems [53]. Regardless of this, one can calculate simple flows or approximate solutions with the aid of a computer. The only way to find an approximation of the solution - except for trivial or simplified cases - is to solve (2.1) numerically. To that end (2.1) is typically discretized to reduce the infinite number of degrees of freedom to a finite number.

Viscous Scaling All the four independent physical parameters of the system (side length, density, kinematic viscosity and lid velocity) can be expressed in three fundamental units (length, time, and mass). The π-Buckingham theorem implies that the Navier–Stokes equations can be recast into a system of equation involving only one parameter: the Reynolds number, denoted Re. Throughout this thesis, we will use a viscous scaling. We use the length of the domain, the kinematic viscosity and the density of the fluid to describe the relevant spatial, temporal, velocity and pressure scales:

$$\boldsymbol{x} = L\,\boldsymbol{x}^*, \quad t = \frac{L^2}{\nu}\,t^*, \quad \boldsymbol{U} = \frac{\nu}{L}\,\boldsymbol{U}^*, \quad P = \frac{\rho\nu^2}{L^2}\,P^*,$$

where the starred quantities are dimensionless quantities. This leads to

$$\left(\frac{\partial}{\partial t^*} + \boldsymbol{U}^* \cdot \nabla_*\right)\boldsymbol{U}^* = -\nabla_* P^* + \Delta_* \boldsymbol{U}^*, \tag{2.2a}$$

$$\nabla_* \cdot \boldsymbol{U}^* = 0, \tag{2.2b}$$

where ∇_* is the nabla operator in the dimensionless coordinates. In this scaling, the Reynolds number appears in the boundary conditions. In the case of a lid-driven cavity, the boundary conditions are then

$$\boldsymbol{U}^* = (\mathrm{Re}, 0, 0)^{\mathrm{T}} \text{ at the lid, and} \quad \boldsymbol{U}^* = 0 \text{ at the walls,} \tag{2.3}$$

where the Reynolds number Re is defined as

$$\mathrm{Re} = \frac{U_{\mathrm{lid}} L}{\nu}.$$

In the rest of the thesis, the $*$ symbol will be dropped for the sake of a better readability. Note that in the frequently used convective scaling, $1/\mathrm{Re}$ appears in front of the viscous term.

2.2 The Navier–Stokes Equations as a Dynamical System

The Navier–Stokes equations can be seen as a dynamical system in the form

$$\frac{\partial}{\partial t}\mathcal{B}\boldsymbol{q} = \mathcal{F}(\boldsymbol{q}). \tag{2.4}$$

In this case, $\boldsymbol{q} = (\boldsymbol{U}, P)^{\mathrm{T}}$, $\mathcal{B}$ is a operator selecting the variables for which their variations in time explicitly appears in the equations, *i.e.* the velocity components:

$$\mathcal{B} = \begin{pmatrix} \mathbf{1}_{d\times d} & \mathbf{0}_{d\times 1} \\ \mathbf{0}_{1\times d} & \mathbf{0}_{1\times 1} \end{pmatrix} \tag{2.5}$$

and the non-linear vector operator $\mathcal{F}$ is

$$\mathcal{F}(\boldsymbol{q}) = \begin{pmatrix} -(\boldsymbol{U}\cdot\nabla)\boldsymbol{U} - \nabla P + \Delta \boldsymbol{U} \\ \nabla \cdot \boldsymbol{U} \end{pmatrix}, \tag{2.6}$$

and the boundary conditions (2.3). The first line of the operators correspond to the d momentum equations, and the last line to the incompressibility constraint.

In this dissertation, we will focus on particular trajectories of the dynamical system that are the fixed points of $\mathcal{F}$. They do not depend on time and for that reason, they are solutions of the steady problem

$$\mathcal{F}(\boldsymbol{q}_0) = 0. \tag{2.7}$$

Finding the roots $\boldsymbol{q}_0$ can be done analytically in some simple cases, however, most of the time one has to apply a root finding algorithm like a Newton method. Of interest is also the *stability* the steady solution $\boldsymbol{q}_0$. But let us first define what we mean by that.

2.2.1 Stability of an Equilibrium

We call an equilibrium $\boldsymbol{q}_e(\boldsymbol{x}, t)$ a trajectory in the phase space which satisfies some temporal symmetry. A fixed-point $\boldsymbol{q}_0(\boldsymbol{x}, t)$ is invariant to translations in time *i.e.* $\boldsymbol{q}_0(\boldsymbol{x}, 0) - \boldsymbol{q}_0(\boldsymbol{x}, t) = 0$, while a closed orbit of period T $\boldsymbol{q}_T(\boldsymbol{x}, t)$ satisfies the relation $\boldsymbol{q}_T(\boldsymbol{x}, t) - \boldsymbol{q}_T(\boldsymbol{x}, t + T) = 0$.

There are different definitions of stability of an equilibrium. Three of them are presented here with order of increasing restriction.

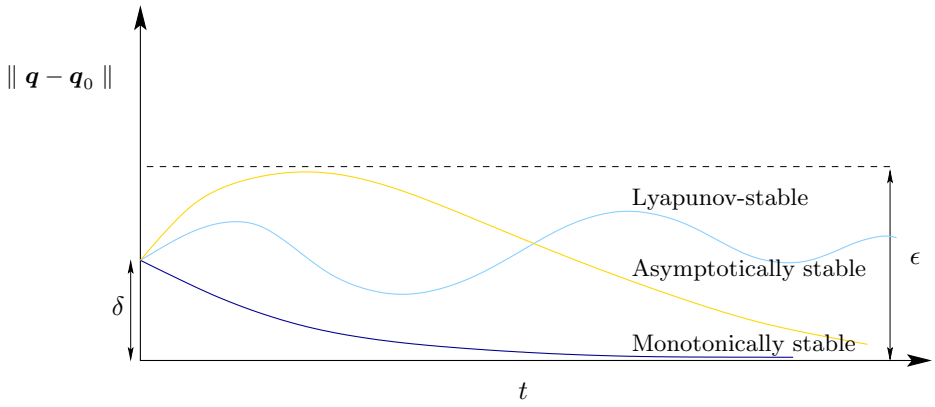

FIGURE 2.2 – Sketch illustrating the different stability definitions.

Lyapunov Stability The equilibrium $\boldsymbol{q}_e$ is said to be Lyapunov-stable if $\forall \epsilon > 0, \exists \delta(\epsilon) > 0$ such that if $\| \boldsymbol{q}(\boldsymbol{x}, 0) - \boldsymbol{q}_e(\boldsymbol{x}, 0) \| < \delta$ then $\forall t > 0$ we have $\| \boldsymbol{q}(\boldsymbol{x}, t) - \boldsymbol{q}_e(\boldsymbol{x}, t) \| < \epsilon$. In other words, if the solution $\boldsymbol{q}$ is initiated close enough to the equilibrium $\boldsymbol{q}_0$ (within a distance δ in some norm), it will stay close "enough" for all future times (within a distance ϵ).

Asymptotic Stability An equilibrium is said to be *asymptotically* stable if it is Lyapunov stable and $\exists \delta > 0$ such that if $\| \boldsymbol{q}(\boldsymbol{x}, 0) - \boldsymbol{q}_e(\boldsymbol{x}, 0) \| < \delta$, then $\lim_{t \to \infty} \| \boldsymbol{q}(\boldsymbol{x}, t) - \boldsymbol{q}_e(\boldsymbol{x}, t) \| = 0$. If the Lyapunov stability allowed for a little room ϵ between one perturbed solution and the equilibrium in the long run, this is not the case of the asymptotic stability, which requires that at an infinite time, the perturbed trajectory returns to the equilibrium.

Monotonic Stability An equilibrium is said to be *monotonically* stable if it is asymptotically stable and if $\exists \alpha > 0, \exists \beta > 0$ and $\exists \delta > 0$ such that if $\| \boldsymbol{q}(\boldsymbol{x}, 0) - \boldsymbol{q}_e(\boldsymbol{x}, 0) \| < \delta$ then $\| \boldsymbol{q}(\boldsymbol{x}, t) - \boldsymbol{q}_e(\boldsymbol{x}, t) \| < \alpha \| \boldsymbol{q}(\boldsymbol{x}, 0) - \boldsymbol{q}_e(\boldsymbol{x}, 0) \| \, \mathrm{e}^{-\beta t}$.

While asymptotic stability only required convergence as time goes to infinity and therefore allowed for intermediate growth of the perturbation in some norm, monotonic stability requires that if the initial distance from the equilibrium is small enough, the perturbation decays exponentially. Sometimes this is also called *exponentially* stable. The difference between these definitions of stability is sketched in fig. 2.2.

Studying the Lyapunov stability is particularly relevant for Hamiltonian systems that preserve energy. A small change of energy in the initial condition leads to a change in the total system energy. Since the energy is preserved the new state can be close to the initial one, but is never equal to it. The asymptotic stability is characteristic for dissipative system, which is the case of viscous flows. If the system is stable, a small energy addition to a dissipative system will be dissipated, so that it will return to the stable state. The monotonic instability should be considered together with a more general case of so-called "non-modal" instability, and is not relevant to the present

study.

2.3 Linear Stability Analysis

The linear stability analysis considers small perturbations at all times such that non-linear terms can be neglected. If a basic state (equilibrium) is linearly stable (all small perturbations decay exponentially as $t \to \infty$), then the basic state is asymptotically stable. For more details and extensions, we shall refer to the following non-exhaustive list of classical text books [35, 47, 46, 64, 71, 147].

2.3.1 General Case

Let us decompose the state variable $\boldsymbol{q}$ in the vicinity of a fixed point $\boldsymbol{q}_0$ as

$$\boldsymbol{q}(\boldsymbol{x}, t) = \boldsymbol{q}_0(\boldsymbol{x}) + \boldsymbol{q}'(\boldsymbol{x}, t),$$

where $\boldsymbol{q}'$ is an infinitesimal deviation from a fixed point $\boldsymbol{q}_0$ and in some norm $\| \boldsymbol{q}' \| \ll 1$. Inserting this decomposition in (2.4), and making use of (2.7) yields

$$\begin{aligned} \frac{\partial}{\partial t}\mathcal{B}\boldsymbol{q}' &= \mathcal{F}(\boldsymbol{q}_0 + \boldsymbol{q}') \\ &= \mathcal{F}(\boldsymbol{q}_0) + \frac{\partial \mathcal{F}(\boldsymbol{q}_0)}{\partial \boldsymbol{q}_0} \cdot \boldsymbol{q}' + NL(\boldsymbol{q}') \\ &= 0 + \mathcal{A}(\boldsymbol{q}_0) \cdot \boldsymbol{q}' + \mathcal{O}(\| \boldsymbol{q}' \|^2) \end{aligned}$$

where $\mathcal{A}(\boldsymbol{q}_0)$ is the linearization of the non-linear operator $\mathcal{F}$ around the fixed point $\boldsymbol{q}_0$, and $NL(\boldsymbol{q}')$ are the non-linear higher order terms. Neglecting this non-linear part gives the linearized equations for the perturbations

$$\frac{\partial}{\partial t}\mathcal{B}\boldsymbol{q}' = \mathcal{A}(\boldsymbol{q}_0) \cdot \boldsymbol{q}'.$$

In the same manner, inserting the deviations in the boundary conditions of the system yields homogeneous boundary conditions for the linear problem.

As the operator $\mathcal{A}(\boldsymbol{q}_0)$ is linear and its coefficients are constant in time, one can decompose the solution as a superposition of solutions. Using homogeneity in time, one can decompose the perturbation as being the sum of normal modes

$$\boldsymbol{q}'(\boldsymbol{x}, t) = \sum_i \hat{\boldsymbol{q}}_i(\boldsymbol{x}) \mathrm{e}^{\gamma_i t} \quad + \text{c.c.}, \tag{2.8}$$

where $\gamma_i \in \mathbb{C}$, the mode $\hat{\boldsymbol{q}}_i$ is a vector field that can be complex valued, and 'c.c.' denotes the complex conjugate. The real part $\Re(\gamma_i)$ denotes the growth rate of the mode, while the imaginary part $\Im(\gamma_i)$ its angular frequency. Inserting this decomposition into the linearized equations gives then a generalized eigenvalue problem:

$$\gamma_i \mathcal{B}\hat{\boldsymbol{q}}_i = \mathcal{A}(\boldsymbol{q}_0) \cdot \hat{\boldsymbol{q}}_i. \tag{2.9}$$

Depending on the signs of the real part of the eigenvalues, the linear stability of the system can be characterized.

- If $\max_i \Re(\gamma_i) < 0$ then the equilibrium is *asymptotically stable*.
- If $\max_i \Re(\gamma_i) = 0$ then the equilibrium is *marginally stable*.
- If $\max_i \Re(\gamma_i) > 0$ then the equilibrium is *unstable*.

In case of marginal stability the linear stability is not conclusive and the non-linear part of the dynamical system might play a relevant role for the stability of the system. Furthermore the imaginary part of the eigenvalue gives information on the oscillatory nature of the perturbation.

- If $\Im(\gamma_i) = 0$ the perturbations associated with the eigenmode is *not* oscillating.
- If $\Im(\gamma_i) \neq 0$ the perturbations associated with the eigenmode is oscillating, with an oscillation frequency $\omega = \Im(\gamma_i)$.

To characterize the stability boundary of the dynamical system with respect to a parameter α, one needs to find the critical parameter α_c such that $\max_i \Re(\gamma_i(\alpha_c)) = 0$. Linear instability is sufficient for instability. But some systems may become unstable despite of linear stability. They may be unstable depending on the magnitude of the perturbation, the equilibrium is then *conditionally stable*.

2.3.2 Linear Stability Analysis Applied to the Navier–Stokes Equations

In case of the Navier–Stokes equations, the variable $\boldsymbol{q} = (\boldsymbol{U}, P)^{\mathrm{T}}$ is decomposed into the fixed point $\boldsymbol{q}_0 = (\boldsymbol{u}_0, p_0)^{\mathrm{T}}$ also called *basic flow* or *basic state* and the perturbation $\boldsymbol{q'} = (\boldsymbol{u'}, p')^{\mathrm{T}}$. Inserting this decomposition in (2.2a) gives the non-linear equation for the perturbation:

$$\left(\frac{\partial}{\partial t} + \boldsymbol{u_0} \cdot \nabla\right) \boldsymbol{u'} + \boldsymbol{u'} \cdot \nabla \boldsymbol{u}_0 + \boldsymbol{u'} \cdot \nabla \boldsymbol{u'} = -\nabla p' + \Delta \boldsymbol{u'}, \tag{2.10a}$$

$$\nabla \cdot \boldsymbol{u'} = 0\ . \tag{2.10b}$$

Neglecting the non-linear terms, we obtain the linearized Navier–Stokes equations:

$$(\frac{\partial}{\partial t} + \boldsymbol{u_0} \cdot \nabla)\boldsymbol{u'} + \boldsymbol{u'} \cdot \nabla \boldsymbol{u}_0 = -\nabla p' + \Delta \boldsymbol{u'}, \tag{2.11a}$$

$$\nabla \cdot \boldsymbol{u'} = 0. \tag{2.11b}$$

As in (2.8) the perturbation is decomposed into normal modes of complex amplitudes $\hat{\boldsymbol{q}}_i = (\hat{\boldsymbol{u}}_i, \hat{p}_i)$, and we obtain the generalized eigenvalue problem

$$-\boldsymbol{u_0} \cdot \nabla \hat{\boldsymbol{u}}_i - \hat{\boldsymbol{u}}_i \cdot \nabla \boldsymbol{u}_0 - \nabla \hat{p}_i + \Delta \hat{\boldsymbol{u}}_i = \gamma_i \hat{\boldsymbol{u}}_i, \tag{2.12a}$$

$$\nabla \cdot \hat{\boldsymbol{u}}_i = 0, \tag{2.12b}$$

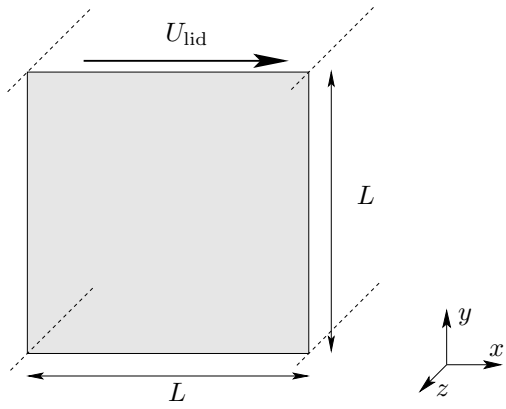

FIGURE 2.3 – Sketch of an infinitely extended lid-driven cavity of square cross section.

together with the boundary conditions of the perturbation velocity mode $\hat{\boldsymbol{u}}_i = (0,0,0)^{\mathrm{T}}$ at the moving and steady walls. The Reynolds number appears then only in the boundary equation of the basic state. To find the linear stability boundary, one has to find the Reynolds number Re_c for which the leading eigenvalue has a real part equal to zero.

2.3.3 Finite Size Geometries versus Infinitely Extended Geometries

So far, the example setup that we considered is bounded in all three spatial directions, we can say that the domain has a *finite size*. However, one could also have a setup with an homogenous spanwise direction in which the flow is not bounded, as sketched for instance in fig. 2.3. We can say that the domain is *infinitely extended*. In that case the basic flow variables could exhibit a translational invariance in the spanwise direction z [1].

In case of *finite size* geometry, both the basic state and the perturbations do not have spatial homogeneous direction. In this regard, no further assumptions can be made with respect to the general case and the Jacobian of the system $\mathcal{A}(\boldsymbol{q}_0)$ is a only real valued operator. This has the consequence that imaginary eigenvalues and eigenmodes of this operator arise in complex conjugated pairs [2]. From the structure of (2.8) one can see that the perturbation associated to the eigenmode is then the same as the one of associated with it conjugate since

$$\hat{\boldsymbol{q}}_i \mathrm{e}^{\gamma_i t} + \hat{\boldsymbol{q}}_i^* \mathrm{e}^{\gamma_i^* t} = \hat{\boldsymbol{q}}_j^* \mathrm{e}^{\gamma_j^* t} + \hat{\boldsymbol{q}}_j \mathrm{e}^{\gamma_j t},$$

where the subscript j denotes the complex conjugate mode to mode i, *i.e.* $\lambda_j = \lambda_i^*$ and $\hat{\boldsymbol{q}}_j = \hat{\boldsymbol{q}}_i^*$.

1. The basic flow could also be periodic in z but this is not treated here.
2. If γ_i, $\hat{q}_i$ are eigenvalue and eigenvector of the real valued operator $\mathcal{A}(\boldsymbol{q}_0)$, then $\gamma_i^* \hat{\boldsymbol{q}}_i^* = (\gamma_i \hat{\boldsymbol{q}}_i)^* = (\mathcal{A}(\boldsymbol{q}_0) \cdot \hat{\boldsymbol{q}}_i)^* = \mathcal{A}^*(\boldsymbol{q}_0) \cdot \hat{\boldsymbol{q}}_i^* = \mathcal{A}(\boldsymbol{q}_0) \cdot \hat{\boldsymbol{q}}_i^*$.

In case of an *infinitely extended* geometry, one can restrict the basic state to depend on one spatial variable less. In the case sketched in fig. 2.3, the basic flow exhibits a translational symmetry in the z-direction, and one can restrict the basic flow variable to be two dimensional, *i.e.* $\boldsymbol{q}_0 = \boldsymbol{q}_0(x, y)$. However, the perturbations can be three dimensional, that is $\boldsymbol{q}' = \boldsymbol{q}'(x, y, z)$, and using the homogeneity in z, one can apply a Fourier transform in the z-direction. Using the linearity of the system of equations one can consider the perturbation associated with only one wavenumber $k \in \mathbb{R}$, *i.e.*

$$\boldsymbol{q}'(x, y, z, t) = \sum_i \hat{\boldsymbol{q}}_i(x, y, k) \mathrm{e}^{\gamma_i t + \mathrm{i} k z} \quad + \text{c.c.} \tag{2.13}$$

The wavenumber k is then an additional parameter. The eigenvalue problem reads then

$$\gamma_i \mathcal{B} \hat{\boldsymbol{q}}_i = \mathcal{A}(\boldsymbol{q}_0, k) \cdot \hat{\boldsymbol{q}}_i \tag{2.14}$$

and $\mathcal{A}$ is a complex valued operator. One can then distinguish a propagation speed c given by

$$c = -\frac{\Im(\gamma_i)}{k}$$

and the direction of propagation is given by the sign of c. It is of course *a priori* not known since it depends on the eigenvalue.

For symmetry reasons, pairs of conjugate eigenvalues arise. The perturbation associated to one eigenmode is propagating in one direction and the one associated to the conjugate eigenvalue propagates in the opposite direction. However, this is not necessarily the case: for instance if there was a non-zero spanwise component of the basic flow (for example due to a spanwise pressure gradient or the lid motion having a non-zero spanwise component), the property $\mathcal{A}(\boldsymbol{q}_0, k) = \mathcal{A}(\boldsymbol{q}_0, k)^*$ is not verified anymore and the eigenvalues do not necessarily arise in conjugate pairs.

In contrast with the finite size geometry case, the Reynolds number is not the only parameter anymore. A second parameter the wavenumber k can be continuously varied and one can find pairs of parameters Re_n and k_n such that the real part of the leading eigenvalue is zero: $\Re(\gamma_i(\mathrm{Re}_n, k_n)) = 0$. These pairs of parameters form the *neutral* curves $\mathrm{Re}_n(k_n)$, and form the ensemble of potential critical parameters $\{(\mathrm{Re}_n, k_n)\}$. The critical pair of parameters Re_c and k_c is defined as the pair of neutral parameters having the lowest Re_n. In other words

$$(\mathrm{Re}_c, k_c) = \underset{(\mathrm{Re},k)\in\{(\mathrm{Re}_n,k_n)\}}{\arg\min} (\mathrm{Re})\,. \tag{2.15}$$

This amounts to a finding a minimum and various strategies can be adopted. For more details, we refer to Chapter 3.

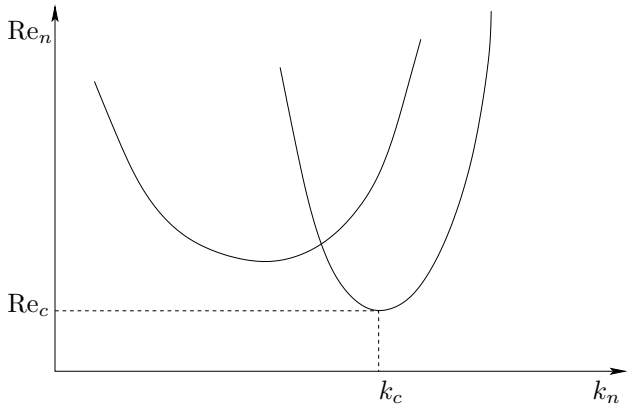

FIGURE 2.4 – Sketch illustrating the definition of neutral curves $Re_n(k_n)$ and of critical parameters (Re_c, k_c). The two solid lines denote two different neutral curves at which different modes are marginally stable.

2.4 A Posteriori Energy Budgets

2.4.1 The Reynolds-Orr Equation

In order to understand the mechanisms of the instability associated with the critical mode, examining carefully at the energy transfer between the basic state and the perturbation associated with the mode can be relevant. To that end, we define the total kinetic energy of the perturbation $\mathcal{E}(t)$ as the integral over the volume V occupied by the fluid of the local kinetic energy of the perturbation:

$$\mathcal{E}(t) = \frac{1}{2}\int_V \boldsymbol{u}' \cdot \boldsymbol{u}' \, \mathrm{d}V \ . \tag{2.16}$$

We note that the rate of change of the total kinetic energy can be expressed as a function of the time derivative of the perturbation velocity:

$$\int_V \frac{\partial}{\partial t}\mathcal{E} \, \mathrm{d}V = \int_V \frac{1}{2}\frac{\partial}{\partial t}\boldsymbol{u'}^2 \, \mathrm{d}V = \int_V \boldsymbol{u'}\frac{\partial}{\partial t}\boldsymbol{u'} \, \mathrm{d}V. \tag{2.17}$$

Using the non-linear equations for the perturbations (2.10a), performing integration by parts, using the incompressibility constraint, and the fact that $\boldsymbol{u'} \cdot \boldsymbol{n} = 0$ where $\boldsymbol{n}$ is the outward pointing normal of the boundary, one obtains the Reynolds-Orr equation

$$\frac{\partial \mathcal{E}}{\partial t} = -\int \boldsymbol{u}' \cdot (\boldsymbol{u}' \cdot \nabla \boldsymbol{u}_0) \, \mathrm{d}V - \int \nabla \boldsymbol{u}' : \nabla \boldsymbol{u}' \mathrm{d}V. \tag{2.18}$$

In particular, one can inspect the perturbation associated to one eigenmode,

$$\boldsymbol{u}' = \hat{\boldsymbol{u}}_i \mathrm{e}^{\lambda_i t} + \mathrm{c.c.} \tag{2.19}$$

It is important to note that if one uses the eigenmode instead *via*

$$\int_V \lambda_i \hat{\boldsymbol{q}}_i^* \cdot \mathcal{B} \cdot \hat{\boldsymbol{q}}_i \mathrm{d}V = \int_V \lambda_i \hat{\boldsymbol{q}}_i^* \cdot \mathcal{A}(\boldsymbol{q}_0) \cdot \hat{\boldsymbol{q}}_i \mathrm{d}V, \tag{2.20}$$

one obtains a different Reynolds-Orr equation as imaginary terms do not vanish, see [62].

2.4.2 Energy budgets

The Reynolds–Orr equation can be rewritten as

$$\frac{1}{D^*}\frac{\partial}{\partial t}\mathcal{E} = -1 + \sum_{j=1}^{4}\int_V i_j \,\mathrm{d}V, \tag{2.21}$$

which has been rescaled here by the dissipative term

$$D^* = \int_V D \,\mathrm{d}V = \int_V \nabla \boldsymbol{u'} : \nabla \boldsymbol{u'} \,\mathrm{d}V,$$

and where

$$\begin{aligned} i_1 &= -\frac{1}{D^*}\boldsymbol{u}_\perp \cdot (\boldsymbol{u}_\perp \cdot \nabla)\,\boldsymbol{u}_0, \\ i_2 &= -\frac{1}{D^*}\boldsymbol{u}_\parallel \cdot (\boldsymbol{u}_\perp \cdot \nabla)\,\boldsymbol{u}_0, \\ i_3 &= -\frac{1}{D^*}\boldsymbol{u}_\perp \cdot \big(\boldsymbol{u}_\parallel \cdot \nabla\big)\,\boldsymbol{u}_0, \\ i_4 &= -\frac{1}{D^*}\boldsymbol{u}_\parallel \cdot \big(\boldsymbol{u}_\parallel \cdot \nabla\big)\,\boldsymbol{u}_0, \end{aligned} \tag{2.22}$$

in which the perturbation velocity has been decomposed into components tangential and perpendicular to the basic state, as done in [5]

$$\boldsymbol{u}_\parallel = \frac{(\boldsymbol{u}_0 \cdot \boldsymbol{u'})\boldsymbol{u}_0}{\parallel \boldsymbol{u}_0 \parallel^2} \quad \text{and} \quad \boldsymbol{u}_\perp = \boldsymbol{u'} - \boldsymbol{u}_\parallel.$$

This decomposition is particularly useful in order to know where and which mechanisms are efficient in extracting the energy from the basic state. Crudely simplifying for the analogy, let us consider that the basic flow has a linear velocity profile and is constant in streamwise direction as depicted in fig. 2.5. Moreover we shall see in Chapters 4, 5 and 6 that the mechanism represented by i_2, is in most of the cases responsible for the larger part of the growth rate of the kinetic perturbation energy. We follow the interpretation of the sign of i_2 given by Albensoeder *et al.* [5]. In fig. 2.5, the upper left and lower right quadrants are filled in blue to indicate that i_2 is positive when then perturbation velocity $\boldsymbol{u'}$ lies in these quadrants.

In the upper left quadrant, the production of perturbation energy comes from the transport downstream (as $\boldsymbol{u}_\parallel \cdot \boldsymbol{e}_\parallel > 0$) of the high momentum of the basic flow to regions with a low momentum. In the lower right quadrant, the production of perturbation energy comes from the transport of low momentum from the basic flow to regions with a higher momentum, upstream (as $\boldsymbol{u}_\parallel \cdot \boldsymbol{e}_\parallel < 0$). In the other quadrants, i_2 has a stabilizing effect. Albensoeder *et al.* [5] argued as well that if the basic

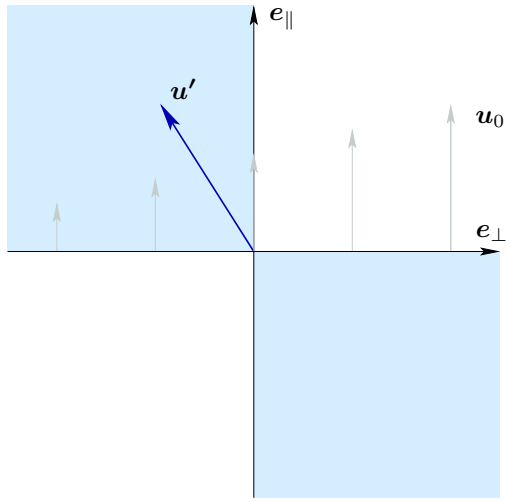

FIGURE 2.5 – Explanation of the sign of i_2 depending on the orientation of $\boldsymbol{u'}$ with respect to $\boldsymbol{u}_0$. The basic flow is depicted with the grey arrows, while the pertubration velocity is shown in dark blue. Depending on the direction of the velocity perturbation, the sign of i_2 changes. If the dark blue arrow lies in a light blue quadrant, i_2 is positive, otherwise i_2 is negative.

flow streamlines are curved, and that the momentum is decreasing radially outward (where the considered radius is the streamline curvature radius, or the radius from the center of a vortex), then high values of i_2 in such a region is a marker for an centrifugal instability. In later chapters, we shall argue in the same way, although for two-dimensional basic inviscid flows, more a elaborated local criteria for centrifugal instability have been introduced by Bayly *et al.* [19] or Sipp & Jacquin [163].

Another interpretation is given by Loiseau *et al.* [100], taking an anolgy with structures observed in shear flows [50, 26] or wall-bounded turbulence [36]. The streamwise component of the perturbation could be associated to low- or high-speed *streak*, depending on whether $\boldsymbol{u}_\parallel \cdot \boldsymbol{u}_0 < 0$ or $\boldsymbol{u}_\parallel \cdot \boldsymbol{u}_0 < 0$, while the perpendicular component of the perturbation could represent a *vortex*. With this simplification in mind, the mechanisms behind i_1, i_2, i_3 and i_4 can respectively be thought as

- a self promoting mechanism where counter-rotating vortices extract energy from the basic flow and promote itself.
- a *lift-up* mechanism: counter-rotating vortices extract the energy from the basic flow and in turn promotes streaky structures.
- an *anti-lift-up* mechanism: streaks extract the energy from the basic flow and promotes vortex structures.
- a self promoting mechanism where streaks extract the energy from the basic flow and promote themselves.

Depending on their average sign, one can then clearly see if a mechanism is responsible for quenching or promoting the considered eigenmode. If the numerical

implementation is correct the production rate should be equal to 1 when the mode is neutral or critical, less than one when the mode stable - that is that the viscous effects dissipate more energy than what can be extracted - and conversely if the mode is unstable.

3 Numerical Methods

In this chapter, the methods used throughout the thesis will be presented. In a first part we will describe the spatial discretization used in the Finite Element method (FEM) library FEniCS [97, 8], and in Nek5000 which uses the Spectral Element Method (SEM), introduced by Patera [120]. In general, these methods are very similar in that they both are Galerkin projections. Then, the temporal discretization used in Nek5000 will be explicated. A presentation of the methods employed to perform a linear stability analysis will follow in a natural order: first methods to solve the basic flow and then technique to solve large eigenvalue problems. In these both steps the method of solution strongly depends on the size of the problem, *i.e.* whether the problem is 3D or whether the basic flow is 2D and the perturbation are described by Fourier modes in the spanwise direction.

3.1 Spatial Discretizations

3.1.1 Galerkin Methods

Galerkin methods are a subgroup of the so-called methods of *mean weighted residuals* (MWR) [56]. The assumption of the MWR methods is that the solution u can be sufficiently well approximated by linear combination of functions ϕ_i called trial functions. The unknowns are the coefficients u_i multiplying these trial functions and can be found by minimization in some norm of the residual

$$\mathcal{R} = \mathcal{L}\left(u - \sum_{i=1}^{N} u_i \phi_i\right), \tag{3.1}$$

where $\mathcal{L}$ is the (non)linear operator. In particular one can define norms with a weight function

$$\int_V W_n \mathcal{R} \, \mathrm{d}V = 0, \quad n = 1, ..., N \tag{3.2}$$

which leads then to N equations, and where W_n are the weight functions, also called test functions. The method obtained depends on the choice of the test functions. In

the case of Galerkin methods, the test functions are set to be the same as the trial functions, and (3.1.1) is called *weak* or *variational formulation*.

Notations Before going further, let us denote the L^2 scalar product of two vector fields $\boldsymbol{a}$, $\boldsymbol{b}$ defined on the volume V

$$\langle \boldsymbol{a}, \boldsymbol{b} \rangle = \int_V \boldsymbol{a} \cdot \boldsymbol{b} \, \mathrm{d}V \tag{3.3}$$

Moreover, let us recall the definition of the Sobolev spaces. The functional space $L^2(V)$ is the space of function with support in V that are square integrable

$$L^2(V) = \left\{ f \text{ such that } \langle f, f \rangle^{1/2} < \infty \right\}. \tag{3.4}$$

The functional space $H^1(V)$ further requires that the first spatial derivatives of the function f are also square integrable

$$L^2(V) = \left\{ f \in L^2(V) \text{ such that } \left(\langle f, f \rangle + \langle \nabla f, \nabla f \rangle \right)^{1/2} < \infty \right\}. \tag{3.5}$$

We note $H_0^1(V)$ and $H_b^1(V)$ the restriction of of $H^1(V)$ to the functions satisfying homogeneous and non-homogeneous Dirichlet boundary conditions, respectively.

Variational Formulation

In the case of the Navier–Stokes equations the variational formulation is obtained by multiplying (2.2a) by the test functions $\boldsymbol{v}$ and q and integrating the equations, and performing integration by part of viscous terms, and eventually the pressure term as well. The variational formulation reads

$$\text{Find } (\boldsymbol{u}, p) \in H_b^1(V)^d \times L^2(V) \text{ such that}$$

$$\left\langle \left(\frac{\partial}{\partial t} + \boldsymbol{u} \cdot \nabla \right) \boldsymbol{u}, \boldsymbol{v} \right\rangle + \langle \nabla \boldsymbol{u}, \nabla \boldsymbol{v} \rangle - \langle p, \nabla \cdot \boldsymbol{v} \rangle = 0, \quad \forall \boldsymbol{v} \in H_0^1(V)^d \tag{3.6a}$$

$$-\langle \nabla \cdot \boldsymbol{u}, q \rangle = 0, \quad \forall \boldsymbol{q} \in L_0^2(V) \tag{3.6b}$$

where d is the dimension of the velocity vector. In case of non-homogeneous Neumann boundary conditions, one would have extra integral terms, which we do not consider here. From the structure of this variational formulation, one can recognize that this problem is a saddle problem and that in the Navier–Stokes equations, the pressure plays the role of a Lagrangian multiplier of the continuity constraint.

In practice, one needs to find a sufficient approximation of these Sobolev spaces and it is done by limiting the choice of functions to piecewise polynomials of some degree. For instance, one can then discretize the velocity, the pressure and their test

functions in their respective basis of N_u and N_p piecewise polynomials $\boldsymbol{\pi}_i^u$ and π_i^p. That is

$$\boldsymbol{u}_h = \sum_{i=1}^{N_u} u_i \boldsymbol{\pi}_i^u(\boldsymbol{x}), \quad p_h = \sum_{i=1}^{N_p} p_i \pi_i^p(\boldsymbol{x})$$

where $\boldsymbol{u}_h$ and p_h are the velocity and pressure expressed in these bases, and we note $\mathbf{u} \in \mathbb{R}^{N_u}$ and $\mathbf{p} \in \mathbb{R}^{N_p}$ the vectors collecting the coefficients u_i and p_i. As mentioned earlier, in Galerkin methods the test functions $\boldsymbol{v}_h^n$ and $\boldsymbol{q}_h^m$ are nothing else than the functions composing the basis. All the terms in the variational form (3.6a) can then be expressed, for the test functions $\boldsymbol{\pi}_n^u$, π_m^p

$$\left\langle \frac{\partial}{\partial t}\boldsymbol{u}_h, \boldsymbol{v}_h^n \right\rangle = \sum_{i=1}^{N_u} \frac{\partial u_i}{\partial t} \sum_{n=1}^{N_u} \int_\Omega \boldsymbol{\pi}_i^u \cdot \boldsymbol{\pi}_n^u \mathrm{d}\boldsymbol{x} \tag{3.7}$$

$$\langle (\boldsymbol{u}_h \cdot \nabla)\, \boldsymbol{u}_h, \boldsymbol{v}_h^n \rangle = \sum_{i=1}^{N_u} u_i^2 \sum_{n=1}^{N_u} \int_\Omega \left[(\boldsymbol{\pi}_i^u \cdot \nabla)\, \boldsymbol{\pi}_i^u \right] \cdot \boldsymbol{\pi}_n^u \mathrm{d}\boldsymbol{x}, \tag{3.8}$$

$$\langle \nabla \boldsymbol{u}_h, \nabla \boldsymbol{v}_h^n \rangle = \sum_{i=1}^{N_u} u_i \sum_{n=1}^{N_u} \int_\Omega \nabla \boldsymbol{\pi}_i^u : \nabla \boldsymbol{\pi}_n^u \mathrm{d}\boldsymbol{x}, \tag{3.9}$$

$$\langle p, \nabla \cdot \boldsymbol{v} \rangle = \sum_{i=1}^{N_p} p_i \sum_{n=1}^{N_u} \int_\Omega \pi_i^p \nabla \cdot \boldsymbol{\pi}_n^u \mathrm{d}\boldsymbol{x}, \tag{3.10}$$

$$\langle \nabla \cdot \boldsymbol{u}_h, q_h \rangle = \sum_{i=1}^{N_u} u_i \sum_{n=1}^{N_p} \int_\Omega \pi_n^p \nabla \cdot \boldsymbol{\pi}_i^u \mathrm{d}\boldsymbol{x}. \tag{3.11}$$

The double sums can be recast in matrix vector formulations and the discretized variational formulation of the whole problem reads then

$$\begin{pmatrix} \partial/\partial t\, \mathbf{M} + \mathbf{C}(\mathbf{u}) + \mathbf{K} & \mathbf{D}^T \\ \mathbf{D} & 0 \end{pmatrix} \begin{pmatrix} \mathbf{u} \\ \mathbf{p} \end{pmatrix} \tag{3.12}$$

where $\mathbf{M}$, $\mathbf{C}(\mathbf{u})$, $\mathbf{K}$, and $\mathbf{D}$ are the matrix representation of (3.7, 3.8, 3.9 and 3.11), respectively. $\mathbf{M}$ is called *mass* matrix, and can be seen as being an approximation of the integral operation, $\mathbf{C}(\mathbf{u})\mathbf{u}$ represent the (non-linear) convection term, $\mathbf{K}$ is the *stiffness* matrix and represents the Laplacian operator, and finally $\mathbf{D}^T$ and $\mathbf{D}$ discretizations of the gradient and the divergence.

The difference between FEM as implemented in FEniCS and SEM in Nek5000 lies essentially in the choice of the test/trial functions, how the integration is performed and the shape of the elements. Although, one could argue that SEM are actually a particular example of FEM - Higher Order Finite Element Methods - and mainly historical reasons are at the origin of the different nomenclature. In fact, the "classical" finite element method uses Lagrangian or Hermitian polynomials at relatively low polynomial order ($p = 1, 2, 3$), while the SEM is based on some specific quadratures and Legendre polynomials of high order (typically $p > 5$) [74, 168].

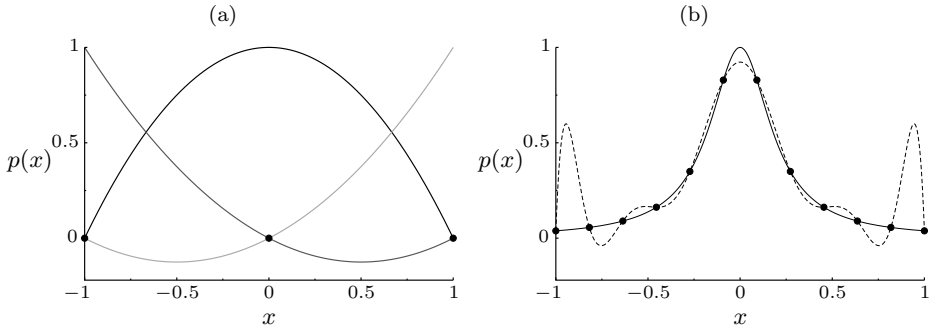

FIGURE 3.1 – (a) Lagrange polynomials of the 2nd order polynomial basis (solid lines), using a uniform quadrature. Quadrature points are shown by the black filled circles. (b) The evaluation of the function $f : x \to 1/(1 + 25x^2)$ is shown by a full line while the Lagrange interpolant of order 11 defined on a uniform quadrature is shown by the dashed line. Evaluations of f at the quadrature points are by black filled circles.

3.1.2 Finite Elements Method using FEniCS

According to FEniCS website,

> FEniCS is a popular open-source (LGPLv3) computing platform for solving partial differential equations (PDEs). FEniCS enables users to quickly translate scientific models into efficient finite element code. With the high-level Python and C++ interfaces to FEniCS, it is easy to get started, but FEniCS offers also powerful capabilities for more experienced programmers.

In this thesis, this finite element library has been used only to solve two-dimensional steady flow and related eigenvalue problems from linear stability, as the number of degrees of freedoms remains relatively low, *i.e.* of the order $\mathcal{O}(10^5)$. The variational formulations used then follow the variational formulation presented earlier, with some modifications depending on the symmetries of the system. To solve linear systems, the MUMPS library[10, 9] is used.

Taylor-Hood Element

In the FEniCS nomenclature, the most basic element basis for scalar fields is called Lagrange element and the quadrature used for the integration is uniformly distributed. In fig. 3.1a the three functions composing the basis of second order polynomials defined on [-1,1] is shown. By default, elements on FEniCS are triangles, for more details on meshing in FEniCS, see Alnaes *et al.* [8]. In the case of the Navier–Stokes equations, the velocity is a vector field and pressure a scalar field, and the variational formulation is one of a saddle problem. The Ladyzhenskaya–Babuška–Brezzi condition ensures that there is a solution of the saddle problem under certain conditions. It requires that the polynomial order of the pressure has to be lower than that of the velocity. In

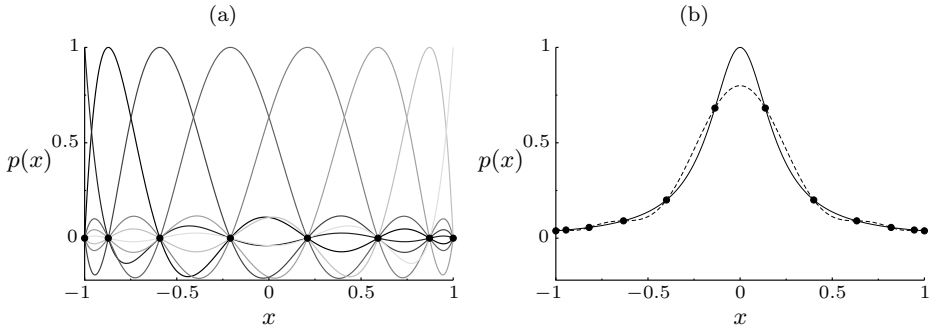

FIGURE 3.2 – (a) Legendre polynomials of the 7th order polynomial basis (solid lines), using a Gauss-Legendre-Lobatto quadrature (black filled circles). (b) The evaluation of the function $f : x \to 1/(1+25x^2)$ is shown by a full line while the Lagrange interpolant of order 11 defined on a uniform quadrature is shown by the dashed line. Evaluations of f at the quadrature points are by black filled circles.

the case of classical Taylor–Hood elements, one discretize velocity and pressure with piecewise polynomial of order 2 and 1, respectively. One could eventually use higher orders, but in the current implementation of FEniCS, only uniform grid are used. That can lead to spurious oscillations as shown in fig. 3.1b, where the function $x \to 1/1+25x^2$ is interpolated using Lagrange polynomials of order 11, on a uniform grid. Therefore when using FEniCS and Taylor-Hood elements, we shall restrict ourselves to low polynomial orders.

3.1.3 Spectral Element Method using Nek5000

In Nek5000, careful use of high-order polynomials is made. Lagrange interpolants are defined using Gauss–Legendre–Lobatto (GLL) quadrature (it includes quadrature nodes on the boundaries of the element) for the velocity and using Gauss-Legendre (GL) (quadrature nodes only inside the element) for the pressure. The polynomials of the 7th order basis defined with the GLL quadrature is displayed in fig. 3.2a. Similarly as in the FEM, the interpolation of a fractional functions is displayed for interpolation order 11 in fig. 3.2b. In contrast to the uniform grid distribution (fig. 3.1b), Runge oscillations seem to be damped because of the Gauss-type distribution of the nodes.

Moreover, an interesting property of these polynomials is that by construction, computing with the corresponding quadrature the integral $\int_{-1}^{1} L_i L_j \mathrm{d}x = w_i \delta_{i,i}$, where L_i are the Lagrange polynomials, w_i the weights of the quadrature and $\delta_{i,j}$ the Kronecker delta. The mass matrix is then diagonal and shown in fig. 3.3a for three 1-dimensional elements of order 5, defined on a GLL quadrature. This is, from a computational point of view an important property since its inverse is also diagonal and can be used as a preconditioner. Conversely, the stiffness matrix is block diagonal. Only quadrilateral mesh elements can be used in Nek5000. Although complex curved geometry could be handled through curvilinear formulation, the setups that we study are very simple and only rectangular or squared elements are used.

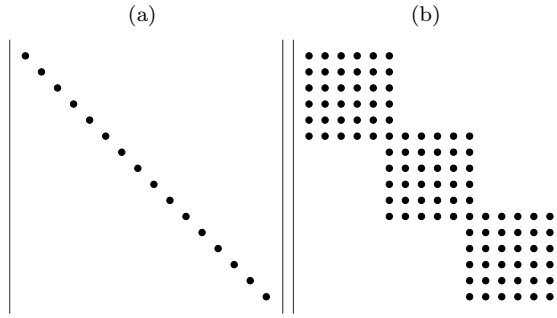

FIGURE 3.3 – Global mass matrix (a) and stiffness matrix (b) of 3 one dimensional spectral elements of polynomial order 5.

Moreover, the global matrices are never assembled in Nek5000, which uses a *matrix-free* approach. Instead of building the actual matrices, only their application on a vector is computed. This is only an advantage for large problems where the matrix cannot be kept in memory. This is especially relevant for higher-order polynomials, because the stiffness matrix is dense and loading the large block matrices would take more time than recomputing the coefficients. The algorithms to solve linear system are then restricted to Krylov based algorithms (GMRES, CG, ...), since the matrix itself cannot be accessed. This can be particularly efficient on modern and parallel architectures.

3.2 Temporal Discretization

FEniCS was only used to compute steady flows, and related eigenvalue problems. For time-dependent problems or larger problems, *i.e.* more than one million unknowns, Nek5000 is used. It is an unsteady solver, which relies on a particular time discretization, which will be briefly explained here. Most of this section follows Deville *et al.* [43].

The non-linearity of the Navier–Stokes equation arises only in the convection term $\mathbf{C}(\mathbf{u})$. To avoid having to solve a non-linear problem at each time step, a classical approach is to use a semi-implicit time-discretization. More precisely the diffusion and pressure terms are treated implicitly while the non-linear convective terms are treated explicitly. By doing so, the linear problem that is solved at each time step has also been made symmetric. To further enhance the prediction of the non-linear term, one can use an extrapolation procedure, based on the results of the previous time steps. The temporal scheme implemented in Nek5000 is called $\mathrm{BDF}_k/\mathrm{EXT}_k$, which stands for Backward Differentiation Formula of order k, and EXTrapolation of order k, the higher the order, the less stable is the scheme, but also the more accurate.

TABLE 3.1 – $\mathrm{BDF}_k/\mathrm{EXT}_k$ coefficients α_i γ_i as defined in (3.13a).

k	α_0	α_1	α_2	α_3	γ_0	γ_0	γ_0
1	1	-1			1		
2	3/2	-4/2	1/2		2	-1	
3	11/6	-18/6	9/6	-2/6	3	-3	1

Applied to the (3.12), this gives, in case of constant time steps Δt

$$\mathbf{M}\sum_{i}^{k}\frac{\alpha_i}{\Delta t}\mathbf{u}^{n+1-i}+\mathbf{K}\mathbf{u}^{n+1}+\mathbf{D}^T\mathbf{p}^{n+1}=-\sum_{j=n-2}^{n}\gamma_j\mathbf{C}(\mathbf{u})^j, \tag{3.13a}$$

$$\mathbf{D}\mathbf{u}^{n+1}=0, \tag{3.13b}$$

where α_i and γ_j are defined as in table 3.1 up to $k=3$ which is the highest time discretization order implemented in Nek5000. One can further decompose the pressure $\mathbf{p}^{n+1}=\mathbf{p}^n+\delta\mathbf{p}^{n+1}$, where the increment $\delta\mathbf{p}^{n+1}$ naturally goes to zero when the flow is steady. The pressure increment substitutes the pressure as the unknown for enforcing the continuity of the next time step velocity. Gathering all the explicit velocity terms in $\mathbf{f}$, the previous system of equation can be recast in the form

$$\begin{pmatrix}\mathbf{H} & \mathbf{D}^T\\ \mathbf{D} & \mathbf{0}\end{pmatrix}\begin{pmatrix}\mathbf{u}^{n+1}\\ \delta\mathbf{p}^{n+1}\end{pmatrix}=\begin{pmatrix}\mathbf{f}-\mathbf{D}^T\mathbf{p}^n\\ \mathbf{0}\end{pmatrix}, \tag{3.14}$$

where $\mathbf{H}$ is the discretization of the Helmholtz operator which depends on Δt. To gain generality one can modify it to

$$\begin{pmatrix}\mathbf{H} & -\mathbf{H}\mathbf{Q}\mathbf{D}^T\\ -\mathbf{D} & \mathbf{0}\end{pmatrix}\begin{pmatrix}\mathbf{u}^{n+1}\\ \delta\mathbf{p}^{n+1}\end{pmatrix}=\begin{pmatrix}\mathbf{f}-\mathbf{D}^T\mathbf{p}^n\\ \mathbf{0}\end{pmatrix}+\begin{pmatrix}\mathbf{r}^{n+1}\\ \mathbf{0}\end{pmatrix}, \tag{3.15}$$

where the residual $\mathbf{r}^{n+1}$ is accounting for the changes in the matrix, and $\mathbf{Q}$ is an arbitrary matrix. This matrix vector problem can be solved using a LU decomposition, which gives two sub-problems:

$$\begin{pmatrix}\mathbf{H} & \mathbf{0}\\ -\mathbf{D} & -\mathbf{D}\mathbf{Q}\mathbf{D}^T\end{pmatrix}\begin{pmatrix}\mathbf{u}^{*}\\ \delta\mathbf{p}^{n+1}\end{pmatrix}=\begin{pmatrix}\mathbf{f}-\mathbf{D}^{\mathbf{T}}\mathbf{p}^{\mathbf{n}}\\ 0\end{pmatrix} \tag{3.16}$$

and

$$\begin{pmatrix}\mathbf{I} & \mathbf{Q}\mathbf{D}^T\\ \mathbf{0} & \mathbf{I}\end{pmatrix}\begin{pmatrix}\mathbf{u}^{n+1}\\ \delta\mathbf{p}^{n+1}\end{pmatrix}=\begin{pmatrix}\mathbf{u}^{*}\\ \mathbf{p}^{n+1}\end{pmatrix}, \tag{3.17}$$

where the intermediate velocity $\mathbf{v}^*$ is not divergence free, and for the sake of simplicity the term with the residual has been neglected. Depending on the choice of $\mathbf{Q}$, different methods can be obtained. For instance if $\mathbf{Q}=\mathbf{H}^{-1}$ exactly, one recovers the exact same equations as before, and this is known as the Uzawa method. However, the inversion of $\mathbf{H}$ is not straightforward, and the Blair-Perot method is implemented in Nek5000, that is $\mathbf{Q}=\Delta t/\alpha_0\mathbf{M}^{-1}$. Keeping this in mind and observing (3.16), one can

easily see that the first line is a first guess of the velocity field, and the second line the Poisson equation for the pressure changes. The second system of equations is nothing else than the projection of the non divergence free velocity $\mathbf{u}^*$ onto the divergence free velocity $\mathbf{u}^{n+1}$. This is actually the origin of the well known projection method. The inversion of the mass matrix is trivial since it is diagonal. Using this diagonal matrix, it can be shown that the terms linked to the residuals $\mathbf{r}^{n+1}$ decay with $\mathcal{O}(\Delta t^2)$. Had not we used this decomposition of $\mathbf{p}^{n+1}$, the scheme would have been of order $\mathcal{O}(\Delta t)$ and eventually the residual would not have vanished when reaching a steady state. By setting $\mathbf{Q} = \Delta t/\alpha_0 \mathbf{M}^{-1}$, we approximated $\mathbf{H}^{-1}$ with a first-order approximation, one can naturally use higher order approximations of that inverse, yielding 4th or 6th order of accuracy in the time splitting. However, that would require a higher order time integration scheme, and domain of stability of the BDF_k schemes would shrink even more.

3.3 Computation of Steady States

We saw in Chapter 2 that studying the linear stability analysis of an equilibrium $\boldsymbol{q}_0$ required two steps: the first one being solving for the *non-linear* steady state equation. The objective of this section is to explain the different methods to accomplish that goal. The first idea is to use a Newton method. However, we will see that it has strong limitations in this context, and some state-of-the-art methods to circumvent these problems will be presented.

3.3.1 Newton Method

Algorithm

The Newton method is probably the most used method for solving non-linear system in the form $\mathcal{F}(\boldsymbol{x}) = 0$ and will only be briefly presented here only for completeness. Here, we apply it as the continuous level, however, it is possible to derive it as well after discretization. The Newton method is initiated using a first guess for the solution $\boldsymbol{x}_0$ and follows the steps:

1. Solve the linear system $\nabla\mathcal{F}(\boldsymbol{x}^k) \cdot \delta\boldsymbol{x}^k = -\mathcal{F}(\mathbf{x}^k)$;
2. Set the new iterate $\boldsymbol{x}^{k+1} = \boldsymbol{x}^k + \delta\boldsymbol{x}^k$;
3. Stopping criterion can be set with the norm of the increment $\parallel \delta\boldsymbol{x}_k \parallel$ or the norm of the residual $\parallel \mathcal{F}(\boldsymbol{x}_{k+1}) \parallel$.

In the case of the discretization of the steady Navier–Stokes equations using a Galerkin approach, the non-linear steady problem 2.7 that has to be solved to find the

steady state $\boldsymbol{q}_0 = (\boldsymbol{u}_0, p_0)$ reads

$$\int_V (\boldsymbol{u}_0^k \cdot \nabla)\boldsymbol{u}_0^k \cdot \boldsymbol{v}\,\mathrm{d}V + \int_V p_0^k \nabla \cdot \boldsymbol{v}\,\mathrm{d}V + \int_V \nabla \boldsymbol{u}_0^k : \nabla \boldsymbol{v}\,\mathrm{d}V = 0, \tag{3.18a}$$

$$\int_V q \nabla \cdot \boldsymbol{u}_0^k\,\mathrm{d}V = 0, \tag{3.18b}$$

where k is the index of the current step of the Newton algorithm. The linearization of (3.18a) around the current iterate $\boldsymbol{q}^k = (\boldsymbol{u}_0^k, p_0^k)$, $\nabla J(\boldsymbol{q}_0^k) \cdot \delta \boldsymbol{q}^k$ is given by

$$\int_V (\boldsymbol{u}_0^k \cdot \nabla)\delta\boldsymbol{u}^k \cdot \boldsymbol{v}\,\mathrm{d}V + \int_V (\delta\boldsymbol{u}^k \cdot \nabla)\boldsymbol{u}_0^k \cdot \boldsymbol{v}\,\mathrm{d}V + \int_V \delta p^k \nabla \cdot \boldsymbol{v}\,\mathrm{d}V + \int_V \nabla \delta\boldsymbol{u}^k : \nabla \boldsymbol{v}\,\mathrm{d}V = 0, \tag{3.19a}$$

$$\int_V q \nabla \cdot \delta\boldsymbol{u}^k\,\mathrm{d}V = 0. \tag{3.19b}$$

Using the same discretization as presented above, one obtains a vector corresponding to the discretized Navier–Stokes equations evaluated at $\boldsymbol{q}_0^k$, and the Jacobian matrix. Note that in case of a 3D linear stability analysis, it would correspond to the stability matrix, whereas for infinitely extended systems they differ since the wavelength of normal mode does not appears here.

Limitations for Large Problems

While the Newton method performs well for small systems, assembling and solving the linear system of equations can be quite problematic for large systems. In fact, one has to compute and store in memory the whole Jacobian matrix. Let us make a quick estimation: take 2000 3D elements of order 7 for the velocity and 5 for the pressure, the matrix itself would already be composed of 2.5×10^9 entries, so about 30Gb. For larger problem, for instance boundary layer flows, the number of element is orders of magnitude higher [174] making it most likely impossible to handle.

To circumvent the problems associated with huge problems, numerous techniques are available. Among them, Newton-Krylov methods [77] have been used extensively for tracking periodic orbits. They can also be employed to find steady states but they often turn out to be poorly conditioned, and preconditioning in an iterative matrix-free framework might be difficult [178]. In case the system is unstable to oscillating perturbations, a method commonly used is to filter these oscillations. Naturally, this works only in case the perturbation is oscillating, and cannot recover unstable steady equilibria to non-oscillating perturbations. Recently, the `BoostConv` algorithm has been proposed by Citro *et al.* [39]. It is based on a recombination of the residuals and fairly simple to implement. In case the basic flow exhibits more spatial symmetries than the perturbations, another option is to enforce symmetry that only the basic flow exhibits by imposing a boundary condition and later reconstruct the whole flow field. For a comprehensive review on that matter, we refer to Loiseau *et al.* [99].

3.3.2 Selective Frequency Damping

Unlike in the Newton method, we use here a time-dependent solver to obtain the steady basic flow. If the basic state is stable, one can run the solver until the variations of the velocity are smaller than some tolerance, in some norm. However, if the basic flow is unstable this approach will not be successful. Selective Frequency Damping (SFD) is a method that has been introduced by Åkervik *et al.* [2], to stabilize the basic flow when it is subject to (growing) oscillations. Indeed, this method is nothing else than a low-pass filter, and is often used in control theory. Once the oscillations have been damped, the velocity field obtained corresponds to the basic flow. Practically, this methods amounts to adding an equation for the filtered velocity $\bar{\boldsymbol{u}}$, and a forcing term in the momentum equations. The set of equations becomes

$$\left(\frac{\partial}{\partial t}\boldsymbol{u} + \boldsymbol{u}\cdot\nabla\right)\boldsymbol{u} = -\nabla p + \Delta\boldsymbol{u} - \chi\left(\boldsymbol{u} - \bar{\boldsymbol{u}}\right), \tag{3.20a}$$

$$\nabla\cdot\boldsymbol{u} = 0 \tag{3.20b}$$

$$\frac{\partial}{\partial t}\bar{\boldsymbol{u}} = \omega_c\left(\boldsymbol{u} - \bar{\boldsymbol{u}}\right), \tag{3.20c}$$

where ω_c is the cut off frequency of the low-pass filter and χ is the strength of the filter. This additional equation can straightforwardly be integrated in time using the same $\mathrm{BDF}_k/\mathrm{EXT}_k$ integration-schemes presented above. Necessary conditions for this technique to damp oscillations are (a) that the cut off frequency ω_c should be smaller than the lowest frequency of the unstable oscillating mode $\Im(\gamma_i)$ (typically at least twice as small), and (b) that the filter strength χ is larger than the growth rate of the perturbation $\Re(\gamma_i)$. Obviously the rate of convergence of this technique strongly relies on the choice of these parameters [98, 30]. Some attempts to optimize this technique have been made by Jordi *et al.* [70], Cunha *et al.* [40], where either using a reduced system of equation or by use of dynamical mode decomposition, they try to obtain an optimal parameter pair,(χ, ω_c) to suppress the oscillations faster.

3.3.3 `BoostConv` Algorithm

To obtain the basic steady flow $(\boldsymbol{u}_0, p_0)^{\mathrm{T}}$, another way is to solve the governing nonlinear system of equations using the `BoostConv` algorithm, recently proposed by Citro *et al.* [39]. The method is based on the acceleration of the convergence of an iterative method of solution. In the following a short description of the algorithm is provided. For further details the reader is referred to Loiseau *et al.* [99] and Bucci [29].

This approach relies on the use of a transient solver. This transient solver can be represented as

$$\boldsymbol{x}_{n+1} = \boldsymbol{x}_n + \mathbf{B}\cdot\boldsymbol{r}_n, \tag{3.21}$$

where $\boldsymbol{x}_{n+1}$ is the next iterate, $\mathbf{B}$ represents the time integration operator for a chosen time interval Δt_B, and $\boldsymbol{r}_n$ is the residual, defined by the equation

$$\boldsymbol{r}_n = \mathbf{A}\cdot\boldsymbol{x}_n - \boldsymbol{b}, \tag{3.22}$$

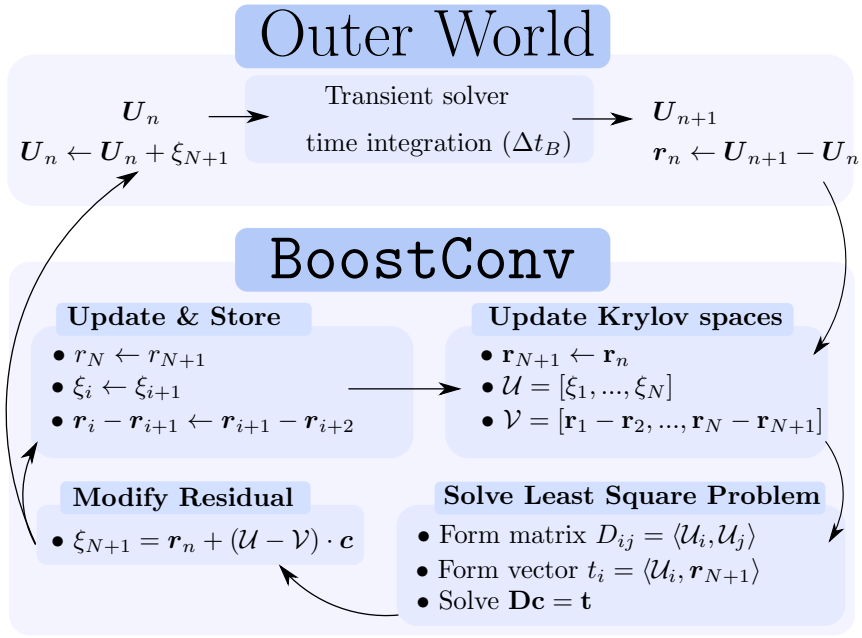

FIGURE 3.4 – Sketch of the `BoostConv` Algorithm

where $\mathbf{A}$ is the steady operator, possibly non-linear. $\boldsymbol{r}_n$ can be thought as the time derivative, when it cancels, $\boldsymbol{x}_n$ is the solution of the steady problem. Like many other iterative algorithms, the residual $\boldsymbol{r}_n$ is subject to minimization. Applying the operator $\mathbf{A}$ on (3.21) and using (3.22), one obtains

$$\boldsymbol{r}_{n+1} = \boldsymbol{r}_n - \mathbf{C} \cdot \boldsymbol{r}_n, \tag{3.23}$$

where $\mathbf{C} = -\mathbf{A} \cdot \mathbf{B}$. We introduce the modified residual $\boldsymbol{\xi}(\boldsymbol{r}_n)$, which is designed such that the next residual $\boldsymbol{r}_{n+1}$ cancels, *i.e.*

$$\boldsymbol{r}_{n+1} = \boldsymbol{r}_n - \mathbf{C} \cdot \boldsymbol{\xi}(\boldsymbol{r}_n) = 0. \tag{3.24}$$

Requiring $\boldsymbol{r}_{n+1} = 0$ leads to a linear system of equations

$$\boldsymbol{r}_n = \mathbf{C} \cdot \boldsymbol{\xi}(\boldsymbol{r}_n). \tag{3.25}$$

The objective of the method is to find the best (non trivial) $\boldsymbol{\xi}$. Computing the operator $\mathbf{C}$ would be a very hard task, to avoid that, we introduce two Krylov spaces

$$\mathcal{U} = \{\boldsymbol{r}_1, \boldsymbol{r}_2, \dots \boldsymbol{r}_N\} \qquad \text{and} \qquad \mathcal{V} = \{\boldsymbol{r}_1 - \boldsymbol{r}_2, \boldsymbol{r}_2 - \boldsymbol{r}_3, \dots \boldsymbol{r}_N - \boldsymbol{r}_{N+1}\} \tag{3.26}$$

of dimension N are generated and are related to each other using (3.23), by $\mathcal{V} = \mathbf{C} \cdot \mathcal{U}$. One can then express

$$\boldsymbol{\xi} = \mathcal{U} \cdot \boldsymbol{c}, \tag{3.27}$$

where $\boldsymbol{c} \in \mathbb{R}^N$, is a linear combination of the vectors composing $\mathcal{U}$. The components of $\boldsymbol{c}$ can be obtained by solving the least-squares problem

$$\boldsymbol{c} = \arg\min |\boldsymbol{r}_n - \mathcal{U} \cdot \boldsymbol{c}|^2. \tag{3.28}$$

This leads to a small linear system of N equations

$$\mathcal{U}^{\mathrm{T}}\mathcal{U} \cdot \boldsymbol{c} = \mathcal{U}^{\mathrm{T}} \cdot \boldsymbol{r}_n, \tag{3.29}$$

which can be solved by direct methods. Here, we solve (3.29) using the LU factorization. So far we only expressed $\mathbf{C}\cdot\boldsymbol{\xi}$ in a specific basis, which, alone, does not accelerate convergence. The key idea of [39] is to also express the new residual $\boldsymbol{\rho} = \boldsymbol{r}_n - \mathbf{C} \cdot \boldsymbol{\xi}_n$ which (3.27) introduces in (3.25) using the Krylov space $\mathcal{V}$ such that

$$\boldsymbol{\rho} = \boldsymbol{r}_n - \mathcal{V} \cdot \boldsymbol{c}. \tag{3.30}$$

Adding this residual to (3.27) yields

$$\boldsymbol{\xi}_n = \boldsymbol{r}_n + (\mathcal{U} - \mathcal{V}) \cdot \boldsymbol{c}. \tag{3.31}$$

By replacing the residual $\boldsymbol{r}_n$ in (3.21) by the corrected value $\boldsymbol{\xi}_n$ the convergence is much accelerated, while the extra load to compute $\boldsymbol{\xi}_n$ is negligible for large systems. It is based on a combination of residuals in low-dimensional Krylov spaces $\mathcal{U}$, $\mathcal{V}$ of dimension N. These Krylov spaces are fed in a cyclic fashion, meaning that the data written N iterations before will be overwritten by the data obtained at the current iteration. For further details and explanations on the acceleration, we refer e.g. to Bucci [29].

The two parameters on which this method depends are the dimension N of the Krylov space, and the time Δt_B between two calls. Typically a small Krylov space is enough, but the dimension has to be set in accordance with Δt_B such that potential oscillations can be seen, *i.e.* respect a Nyquist criterion. From a practical point of view, the fact that there is no parameter depending on the growth rate of the perturbation is a considerable advantage. The workflow to apply the `BoostConv` algorithm is shown in fig. 3.4.

Compared to the SFD, the `BoostConv` algorithm is usually faster, and allows recovering basic states which are unstable to non-oscillatory perturbations. Especially once the residual has been sufficiently reduced, the convergence curve is very steep (see fig. 3.6).

This `BoostConv` algorithm can be implemented on the basis of the time-dependent solver with only minor changes. For all calculations we use a Krylov space dimension of $\dim(\mathcal{K}) = 10$. As a side note, this algorithm can also be used to recover periodic orbits of known period without implementation changes: one only has to call the function with $\Delta t_B = T_p$, where T_p is the period.

3.3.4 Symmetries

Using symmetries of the problem, if there are any, can also be a very good alternative to the previous methods to find steady states. In simple geometries, the basic flow

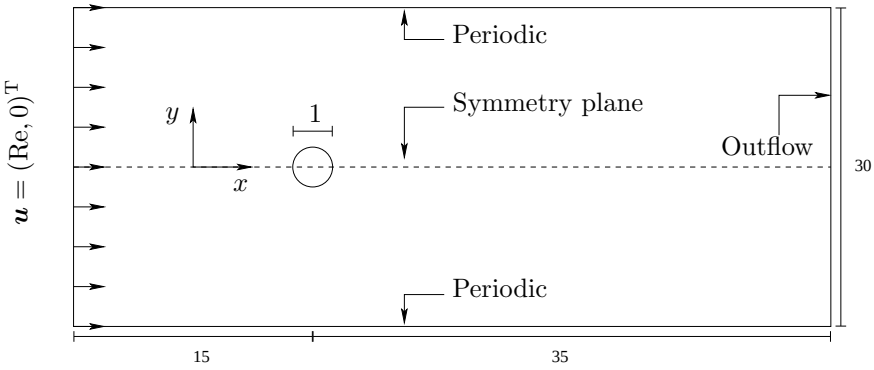

FIGURE 3.5 – Sketch of the flow past a cylinder.

often exhibits more spatial symmetry than the perturbation, and in some cases one can eventually take advantage of it. For instance in the case of a flow past a cylinder sketched in fig. 3.5, the basic flow is symmetric with respect to the x-axis, whereas the most dangerous mode is not. Then limiting the solutions to the subspace of symmetric solutions naturally leads to the steady basic flow. This approach can be faster than a SFD, since by design the most unstable perturbations are not present, and do not need to be damped. On one hand, this approach necessitates to generate a second mesh (half of the full mesh). On the other hand, the number of unknowns being twice as small, the CPU time needed is consequently lower.

In order to quickly compare the performance of these methods, we use the test case of the flow past a cylinder sketched in fig. 3.5 at $\mathrm{Re} = 100$, so beyond the critical Reynolds number which is about 50. If the flow evolves freely without any control or symmetry being imposed, the system evolves toward a limit cycle. The uncontrolled case is shown by the blue curve in fig. 3.6. If the low pass filter is applied (orange in fig 3.6), the oscillations are damped and as one can see that it converges rather slowly in the long term.

The `BoostConv` shown in red performs the best in term of iterations needed to converge. One could argue that changing the parameters could change the performance of SFD and `BoostConv`, but generally speaking the latter is faster. For more details, we refer the reader to [29, 99]. Finally, applying a symmetry constraint along the x-axis is possible, and the residual multiplied by 2 is shown in green. One notices the same decay of the residual as for the SFD but the convergence slope seems to be steeper. Moreover the computation finished twice as fast as the other simulations (all on one core).

3.4 Eigenvalue Problems

The second step to investigate the linear stability of a problem at a given parameter is to solve the eigenvalue problem (2.9). To solve large eigenvalue problems, many techniques have been developed in the past century. First came the power iteration

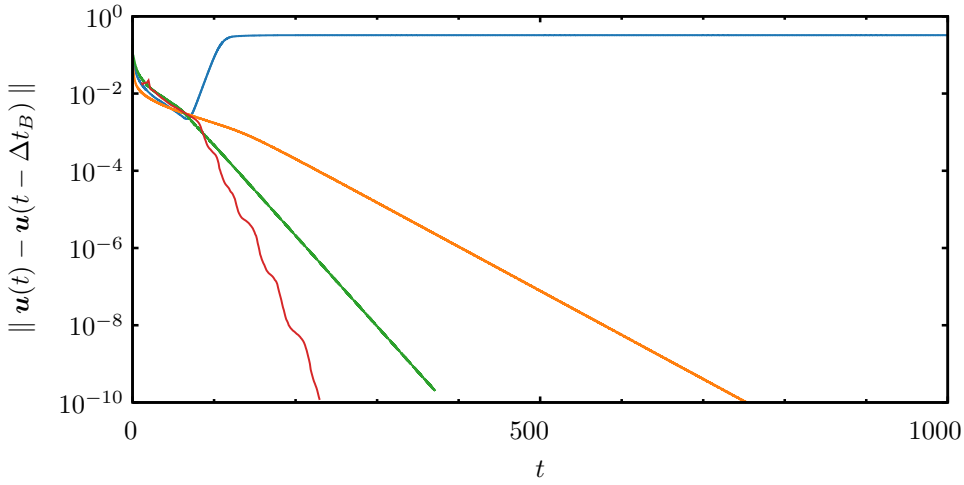

FIGURE 3.6 – Evolution of the residual for the flow over a cylinder at Re = 100 for the system without any control (blue), with SFD parameters $\chi = 0.5, \omega_c = 0.5$ (orange), with `BoostConv` parameters $N = 10, \Delta t_B = 1$ (red), and imposing a symmetry condition along the x-axis (green).

[141], which can give information only on the largest eigenvalue and eigenmode of the operator. For symmetric problem, one could use Lanczos method [88] as well, but in the linearized Navier-Stokes equations, the convection term makes the problem non-symmetric and these algorithms cannot be used. Using a Gram-Schmidt orthogonalization procedure, the Arnoldi algorithm [13] and its extension Implicitly Restarted Arnoldi Method [89] have become nowadays standards for generalized eigenvalue problems.

3.4.1 Power Iteration

The Krylov space of dimension n of a linear operator $\mathbf{A}$ of dimension $m \times m$ is defined as

$$\mathcal{K}_n(\mathbf{A}, \boldsymbol{v}) = \left[\boldsymbol{v}, \mathbf{A}\boldsymbol{v}, \mathbf{A}^2\boldsymbol{v}, ..., \mathbf{A}^{n-1}\boldsymbol{v}\right],$$

where $\boldsymbol{v}$ is an arbitrary vector. As n grows, this sequence of vector converges toward the eigenvector corresponding to the largest eigenvalue of the matrix. It is the eigenvector for which the norm $\| \mathbf{A}^n\boldsymbol{v} \|$ decays the slower with n, or grows the faster with n depending on the real part of the eigenvalue.

However, this method is requires a lot of computational power, although only the last vector $\mathbf{A}^{n-1}\boldsymbol{v}$ is kept, and the rest of the Krylov basis remains useless. This method can converge slowly depending on the spectrum of the operator: if two eigenvalues are very close to each other, the relative decay/growth of one compared to the other might be moderate.

Generally, the Krylov basis is not orthogonal and could be orthogonalized using a simple Gram-Schmidt algorithm, and more information could be extracted from it.

This is the principle of the Arnoldi algorithm.

3.4.2 Arnoldi Method

The goal of this iterative method is to obtain a restriction of the high dimensional linear operator $\mathbf{A}$ to the n-Krylov subspace. One builds a collection of k orthogonal vectors $\mathbf{V}_k = [\boldsymbol{v}_i, i = 1 : k]$,

$$\boldsymbol{v}_{k+1} = \mathbf{A}\boldsymbol{v}_k - \sum_{j=1}^{k} (\mathbf{A}\boldsymbol{v}_k, \boldsymbol{v}_j)\, \boldsymbol{v}_j. \tag{3.32}$$

To understand what happens, it is convenient to look at it from a matrix point of view. Let us gather the coefficients of the Gram-Schmidt orthogonalization in an upper Hessenberg matrix $\mathbf{H}_k \in \mathbb{C}^{k\times k}$, where $H_{k,ji} = (\mathbf{A}\boldsymbol{v}_i, \boldsymbol{v}_j)$. One can then rewrite (3.32) as

$$\mathbf{A}\mathbf{V}_k = \mathbf{V}_k\mathbf{H}_k - h_{k+1,k}\boldsymbol{v}_{k+1}\boldsymbol{e}_{k+1}^T. \tag{3.33}$$

the rightmost term of this equation is the rest, and is orthogonal to the constructed basis (Galerkin property). As $\mathbf{V}_k$ is orthonormal, one gets

$$\mathbf{H}_k = \mathbf{V}_k^H \mathbf{A}\mathbf{V}_k, \tag{3.34}$$

where the superscript H denotes the transpose conjugate. From (3.34) one can see that the Hessenberg matrix is a restriction of the linear operator to some Krylov subspaces. Furthermore, the eigenvalues of $\mathbf{H}_k$,also called *Ritz eigenvalues*, converge towards those of $\mathbf{A}$. For more details, the reader is referred to [176, 12]. As the matrix $\mathbf{H}_k$ is relatively small, eigenvalues μ_i and eigenvectors $\boldsymbol{y}_i$ can be numerically computed using a QR algorithm. They are related to the eigenpairs $\gamma_i, \hat{\boldsymbol{v}}$ of the linear operator by

$$\mu_i \approx \gamma_i \quad \text{and} \quad \hat{\boldsymbol{v}} \approx \mathbf{V}_k\boldsymbol{y}_i.$$

The Arnoldi method has two drawbacks: it becomes more and more resource consuming as k increases, and might require huge amount of memory, and there is no optimal Krylov space dimension n that ensures convergence. To remedy these problems, several techniques have been proposed: a variation of that algorithm called the Implicitely Restarted Arnoldi method (IRAM) has been proposed by Lehoucq & Sorensen [89] and a second one relies on a Schur decomposition [170]. As the IRAM is available in the ARPACK Library, it is used to solve the eigenvalue problem, as implemented in [122, 123] when using Nek5000, and is called in scipy's function `linalg.eigs`. Following the notation of [89], one first builds a length k Arnoldi factorization, evaluates the eigenvalues of $\mathbf{H}_k$ and sort then according to some user defined criterion (by largest real part or magnitude for instance) into a *wanted* set $\{\mu_j : j = 1 : m\}$ and an *unwanted* set $\{\mu_j : j = m+1 : k\}$. If the convergence of the first n_W *wanted* eigenvalues is not satisfying, IRAM performs the first $k - m$ iterations of a QR algorithm on $\mathbf{H}_k$ such that

$$\mathbf{H}_k\mathbf{Q}_k = \mathbf{Q}_k\mathbf{H}_k^+$$

Defining $\mathbf{Q}_m$ the first m columns of $\mathbf{Q}_k$, multiplying (3.33) by $\mathbf{Q}_m$ one obtains a *deflated* decomposition

$$\mathbf{A}\mathbf{V}_k\mathbf{Q}_m = \mathbf{V}_k\mathbf{Q}_m\mathbf{H}_m^+ + \boldsymbol{f}_m^+\boldsymbol{e}_m^T,$$

where $\mathbf{H}_m^+$ is the leading submatrix of order m. The right hand side is composed of the new reduced Hessenberg matrix, the reduced Krylov basis, and the residual that will be used to restart the Arnoldi iterations. This process of reduction is called *deflation*.

3.4.3 Time Stepping

The application of IRAM directly to the Jacobian matrix of the linearized Navier–Stokes equations is possible for small problems (e.g. two-dimensional). Fully three-dimensional problems become more challenging regarding the memory requirements.

According to Theofilis [174], the discretized Jacobian of would need Terabytes of storage in the case of a boundary layer. Therefore, the storage in memory of such a large matrix is hardly possible and the calculations would slow down, because most of the computer's work would be to fetch the information.

To palliate this problem, Marcus & Tuckerman [103] and Edwards *et al.* [49] used a time stepping approach, which was then popularized by Bagheri *et al.* [16]. Projecting the velocity on the divergence-free vector space, the dynamical system linearized around its equilibrium $\boldsymbol{u}_0$ can be simply recast as

$$\frac{\partial}{\partial t}\boldsymbol{u}' = \mathcal{A}(\boldsymbol{u}_0)\boldsymbol{u}',$$

where $\mathcal{A}(\boldsymbol{u}_0)$ is the projection of the Jacobian matrix onto the divergence-free space. The solution of this system can be expressed as

$$\boldsymbol{u}'(t=\Delta t) = \underbrace{\mathrm{e}^{\mathcal{A}t}}_{M(\Delta t)}\boldsymbol{u}'(t=0).$$

The operator $\mathrm{e}^{\mathcal{A}\Delta t}$ is the so-called *exponential propagator* or also *time propagator* of the system. Seemingly, taking the exponential of the operator does not look like it will help with the memory problem since computation of the matrix exponential is usually very costly. However, one notes that $\boldsymbol{u}'(\Delta t)$ corresponds both to the evaluation of this propagation operator on the initial perturbation and the output of the linearized solver after a time Δt given the initial perturbation. Computing the action of the operator $M(\Delta t)$ on a vector $\boldsymbol{u}'$ is quite straightforward, and does not require the colossal task of forming the matrix. Besides, instead of assembling the matrix and performing the matrix-vector products in the Arnoldi method, one can use only its evaluation: the integrated perturbation after Δt. The choice of the Δt is of course very important and mainly depends on the oscillations that one expects, and has to follow a Nyquist-Shannon criterion.

The propagator matrix and the Jacobian matrix being simply related, the Ritz pairs μ_i, obtained by the Arnoldi method on the propagator operator are related to

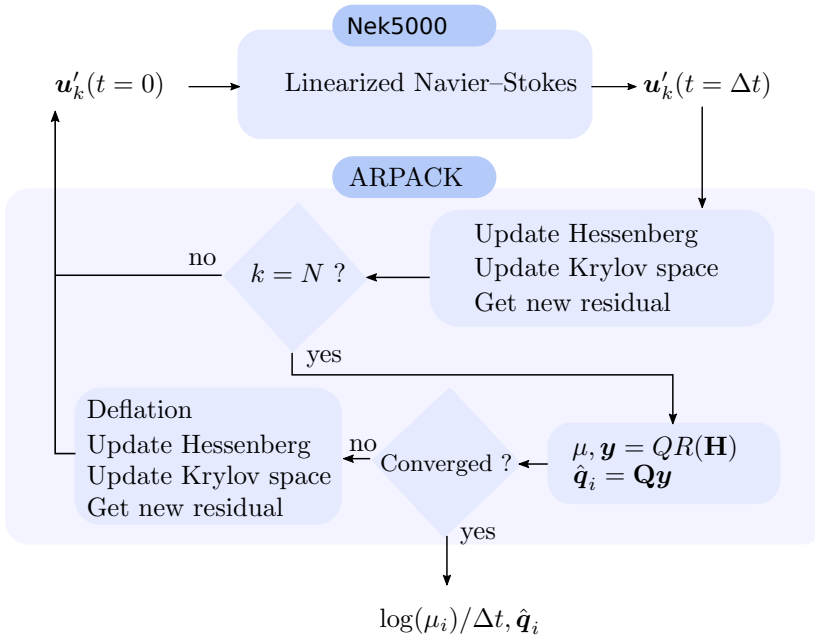

FIGURE 3.7 – Sketch illustrating the time stepping technique as used in this thesis.

the eigenvalues γ_i of the Jacobian by

$$\gamma_i = \frac{\log \mu_i}{\Delta t}, \tag{3.35}$$

and the eigenvectors stay the same.

3.5 Additional Methods for Infinitely Extended Systems

3.5.1 Finding the Critical Wavelength

As mentioned in the section 2.3.3, in case of infinitely extended systems where the basic flow is homogeneous in one direction, finding the critical Reynolds number necessitates to find the critical pair (Re_c, k_c) where k_c is the wavenumber for which the Reynolds number is minimal.

Finding the critical Reynolds number involves (a) finding the zero of the largest growth rate for given wave number yielding the neutral Reynolds number Re_n, and (b) minimizing the neutral Reynolds number with respect to the wave number.

(a) To find the neutral Reynolds number Re_n at which the largest growth rate vanishes for given k, Re_n is estimated by $\mathrm{Re}^{(1)}$ and a linear stability analysis is performed for $\mathrm{Re}^{(1)}$ and for a slightly different Reynolds number $\mathrm{Re}^{(2)} = \mathrm{Re}^{(1)} + \delta\mathrm{Re}$

where $\delta\mathrm{Re}$ is small, e.g. 100 times smaller than $\mathrm{Re}^{(1)}$. The linear interpolation to zero of the maximum growth rates obtained for $\mathrm{Re}^{(1)}$ and for $\mathrm{Re}^{(2)}$ determines $\mathrm{Re}^{(3)}$. If the absolute value of the largest growth rate for $\mathrm{Re}^{(3)}$ is still larger than a given tolerance ϵ, $\mathrm{Re}^{(4)}$ is found by quadratic interpolation to zero of the largest growth rates obtained for the previous three Reynolds numbers. The iteration continues until the convergence condition $|\sigma| < 10^{-4}$ is met.

(b) The wave number k_c at which the neutral Reynolds number takes its minimum can be estimated by $k_{\max}$ at which the growth rate of the most dangerous eigenmode takes its maximum. This corresponds to minimizing the function $k \to -\Re(\gamma(k))$ at a given Reynolds number Re which leads to the minimization problem

$$k_{\max}(\mathrm{Re}) = \arg\min\left(-\Re(\gamma\left(k, \mathrm{Re}\right))\right). \tag{3.36}$$

To that end, one can compute the sensitivity of the eigenvalue γ_i with respect to changes of the wave number

$$\frac{\partial \gamma_i}{\partial k} = -2k - \mathrm{i}\left\langle w_0 \hat{\boldsymbol{u}}_{\boldsymbol{i}}, \hat{\boldsymbol{u}}_i^\dagger \right\rangle - \mathrm{i}\left\langle \hat{p}_i, \hat{w}_i \right\rangle - \mathrm{i}\left\langle \hat{w}_i, \hat{p}_i^\dagger \right\rangle, \tag{3.37}$$

where $\langle a, b\rangle = \int_V a^* b \,\mathrm{d}V$, the asterisk $(*)$ denotes the complex conjugate and the dagger $(\dagger)$ indicates the adjoint of the i-th eigenmode (see Appendix A for the derivation). This sensitivity can then be used in a minimization algorithm, e.g. the Broyden–Fletcher Goldfarb–Shanno (BFGS), to find the local minimum.

Once the critical wave number $k_{\max}$ has been estimated it is used to return to step (a) and find the corresponding neutral Reynolds number which improves on Re_c. A couple of iterations between the two steps (a) and (b) is usually sufficient to find k_c and Re_c with high accuracy. The iteration is terminated as soon as $|\Delta\mathrm{Re}| + |\Delta k| < 10^{-3}$, where $\Delta\mathrm{Re}$ and Δk denote the updates of Re and k, respectively, after one full iteration step consisting of (a) and (b).

BFGS: a Quasi-Newton Algorithm

In order to find the critical wavelength for an infinitely extended system, we made use of the Broyden–Fletcher Goldfarb–Shanno (BFGS) algorithm. Although it was not implemented but only used in the framework of this thesis, it is briefly explained. For more details, see e.g. [15]. In the case of a minimization or maximization problem, the zeros of the gradient of the function is of interest, and the Newton method can be recast into

$$\boldsymbol{x}^{n+1} = \boldsymbol{x}^n - \mathbf{H}_f^{-1} \nabla f \ . \tag{3.38}$$

Very often the Hessian matrix $\mathbf{H}_f$ is not available analytically and one has to find a way to approximate this matrix. A method doing such approximation is called a Quasi-Newton method.

To initialize the BFGS algorithm, one has to provide a first guess for the solution $\mathbf{x}_0$ and for the approximate Hessian matrix $\mathbf{H}_0$, typically the latter is set to identity.

1. Find the direction $\boldsymbol{p}$ by solving $\mathbf{H}_k \boldsymbol{p} = \nabla f(x_k)$.

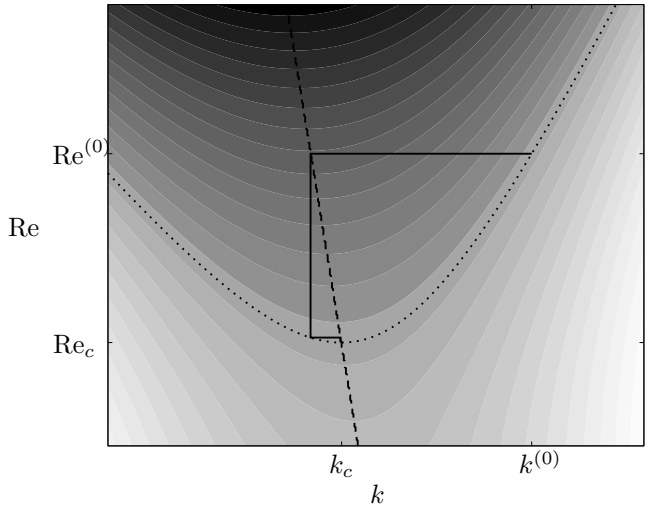

FIGURE 3.8 – Sketch illustrating the critical parameter search. Grey shades denote the real part of the eigenvalue, which is zero on the dotted line. The dashed line represent the maximum of the eigenvalue over k at a given Re. The full line shows the first iterations of the search. A search of maximum corresponds to the horizontal line, while a root search is a vertical line.

2. Find the step size s using a line search algorithm, that is $s = \arg\min_d \nabla f(\boldsymbol{x}_k + d\boldsymbol{p})$.

3. Set the increment $\mathbf{s}_k = s\,\boldsymbol{p}$, and $\boldsymbol{x}_{k+1} = \boldsymbol{x}_k + \boldsymbol{s}_k$.

4. Compute the difference between the gradient of two iterates and set $\boldsymbol{y}_k = \nabla f(\boldsymbol{x}_{k+1}) - \nabla f(\boldsymbol{x}_k)$.

5. Update the approximation of the Hessian

$$\mathbf{H}_{k+1} = \mathbf{H}_k + \frac{\boldsymbol{y}_k \boldsymbol{y}_k^T}{\boldsymbol{y}_k^T \boldsymbol{s}_k} - \frac{\mathbf{H}_k \boldsymbol{s}_k \boldsymbol{s}_k^T \boldsymbol{H}_k^T}{\boldsymbol{s}_k^T \mathbf{H}_k \boldsymbol{s}_k}.$$

6. The stopping criterion can be set using the norm of the increment or the norm of the residual.

Although the Hessian matrix can be numerically inverted, there exists an analytical inversion using the Sherman-Morrison formula to invert the sum of an invertible matrix and outer product. For large systems, computing and storing the Hessian can be a limiting factor, and a lighter version of the BFGS algorithm, using only smaller matrices for the Hessian approximation can be used. It is called L-BFGS-B. This latter algorithm will be used to stabilize or destabilize a thermocapillary driven cavity with a designed heat flux, see Chapter 5.

3.5.2 Continuation Method Based on Polynomials

To find (Re_c, k_c) as a function of a third parameter α using the above iteration, a good initial guess is required. This is obtained by extrapolating the converged critical data obtained for previous values of α. Based on the $N+1$ known data $(\alpha_i, \mathrm{Re}_{c,i}, k_{c,i})$ for $i \in 0, \ldots, N$ the distance function from the first point $(\alpha_0, \mathrm{Re}_{c,0}, k_{c,0})$

$$d_i = \sqrt{(\alpha_i - \alpha_0)^2 + a\,(\mathrm{Re}_{c,i} - \mathrm{Re}_{c,0})^2 + (k_{c,i} - k_{c,0})^2} \tag{3.39}$$

is evaluated for $i = 1, \ldots, N$, where the Nth point is the point found in the last converged iteration. The coefficient $a = 0.1$ has been selected in order to improve the condition number of the fit, because the Reynolds number is typically two to three orders of magnitude larger than α and k, which also applies to their variations. Based on the parametrization d_i each of the three quantities $(\alpha, \mathrm{Re}_c, k_c)$ is fitted by a polynomial of maximum order three $P_f(d_i)$, where $f \in [\alpha, \mathrm{Re}_c, k_c]$. The coefficients are obtained by least-squares minimization of the functional $\sum_{i=1}^{N} w_i \left[f_i - P_f(d_i)\right]^2$, where the weights w_i are selected to give preference to the last point by setting $w_i = i$. The three polynomials obtained are then evaluated for $d > d_N$ to arrive at the new initial guess for $(\alpha_{N+1}, \mathrm{Re}_{c,N+1}, k_{c,N+1})$. Using a low polynomial order $(P \in \mathbb{P}_3)$ renders the method stable.

4

Linear Stability Analysis of Obliquely-Driven Rectangular Cavities

The flow of an incompressible fluid in a cavity of rectangular cross section, driven by the tangential motion of one or more lids is of general importance in fluid mechanics. The system is an an important benchmark but also encompasses fundamental problems. Together with the von Karmán vortex street, it is one of the main benchmark tests for a numerical solver. Owing to its simple geometry and, in particular, the absence of curved boundaries, the mesh generation does not need elaborate techniques since a simple tensor grid is sufficient and the implementation of the Dirichlet boundary conditions is also straightforward. The reader is referred to [154, 87] for comprehensive reviews on the subject.

Historically, the first two-dimensional steady flows computations are due to Kawaguti [75] and Burggraf [31] who used finite-difference schemes on a 11×11 and a 40×40 tensor grid, respectively. As the computational resources increased, highly-resolved benchmark data were obtained in the early 80s by Ghia *et al.* [63] and Schreiber & Keller [149] who computed steady flows up to $\mathrm{Re} = 10^4$. Later on Botella & Peyret [22] employed a spectral method together with the singularity subtraction method [23] to avoid an excessive deterioration of the exponential convergence of the spectral method by the singular boundary condition. The same method has been employed by Albensoeder & Kuhlmann [3] to treat three-dimensional cases, providing benchmark data for specific aspect ratios.

While benchmark data have been gathered, the lid-driven cavity naturally served as test bed for the development of numerical schemes. For instance De Vahl Davis & Mallinson [42] examined several schemes for convection and their stability, and Ku *et al.* [82] tested a psoeudospectral Chebyshev method. Eventually, Tuann & Olson [177] reviewed different schemes for recirculating flows. All were tested using the lid-driven cavity.

In the mean time, experiments were also carried out. Pan & Acrivos [119] investi-

gated experimentally the length of the core vortex as a function of the length-to-depth ratio of the cavity. More in-depth experimental studies were carried on by Koseff Koseff *et al.* [81], Koseff & Street [80, 79, 78] and Prasad & Koseff [133]. They investigated a square cavity with a spanwise aspect ratio of 3 driven by a plate at its top surface and discovered the presence of three-dimensional Taylor–Görtler vortices (TGV) at $\mathrm{Re} = 3000$, developing along the curved boundary layer next to the bottom corners. These vortices could obviously not be observed in two-dimensional simulations. The discovery of the Taylor–Görtler vortices stimulated further research on the laminar-turbulent transition.

In two-dimensional numerical simulations, the two-dimensional steady flow becomes unstable to two-dimensional perturbations at a relatively high Reynolds number. Shen [155] found the existence of a Hopf bifurcation at $\mathrm{Re}_c \approx 10^4$. However, due to the smoothing of the lid velocity that was implemented, the critical Reynolds number is over-estimated. Much more accurate, Auteri *et al.* [14] found that the Hopf bifurcation arises at $\mathrm{Re}_c = 8018.2 \pm 0.6$. The bifurcating limit cycle was reconstructed by Auteri *et al.* [14], Peng *et al.* [121], or Bruneau & Saad [28]. The high critical Reynolds number was further confirmed by linear stability analyses of Poliashenko & Aidun [128], Fortin *et al.* [58] or Sahin & Owens [142]. The critical Reynolds at which the system is unstable to two-dimensional oscillating perturbation was $\mathrm{Re}_c = 7763 \pm 2\%$, $\mathrm{Re}_c = 8000$ and $\mathrm{Re}_c = 8069.76$, respectively.

Assuming the square cavity to be infinitely extended in its spanwise direction and allowing the perturbation to be three-dimensional, Ramanan & Homsy [134],Ding & Kawahara [44, 45] could find a critical Reynolds numbed of $\mathrm{Re}_c = 920$ and critical wavelength of $\lambda_c = 0.84$. The neutral mode found could correspond to the TGV that were described in the experiments of Koseff & Street [78]. However, they apparently missed a mode with a lower wavelength which was found by Albensoeder *et al.* [5] at $\mathrm{Re}_c = 786$ and wavelength $\lambda_c = 0.407$. This latter study investigated the flow instability as a function for the depth-to-width aspect ratio $\Gamma \in [0.1, 4]$. For deep cavities, the depth of the cavity seems to become less and less relevant for the critical Reynolds number, as the critical mode arises around the limit of the first vortex immediately below the moving lid. For a square cavity, the local rate of production of kinetic perturbation energy is maximal close to the corner upstream to the moving lid and forms some banana-like structures. This instability was shown to be of centrifugal origin: there is an exchange of momentum from a region at small distance from the vortex (small radius) center with a fluid having a large momentum to a region at larger radius (far from the center of the vorter) with a lower momentum. For more on centrifugal instabilities in inviscid flows, we refer to Bayly *et al.* [19]and Sipp & Jacquin [163]. The results of Albensoeder *et al.* [5] are in agreement with the experiments carried by Siegmann-Hegerfeld *et al.* [161]. Besides Theofilis *et al.* [175] confirms numerically the results of [5] for a square cavity but results differ for other aspect ratios.

In cavities of finite spanwise dimension, the flow stability is affected by the end walls. Aidun *et al.* [1] observed experimentally that the flow in cavity of square cross section with a throughflow and spanwise aspect ratio of 3 remained stationary until $\mathrm{Re} = 875 \pm 50$, and found multiple steady cellular flows for $\mathrm{Re} < 500$ which might

be reached through finite-amplitude perturbations only. Siegmann-Hegerfeld *et al.* [162] investigated larger spanwise aspect ratios up to 10 and noted that the TGV were present in the center of the cavity but that end walls effect were preventing the vortices to form in wide regions next to the end walls. This was also confirmed numerically by Albensoeder & Kuhlmann [4], who compared the wavelength of the vortices in case of end walls and for periodic boundary conditions in the spanwise direction. They found that the wavelength of the TGV were agreeing with the one predicted by the linear stability analysis of the infinitely extended system. However, the fact that the end wall effects dominate on a large span of the cavity can delay the appearance of the vortices.

Strongly end-wall dominated cavities became of interest as Feldman & Gelfgat [55] investigated the onset of time-dependent flow in a cubic cavity. They found a critical Reynolds number of $\mathrm{Re}_c \approx 1900$. Further experiments Liberzon *et al.* [95] showed, using water and glycerol as working fluids, that the flow does destabilize between $\mathrm{Re} = [1700, 1950]$. Although there was some discrepancy concerning the critical Reynolds number, the frequency of the oscillation compared very well. Kuhlmann & Albensoeder [85] found that the steady flow undergoes a slightly subcritical Hopf bifurcation and that the limit cycle is unstable in form of bursts breaking the mirror symmetry of the flow after a long integration time. These results were further confirmed by Loiseau *et al.* [100]. They also found that during these bursting events, the system visits a second limit cycle. Finally Lopez *et al.* [101] could isolate the unstable quasi-periodic states linking the two limit cycles and clarify the scenario using symmetries and edge-state tracking.

Povitsky [131, 132] investigated the steady flow in a cubic cavity when the lid moves diagonally. He noted the higher number of vortices and a higher mean momentum than in the canonical case. Due to the confined geometry and the diagonal driving, the viscous effect are very strong at the downtream end of the lid and the flow returns earlier to the bulk than in the classical case. This leads to vortices in the bulk which are mirror symmetric with respect to the diagonal plane, but the steady flow structure is much more complicated (10 transverse vortices) than in the classical case (4 corner vortices) and the mixing properties of the flow are enhanced. Feldman [54] was interested in the temporal evolution of the system and found a supercritical Hopf bifurcation in which the flow oscillations breaks the mirror symmetry with respect to the diagonal plane. According to Feldman [54], the oscillations saturate and, unlike in the classical case, the limit cycle seems to be stable. The time-dependent perturbation flow seems to have a rather complicated structure, stemming from the intricate basic flow structure. A streamwise vortex, centered on the diagonal plane, which alternates its sense of rotation seems to be the essential feature of the perturbation flow. Apparently, the end-wall effects on the flow structure are potentially of greater importance than in the classical case. Benchmark data for the critical Reynolds number was provided by Gelfgat [60] for the diagonally driven cubic cavity flow. In the same study, a linear stability of the flow was carried. Using Rayleigh and Bayly criteria and that the perturabation did not arise in pair of vortices with the core of the vortex aligned with the flow. Gelfgat [60] came then to the conclusion that the flow instability was not centrifugal.

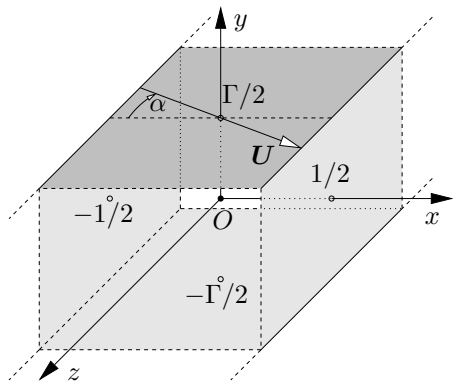

FIGURE 4.1 – Geometry of the problem with cartesian coordinates centred in the cavity (O) and a lid (dark grey) moving tangentially with velocity $\boldsymbol{U}$ under an angle α with respect to the x axis.

Despite extensive stability analyses of the classical lid-driven cavity, only Theofilis *et al.* [175] considered the stability analysis of the infinitely extended system for rectangular cavities driven with an oblique motion of the lid. They scrutinized three different angles: $\pi/4$, $\pi/2$ and $3\pi/4$ and did not find any unstable mode below $\mathrm{Re} = 800$ for these angles. The aim of this chapter is to fill the gap and provide the linear stability boundaries as a quasi-continuous function of the angle the lid velocity makes with the walls.

After introducing the mathematical description of the problem in §4.1, the code will be verified against data available in the literature. Our findings for a square cavity, as well as for representative shallow and deep cavities of height-to-width aspect ratio 1/2 and 2 will be presented in §4.3. Flow structures and instability mechanisms will be investigated by the considering the production rates of kinetic perturbation energy. We shall provide an explanation for the strong stabilization of the basic flow at large angles, which, in the limit, corresponds to a bounded Couette flow. Finally, the common features of the instabilities found are discussed and their link to Couette flows in §4.4 conclude this work.

4.1 Formulation of the Problem

We consider the incompressible flow of a Newtonian fluid with density ρ and kinematic viscosity ν in a rectangular cavity. The width d in x direction and the height h in y direction define the aspect ratio $\Gamma = h/d$. In the z direction the cavity is assumed to be infinitely extended. The origin of the coordinate system is placed in the centre of the (x, y) cross section. The flow is driven by the steady tangential motion of a lid at the top $y = h/2$ of the cavity. The lid-velocity vector $\boldsymbol{U} = U\,(\cos\alpha\boldsymbol{e}_x + \sin\alpha\boldsymbol{e}_z)$, where $\boldsymbol{e}_x$ and $\boldsymbol{e}_z$ are the unit vectors in x and z direction, respectively, is inclined with respect to the x axis with inclination angle α (fig. 4.1).

Using the length, time, velocity and pressure scales d, d^2/ν, ν/d and $\rho\nu^2/d^2$,

respectively, the fluid flow is governed by the non-dimensional Navier–Stokes and continuity equations

$$\frac{\partial \boldsymbol{u}}{\partial t} + \boldsymbol{u}\cdot\nabla\boldsymbol{u} = -\nabla p + \nabla^2\boldsymbol{u}, \tag{4.1a}$$

$$\nabla\cdot\boldsymbol{u} = 0, \tag{4.1b}$$

where $\boldsymbol{u}(\boldsymbol{x},t) = (u,v,w)$ is the velocity vector and $p(\boldsymbol{x},t)$ the pressure field. Equations (4.1) must be solved subject to the boundary conditions

$$\boldsymbol{u}(x=\pm 1/2) = 0, \tag{4.2}$$

$$\boldsymbol{u}(y=-\Gamma/2) = 0, \tag{4.3}$$

$$\boldsymbol{u}(y=\Gamma/2) = \mathrm{Re}(\cos\alpha, 0, \sin\alpha)^{\mathrm{T}}. \tag{4.4}$$

Furthermore, we consider the case of a vanishing pressure gradient in z direction, $\partial p/\partial z = 0$. The problem is thus defined by three parameters: the aspect ratio Γ, the inclination angle α, and the Reynolds number

$$\mathrm{Re} = \frac{Ud}{\nu}. \tag{4.5}$$

Due to the translation invariance of the problem in z and t the governing equations allow for a steady two-dimensional basic flow $\boldsymbol{u}_0(x,y)$ which only depends on x and y.

We are interested in the linear stability boundary, expressed by $\mathrm{Re}_c(\Gamma,\alpha)$, at which the two-dimensional basic flow becomes unstable to three-dimensional perturbations. Linearizing (4.1) with respect to small perturbations of the basic flow yields the linear perturbation equations

$$\frac{\partial \boldsymbol{u}}{\partial t} + \boldsymbol{u}_0\cdot\nabla\boldsymbol{u} + \boldsymbol{u}\cdot\nabla\boldsymbol{u}_0 = -\nabla p + \nabla^2\boldsymbol{u}, \tag{4.6a}$$

$$\nabla\cdot\boldsymbol{u} = 0, \tag{4.6b}$$

where now $\boldsymbol{u}$ and p denote the deviations from the basic state.

Owing to the homogeneity in z-direction, these equations may be solved using normal-modes

$$\begin{pmatrix} \boldsymbol{u} \\ p \end{pmatrix} = \begin{pmatrix} \hat{\boldsymbol{u}}(x,y) \\ \hat{p}(x,y) \end{pmatrix} \mathrm{e}^{\gamma t + \mathrm{i}kz} + \text{c.c.}, \tag{4.7}$$

where $k\in\mathbb{R}$ is a real wave number, $\gamma = \sigma + \mathrm{i}\omega \in \mathbb{C}$ a complex growth rate with real growth rate σ and frequency ω, and c.c. denotes the complex conjugate. Inserting this ansatz into the perturbations equations (4.6) we are left with

$$-\gamma\hat{u} = (\hat{u}\partial_x + \hat{v}\partial_y)\,u_0 + (u_0\partial_x + v_0\partial_y + \mathrm{i}kw_0)\,\hat{u} + \partial_x\hat{p} - (\partial_x^2+\partial_y^2)\hat{u} + k^2\hat{u}, \tag{4.8a}$$

$$-\gamma\hat{v} = (\hat{u}\partial_x + \hat{v}\partial_y)\,v_0 + (u_0\partial_x + v_0\partial_y + \mathrm{i}kw_0)\,\hat{v} + \partial_y\hat{p} - (\partial_x^2+\partial_y^2)\hat{v} + k^2\hat{v}, \tag{4.8b}$$

$$-\gamma\hat{w} = (\hat{u}\partial_x + \hat{v}\partial_y)\,w_0 + (u_0\partial_x + v_0\partial_y + \mathrm{i}kw_0)\,\hat{w} + \mathrm{i}k\hat{p} - (\partial_x^2+\partial_y^2)\hat{w} + k^2\hat{w}, \tag{4.8c}$$

$$0 = \partial_x\hat{u} + \partial_y\hat{v} + \mathrm{i}k\hat{w}. \tag{4.8d}$$

Together with the boundary conditions $\hat{\boldsymbol{u}}(x = \pm 1/2) = \hat{\boldsymbol{u}}(y = \pm\Gamma/2) = 0$ this system of equations constitutes a generalized eigenvalue problem with eigenvectors $(\hat{\boldsymbol{u}}, \hat{p})$ and eigenvalues γ. The eigenvalue $\gamma(k, n; \Gamma, \alpha, \mathrm{Re})$ depends on the wave number k of the disturbance, the three parameters $(\Gamma, \alpha, \mathrm{Re})$, and on the index n numbering the discrete set of solutions for given k. For given Γ and α neutral stability boundaries $\mathrm{Re}_n(k, n)$ are defined by $\sigma(\mathrm{Re}) = 0$. Finally, the critical Reynolds number Re_c is the lowest neutral Reynolds number, equivalent to $\max_{k,n} \sigma(\mathrm{Re}) = 0$.

4.2 Methods of Solution

All differential equations are discretized with triangular elements on a rectangular domain (x, y) using the finite element library FEniCS [8]. To properly resolved the flow fields near the boundaries the mesh is refined towards all walls by subsequently doubling of the number of grid points within 5%, 1% and 0.5% of the width and the height of the cavity. Taylor–Hood elements are employed which implement a quadratic interpolation for the velocity fields and a linear interpolation for the pressure.

4.2.1 Basic State

The steady two-dimensional flow $(\boldsymbol{u}_0, p_0)$ is computed using Newton–Raphson iteration already implemented in the FEniCS framework, where only the variational formulation and boundary conditions are needed. Absolute and relative convergence criteria on the L_2 norm of the residuum are set to 10^{-10} and 10^{-8}, respectively. During tracking the stability boundary, the basic state calculation is typically terminated due to the absolute convergence criterion. The converged basic flow field enters the linear stability analysis parametrically.

4.2.2 Linear Stability Analysis

To solve the generalized eigenvalue problem, we use the ARPACK library [89] in a shift-invert mode with a spectral shift of 1. The eigenvalues close to this spectral shift should be the well captured by the solver. In order to ensure that the method captures all the eigenvalues of interest the Krylov space dimension is set to 300, while the number of converged eigenvalues required to assume convergence is set to 50. We noticed that when lowering both these numbers some eigenvalues would not be captured, in particular in the restabilisation of mode III, for $\Gamma = 1$.

To find the critical Reynodls number for given (Γ, α), we used the technique described in subsections 3.5.1 and 3.5.2, using eigenvalue sensitivity to wavenumber variations to feed a BFGS algoritm together with a polynomial continuation method.

λ_2-criterion

To better observe the presence of vortices in the perturbation associated to critical eigenmodes, one can use the λ_2-criterion, introduced by Jeong & Hussain [69]. Let us decompose the gradient of the velocity into a symmetric and anti-symmetric part

$$\mathbf{S} = \frac{1}{2}\left(\nabla \boldsymbol{u}' + \nabla \boldsymbol{u}'^{\mathrm{T}}\right) \quad \text{and} \quad \boldsymbol{\Omega} = \frac{1}{2}\left(\nabla \boldsymbol{u}' - \nabla \boldsymbol{u}'^{\mathrm{T}}\right). \tag{4.9}$$

The criterion is based on that at least two of the sorted eigenvalues $(\lambda_1, \lambda_2, \lambda_3)(\boldsymbol{x})$ of $\mathbf{S}^2 + \boldsymbol{\Omega}^2$ should be negative in the core of a vortex. Therefore λ_2 should be negative in the vortex core, and a vortex can be represented as a connected region where λ_2 is continuously negative. To visualize vortices, one can then plot the contours of a negative isovalue of λ_2.

4.2.3 Code Verification

In a first step a grid-convergence study for the critical Reynolds and wave numbers is carried out. Table 4.1 shows (Re_c, k_c) as function of the grid resolution for three aspect ratios Γ and $\alpha = 0°$. Grid convergence is clearly obtained and the converged results compare very well, i.e. within 1%, with the reference results of Albensoeder *et al.* [5] and Theofilis *et al.* [175]. The data suggest that a mesh of 40×40 provides already very accurate results for $\Gamma = 1$. Note that the grid specified represents the grid with equidistant spacing, the actual grid used is refined towards the walls as specified above such that the formal 40×40 resolution practically is made of 13976 elements or 95328 degrees of freedom. With similar arguments, the initial grids 40×80 and 80×40 for $\Gamma = 2$ and $\Gamma = 1/2$, respectively, are used for the stability analysis for $\alpha > 0°$.

To verify the growth rate σ and the oscillation frequency ω as functions of the wave number k we consider $\Gamma = 1$ and $\alpha = 0°$ for which reference data are available in the literature. To that end the most dangerous mode has been computed for $\mathrm{Re} = 200$ and $\mathrm{Re} = 1000$. Figure 4.2 shows the growth rates and oscillation frequencies of the fastest growing mode for $\mathrm{Re} = 200$ (dashed lines) and $\mathrm{Re} = 1000$ (full lines) in comparison with the results of Ding & Kawahara [45] (□) and Albensoeder *et al.* [5] (○). For $\mathrm{Re} = 200$ an excellent agreement is found for all k considered using the basic grid resolution of 40×40. The numerical results for $\mathrm{Re} = 1000$ also show a good agreement with the reference data for the frequency ω. Agreement of the growth rate σ obtained for the current resolution with the reference data is acceptable. Typically, our results are in-between the two reference data sets and tend to compare slightly better with those of Ding & Kawahara [45] than with those of Albensoeder *et al.* [5].

4.2.4 Non-Linear Numerical Simulation

For the purpose of an additional verification we also carried out full numerical simulations of the time-dependent three-dimension flow. To that end the problem (4.1) was solved employing the spectral element code Nek5000.

TABLE 4.1 – Critical Reynolds number Re_c and wave number k_c as functions of the grid resolution for $\alpha = 0°$. The column labelled 'Grid' refers to the initial grid size before refinement, n_T denotes the number of triangles, while n_DOF is the number of degrees of freedom.

Author	Γ	Grid	n_T	n_DOF	Re_c	k_c
Present	1	16×16	1032	7160	811.96	14.71
Present	1	20×20	3520	25124	788.52	15.29
Present	1	30×30	6136	43248	787.16	15.34
Present	1	40×40	13976	95328	786.39	15.37
Present	1	50×50	18896	128428	785.93	15.38
Present	1	60×60	24792	167872	785.63	15.39
[5]	1	spectral 141×141			786.3 ± 6	15.43 ± 0.06
[175]	1	spectral 48×48			782.61	15.37
Present	2	10×20	1268	9100	455.29	1.7146
Present	2	20×40	7008	48916	445.95	1.7181
Present	2	30×60	12324	85150	445.57	1.7178
Present	2	40×80	24064	163140	444.90	1.7183
[5]	2	spectral 141×141			446.3 ± 10	1.715 ± 0.012
Present	0.5	32×16	2716	19016	711.15	10.662
Present	0.5	40×20	7008	48916	709.71	10.655
Present	0.5	60×30	12324	85150	707.69	10.646
Present	0.5	80×40	24064	163140	706.70	10.642
[5]	0.5	spectral 141×141			706.1 ± 7	10.63 ± 0.1

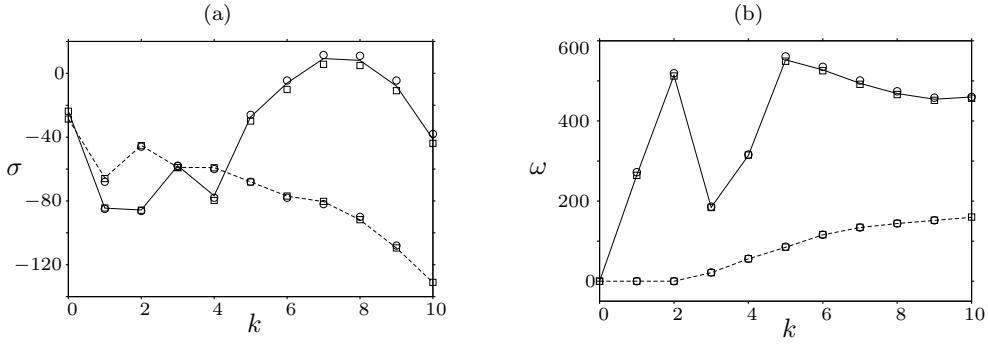

FIGURE 4.2 – (a) Growth rate $\sigma = \Re(\gamma)$ and (b) oscillation frequency $\omega = \Im(\gamma)$ of the most dangerous mode for $\alpha = 0°$, $\Gamma = 1$ for $\mathrm{Re} = 200$ (dashed lines) and $\mathrm{Re} = 1000$ (full lines). Results are given for the base-grid resolution of 40×40 in comparison with data of Ding & Kawahara [45] (□) and Albensoeder *et al.* [5] (○).

For these calculations the flow was assumed periodic in z with a wavelength corresponding to $2\pi/k_c$. Using a regular tensor mesh composed of $N_x \times N_y \times N_z = 20 \times 20 \times 10$ elements of polynomial order $p = 6$ for the velocity and $p = 4$ for the pressure, simulations are carried out for $\Gamma = 1$ with $\alpha = 22.5°$. Temporal integration was performed using a 3rd order Adams–Bashforth scheme with 3rd order extrapolation of the convective terms.

4.3 Results

4.3.1 Basic Flow

The basic flow $\boldsymbol{u}_0 = \boldsymbol{u}_0^{2D} + \boldsymbol{u}_0^{C}$ can be decomposed into a recirculating two-dimensional cavity flow $\boldsymbol{u}_0^{2D}(x, y)$ driven by the reduced Reynolds number $\mathrm{Re}\cos\alpha$, and the parallel bounded Couette flow $\boldsymbol{u}_0^{C}(x, y) = w_0^{C}(x, y)\boldsymbol{e}_z$ driven by the effective Reynolds number $\mathrm{Re}\sin\alpha$. The recirculating part $\boldsymbol{u}_0^{2D}$ of the flow field is independent of the Couette part of the flow, because $\nabla \cdot \boldsymbol{u}_0 = \nabla \cdot \boldsymbol{u}_0^{2D} = 0$ and the non-linear coupling terms $\boldsymbol{u}_0^{C} \cdot \nabla \boldsymbol{u}_0^{2D} = 0$ vanishes. On the other hand, the parallel Couette part of the flow $\boldsymbol{u}_0^{C}$ depends on the recirculating part of the flow and results from a linear equation balancing viscous diffusion and advection by $\boldsymbol{u}_0^{2D}$ in the (x, y) plane. The strength of both parts of the flow are related to each other via the Reynolds number and the inclination angle.

In the combined basic flow $\boldsymbol{u}_0$ fluid elements have helical trajectories. This flow structure also arises in the context of air motion in street canyons driven by oblique wind directions [see e.g. 185, 169]. The projections of the fluid trajectories onto the (x, y) plane correspond to the closed streamlines of the recirculating part $\boldsymbol{u}_0^{2D}$ of the flow. The pitch of the fluid trajectories is determined by the spanwise component $\boldsymbol{u}_0^{C}$. Because of the spanwise velocity is considerably stronger near the moving lid than in the bulk of the cavity, fluid elements are transported in the z direction mainly in the upper part of the cavity. Due to the monotonic decay of the magnitude of $\boldsymbol{u}_0^{C}$ from the lid, the mean spanwise velocity of fluid elements is always less than span component of the lid velocity.

In the limit $\alpha \to 0$ the classical lid-driven cavity flow is recovered with $\boldsymbol{u}_0^{C} = 0$. The stability boundary has been investigated by several authors with [5] perhaps providing the most comprehensive stability results quasi-continuously covering the range of aspect ratios $\Gamma \in [0.2, 4]$. In the other limit of $\alpha \to \pi/2$, the recirculating part $\boldsymbol{u}_0^{2D} = 0$ vanishes and the basic flow arises as a pure bounded Couette flow in a rectangular channel which can be given as an infinite series

$$w_0^{C} = \mathrm{Re} \sum_{n=0}^{\infty} \frac{4(-1)^n}{(2n+1)\pi} \frac{\sinh[(2n+1)\pi(y+\Gamma/2)]}{\sinh[(2n+1)\pi\Gamma]} \cos[(2n+1)\pi x]. \tag{4.10}$$

The stability of this basic flow has been considered by Theofilis *et al.* [175]. No unstable modes have been found by these authors, even for Reynolds numbers as large as $\mathrm{Re} = 5000$. Our linear stability analysis also indicates the basic flow is linearly stable, at least up to $\mathrm{Re} = 3000$. Since the critical Reynolds numbers for lid-driven

cavity flows for $\alpha = 0°$ and $\Gamma \gtrsim 0.5$ satisfy $\mathrm{Re}_c < 10^3$ [5], a strong stabilization of the basic flow is expected as $\alpha \to \pi/2$.

The linear stability boundary $\mathrm{Re}_c(\alpha, \Gamma)$ depends on the inclination angle α and the cross sectional aspect ratio Γ. For this reason calculations have been carried out for selected aspect ratios, varying α quasi-continuously.

4.3.2 Linear Stability for $\Gamma = 1$

Neutral Reynolds and wave numbers for $\Gamma = 1$ are shown in fig. 4.3 as functions of the inclination angle α. The critical Reynolds number (full bold lines) is made of different segments belonging to different neutral curves (full lines, color coded) leading to qualitatively different critical modes, depending on α. As α approaches $\pi/2$ the critical wave number becomes very small, indicating the critical mode becomes nearly two-dimensional. Numerical data for the critical parameters are listed in table 4.2.

Modes I and II

At $\alpha = 0°$ the classical Taylor–Görtler mode [mode I, 5] with relatively high wave number is recovered. As the inclination angle increases from zero, the Taylor–Görtler mode I with a small wavelength evolves continuously and changes only slightly due to the Couette part of the basic flow. While the Taylor–Görtler mode I is stationary for $\alpha = 0°$, the Görtler vortices drift in positive z direction with a phase velocity which increases as α increases. From fig. 4.3(b,c) it can be observed that the phase velocity of the Görtler mode increases nearly linearly with α.

When α is increased the basic flow is slightly stabilized until, at $\alpha \approx 4.3$, the critical mode I changes to mode II which has a similar wave number. Mode II very much resembles mode I and the corresponding neutral stability boundary extends down to $\alpha = 0°$ (not shown). At $\alpha = 0°$ mode II is only the second most dangerous mode and, to the best of our knowledge, it has not yet been reported in the literature.

The neutral mode II is illustrated in fig. 4.4 for $\alpha = 6°$. Shown is the perturbation velocity field $\boldsymbol{u}$ in the plane $y = 0$ (fig. 4.4(a)) and in a plane $z = \text{const.}$ (fig. 4.4(b)) in which the energy production rate i takes its global maximum. In addition fig. 4.4(b) shows the basic state in form of streamlines of $\boldsymbol{u}_0^{\mathrm{2D}}$ and, in color from yellow to red, the magnitude of $\boldsymbol{u}_0^{\mathrm{C}}$. The energy transfer to the critical mode primarily arises in the boundary layer of $\boldsymbol{u}_0^{\mathrm{2D}}$ with curves streamlines in regions where the direction of the perturbation flow makes and angle of approximately 45° with respect to the streamlines. Finally, fig. 4.4(c) shows a three-dimensional view over two wavelengths of the isosurfaces of the energy production rate i at 10% of its maximum value $i_{\max}$. The region where the $i > 0.1 \times i_{\max}$ is also indicated by the blue areas in fig. 4.4(b). Comparing fig. 4.4(c) with fig. 4.4(a) it is clear that banana-shaped regions of high energy transfer mirror the perturbation vortex structures which they feed. The perturbation vortices are just located in-between to neighbouring isosurfaces of i shown in fig. 4.4(c).

Mode II very much resembles the classical Taylor–Görtler mode I for $\alpha = 0°$ [5]

TABLE 4.2 – Critical data and integral production rates of kinetic energy as functions of the aspect ratio Γ and the inclination angle α of the lid motion.

Γ	α [°]	mode	Re_c	k_c	ω_c	I_1	I_2	I_3	I_4	$\sum_n I_n$
0.5	0.00	I	706.7	10.64	−818.87	0.1059	0.6128	0.1016	0.1796	1.000
	15.00	I	600.6	11.00	−323.27	0.2029	0.5943	0.1118	0.0910	1.000
	40.00	I	858.7	9.05	−2070.37	0.4200	0.5433	0.0595	−0.0228	1.000
	50.00	II	1112.1	7.81	−1234.75	0.0712	0.7796	0.1039	0.0453	1.000
	65.00	III	984.0	4.13	−1237.96	0.1293	0.8427	0.0556	−0.0277	1.000
	75.00	III	1304.7	2.56	−1112.10	0.0774	0.9344	0.0256	−0.0375	1.000
1	0.0	I	786.4	15.37	0.00	0.0405	0.6784	0.1795	0.1015	1.000
	2.50	I	792.4	15.34	−225.42	0.0418	0.6787	0.1798	0.0996	1.000
	6.00	II	795.07	15.27	−0.876	0.0396	0.6847	0.1793	0.0965	1.000
	0.0	III	937.74	7.39	−460.26	0.0012	0.6787	0.1922	0.1279	1.000
	22.50	III	619.9	6.96	−454.55	0.0740	0.6717	0.2219	0.0323	1.000
	40.00	IV	834.2	7.76	−278.25	0.0166	0.8234	0.1434	0.0164	1.000
	60.00	V	637.3	4.59	−524.45	0.0415	0.9066	0.0750	−0.0233	1.000
	67.50	VI	643.3	3.19	−629.57	0.0730	0.9327	0.0548	−0.0606	1.000
	75.00	VII	631.6	1.82	−253.10	0.0044	0.9447	0.0189	0.0319	1.000
2	0.00	I	444.90	1.72	0.00	−0.0283	0.7363	0.0803	0.2117	1.000
	50.00	I	269.09	1.75	−107.51	0.0438	0.8276	0.1193	0.0093	1.000
	75.00	I	483.94	1.11	−182.74	0.0070	0.9559	0.0269	0.0102	1.000
	85.00	II	1159.19	0.68	−159.68	−0.0029	0.9076	0.0016	0.0937	1.000

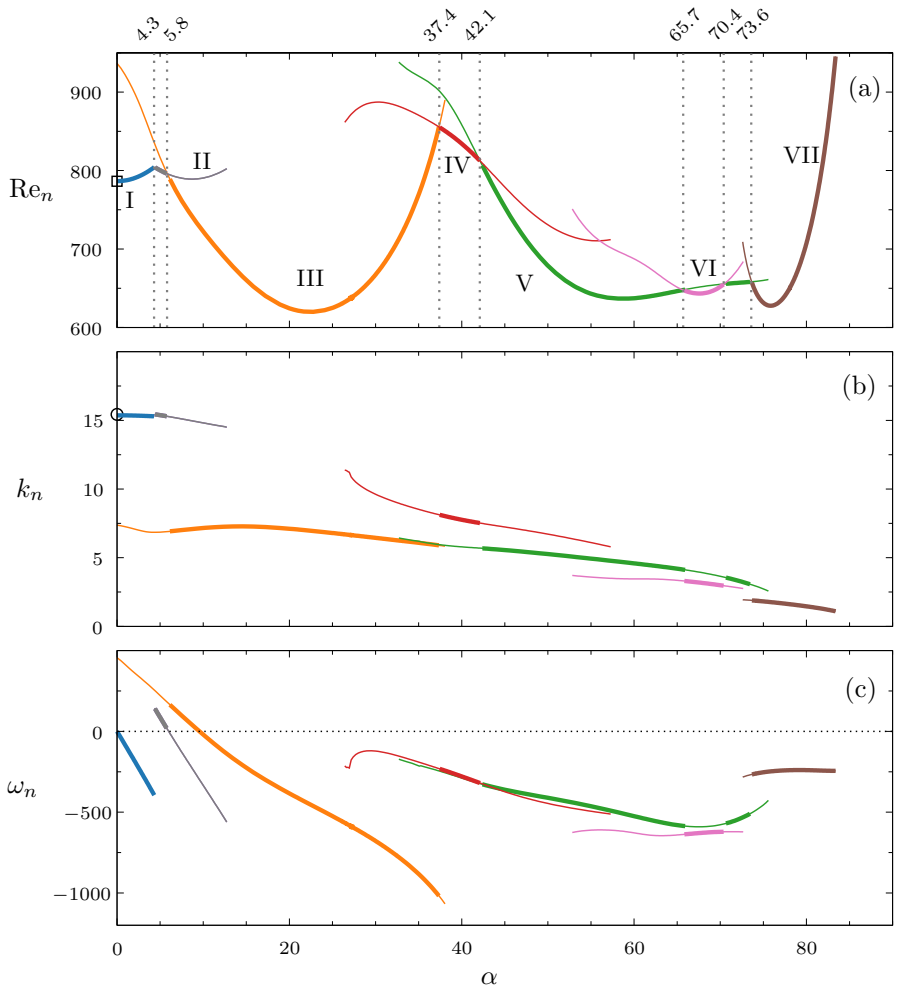

FIGURE 4.3 – Neutral Reynolds number (top), wave number (middle) and angular frequency (bottom) as functions of α for $\Gamma = 1$ for the most dangerous modes. Bold lines indicate the critical values. Different branches are distinguished by colour and capital Roman numbers. The numbers at the top of the upper panel denote the angles at which critical curves intersect (vertical dotted lines). The square (□) and the circle (○) indicate the critical Reynolds and wave number, respectively, obtained by Albensoeder *et al.* [5] for $\alpha = 0°$.

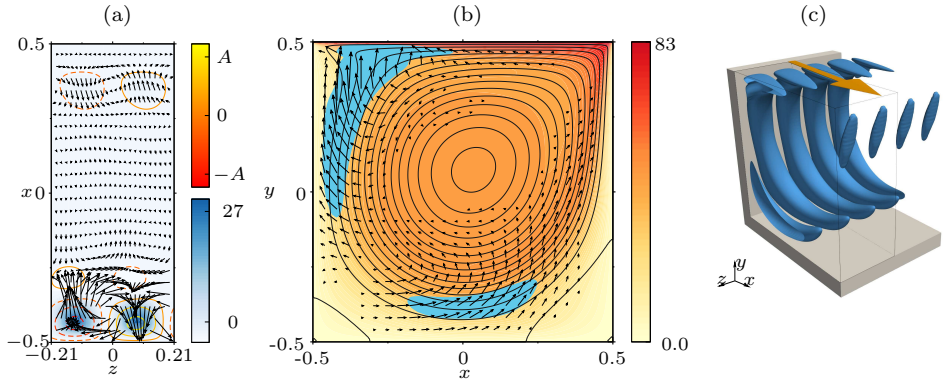

FIGURE 4.4 – Mode II (grey in fig. 4.3) over one period in z for $\alpha = 6°$, $\mathrm{Re}_n = 795.07$, $k_n = 15.27$. (a) Shown are the perturbation velocity vector field (u, w) in the plane $y = 0$ (arrows), the perturbation velocity v (orange) normal to $y = 0$ with $v > 0$ (full lines) and $v < 0$ (dashed lines), and the total local production i (blue shading). (b) Perturbation velocity vectors (u, v) in the plane $z = \text{const.}$ in which i takes its maximum, streamlines of $\boldsymbol{u}_0^{\mathrm{2D}}$, magnitude of $\boldsymbol{u}_0^{\mathrm{C}}$ (yellow–red), and the region in which $i > 0.1 \times i_{\max}$ (blue). (c) Isosurfaces of i on which $i = 0.1 \times i_{\max}$ shown over two periods in z. The lid motion is indicated by the orange arrow.

with strong vortices on the wall at $x = -1/2$, upstream of the moving lid where the energy production peaks. On the downstream wall at $x = 1/2$ the vortices are much weaker. The weak vortices on the downstream wall are slightly offset in positive z direction as compared to the vortices on the upstream wall, as a result of the Couette part of the basic flow. Hence, the vortices are slightly helical with a small pitch. For $\alpha < 5.9$ this mode propagates in the negative spanwise direction as can be seen from fig. 4.3(c).This means that for the small range of α for which this mode is the critical mode it propagates against the z component of the lid velocity. Progressively the phase velocity diminishes and changes sign such that for $\alpha > 5.9$ the wave propagates in the same z direction as the lid. Again, the propagation speed seems to scale linearly with the yaw angle α.

Mode III

Near $\alpha = 5.8°$ the critical mode II (grey) changes to mode III (orange in fig. 4.3) which has approximately half the wave number as the low-α Taylor–Görtler modes. It can be seen from fig. 4.3 that the neutral mode III originates from $\alpha = 0°$ and has already been reported [45, 5]. Unlike mode I, which is stationary at $\alpha = 0°$, mode III is oscillatory at $\alpha = 0°$ and arises as a pair of waves traveling in the $\pm z$ directions. As α increases from zero the degeneracy of the neutral Reynolds number removed and the basic flow is strongly destabilised with respect to the mode which propagates in the negative z direction (opposing the direction of the Couette part of the basic flow), while the basic state is stabilised with respect to the complex conjugate mode which travels in the positive z direction. This behavior can be inferred from the slope $\partial \mathrm{Re}_n^{\mathrm{III}} / \partial \alpha|_{\alpha=0} \neq 0$ in fig. 4.3. After the neutral mode III has become critical for

$\alpha > 5.8°$ the propagation direction of mode III turns in the positive z direction at $\alpha = 9.6°$ (fig. 4.3(c)). For $\alpha \lesssim 15°$, ω_n depends approximately linearly on α, whereas for $\alpha \gtrsim 15°$ the magnitude of the frequency increases monotonically indicating an increasing phase velocity of this mode as α increases.

Mode III is illustrated in fig. 4.3 for $\alpha = 0°$ (left column), 22.5° (middle columns) and 35° (right column), showing the same quantities as in fig. 4.4. Similar to mode II the critical mode III arises as vortices which are the strongest on the upstream wall $x = -1/2$. The vortices, best seen in fig. 4.5(b) for $\alpha = 22.5°$, have a similar size in wall-normal direction in both cases. However, different from mode II at $\alpha = 6°$, mode III has a much larger wavelength throughout the range of yaw angles over which it is critical (cf. figs. 4.3 and 4.5). Near the downstream wall we do not find the same vortices. Rather, in the plane $y = 0$ larger-scale vortex structures occupying the full width of the cavity can be identified. Furthermore, the pitch of the vortices of mode III is larger than the one for mode II which can be seen by correlating the vortex structures (e.g. the isolines of v in the plane $y = 0$) on the two walls at $x = \pm 1/2$.

Common to modes I, II and III they all extract most of their energy from the basic state in the curved boundary layer of $\boldsymbol{u}_0^{\mathrm{2D}}$ on the upstream wall [see also 5]. In addition, we also find minor contributions to the energy production near the bottom of the cavity. Correspondingly, the energy budgets of all three modes are very similar (Table 4.2). All modes destabilise the basic flow primarily through the process described by I_2. Therefore, the modes I, II and III may be called spiral Taylor–Görtler vortices.

For a constant Reynolds number the shear rate in the curved boundary layer of $\boldsymbol{u}_0^{\mathrm{2D}}$, which is responsible for the Taylor–Görtler instability, becomes weaker like $\sim \cos\alpha$ as α is increased. Therefore, a certain stabilization of the basic flow might be expected with respect to modes which build on the Görtler mechanism. However, this is not the case. Rather, the critical Reynolds number for mode III decreases and reaches a minimum near $\alpha \approx 22.5°$. This behavior can be explained by the additional shear in z direction from which kinetic energy can be extracted. The shear is provided by the Couette part of the basic flow w_0^{C} which exhibits a plateau in the centre of the cavity. Furthermore, the vortex structures of mode III at $\alpha = 22.5°$ are larger than at $\alpha = 0$ (fig. 4.5(a,b)). Associated with the structural changes of the critical mode, also the region of energy production within which i_2 (lift-up) is dominant changes and, for increasing α, extends over the bottom of the cavity up to the wall downstream of the moving lid (fig. 4.5). Interestingly, the extended isosurfaces of perturbation-energy production for $\alpha = 0°$ make an angle of $\approx 25°$ with respect to the direction of motion of the lid (fig. 4.5(g)). As the yaw angle α is increased the orientation of the production isosurfaces, and thus the perturbation vortices, turns into the direction of the lid velocity such that, near the minimum of the critical Reynolds number neutral at $\alpha \approx 22.5°$, the perturbation-energy production surfaces are approximately aligned parallel to the (x, y) plane (fig. 4.5(h)).

Mode IV and V

Beyond $\alpha \approx 22.5°$ (minimum of $\mathrm{Re}_c^{\mathrm{III}}(\alpha)$) mode III is less efficient in extracting energy from the basic flow and for $\alpha > 37.4°$ mode IV (red in fig. 4.3) becomes critical, with a

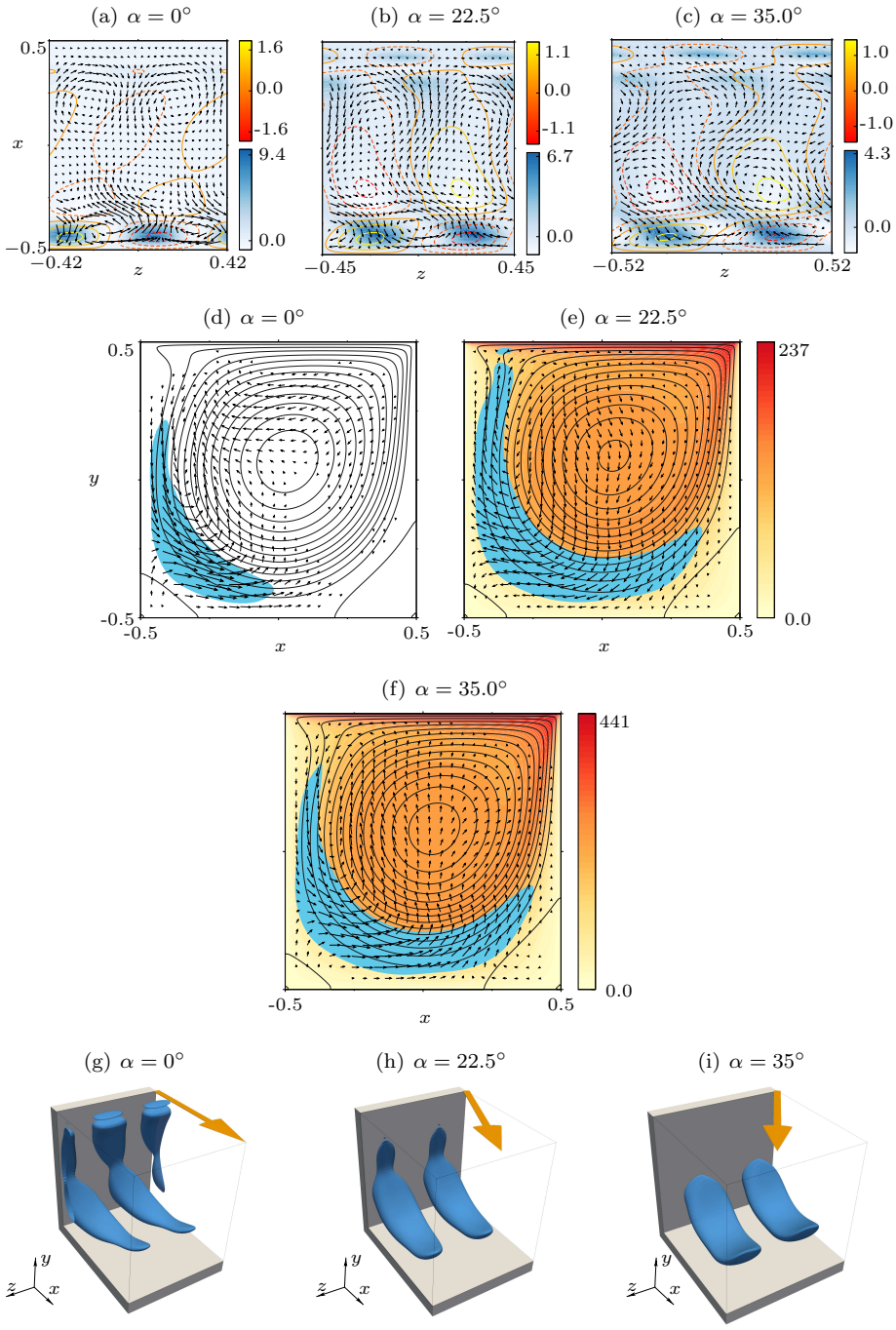

FIGURE 4.5 – Neutral mode III for $\alpha = 0°$ (a,d,g), 22.5° (b,e,h) and 35° (c,f,i). Shown are the same quantities as in fig. 4.4, except that (g,h,i) show only one period in z.

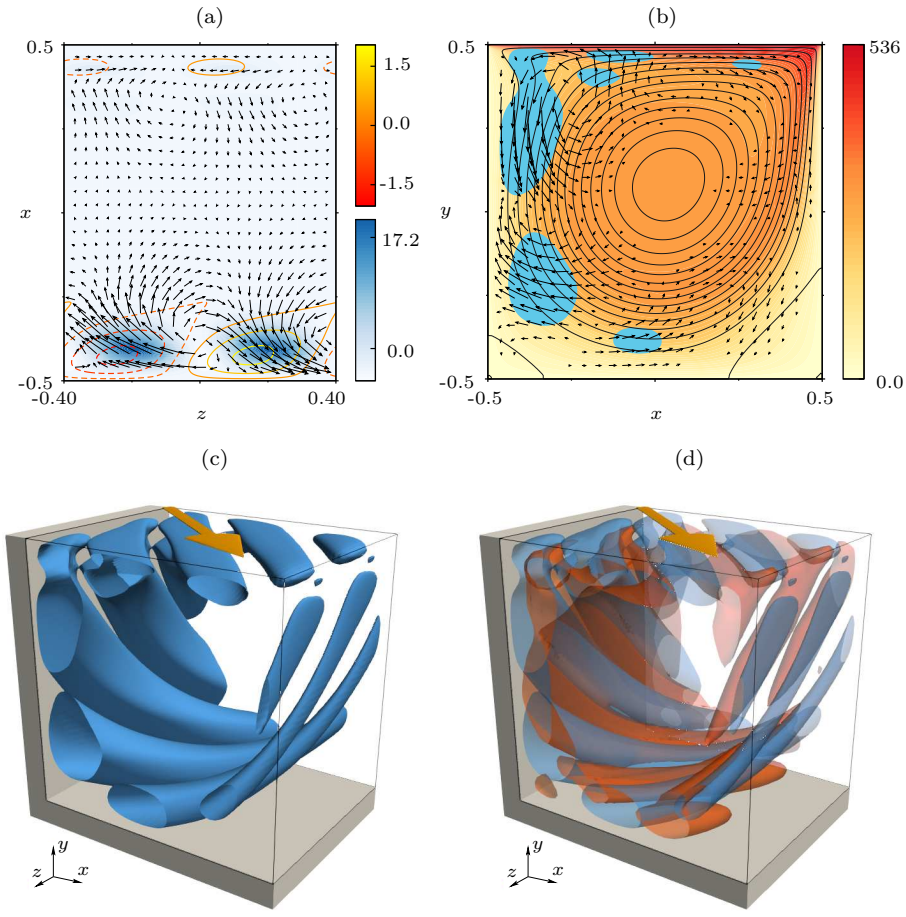

FIGURE 4.6 – Critical mode IV (red in fig. 4.3) at $\alpha = 40°$, $\mathrm{Re}_c = 637.3$, and $k_c = 4.59$. All quantities as in fig. 4.4, except for (c) which shows isosurfaces at $i = 0.03 \times i_{\max}$. The box extends of one wavelength in z. (d) isocontour of the vortex centerline criterion $\lambda_2 = -5$ is shown in orange while the same isocontour for the production rate as in (c) is in blue, to convince the reader that they are somehow equivalent.

critical wave numbers $k_c \approx 8$, slightly larger than for mode III, and phase velocity ω/k nearly twice as slow as the one of mode III. The lift up mechanism I_2 becomes even more preponderant in the perturbation energy budget, while I_3 (anti-lift up) decreases to 14 % for $\alpha = 40°$ (table 4.2). Mode IV is visualized in fig. 4.6 for $\alpha = 40°$. As can be seen from fig. 4.6(c) the isosurfaces of the total local production rate i are approximately aligned with the basic flow and extend in a spiral fashion about the center of the basic swirling vortex. Likewise the perturbation vortices, well visible in fig. 4.6(b) spiral about the basic vortex core. These vortices which are centered between two neighbouring regions of high energy production are also visualized by isosurfaces of the λ_2-criterion introduced by Jeong & Hussain [69] $\lambda_2 = -5$ in fig. 4.6(d). One can see that between each thread of production rate isosurface (blue) is a vortex centerline (orange). From fig. 4.6(c) one can identify seven segments of elongated energy production regions corresponding to seven perturbation vortices. Close to the lid, one could see a double structure of production rate (better seen in fig. 4.6(c), and in the next figures). In fact, these two threads are surrounding a single vortex. The presence of the upper thread is due to the strong gradients of the basic flow close to the lid, while the lower one is only due to the perturbation vortex. The spiralling energy-production surfaces and the associated vortices close on themselves after 3.5 periods in z direction after having completed one full revolution about the basic vortex, thus the average pitch is $7\lambda_c/2$. The vortices are initiated along the wall downstream of the lid and grow in size as they evolve in direction parallel to the basic flow. After passing the bottom wall, the vortices attain their maximum size when they reach the upstream wall (also visible in fig. 4.6(a)), where also the local production i reaches its maximum, before being damped by the strong perturbation-energy dissipation near the moving lid (not shown). Figure 4.6(b) confirms the vortices gaining in strength as they extend from the downstream to the upstream wall.

Unlike modes I, II and III, the axes of the perturbation vortices of mode IV are strongly deflected from the (x, y) plane. In this respect, the critical mode IV is a members of another family of modes whose vortex structures are primarily aligned in the z direction.

Mode IV is critical only within a relatively small range of inclination angles. For $\alpha > 42.1°$ mode V (green in fig. 4.3) becomes critical. It is illustrated in fig. 4.7. The critical mode has a similar spiral structure as mode IV, but with 5 vortices arranged about the circumference of the basic vortex flow and cutting through the periodic unit cell. Figure 4.7(c) shows the corresponding isosurfaces of $i = 0.03 \times i_{\max}$.Thus the average pitch of the perturbation vortices is $5\lambda_c/2$.

It is worth noting that mode V has a wave number very close to the one of Mode III (fig. 4.3(b)). This property may lead to complex non-linear mode interactions near $\alpha = 40°$. Technically, the similarity of the critical wave numbers makes the numerical tracking slightly more difficult.

Modes VI and VII

Mode V remains is critical in the range of $\alpha \in [42.1°, 65.7°]$ and $\alpha \in [70.4°, 73.6°]$. Between these two ranges, mode V is replaced by mode VI (pink in fig. 4.3) within

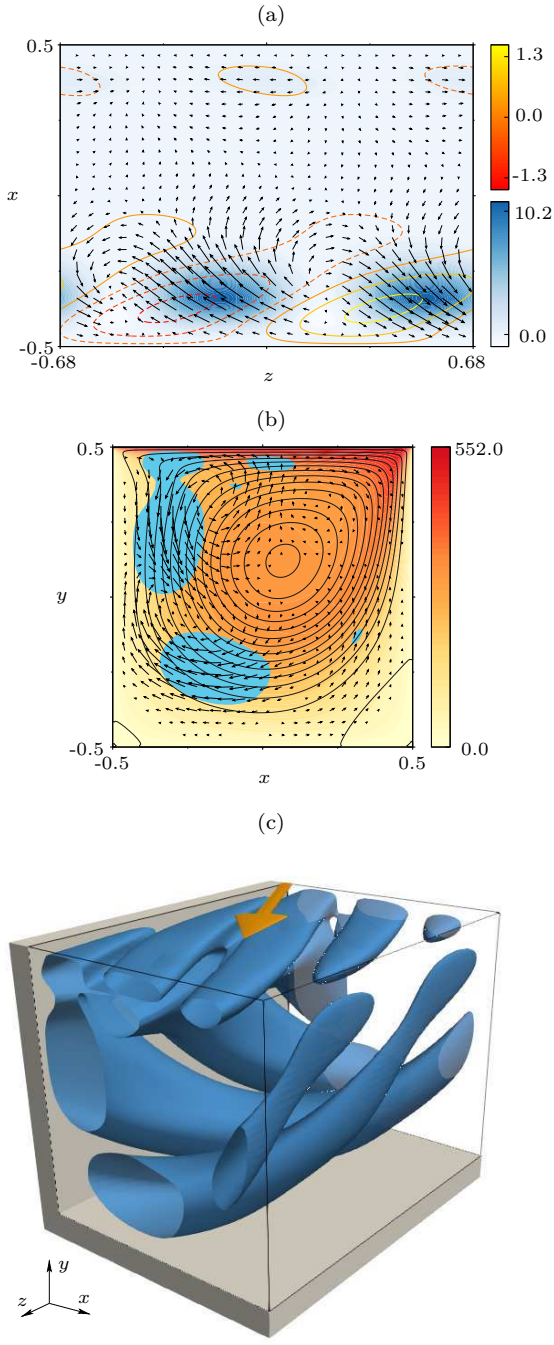

FIGURE 4.7 – Critical mode V (green in fig. 4.3) for $\alpha = 60°$, $\mathrm{Re}_c = 637.34$ and $k_c = 4.59$. All quantities as in fig. 4.6.

$\alpha \in [65.7°, 70.4°]$. Finally, mode VII (brown in fig. 4.3) appears to be the critical mode for $\alpha > 73.6°$.

The structures of modes VI and VII are illustrated in figs. 4.8 and 4.9, respectively. They are similar as for mode V (fig. 4.7), but the critical wavelength λ_c is increasing with α. Moreover as the angle increases, the strength of the vortices close to the downstream edge of the lid decreases dramatically, not making it possible to state whether they are still spiraling or if it consists of distinct vortices being generated along the downstream recirculation zone. Consistent with the fact that the cross-sectional flow becomes weaker, the perturbation eddies are slowly migrating towards the center of bulk, while the main vortex of the basic flow moves toward to top downstream corner. This is best seen comparing fig. 4.6(b,c) and 4.9(b,c). Mode VII undergoes a dramatic stabilization for $\alpha \gtrsim 80°$, rapidly reaching critical Reynolds number which are beyond those for which our numerical solver has been designed. Most likely, critical modes of the linear analysis become increasingly crowded and stabilized as $\alpha \to 90°$.

General Properties of the Critical Modes for $\Gamma = 1$

All critical modes found for $\Gamma = 1$ are destabilized by the lift-up mechanism represented by i_2 whose integral contribution ranges from 68 % for $\alpha = 0°$ to 94 % for $\alpha = 75°$. The energy production is most pronounced near the upstream wall of the cavity. Therefore, we conclude that the mechanism is essentially a modification of the Taylor–Görtler instability which is well established for $\Gamma = 1$. This interpretation is supported by the expectation that the pure Couette part of the flow (4.10) is linearly stable and no linear mechanism can be derived from this parallel shear flow alone. Since the Taylor–Görtler-like vortices are aligned with the direction of the basic flow, the pitch of the vortices of the helical critical modes increases with α. For small α the diameter of the vortices is small, as they scale with the boundary layer thickness of $\boldsymbol{u}_0^{2D}$. Therefore, as α increases, more and more helical vortices penetrate the unit cell defined by one wavelength λ_c of the perturbation flow (see, e.g., fig. 4.6(c)). As the basic flow turns predominantly into the span (z) direction and the critical wavelength increases, the Taylor–Görtler-like vortices become longer and can grow to larger diameters (see figs. 4.6(b) to 4.9(b)), because the characteristic length scale becomes the height of the cavity. Therefore, the trend is reversed and a lesser number of vortices penetrate the unit cell.

Except for mode I which is not traveling in the spanwise direction for $\alpha = 0$, the propagation speed of the neutral modes $c_n = -\omega_n/k_n$ in the spanwise direction at low angle seems to be rather independent of the lid velocity and become more and more affected by it at larger angles. This can been seen from fig. 4.10(b), in which curves of the ratio of the propagation speed and the spanwise lid velocity is varying consequently at small α and flattens as it increases. In contrast, at large angles, the neutral modes propagation speed seems to scale with the lid velocity and the ratio remains almost constant. Naturally all modes are propagating slower (a factor 2) than the lid velocity at large α, since in the bulk of the flow the transport of the perturbation by the basic flow has to be slower than close to the lid. It is worth also appreciating the notable jump of the propagation speed between the mode III

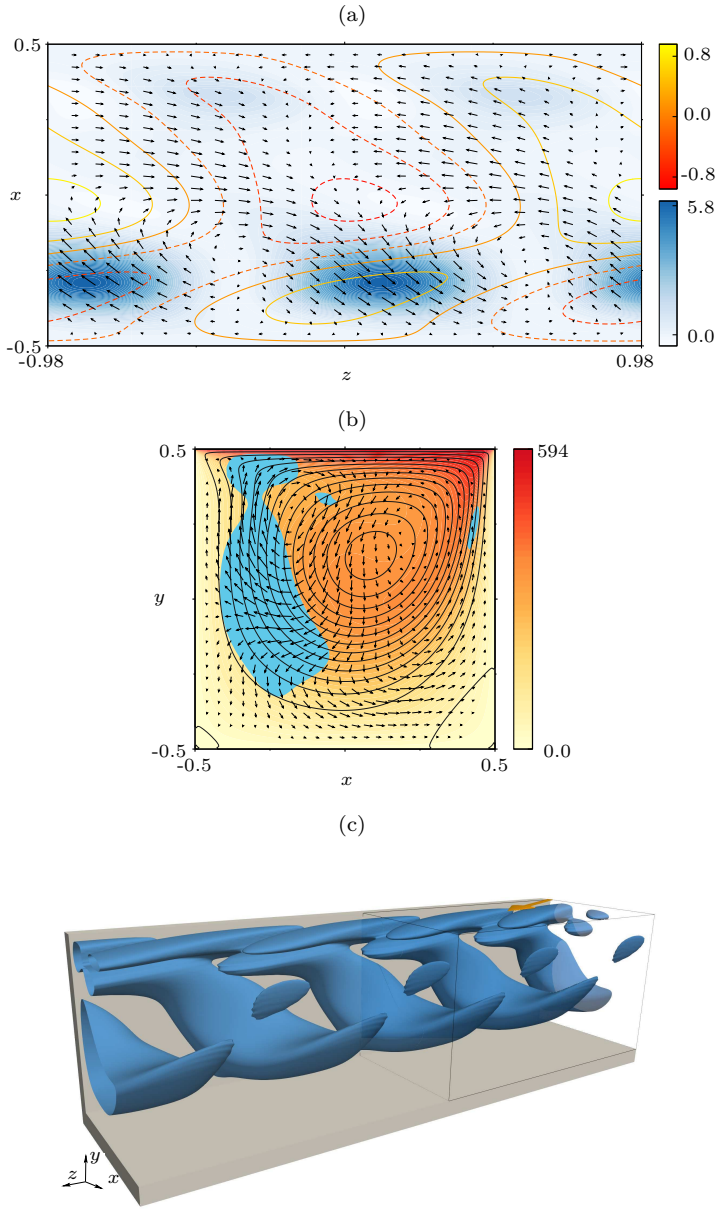

FIGURE 4.8 – Critical mode VI (pink in fig. 4.3) at $\alpha = 67.5°$ $\mathrm{Re}_c = 643.2$, $k_c = 3.19$. All quantities as in fig. 4.4.

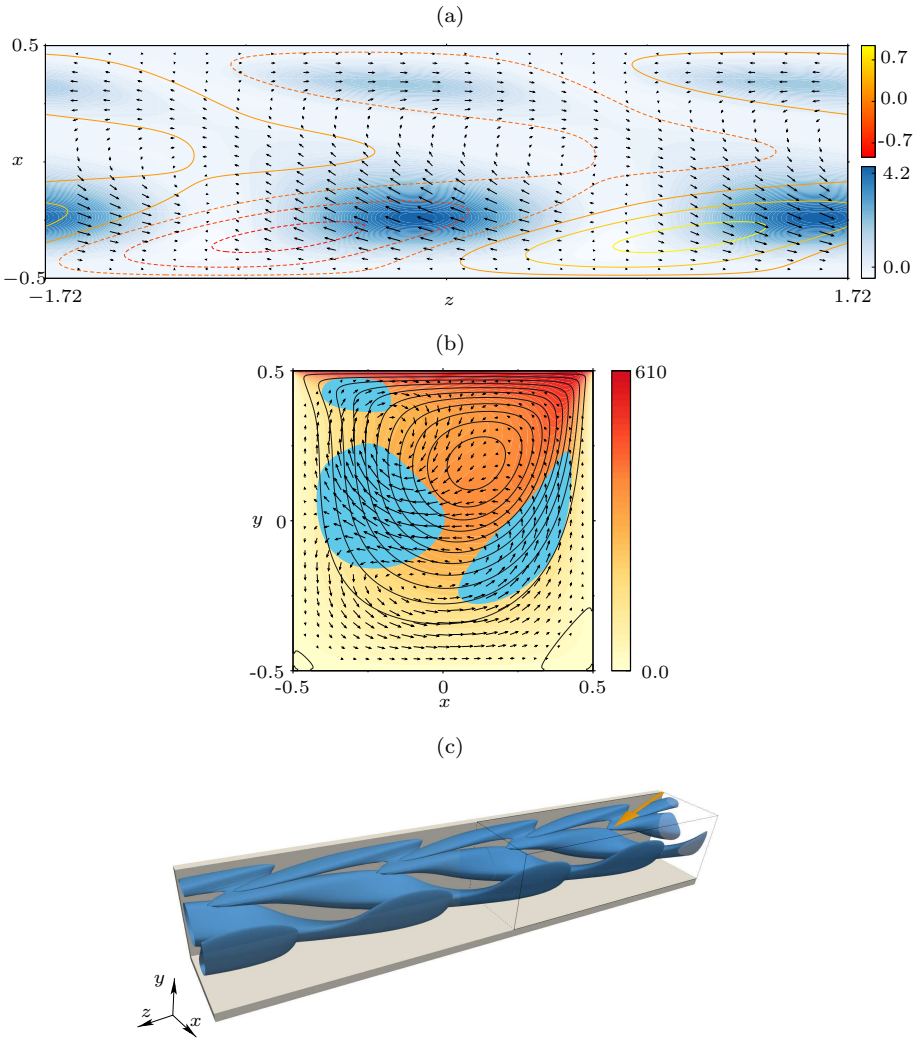

FIGURE 4.9 – Mode VII (brown in fig. 4.3) at $\alpha = 75°$, $\mathrm{Re}_c = 631.6$, $k_c = 1.82$. All quantities as in fig. 4.4.

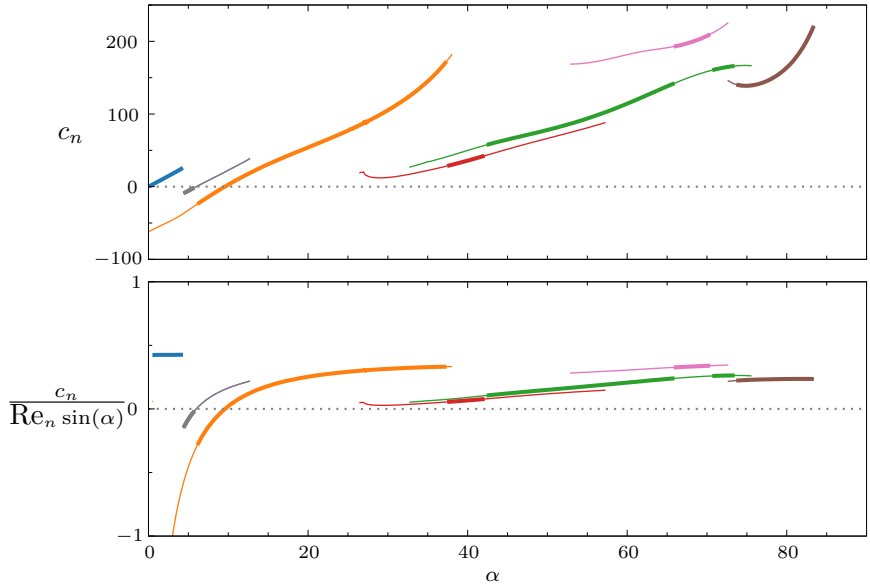

FIGURE 4.10 – (top) Neutral propagation speed c_n, (bottom) propagation speed to spanwise lid-velocity ratio, colors are the same as in fig. 4.3

and mode IV, differentiating clearly the two types of modes. The Taylor-Goertler modes from mode III propagates nearly 6 times faster than the spiraling mode IV when their critical curves intersect, and 5 times faster than mode V which has a similar wave number. Similarly, the direction of the production streaks close to the lid, progressively become more and more aligned with the lid direction. Mode III progressively changes its direction although a shift remains, mode IV is not perfectly aligned wheras mode V,VI,VII are. This is visible for instance in fig. 4.6(c) and 4.7(c).

Figure 4.3 reveals that the critical Reynolds numbers are less than $\mathrm{Re}_c < 800$ for most inclination angles. In particular, $\mathrm{Re}_c(\alpha = 22.5°) = 619.9$ ($k_c = 6.9645$) and $\mathrm{Re}_c(\alpha = 75°) = 631.6$ ($k_c = 1.822$). These results deviate from the ones obtained by Theofilis *et al.* [175] who also performed a linear stability analysis of the same flow for $\alpha = 22.5°$, 45° and 67.5°, but did not find any unstable eigenmode at $\mathrm{Re} = 800$ in the range $k \in [0, 25]$. Since our results are at variance with these previously published data, we carried out an independent non-linear numerical simulation using NEK5000 for $\Gamma = 1$, $\alpha = 22.5°$ and for slightly supercritical conditions $800 > \mathrm{Re} = 650 > \mathrm{Re}_c = 619.9$ and periodic boundary conditions in z with period $\lambda = 2\pi/k_c$. Impulsively starting the lid motion from a state of rest at $t = 0$ we find the basic flow to be established near $t \approx 0.5$. At about the same time small amplitude oscillations of w become visible and start growing exponentially in an oscillatory fashion (fig. 4.11). Fitting the signal $w(t)$ in the greyed area shown in fig. 4.11 by $w_\mathrm{F}(t) = a + b\mathrm{e}^{\sigma_\mathrm{F} t} \sin(\omega_\mathrm{F} t + c)$ we find the growth rate $\sigma_\mathrm{F} = 5.66 > 0$ and the angular frequency $|\omega_\mathrm{F}| = 478.5$. The frequency compare reasonably with the real part $\sigma = 4.63$ and excellently with the imaginary part $|\omega| = 475.7$ of the eigenvalue obtained for the same parameter set. The deviations amount to 18% and 0.6%, respectively. The discrepancy in the real part can be explained

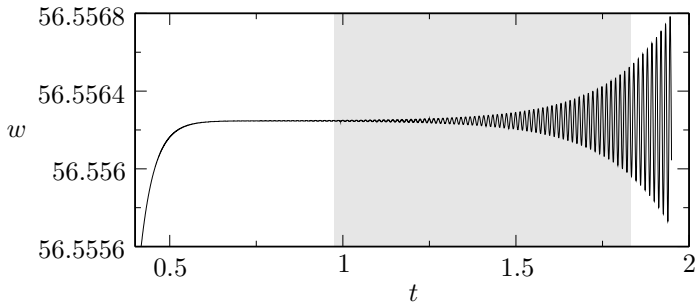

FIGURE 4.11 – Spanwise velocity component $w(-0.4, 0.4, 0)$ obtained by non-linear numerical simulation using NEK5000. The lid motion is impulsively started from rest at $t = 0$. Shown is the saturation phase of the basic flow and the subsequent exponential growth of an oscillatory perturbation. The parameters are $\Gamma = 1$, $\alpha = 22.5°$, $k = 6.96$, and $\mathrm{Re} = 650 > \mathrm{Re}_c = 619.9$. Note, the position $z = 0$ of the monitoring point is arbitrary. The range on which the fit is performed is shown in grey.

as it varies quickly in the vicinity of these parameters. Besides, critical Reynolds, estimated by the fitting the evolution of the amplitude of the limit cycle on which the system settles is bracketed $\mathrm{Re}_{c,nek} \in [613, 614]$, and is in good agreement with the one of the linear stability $\mathrm{Re}_c = 619.9$. This independent simulation demonstrates the instability of the basic flow with a critical Reynolds number $\mathrm{Re}_c < 650$, consistent with the present linear stability analysis.

4.3.3 Linear Stability for $\Gamma = 0.5$

An overview on the linear linear stability analysis for a shallow cavity with $\Gamma = 0.5$ is shown in fig. 4.12. For the classical case with $\alpha = 0°$ we find $\mathrm{Re}_c = 706.7$, $k_c = 10.64$ and $\omega_c = 818.9$. This is in very good agreement (differences less than 1%) with the result of Albensoeder *et al.* [5] who obtained $\mathrm{Re}_c = 706.1 \pm 7$, $k_c = 10.63 \pm 0.01$ and $\omega_c = 819.9 \pm 4$. Except for k_c our result is also in good agreement with the data of Theofilis *et al.* [175] (mode T2 from their table 7: $\mathrm{Re}_c = 720.18$, $k_c = 11.40$, $\omega_c = 838$).

Mode I

The critical mode I at $\alpha = 0°$ is oscillatory and arises has a pair of waves with relatively short wavelength which propagate in positive or negative z direction. As α increases, the degeneracy of the critical parameters is removed. While the wave propagating in the positive z direction is stabilized, the wave propagating in the negative z direction, opposite to the z component of the lid velocity vector, is destabilized and becomes the critical mode. As α increases the phase velocity of the critical mode slows down and the mode become stationary at $\alpha = 10.1°$. For larger yaw angles the mode starts propagating again, but now in the direction of the spanwise lid motion.

For shallow cavities and elevated Reynolds numbers the basic flow at $\alpha = 0°$ arises as a spanwise vortex near the downstream end of the cavity. As described by Albensoeder *et al.* [5] for $\Gamma = 0.25$ this flow becomes unstable due to a centrifugal

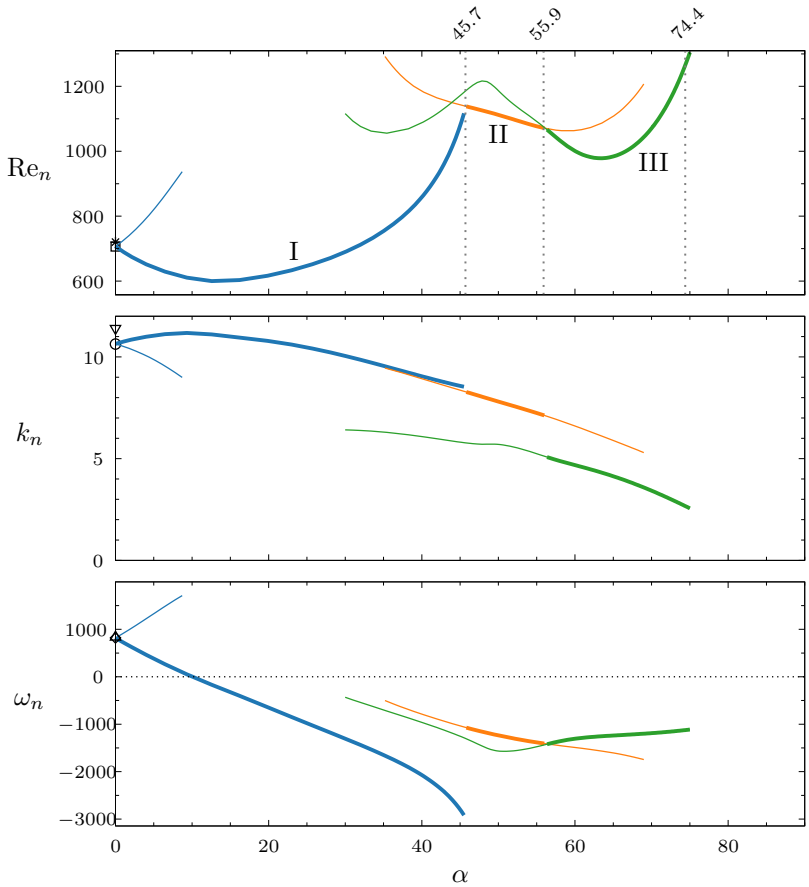

FIGURE 4.12 – Neutral Reynolds numbers (top) wave numbers (middle) and angular frequency (bottom) as functions of α for $\Gamma = 0.5$. Branches are distinguished by color and capital Roman letters. Bold lines indicate critical values. The numbers indicated at the top of the upper plot are the angle at which critical curves intersect. The square (□), the open circle (○), and the diamond (◊) indicate the critical Reynolds number, wave number, and oscillation frequency, respectively, obtained by Albensoeder *et al.* [5]. Corresponding data of Theofilis *et al.* [175] are shown as asterisk (∗) and down- (▽), and up-triangle (△), respectively.

instability in the region where the vortex flow separates from the bottom wall. As α increases the Couette part of the basic flow $\boldsymbol{u}_0^{\mathrm{C}}$ becomes stronger, but the main vortex structure provided by $\boldsymbol{u}_0^{\mathrm{2D}}$ remains dominant. This explains why the mechanics of the critical mode I for $\Gamma = 0.5$ and $\alpha = 15°$, shown in fig. 4.13, is similar as for $\alpha = 0°$. From fig. 4.13(b) the spanwise vortex also arises near the separation of the basic flow from the bottom, indicated by the streamlines of $\boldsymbol{u}_0^{\mathrm{2D}}$. This is also the region of maximum energy transfer i.

The critical mode I at $\alpha = 15°$ is primarily destabilised by the lift up process described by i_2, which arises near the separation line of $\boldsymbol{u}_0^{\mathrm{2D}}$ from the bottom. However, as α increases, the integral contribution I_2 is reduced and cannot explain the destabilisation by about $\Delta\mathrm{Re} \approx 100$ compared to $\alpha = 0°$. However, I_1 gains importance and overcompensates the reduction of I_2 (see table 4.2). The process described by i_1 is responsible for the weaker (with a local local maximum of i at 20% of $\max i$), but growing region of energy transfer near the moving lid, best noticed in figs. 4.13(b) and 4.14(c). Different from i_2, i_1 vanishes in parallel flow, because the energy-transfer process of i_1 requires the direction of the basic flow to change perpendicular to itself. Therefore, i_1 cannot build on gradients of the Couette part of the flow $\boldsymbol{u}_0^{\mathrm{C}}$. Moreover, as the swirling part of the basic flow $\boldsymbol{u}_0^{\mathrm{2D}}$ becomes weaker for increasing α, the destabilisation with α cannot be explained by $\boldsymbol{u}_0^{\mathrm{2D}}$ alone. Therefore, the change of the modal structure accompanied with the increase of α must be responsible for the ability of the critical mode to extract more energy via i_1 from $\boldsymbol{u}_0^{\mathrm{2D}}$, despite of $\boldsymbol{u}_0^{\mathrm{2D}}$ being weaker as compared to $\alpha = 0°$.

Mode I remains the critical mode over a wide range of $\alpha \in [0°, 45.7°]$ with a minimum critical Reynolds number of $\mathrm{Re}_c = 599.5$ at $\alpha = 13.6°$. At $\alpha = 40°$, I_1 and I_2 have become of comparable magnitude with a share of 42% and 54%, respectively, of the total energy budget. The critical mode for $\alpha = 40°$ is shown in fig. 4.14. Compared to $\alpha = 15°$ the flow field of the critical mode has changed. Now it arises mainly as vortices nearly perpendicular to the moving wall which are located near the downstream end of the cavity (fig. 4.14(a)), but slightly tilted (fig. 4.14(b)). This critical mode I is fed by gradients of the basic flow in the downstream half of the cavity, where both the important contributions of i_1 and i_2 are interwoven in a complicated fashion (fig. 4.14(c)).

Modes II and III

As the Couette part of the basic flow becomes dominant upon an increase of α, the critical mode changes to mode II at $\alpha = 45.7$. Mode II has a similar critical wave number as mode I. Mode II is illustrated in fig. 4.15 for $\alpha = 50°$. The structure of mode II is quite different from that of mode I and resembles the critical modes for $\Gamma = 1$ discussed in section 4.3.2. From table 4.2 the lift-up mechanism I_2 dominates the energy budget of the critical mode II, similar as for $\Gamma = 1$. From fig. 4.15(b) one can see different patches (blue) of localized energy production which are arranged around the periphery of the basic vortex $\boldsymbol{u}_0^{\mathrm{2D}}$. These local production region extend as threads in three-dimensions as shown in fig. 4.15(c). The threads of energy production feed energy to the helical-type of perturbation vortices which are visualized in fig. 4.15(d)

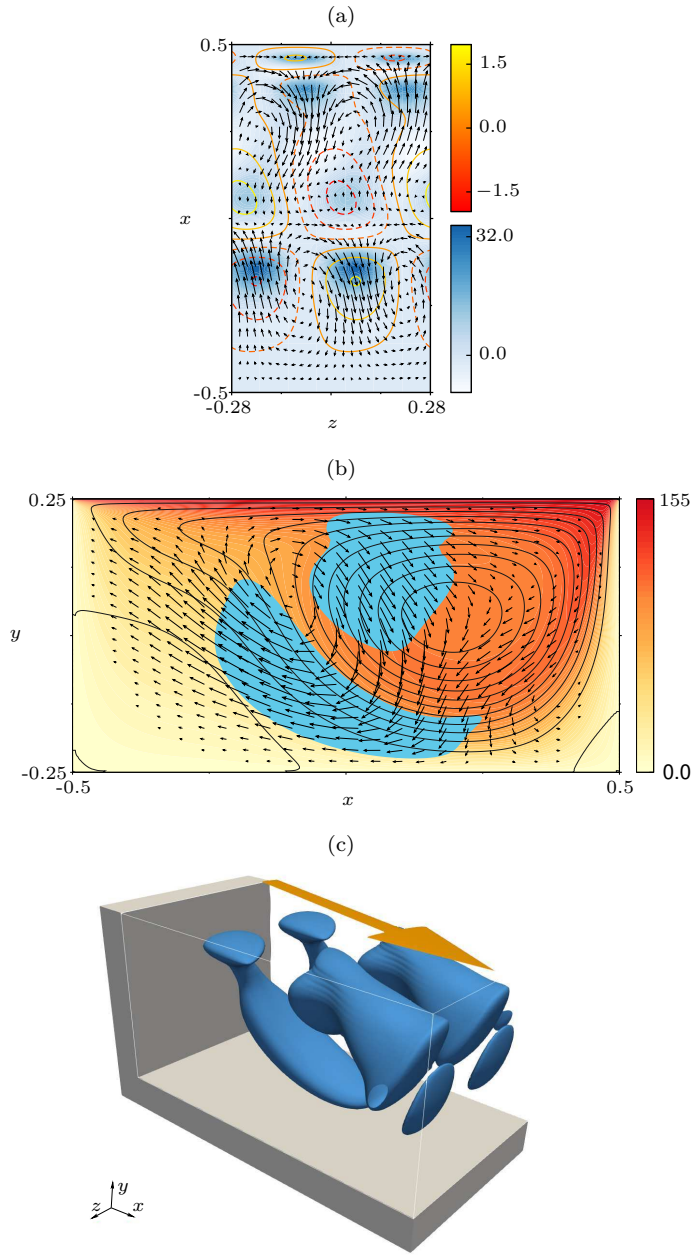

FIGURE 4.13 – Critical mode I (blue in fig. 4.12) for $\Gamma = 0.5$ and $\alpha = 15°$ with $\mathrm{Re}_c = 600.6$ and $k_c = 11.0$. All quantities as in fig. 4.4, except for (c) showing isosurfaces of i at $i = 0.2 \times i_{\max}$.

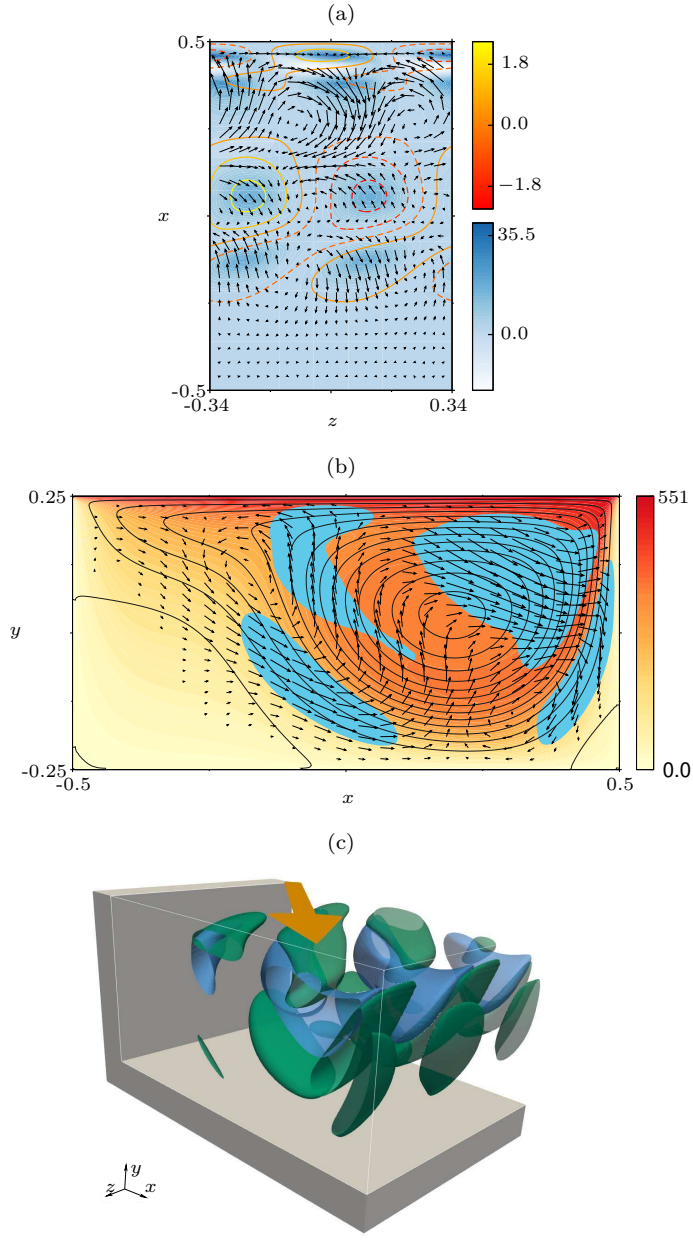

FIGURE 4.14 – Critical mode I (blue in fig. 4.12) for $\Gamma = 0.5$ and $\alpha = 40°$ with $\mathrm{Re}_c = 858.7$ and $k_c = 9.05$. All quantities as in fig. 4.4, except for (c) showing isosurfaces of i at $i = 0.2 \times i_{\max}$.

by isosurfaces of $\lambda_2 = -20$.One can identify 5 spiral vortices in the bulk of the flow which, similarly as mode $IV_{\Gamma=1}, V_{\Gamma=1}$, change their sense of rotation as they pass along the downstream to the lid top corner. From fig. 4.15(d) two weaker vortices counter-rotating vortices can be identified above the recirculation zone, but the total production rate associated with these latter vortices contributes only about 5% to the total energy budget.

As the inclination angle is further increased the energy production I_2 by the lift-up process becomes ever more important than for $\Gamma = 1$ (table 4.2). At $\alpha = 55.9°$ mode III becomes critical. For increasing α the critical curve reaches a local minimum at $\alpha = 63.4°$ beyond which the basic flow is strongly stabilized. As an example for mode III we consider $\alpha = 65°$. The mode is similar to mode II. However, the wavelength of mode III is about twice as long as the one for mode II, and the perturbation vortices are more aligned with the z direction. The critical mode is characterized by a pair of helical vortices which wind about the recirculating basic vortex. One of the two vortices is clearly visible in the cross section shown in fig. 4.16(c), offset with respect to the basic state vortex $\boldsymbol{u}_0^{2D}$ upstream of the moving lid vortex. In the plane shown the vortex is fed by three largest patches (blue) of energy production. The spiral character of the perturbation flow can best be recognized from fig. 4.16(a) which shows isosurfaces of i.The total production I of kinetic energy is mainly due to I_2 with I_1, I_3 and I_4 altogether contributing less than 16% to the total energy transfer. On a further increase of α the basic flow is rapidly stabilised and we did not follow the critical curve beyond $\alpha = 75°$. Up to this inclination angle, mode III remains critical and keeps the same characteristics as for $\alpha = 65°$. Again the vortices are weakening along the downstream lid corner as the angle increases and it becomes less and less evident that the vortices are feeding on themselves.

Comparison of Results for $\Gamma = 0.5$ and $\Gamma = 1$

It seems that the scenario at $\Gamma = 0.5$ is overall similar to what has been observed for square cavity $\Gamma = 1$. Mode $\mathrm{I}_{\Gamma=0.5}$ of the former would correspond to mode $\mathrm{III}_{\Gamma=1}$ of the latter case: The propagation direction for very low yaw angles is opposing the spanwise lid motion and progressively realigning with the lid motion as α increases. Eventually, the critical Reynolds number drops below $\mathrm{Re}_c(\alpha = 0°)$ before increasing to values $\mathrm{Re}_c(\alpha) > \mathrm{Re}_c(\alpha = 0°)$. Furthermore, mode $\mathrm{II}_{\Gamma=0.5}$ and $\mathrm{III}_{\Gamma=0.5}$ would correspond the $\mathrm{V}_{\Gamma=1}$,$\mathrm{VII}_{\Gamma=1}$ and higher modes. It is worth noting that in both $\Gamma = 1$ and $\Gamma = 0.5$ cases, the wave number between mode $III_{\Gamma=1}$ and $V_{\Gamma=1}$ are very close, and this can be found again in the case $\Gamma = 0.5$ where the wave number between $I_{\Gamma=0.5}$ and $II_{\Gamma=0.5}$ are also almost the same. In particular, they seem to have similar structure with helical vortices together with a substantially higher I_2 production rate. This interpretation is also corroborated by the fig. 6 and 16 of Albensoeder *et al.* [5], where the mode of Ding & Kawahara [45] (mode $\mathrm{III}_{\Gamma=1}$) and mode $\mathrm{II}_{\Gamma=0.5}$ seem to be the same.One can anticipate the scenario for $\Gamma = 2$ to be somewhat simpler since the critical Reynolds and wavenumbers for $\alpha = 0°$ remain more or less constant as Γ increases [5].

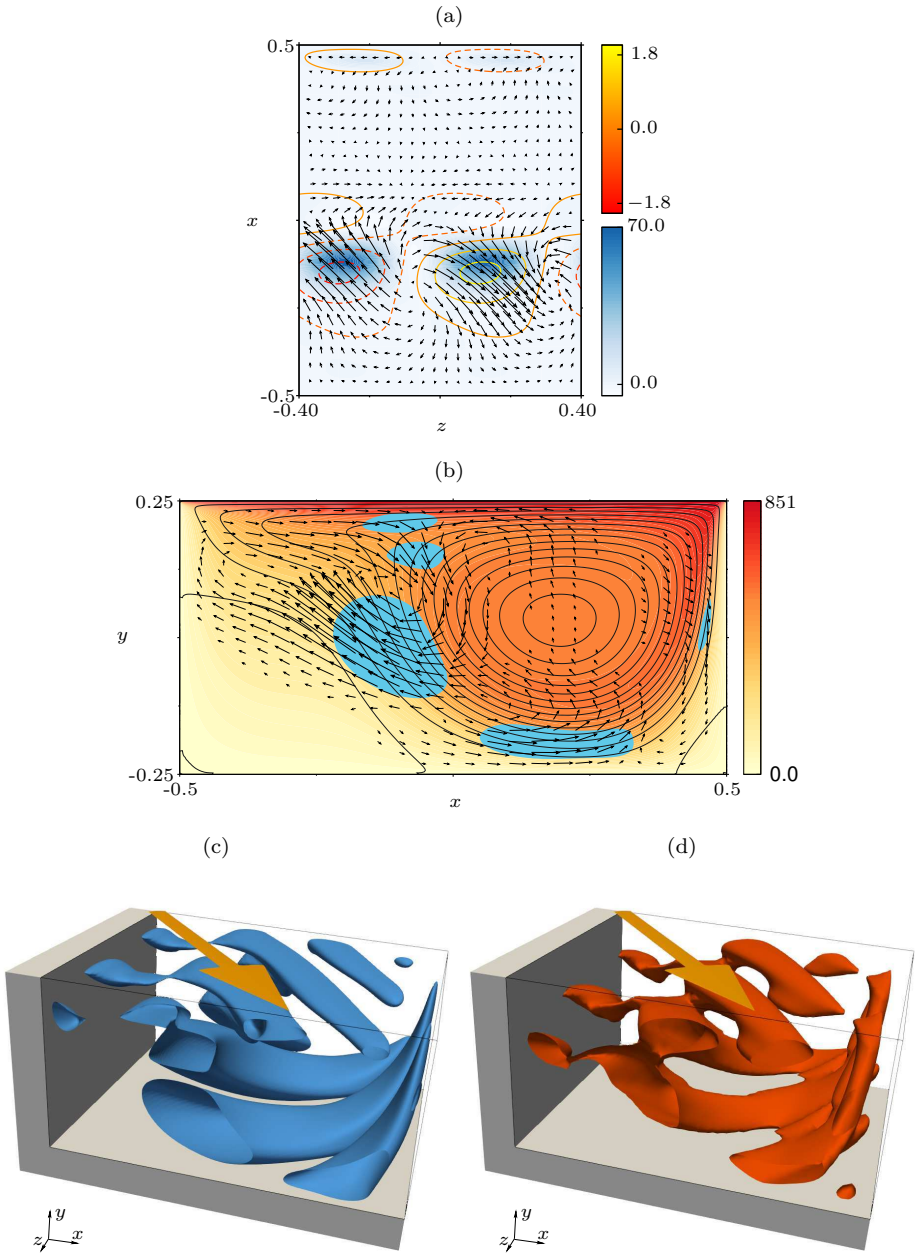

FIGURE 4.15 – Critical mode II (orange in fig. 4.12) for $\Gamma = 0.5$ and $\alpha = 50°$ with $\mathrm{Re}_c = 1112.1$ and $k_c = 7.81$. All quantities as in fig. 4.6, except for the contour of λ_2 which is set to the isovalue of $\lambda_2 = -20$.

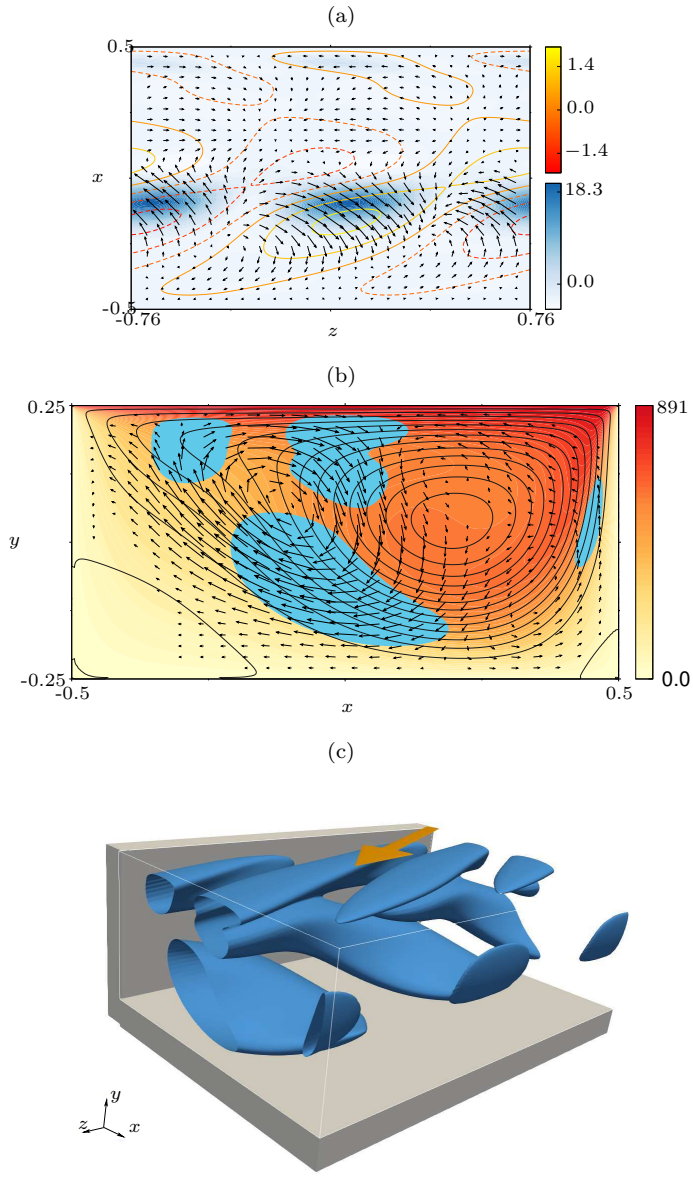

FIGURE 4.16 – Critical mode III (green in fig. 4.12) for $\Gamma = 0.5$ and $\alpha = 65°$ with $\mathrm{Re}_c = 984.0$ and $k_c = 4.13$. All quantities as in fig. 4.4.

4.3.4 Linear Stability for $\Gamma = 2$

An overview on the neutral Reynolds numbers for a deep cavity with $\Gamma = 2$ is shown in fig. 4.17. Again, the critical data for the stationary mode at $\alpha = 0$, $\mathrm{Re}_c(\alpha = 0) = 444.90$ and $k_c(\alpha = 0) = 1.72$, are in good agreement with Albensoeder *et al.* [5] who obtained $\mathrm{Re}_c = 446.3$ and $k_c = 1.71$ (symbols in fig. 4.17). Unlike for the two previous aspect ratios, only two different critical modes arise of which mode I is critical within the large range $\alpha \in [0, 78.9]$ of inclination angles.

As α is increased from zero, the stationary mode starts drifting in positive z direction. But the character of the critical mode does not change very much even at $\alpha = 50°$. The structure of the mode is shown in fig. 4.18. It is very similar to the stationary mode for $\alpha = 0°$ reported in figs. 20 and 21 of Albensoeder *et al.* [5]. The most important region of energy production (again I_2 is dominant) is located in the curved boundary layer of $\boldsymbol{u}_0^{\mathrm{2D}}$ just before the basic vortex flow separates from the downstream wall at $x = 1/2$ (fig. 4.18(b)). In the (x, y) plane the perturbation flow is a vortex slightly offset from the basic state vortex and towards the centre of the cavity. As the perturbation vortex periodically changes its sense of rotation such perturbation leads to a modulation of the total vortex flow as has been observed experimentally for $\Gamma = 1.6$ by Siegmann-Hegerfeld *et al.* [162]. Associated with the perturbation flow is a periodic up- and down-flow region at the midplane $y = 0$ shown in fig. 4.18(a) which arise just at the edge of the basic state vortex.

As the inclination angle is increased the wavelength of the critical mode increases. After the crossover to mode II at $\alpha = 78.9°$ the wavelength is reduced, but it again grows and reaches $\lambda = 9.2$ at $\alpha = 85°$. Accordingly, the structure of the perturbation flow becomes stretched in z direction. This is a consequence of the wall-bounded Couette part $\boldsymbol{u}_0^{\mathrm{C}}$ of the basic flow. Yet, the region near the separation line of the basic flow from the wall at $x = 1/2$ remains of crucial importance for the transfer of kinetic energy to the perturbation (fig. 4.19(b)), now being nearly exclusively due to I_2. As shown in fig. 4.19(a) the critical mode now has significant velocity components w in z direction.The ratios of the magnitude of the perturbation velocity components $\max(u)$ and $\max(v)$ compared to the magnitude of $\max(w)$ for $\alpha = 85°$ ($\alpha = 0°$) are $\max(u)/\max(w) = 0.1950$ (2.2195) and $\max(v)/\max(w) = 0.1456$ (1.8370).

Similar as for $\Gamma = 1$ and $\Gamma = 0.5$, the basic flow is strongly stabilized with respect to linear perturbations as $\alpha \to 90°$ (fig. 4.17). Finally, common to all aspect ratios is the increase with α of the critical wavelengths and an increasing length scale in of the perturbation-flow structures in the cross sections $z = \mathrm{const}$.

4.4 Discussion and Conclusion

The linear stability of the steady flow in a rectangular cavity driven by the oblique motion of a lid has been investigated with respect to spatially periodic perturbations. The parameter space for this problem is made of the Reynolds number Re, the inclination angle of the lid α, and the cross-sectional aspect ratio Γ. Three representative cavities have been investigated: a cavity with a square cross ($\Gamma = 1$), a shallow cavity

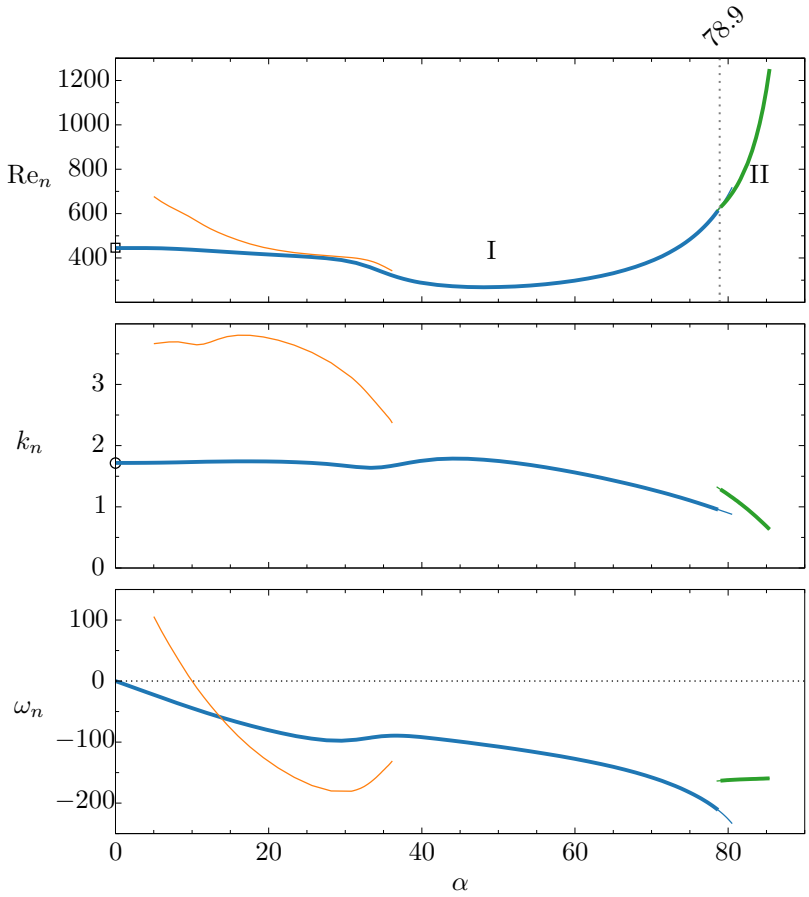

FIGURE 4.17 – Neutral Reynolds numbers (top), wave numbers (middle) and angular frequency (bottom) as functions of α for $\Gamma = 2$. Branches are distinguished by color and capital Roman letters. Bold lines indicate critical values. Different branches are distinguished by colour and capital Roman numbers. The number at the top of the upper panel denotes the angle at which the critical curves intersect (vertical dotted lines). The square (□) and the open circle (○) indicate the critical Reynolds and wave number, respectively, obtained by Albensoeder *et al.* [5].

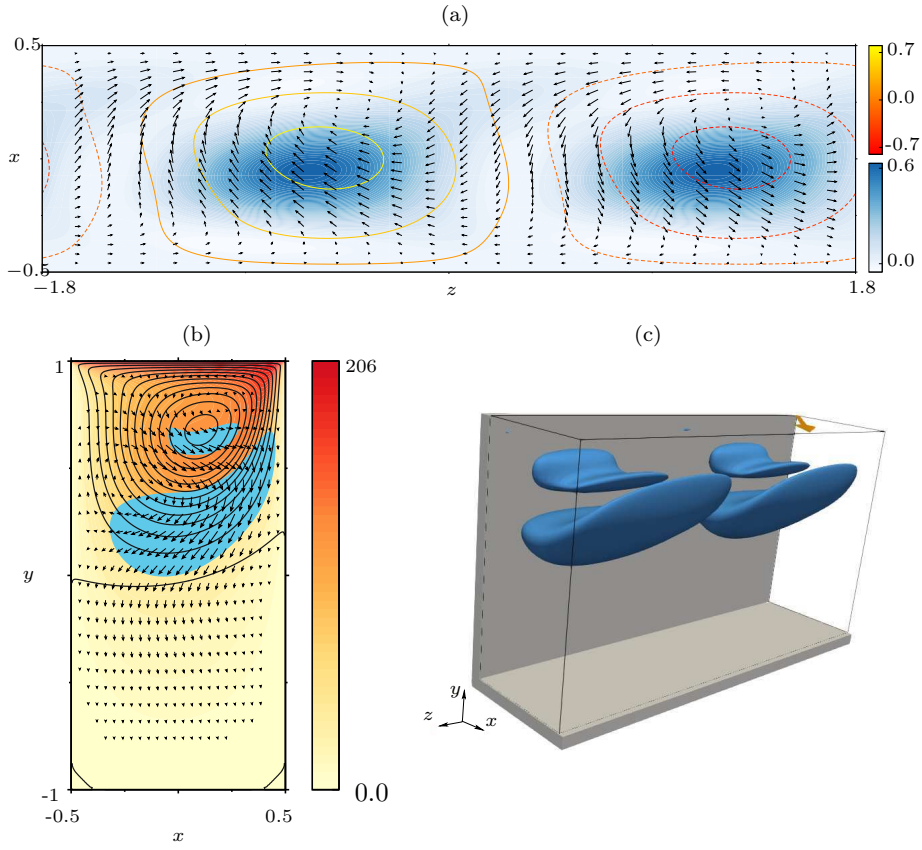

FIGURE 4.18 – Critical mode I (blue in fig. 4.17) for $\Gamma = 2$ and $\alpha = 50°$ with $\mathrm{Re}_c = 269.1$ and $k_c = 1.75$. All quantities as in fig. 4.4.

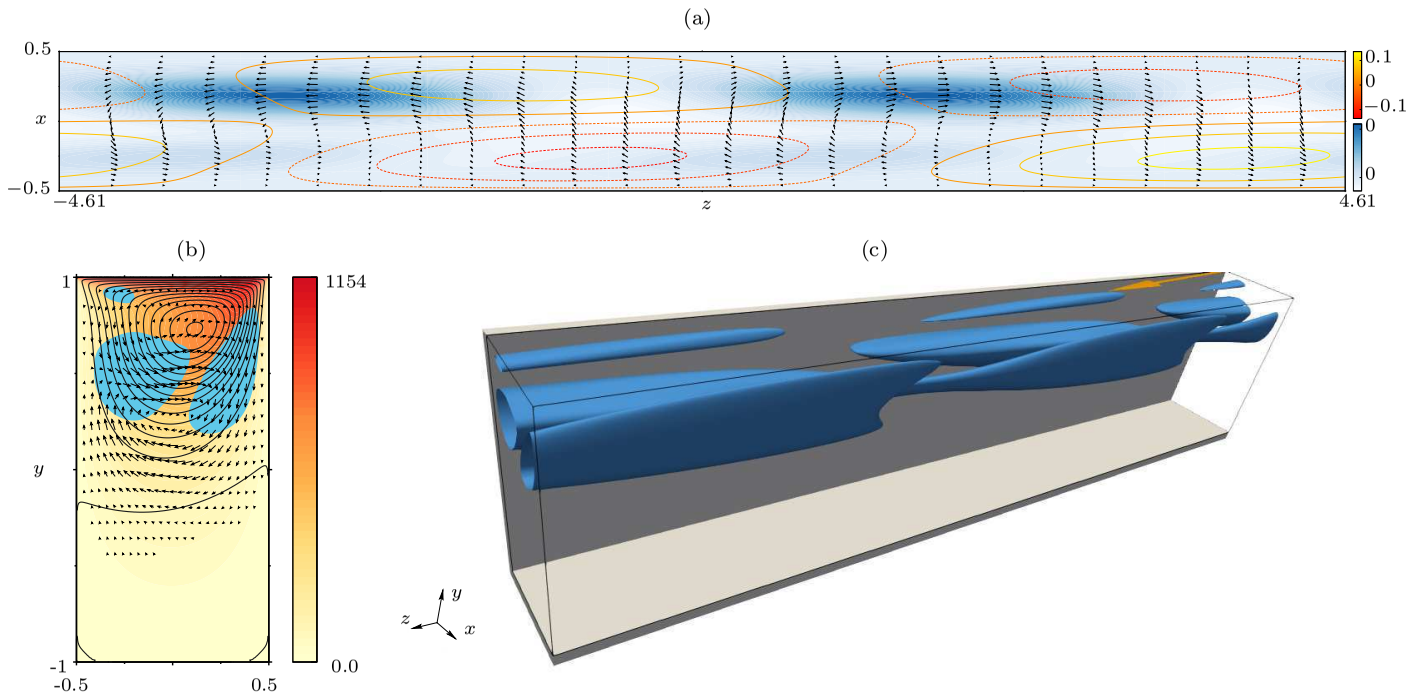

FIGURE 4.19 – $\Gamma = 2$, $\alpha = 85°$, $\mathrm{Re}_c = 1159.2$, $k_c = 0.68$ (c) Isocontour at 10% of the maximum of the perturbation energy production rate. (a),(b) see previous figures.

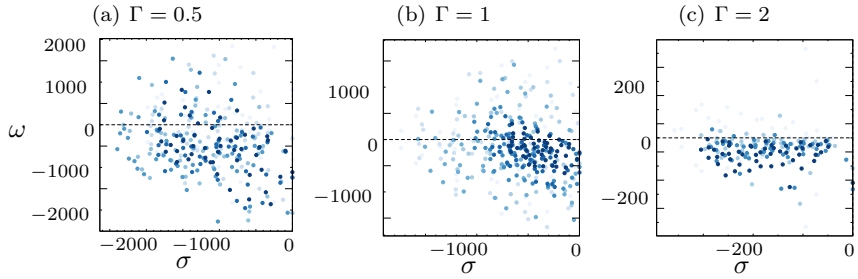

FIGURE 4.20 – Eigenspectra $\gamma = \sigma + \mathrm{i}\omega$ for all cases of table 4.2 distinguished by the aspect ratio Γ. The darker the symbols are, the larger is α.

($\Gamma = 0.5$), and a deep cavity ($\Gamma = 2$).

The basic flow in the obliquely-driven cavity is made of a superposition of two types of motion. One is the well-known two-dimensional cavity flow $\boldsymbol{u}_0^{\mathrm{2D}}(x, y)$, driven by the x component $\mathrm{Re}\cos(\alpha)$ of the normalized lid velocity which is reduced compared to the absolute normalized lid velocity Re. The other part of the flow field is made by the parallel Couette-type of flow $\boldsymbol{u}_0^{\mathrm{C}}(x, y)$ in spanwise direction. It is driven by the spanwise component $\mathrm{Re}\sin(\alpha)$ of the normalized lid velocity. While the recirculating part of the motion is independent of the spanwise motion, the Couette part $\boldsymbol{u}_0^{\mathrm{C}}(x, y) = w_0(x, y)\boldsymbol{e}_z$ of the basic flow is affected by $\boldsymbol{u}_0^{\mathrm{2D}}$ which advects the spanwise momentum w_0. The basic flow is thus made of a swirling flow with non-zero axial (spanwise) velocity and a swirl corresponding to the two-dimensional classical cavity flow.

Critical Reynolds numbers as function of the yaw angle α have been computed for all three aspect ratios. For $\alpha = 0°$ the accurate stability boundaries provided by Albensoeder *et al.* [5] are recovered. The slope $\partial \mathrm{Re}_c/\partial\alpha|_{\alpha=0} = 0$ of the critical curve at $\alpha = 0°$ vanishes for critical modes which are stationary ($\Gamma = 1, \Gamma = 2$), because the isolated real eigenvalue must evolve continuously and symmetrically with respect to α. Therefore, the critical Reynolds number increases from zero and the critical modes start drifting in the direction of the spanwise lid motion (positive z direction). On the other hand, the degeneracy of the critical Reynolds number for oscillatory eigenmodes at $\alpha = 0$ is removed and $\partial \mathrm{Re}_c/\partial\alpha|_{\alpha=0} = \pm a \neq 0$, where $a = \text{const.}$, such that the critical Reynolds number is always reduced and the critical mode for $\alpha > 0$ evolves from one of the degenerate modes at $\alpha = 0°$. For both of such latter cases we find the critical mode which destabilizes the basic state for small α to propagates in the spanwise direction opposite ($\omega > 0$) to the spanwise component of the lid motion. As α increases the critical mode becomes stationary near $\alpha \approx 10°$ and turns propagating parallel to the z component of the lid motion for larger α. In this respect, fig. 4.20 shows the spectra made of all eigenvalues computed for the cases listed in table 4.2. We find more modes propagate in the z direction ($\omega < 0$) the larger α (indicated by the darkness of the symbols). While this is perhaps not so surprising, also the deeper the cavity is, i.e. the larger Γ, the more modes propagate parallel to the z component of the lid motion.

When α is small the basic flow is dominated by the recirculating part part of the

flow $\boldsymbol{u}_0^{2D}$. In this situation all critical modes arise in the curved boundary layer of $\boldsymbol{u}_0^{2D}$ and receive their kinetic energy mainly due to the lift-up process described by $i_2 = -\boldsymbol{u}\cdot(\boldsymbol{u}\cdot\nabla\boldsymbol{u}_0)$. The similarity of the modal structures and the the basic instability mechanism with the ones of the classical lid-driven cavity at $\alpha = 0°$ [78, 5] suggests to call the modes for $\alpha \neq 0°$ *spiral Taylor–Görtler vortices*. Spiral Taylor–Görtler vortices also arise in spherical Couette flow when the inner sphere rotates [152, 115]. Between rotating spheres the Taylor–Görtler vortices near the equator become spiral-shaped due to the meridional flow generated by the Ekman pumping from the polar regions. The spiral Taylor–Görtler vortices may also be related to the helical vortices which arise in a nominally axisymmetric swirling jet [107, 6, 118], although notable differences are the non-constant swirl of the flow and the fact that the vortices switch the sense of rotation along the downstream lid-corner. Consistent with our results, Gallaire & Chomaz [59] discovered that the number of helical vortices in a swirling jet decays as the wave number decreases and Mathur *et al.* [105] found an centrifugal instability in a non-axisymmetric Stuart vortex with a axial throughflow, using the local instability framework (WKBJ) [96]. They established an heuristic criterion which could further confirm the centrifugal nature of the instability in our setup.

For large inclination angles $\alpha \to 90°$ the recirculating part of the basic flow diminishes and the basic flow tends to a confined Couette flow (4.10). As the basic flow becomes more parallel the most dangerous modes become elongated in spanwise direction. In the limit, the energy production terms i_n for $n = 1$, 3 and 4 vanish and only the lift-up term i_2 remains. This trend is also reflected by the integral contributions listed in table 4.2. As long as an even weak recirculating part of the basic flow can provide a feed back from streaks to the nearly streamwise vortices which create the streaks, a linear instability is possible. With the recirculating basic flow getting weaker the feedback becomes weaker and the stability boundary $\mathrm{Re}_c(\alpha)$ increases strongly as $\alpha \to 90°$. This interpretation is consistent with the previous investigation of Theofilis *et al.* [175]. There does not seem to be any linear process which could destabilize the wall bounded Couette flow at $\alpha = 90°$.

For the present system, infinitely extended in the spanwise (z) direction, the pressure gradient of the basic flow $\partial p_0/\partial z = 0$ has been assumed to vanish. A natural extension of the present work could be concerned with the effect of an imposed spanwise pressure gradient. Of particular interest would be the effect on the flow stability of the pressure gradient which leads to a zero mean flow $\int_S w_0(x,y)\mathrm{d}S = 0$, where S is the cross section of the cavity in the (x,y) plane. Such basic flow could model the effect of distant end walls on the bulk-flow instability in the central region of the cavity.

5

Sensitivity Analysis of a Shallow Thermocapillary-Driven Cavity

5.1 Introduction

From striders walking on water to soap solving mazes [173], surface tension effects have always intrigued. At the interface between a liquid and a gas, the cohesion forces of the molecules of the liquid are stronger than the adhesion forces to the other fluid. This force imbalance at the interface leads to a net force directed towards the interior of the liquid, and is responsible for the shape of the interface, defined by the minimum of the interface energy. Surface tension, expressed as the surface energy by unit area, can vary depending on many factors for instance the presence of surfactants or temperature. These variations of surface tension cause an imbalance of forces at the interface, eventually putting the fluids in motion. These type of flow, driven by surface tension variations, are named after Marangoni who conducted experiments in the Tuileries bassin in Paris [102]. Detailed descriptions of surface tension effects can be found e.g. in [92], and historical perspectives in [106, 129].

Typically, surface tension decreases with an increase of the temperature. When the interface is locally heated, the variations of surface tension induce a force along the surface directed toward the region of lower temperature, driving the flow. We say that the flow is thermocapillary driven. This class of flows is important for natural as well as for industrial applications. In particular in crystal growth applications, instabilities due to the thermocapillary effect have been found responsible for the formation of undesired striations, resulting in a non-uniform crystal [67]. If this had the disadvantage of reducing the purity of the crystal, it also motivated investigations on the fundamental instability mechanisms in thermocapillary-driven flows [84].

Among the many techniques for melt growth of crystals, the *floating zone* and *open-boat zone* techniques have been developed [150]. In the floating zone method, the melt forms a liquid bridge between a top rod formed of the crystal and a bottom rod made out of the feed-substance. The melt is kept in a liquid state by a heater nearby (see fig. 5.1), the temperature difference at the surface triggers the thermocapillary effect, while

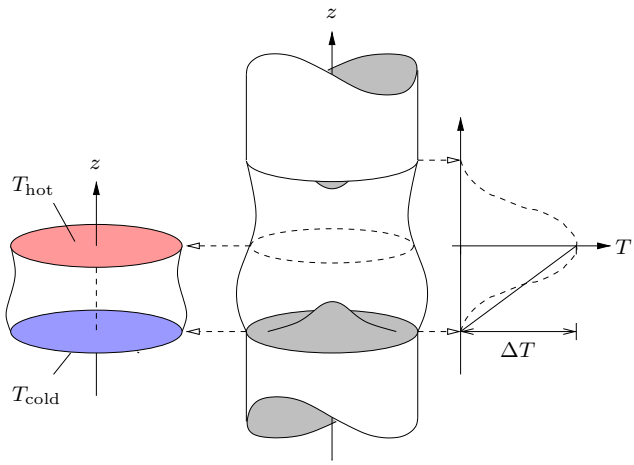

FIGURE 5.1 – Illustration of the simplification of the floating zone to the half zone configuration, taken from Leypoldt [93].

in the bulk buoyancy effects can also arise depending on the size of the system. In fact, both effects arise if the surface tension and the density of the fluid are not constant along the surface and in the volume, respectively. The strength of thermocapillary effects is scaling with the typical length of the domain L, while buoyancy effect with L^3. Surface effects are then of importance, when the domain size is small.

This setup is relatively complex: one has moving solid-liquid boundaries (Stefan Problem), curved interfaces for both solid–liquid and liquid–gas interfaces, different rods diameters, strong variations in the temperature profile, evaporation, among many aspects. Therefore, it has been idealized as illustrated in fig. 5.1: the top rod is kept at a higher temperature than the bottom rod. The liquid bridge formed by the melt has an approximately cylindrical shape, maintained by the mean surface tension. This setup is shown in fig. 5.2(a), and will be referred to later as the *half zone* or *liquid bridge* (LB).

In the *open-boat* method, the melt lays between the crystal and the feed material. It can be idealized as a melt flow in a cavity with a free surface at its top, and heated at different temperatures at its lateral walls. To further simplify the system, the bottom wall and the top surface are supposed to be flat and adiabatic. This setup is shown in fig. 5.2(b), and will be later referred to as the *thermocapillary-driven cavity*. Both these setups received a lot of attention as they are relatively complex from a dynamical system point of view.

In their pioneering work, Smith & Davis [167] investigated the linear stability of an infinite layer, driven by a surface tension gradient stemming from an imposed temperature gradient. They studied a flow with a linear profile, that might be relevant for thin films, and a return flow in which the direction of the velocity changes once along the depth of the layer. This latter flow mimics a infinitely long cavity in the streamwise direction, excluding the lateral end walls, and therefore the depth averaged velocity is zero. In that case, they found the flow to be unstable for all Prandtl numbers to three-

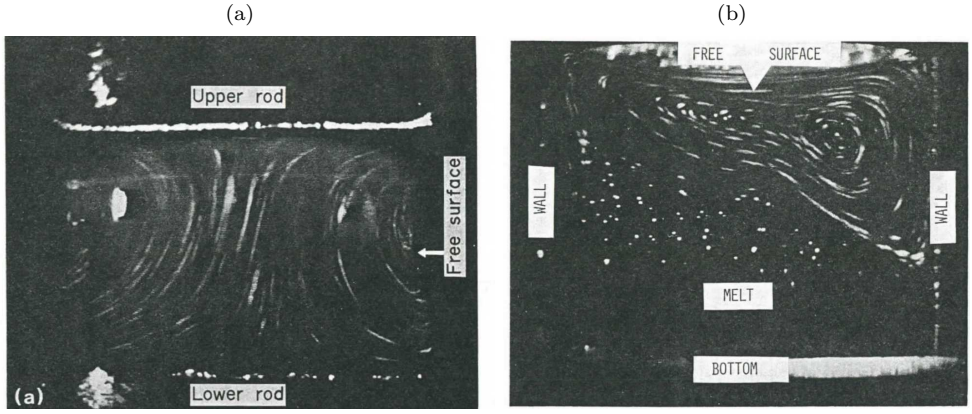

FIGURE 5.2 – (a) Idealized half-zone configuration using $NaNO_3$, upper and lower rod temperature are $360°C$, $350°C$, respectively. Diameter and height are of 6 and 4 mm. The flow is going down close to the free surface, and up in the core. (b) Open-boat configuration in a cavity of length, height and width of 20, 12, 20 mm, temperature at the left and right walls are $380°C$ and $330°C$. At the free surface the flow is going from left to right. Both images are taken from Schwabe [150].

dimensional perturbations propagating obliquely with respect to the direction of the basic flow. These three-dimensional perturbations are called *hydrothermal waves*. This was confirmed experimentally by Daviaud & Vince [41] who used a fluid of $\mathrm{Pr} = 10$, and further reproduced by [143, 144, 32]. Daviaud & Vince [41] investigated a cavity of width and length 10 mm $\times$ 200 mm and varied the height of the liquid. They found the presence of hydrothermal waves when the height of the fluid was less than 2.8 mm, whearas for $h > 2.8$ mm, steady rolls were found to exist.

Numerically, Zebib *et al.* [186] inspected the flow structure and the leading order of the surface deformation in a square cavity driven solely by thermocapillary forces. Carpenter & Homsy [33] simulated two-dimensional thermocapillary flows in a square cavity, and came to the conclusion that thermocapillary effects are dominating the system, provided that the Marangoni number is high enough. The same authors [34] noted that there was some similarity in the steady flow structure between the lid-driven cavity of square cross section and its thermocapillary counterpart and confirmed numerically that the flow remains linearly stable to two-dimensional perturbations up to at least $\mathrm{Re} = 1300$ for a fluid of $\mathrm{Pr} = 10$. Xu & Zebib [182] performed two- and three-dimensional temporal simulations in order to quantify the onset of instability in the thermocapillary-driven cavity as a function of the length-to-depth ratio of the cavity, the Prandtl number and the Reynolds number. Their results confirmed those of Carpenter & Homsy [34] since no two-dimensional instability can be found below a width-to-height aspect ratio of approximately 2.1. Additionally, the critical Reynolds number seems to shrink with the decrease in Prandtl number. Besides, they reported three-dimensional instabilities in a cavity of spanwise finite length $1 \times 3 \times 20$, at Reynolds numbers lower than the two-dimensional ones at $\mathrm{Pr} = 4.4$. At higher Prandtl number $\mathrm{Pr} = 13.9$, they observed a very large damping effect of the end walls on the instability, and the critical Reynolds number increases. Finally, Kuhlmann &

Albensoeder [83] studied the linear stability of the system investigated by Daviaud & Vince [41] and could explain the different mechanisms causing the instability of the flow.

In the mean time, similar studies were conducted in the liquid bridge setup. Neitzel *et al.* [116] and Wanschura *et al.* [181] investigated the linear stability of the liquid bridge, agreeing with experimental findings of e.g. [179]. Wanschura *et al.* [181] computed numerically the critical curve of the Reynolds number as a function of the Prandtl number for a fixed height-to-radius aspect ratio $\Gamma = 1$. They found two different branches depending on the Prandtl number. In the case of low Prandtl numbers $\mathrm{Pr} < 1$, they found a shear instability mainly driven by inertia, corroborating the results of Levenstam [90]. At higher Prandtl numbers $\mathrm{Pr} > 1$, the system becomes unstable to a hydrothermal wave that propagates azimuthally and the critical Reynolds number decreases upon increasing the Prandtl number. Nienhüser & Kuhlmann [117] extended this analysis to non cylindrical flow, and found a similar distinction of the instability mechanism.

It appears that the onset of stability of three-dimensional flow in a liquid bridge depends on the heat transfer at the surface: In fact, for very high Prandtl numbers $\mathrm{Pr} = 49$, [73, 180] showed that depending on the surrounding air temperature (net heat loss and net heat gain, respectively), the critical Reynolds number could decrease by a factor of two, although the heat transfer coefficient was relatively small. Similarly, Mialdun & Shevtsova [110] stressed the dramatic changes of the experimental results they obtained for a $\mathrm{Pr} = 68$ with and without a thermal shield, separating the experimental setup from the external environment. Later, Yasnou *et al.* [184] studied the effect of a co-axial flow of a gas on the stability of the liquid bridge, and observed variations of the flow oscillations depending on the gas temperature.

The motivation for these fundamental research efforts was the appearance of striations gathering impurities in crystal growth, generated by the time-dependent flow. Yet, the time-dependent flow seems to be very sensitive to the heat transfer at the surface and, therefore, it is legitimate to try to control the onset of time dependence to at least attenuate the fluctuations if not remove them completely, with the help of additional heat transfer along the surface.

Guided by this idea, Petrov *et al.* [125, 124] suppressed the oscillations in a liquid bridge *via* a non-linear control algorithm using heat measurements close to the free surface as observable of the system and thermoelectric elements as controllers. They relied on a look-up table constructed beforehand and were able to suppress the instability only for Reynolds numbers 8.5% higher than the critical one. Shiomi *et al.* [160] investigated the placement of heaters and sensors around the liquid bridge in order to better suppress the oscillations. Using a linear control law, they could increase the stability limit by 42% and remove the oscillations. Beyond and until 90% of the uncontrolled stability limit they could damp the oscillation down to 30% of their original amplitude. Similarly, they also studied circular configurations, see [159, 158].

Concomitantly, Benz *et al.* [20] used a laser sheet aligned with the oblique front of the hydrothermal wave in a shallow layer to suppress the instabilities using either active or passive control. In a slightly more complicated framework, Sampath & Zabaras [145]

used an adjoint-based method to optimize the heat flux through the heating wall of an open-boat configuration in order to achieve a certain melt solidification front speed and a desired temperature gradient between the walls using a two-dimensional model taking into account surface tension, buoyancy, Lorentz forces and solidification. Later, Muldoon [112], Muldoon & Kuhlmann [114] also used an adjoint-based method but to suppress the two-dimensional instabilities in a shallow thermocapillary-driven cavity by designing a time and space dependent flux all over the surface. This work was extended to limit the zone on which the control heat flux was applied to a region close to the hot corner [113].

The aim of this study is to provide an explanation on the sensitivity of the system with respect to the heat transfer to the external environment for different Prandtl numbers. Because of the straightforward implementation in Cartesian coordinates, we will focus on the thermocapillary-driven cavity. In a first step, we use advanced tools from linear stability analysis, where the focus is placed on the sensitivity of the leading eigenvalue to changes of the surface heat flux. In a second step, we aim at controlling the global stability of the system by designing an optimal steady heat flux using non-linear programming techniques, combined with the sensitivity analysis developed in the first part.

5.2 Setup and Mathematical Formulations

5.2.1 Formulation of the Problem

The open-boat or thermocapillary-driven cavity setup is shown in fig. 5.3. A fluid with a kinematic viscosity ν, density ρ and thermal diffusivity κ is contained in an open cavity of height H and width W and infinitely extended in the third direction. The fluid is heated and cooled at the lateral walls, and we assume that the walls are at the temperatures T_h and T_c. We note ΔT the temperature difference $\Delta T = T_h - T_c$ and T_0 the mean temperature $T_0 = (T_h + T_c)/2$. The bottom wall is considered to be adiabatic, while a given steady heat flux is imposed on the free surface. The surface tension Σ at the free surface is assumed to depend linearly on temperature

$$\Sigma(T) = \Sigma_0 - \Sigma_1 (T - T_0) + \mathcal{O}\left((T - T_0)^2\right),$$

where Σ_0 is the surface tension at $T = T_0$, and $\Sigma_1 = -\partial\Sigma/\partial T$ is the rate of change of the surface tension with respect to temperature deviating from $T = T_0$. Since typically, $\partial\Sigma/\partial T < 0$, so Σ_1 is positive. It is further assumed that the mean surface tension Σ_0 is asymptotically very large and that $\Sigma_1 \Delta T/\Sigma_0 \to 0$ and therefore the free surface can be approximated as being flat and non deformable. For instance, Kuhlmann & Nienhüser [86] showed for silicon oil liquid bridges that the variations of the surface where less than 0.1% of the liquid bridge radius[see also 157]. We take H, H^2/ν, ν/H, $\rho\nu^2/H^2$ and ΔT as respective scales for length, time, velocity, pressure and temperature. The

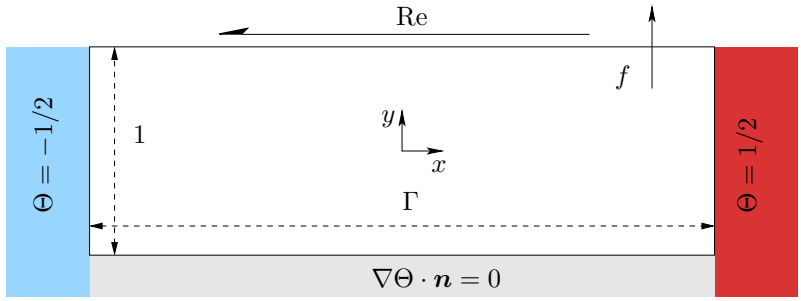

FIGURE 5.3 – Sketch of the thermocapillary-driven cavity setup.

domain $V = [-\Gamma/2, \Gamma/2] \times [-1/2, 1/2]$ and the governing equations can be written as

$$\left(\frac{\partial}{\partial t} + \boldsymbol{U} \cdot \nabla\right) \boldsymbol{U} = -\nabla P + \Delta \boldsymbol{U} \tag{5.1}$$
$$\left(\frac{\partial}{\partial t} + \boldsymbol{U} \cdot \nabla\right) \Theta = \frac{1}{\mathrm{Pr}} \Delta \Theta$$
$$\nabla \cdot \boldsymbol{U} = 0$$

subject to the boundary conditions for $\boldsymbol{U}$

$$\begin{aligned} \boldsymbol{U} &= 0, && \text{at all walls } x = \pm\Gamma/2 \text{ and } y = -1/2, \\ V &= 0, && \text{at the free surface } y = 1/2, \\ \frac{\partial U}{\partial y} + \mathrm{Re}\, \partial\Theta/\partial x &= 0, \end{aligned}$$

and for Θ

$$\begin{aligned} \Theta &= \frac{x}{\Gamma}, && \text{at the lateral walls } x = \pm\Gamma/2, \\ \frac{\partial \Theta}{\partial y} &= f, && \text{at the free surface } y = 1/2, \\ \frac{\partial \Theta}{\partial y} &= 0, && \text{at the bottom wall } y = -1/2, \end{aligned}$$

where we used of the following dimensionless numbers:

$$\Gamma = \frac{W}{H}, \quad \mathrm{Pr} = \frac{\nu}{\kappa}, \quad \mathrm{Re} = \frac{\Sigma_1 \Delta T H}{\rho \nu^2}.$$

5.2.2 Basic Flow and Eigenvalue Problem

Following the same steps as in Chapter 1, we decompose the velocity, pressure and temperature into basic flow and perturbation normal modes

$$\begin{pmatrix} \boldsymbol{u}' \\ \theta' \\ p' \end{pmatrix}(x,y,z,t) = \sum_i \begin{pmatrix} \hat{\boldsymbol{u}}_i \\ \hat{\theta}_i \\ \hat{p}_i \end{pmatrix}(x,y)\mathrm{e}^{\gamma_i t + kz} + \text{c.c.}$$

The basic flow is a solution of a non-linear problem which is essentially the steady two-dimensional version of (5.1). The perturbation modes are solution of the *direct* eigenvalue problem given by

$$\begin{aligned}
\gamma_i\hat{u}_i + u_0\frac{\partial\hat{u}_i}{\partial x} + v_0\frac{\partial\hat{u}_i}{\partial y} \quad &+\hat{u}_i\frac{\partial u_0}{\partial x} + \hat{v}_i\frac{\partial u_0}{\partial y} = -\frac{\partial}{\partial x}\hat{p}_i \quad + \left(\frac{\partial^2}{\partial x^2} + \frac{\partial^2}{\partial y^2} - k^2\right)\hat{u}_i \\
\gamma_i\hat{v}_i + u_0\frac{\partial\hat{v}_i}{\partial x} + v_0\frac{\partial\hat{v}_i}{\partial y} \quad &+\hat{u}_i\frac{\partial v_0}{\partial x} + \hat{v}_i\frac{\partial v_0}{\partial y} = -\frac{\partial}{\partial x}\hat{p}_i \quad + \left(\frac{\partial^2}{\partial x^2} + \frac{\partial^2}{\partial y^2} - k^2\right)\hat{v}_i \\
\gamma_i\hat{w}_i + u_0\frac{\partial\hat{w}_i}{\partial x} + v_0\frac{\partial\hat{w}_i}{\partial y} \quad & = -\mathrm{i}k\hat{p}_i \quad + \left(\frac{\partial^2}{\partial x^2} + \frac{\partial^2}{\partial y^2} - k^2\right)\hat{w}_i \\
\gamma_i\hat{\theta}_i + u_0\frac{\partial\hat{\theta}_i}{\partial x} + v_0\frac{\partial\hat{\theta}_i}{\partial y} \quad &+\hat{u}_i\frac{\partial\theta_0}{\partial x} + \hat{v}_i\frac{\partial\theta_0}{\partial y} = \quad \frac{1}{\mathrm{Pr}}\left(\frac{\partial^2}{\partial x^2} + \frac{\partial^2}{\partial y^2} - k^2\right)\hat{\theta}_i \\
&\frac{\partial\hat{u}_i}{\partial x} + \frac{\partial\hat{v}_i}{\partial y} + \mathrm{i}k\hat{w}_i = 0
\end{aligned} \tag{5.2}$$

subject to the boundary conditions for $\hat{\boldsymbol{u}}_i$

$$\begin{aligned}
\hat{\boldsymbol{u}}_i &= 0 && \text{at all walls } x = \pm\Gamma/2 \text{ and } y = -1/2 \\
\hat{v}_i &= 0 && \text{at the free surface } y = 1/2 \\
\frac{\partial}{\partial y}(\hat{u}_i, \hat{w}_i)^{\mathrm{T}} + \mathrm{Re}\left(\frac{\partial}{\partial x}, \mathrm{i}k\right)^{\mathrm{T}}\hat{\theta}_i &= 0
\end{aligned}$$

and for $\hat{\theta}_i$

$$\begin{aligned}
\hat{\theta}_i &= 0 && \text{at the lateral walls } x = \pm\Gamma/2 \\
\partial\hat{\theta}_i/\partial y &= 0 && \text{at the top and bottom } y = 1/2, y = -1/2
\end{aligned}$$

From the structure of these equations, it is evident that the production of perturbation kinetic energy due to the spanwise velocity component can only be caused by thermocapillary effect, and not from inertia. These inertial production terms do not appear in the perturbation equations and left blank in (5.2).

The eigenvalue γ_i can then be seen as a function $\gamma_i(\mathrm{Re}, \mathrm{Pr}, \Gamma, k, f)$. The next section is concerned with the evaluation of the sensitivity of the eigenvalue with respect to changes of the flux function f.

Additional Terms in the Energy Budget

The kinetic energy budget (2.21) (on page 16) has to be completed by additional terms originating from the thermocapillary stresses. We obtain

$$\begin{aligned}\frac{1}{D^*}\frac{\partial}{\partial t}\mathcal{E} &= -1 + \sum_{n=1}^{4}\int_V i_n \,\mathrm{d}V + \sum_{n=1}^{2}\int_V m_n \,\mathrm{d}S \\ &= -1 + \sum_{n=1}^{4} I_n + \sum_{n=1}^{2} M_n, \end{aligned} \tag{5.3}$$

where m_n can be defined equivalently using the velocity shear or the surface temperature gradient

$$m_1 = -\frac{1}{D^*}u'\frac{\partial u'}{\partial y} = \frac{\mathrm{Re}}{D^*}u'\frac{\partial \theta'}{\partial x}, \tag{5.4}$$

$$m_2 = -\frac{1}{D^*}w'\frac{\partial w'}{\partial y} = \frac{\mathrm{Re}}{D^*}w'\frac{\partial \theta'}{\partial z}. \tag{5.5}$$

and M_n are the integral contributions. Besides, a perturbation thermal energy (in a mathematical sense, nothing to do with the thermodynamics) is defined as $\mathcal{E}_{th} = \theta'^2/2$. Similarly as for the Orr-Reynolds equations (2.17), one express the rescaled rate of change of the thermal energy perturbation flow

$$\frac{1}{D^*_{th}}\frac{\partial}{\partial t}\mathcal{E}_{th} = -1 + \sum_{n=1}^{2}\int_V j_n \,\mathrm{d}V = -1 + \sum_{n=1}^{2} J_n, \tag{5.6}$$

where

$$\begin{aligned} D^*_{th} &= \int_V \nabla\theta' \cdot \nabla\theta' \,\mathrm{d}V \,, \\ j_1 &= -\frac{1}{D^*_{th}}\theta' \boldsymbol{u}'_{\perp} \cdot \nabla\theta_0 \,, \\ j_2 &= -\frac{1}{D^*_{th}}\theta' \boldsymbol{u}'_{\parallel} \cdot \nabla\theta_0 \,. \end{aligned}$$

The local production rate of thermal perturbation energy j_1 corresponds to the temperature perturbation created by the transport of the basic flow temperature by the part of the velocity perturbation that is orthogonal to the basic flow velocity. The second term j_2 corresponds to the temperature perturbation created by the transport of the basic flow temperature by the velocity perturbation parallel to the basic flow velocity.

The velocity perturbation can create a temperature perturbation where only the basic flow temperature is varying. The temperature perturbation has no impact on the velocity perturbation in the bulk of the flow (unlike buoyancy driven flows) but only at the free surface.

5.3 Sensitivity of the Eigenvalues to Variations of the Heat Flux

To obtain the variation of the eigenvalue generated by small changes in the steady heat transfer in the basic flow free surface, we used the framework developed independently by Marquet *et al.* [104] and Hill [66]. Reviews are provided in [164, 165, 37]. Of interest are also the work of Meliga *et al.* [109] for variation in the wall temperature for a compressible flows past a bluff body and Tchoufag *et al.* [172] for the sensitivity to shear stress and normal velocity at a the interface of a bubble.

Briefly, one can consider the eigenvalue γ_i as a function of the heat flux f. The eigenvalue for a small variation of the heat flux at the free surface δf can then be formulated as a Taylor series

$$\gamma_i(f+\delta f) = \gamma_i(f) + \langle \nabla_f \gamma_i, \delta f \rangle_S + \mathcal{O}\left(\| \delta f \|^2 \right),$$

where we used the scalar product

$$\langle a, b \rangle_S = \int_S a^* \, b \, \mathrm{d}S.$$

The sensitivity of the growth rate and of the frequency of the mode can be expressed as

$$\begin{aligned} \nabla_f \sigma_i &= \Re\left(\nabla_f \gamma_i \right), \\ \nabla_f \omega_i &= -\Im\left(\nabla_f \gamma_i \right), \end{aligned}$$

where the minus sign in the sensitivity of the frequency comes from the conjugate in the scalar product. The scalar field $\nabla_f \gamma_i$ is defined for all points at the free surface. Its point-wise value indicates the local contribution of a flux variation in the change of the eigenvalue.

Similarly, one can consider the sensitivity to variations in the basic flow $\nabla_{\boldsymbol{q}_0} \gamma_i$ or sensitivity to small external forces $\nabla_{\boldsymbol{F}} \gamma_i$. Both of them are defined on the volume, and their value at a specific point indicates the local contribution of a basic flow variation or external force variation at that point to the changes of the eigenvalue. For second order sensitivities, we refer to the work of Boujo *et al.* [25].

In this chapter, only the methodology and the workflow to follow will be presented. Only the equations in case of an infinitely extended cavity will be developed. For the derivation of the equations and their general form for arbitrary systems, the reader is referred to Appendix B. In addition to solving the direct eigenvalue problem (5.2), one needs to find the adjoint eigenmodes and eigenvalues. After scaling the adjoint and direct eigenmodes, one can express the sensitivity to basic flow variations. Then, solving for an extra linear system of equations, one obtains a so-called adjoint basic flow, from which one can directly extract the sensitivity to variations in the surface heat transfer.

5.3.1 Adjoint Eigenvalue Problem

The adjoint eigenvalue problem can either be obtained by solving the adjoint of the eigenvalue problem (5.2) by taking the transpose of the complex conjugate, or by discretizing the adjoint equations. The adjoint eigemodes $\hat{\boldsymbol{q}}_i^\dagger$ can be obtained by solving the adjoint eigenvalue problem

$$
\begin{aligned}
\gamma_i^\dagger \hat{u}_i^\dagger - u_0\frac{\partial \hat{u}_i^\dagger}{\partial x} - u_0\frac{\partial \hat{u}_i^\dagger}{\partial y} + \hat{u}_i^\dagger\frac{\partial u_0}{\partial x} + \hat{v}_i^\dagger\frac{\partial v_0}{\partial x} + \hat{\theta}_i^\dagger\frac{\partial \theta_0}{\partial x} &= -\frac{\partial}{\partial x}\hat{p}_i^\dagger + \left(\frac{\partial^2}{\partial x^2} + \frac{\partial^2}{\partial y^2} - k^2\right)\hat{u}_i^\dagger,\\
\gamma_i^\dagger \hat{v}_i^\dagger - u_0\frac{\partial \hat{v}_i^\dagger}{\partial x} - v_0\frac{\partial \hat{v}_i^\dagger}{\partial y} + \hat{u}_i^\dagger\frac{\partial u_0}{\partial y} + \hat{v}_i^\dagger\frac{\partial v_0}{\partial y} + \hat{\theta}_i^\dagger\frac{\partial \theta_0}{\partial y} &= -\frac{\partial}{\partial x}\hat{p}_i^\dagger + \left(\frac{\partial^2}{\partial x^2} + \frac{\partial^2}{\partial y^2} - k^2\right)\hat{v}_i^\dagger,\\
\gamma_i^\dagger \hat{w}_i^\dagger - u_0\frac{\partial \hat{w}_i^\dagger}{\partial x} - v_0\frac{\partial \hat{w}_i^\dagger}{\partial y} &= -\,\mathrm{i}k\hat{p}_i^\dagger + \left(\frac{\partial^2}{\partial x^2} + \frac{\partial^2}{\partial y^2} - k^2\right)\hat{w}_i^\dagger,\\
\gamma_i^\dagger \hat{\theta}_i^\dagger - u_0\frac{\partial \hat{\theta}_i^\dagger}{\partial x} - v_0\frac{\partial \hat{\theta}_i^\dagger}{\partial y} &= \frac{1}{\mathrm{Pr}}\left(\frac{\partial^2}{\partial x^2} + \frac{\partial^2}{\partial y^2} - k^2\right)\hat{\theta}_i^\dagger,\\
\frac{\partial \hat{u}_i^\dagger}{\partial x} + \frac{\partial \hat{v}_i^\dagger}{\partial y} + \mathrm{i}k\hat{w}_i^\dagger &= 0,
\end{aligned}
\tag{5.7}
$$

subject to the boundary conditions for $\hat{\boldsymbol{u}}_i^\dagger$

$$
\begin{aligned}
\hat{\boldsymbol{u}}_i^\dagger &= 0, && \text{at all walls } x = \pm\Gamma/2 \text{ and } y = -1/2,\\
\hat{v}_i^\dagger &= 0, && \text{at the free surface } y = 1/2,\\
\frac{\partial}{\partial y}(\hat{u}_i^\dagger, \hat{w}_i^\dagger) &= 0, &&
\end{aligned}
$$

for the adjoint mode temperature $\hat{\theta}_i^\dagger$

$$
\begin{aligned}
\hat{\theta}_i^\dagger &= 0, && \text{at the lateral walls } x = \pm\Gamma/2,\\
\frac{\partial \hat{\theta}_i^\dagger}{\partial y} - \mathrm{Pr}\,\mathrm{Re}\left(\frac{\partial \hat{u}_i^\dagger}{\partial x} + \mathrm{i}k\hat{w}_i^\dagger\right) &= 0, && \text{at the free surface } y = 1/2,\\
\frac{\partial \hat{\theta}_i^\dagger}{\partial y} &= 0, && \text{at the bottom wall } y = -1/2.
\end{aligned}
$$

One can clearly see from these equations that the adjoint perturbation is transported upstream by the basic flow, and that the production terms of the thermal perturbation are now appearing in the momentum equations. The adjoint perturbation velocity not only builds on basic flow velocity gradients but also on basic temperature gradients. Besides the driving of the flow at the free surface is now at the boundary condition of the temperature and not anymore in the boundary condition of the velocity. By construction, the adjoint eigenvalues $\gamma_i^\dagger$ are the conjugate of the eigenvalues of the direct problem, see Appendix B.

Normalization of the Eigenmode and its Adjoint

For the following subsection to hold, one needs to normalize the eigenmode and its adjoint since they both are defined up to a scaling factor. The scaling that has to be enforced (see Appendix B) is the scalar product of the explicitly time dependent variables

$$\int_V \hat{\boldsymbol{u}}_i^* \cdot \hat{\boldsymbol{u}}_i^\dagger + \hat{\theta}_i^* \hat{\theta}_i^\dagger \, \mathrm{d}V = 1, \tag{5.8}$$

where the superscript $*$ denotes the complex conjugate. For further information the reader is referred to Appendix B.

5.3.2 Sensitivity to Basic Flow Variations

The sensitivity of the eigenvalue to changes in the basic flow - also called *structural* sensitivity - is defined by

$$\nabla_{\boldsymbol{q}_0}\gamma_i = \begin{pmatrix} \nabla_{\boldsymbol{u}_0}\gamma_i \\ \nabla_{\theta_0}\gamma_i \\ \nabla_{p_0}\gamma_i \end{pmatrix} = \begin{pmatrix} -\hat{\boldsymbol{u}}_i^\dagger \cdot \nabla \hat{\boldsymbol{u}}^H + \hat{\boldsymbol{u}}_i^* \cdot \nabla \hat{\boldsymbol{u}}_i^\dagger - \hat{\theta}_i^\dagger \nabla \hat{\theta}^* \\ \hat{\boldsymbol{u}}_i^* \cdot \nabla \hat{\theta}_i^\dagger \\ 0 \end{pmatrix}, \tag{5.9}$$

where the superscript H denote the transpose of the conjugate. In the case of an infinitely extended setup, that gives

$$\begin{aligned}
\nabla_{u_0}\gamma &= -\hat{u}_i^\dagger \frac{\partial \hat{u}_i^*}{\partial x} - \hat{v}_i^\dagger \frac{\partial \hat{v}_i^*}{\partial x} - \hat{w}_i^\dagger \frac{\partial \hat{w}_i^*}{\partial x} + \hat{u}_i^* \frac{\partial \hat{u}_i^\dagger}{\partial x} + \hat{v}_i^* \frac{\partial \hat{u}_i^\dagger}{\partial y} + \hat{w}_i^* k \hat{u}_i^\dagger - \hat{\theta}_i^\dagger \frac{\partial \hat{\theta}^*}{\partial x} \quad , \\
\nabla_{v_0}\gamma &= -\hat{u}_i^\dagger \frac{\partial \hat{u}_i^*}{\partial y} - \hat{v}_i^\dagger \frac{\partial \hat{v}_i^*}{\partial y} - \hat{w}_i^\dagger \frac{\partial \hat{w}_i^*}{\partial y} + \hat{u}_i^* \frac{\partial \hat{v}_i^\dagger}{\partial x} + \hat{v}_i^* \frac{\partial \hat{v}_i^\dagger}{\partial y} + \hat{w}_i^* k \hat{v}_i^\dagger - \hat{\theta}_i^\dagger \frac{\partial \hat{\theta}^*}{\partial y} \quad , \\
\nabla_{w_0}\gamma &= -\mathrm{i}\hat{w}_i^\dagger k \hat{u}_i^* - \mathrm{i}\hat{w}_i^\dagger k \hat{v}_i^* - \mathrm{i}\hat{w}_i^\dagger k \hat{w}_i^* + \hat{u}_i^* \frac{\partial \hat{w}_i^\dagger}{\partial x} + \hat{v}_i^* \frac{\partial \hat{w}_i^\dagger}{\partial y} + \mathrm{i}\hat{w}_i^* k \hat{w}_i^\dagger - \mathrm{i}\hat{\theta}_i^* k \theta_i^\dagger, \\
\nabla_{\theta_0}\gamma &= \hat{u}_i^* \frac{\partial}{\partial x}\hat{\theta}_i^\dagger + \hat{v}_i^* \frac{\partial}{\partial y}\hat{\theta}_i^\dagger + \hat{w}_i^* \mathrm{i} k \hat{\theta}_i^\dagger, \\
\nabla_{p_0}\gamma &= 0.
\end{aligned}$$

In our case the third line is zero since the basic flow velocity has only two components (u, v) and as we consider the basic flow to be two-dimensional, variations of the third one are not allowed. However, if, for instance, a transverse pressure gradient would be imposed in the basic flow equations inducing a non zero spanwise component of the basic flow velocity, the third line would indicate the local effect of variations in the spanwise velocity component. As the expressions above are already lengthy, the decomposition into real and imaginary part will not be given here, but needs to implemented, and numerically validated.

For a given variation of the basic flow $\delta \boldsymbol{q}_0 = (\delta \boldsymbol{u}_0, \delta\theta_0, \delta p_0)$, the (first order) change of the eigenvalue $\delta\gamma_i$ is given by

$$\delta\gamma = \int_V \nabla_{\boldsymbol{q}_0}\gamma^* \cdot \delta \boldsymbol{q}_0 \, \mathrm{d}V. \tag{5.10}$$

5.3.3 Eigenvalue Sensitivity with Respect to Variations of the Source Terms

Once the sensitivity to basic flow variations is obtained, one can compute the so-called adjoint basic flow. To do so, we introduce the adjoint basic flow variables $\boldsymbol{q}_0^\dagger = (\boldsymbol{u}_0^\dagger, \theta_0^\dagger, p_0^\dagger)$. They are the solution of the linear system of equations

$$\left[\frac{\partial}{\partial \boldsymbol{q}_0}\mathcal{B}\right]^\dagger \cdot \boldsymbol{q}_0 \cdot \boldsymbol{q}_0^\dagger = \nabla_{\boldsymbol{q}_0}\gamma, \tag{5.11}$$

where $\partial\mathcal{B}/\partial\boldsymbol{q}_0$ corresponds here to the Jacobian matrix without the terms in k coming from the normal mode ansatz. Practically, this operator comes from the differentiation with respect to the basic flow of the steady 2D Navier–Stokes operator, in which these terms in k do not appear. So if the perturbations are purely two-dimensional, then this operator is the same as the Jacobian matrix. Note that this operator is linear and real valued, therefore one can solve two different problems: one for the real part of the right hand side of (5.11), and one for the imaginary part of (5.11). The adjoint basic flow variables $\boldsymbol{q}_0^\dagger$ correspond to the sensitivity of the eigenvalue to a small additional steady source term $\delta\boldsymbol{F}(\boldsymbol{x})$ in the momentum equations and $\delta q(\boldsymbol{x})$ in the heat equation. Therefore,

$$\nabla_F \gamma_i = \boldsymbol{u}_0^\dagger$$

and

$$\nabla_q \gamma_i = \theta_0^\dagger.$$

Sensitivity to Changes in the Boundary Conditions

Once $\boldsymbol{q}_0^\dagger$ is computed, one can express the sensitivity of the eigenvalue to steady heat flux variations as

$$\nabla_f \gamma = \frac{1}{\mathrm{Pr}}\theta_0^\dagger. \tag{5.12}$$

Note that many other quantities of potential interest can readily be obtained. For instance the sensitivity to changes to shear stress variations at the free surface [see 172]

$$\nabla_\tau \gamma = u_0^\dagger.$$

5.4 Numerical Methods

5.4.1 Implementation

The linear stability analysis is implemented based on the FEM library FEniCS using Taylor–Hood elements for the velocity and pressure, and quadratic continuous elements

TABLE 5.1 – Critical parameters for two- (a) and three-dimensional instabilities (b) obtained by the linear stability analysis for an infinitely extended cavity.

(a) two-dimensional instabilities

Author	Γ	Pr	N	N_{DF}	$\mathrm{Re}_c^{2\mathrm{D}}$	ω_c
Present	3	4.4	20	21219	2035.10	16.5266
Present	3	4.4	40	64527	2027.93	16.5346
Present	3	4.4	80	206029	2027.01	16.5355
Kuhlmann (2008)	3	4.4			2026.6 ± 2.8	16.537 ± 0.006
Present	3	13.9	40	64527	1201.45	11.0726
Present	3	13.9	80	206029	1199.16	11.0726
Kuhlmann (2008)	3	13.9			1197.7 ± 5.4	11.076 ± 0.003

(b) three-dimensional instabilities

Author	Γ	Pr	N	N_{DF}	$\mathrm{Re}_c^{3\mathrm{D}}$	k_c	ω_c
Present	3	4.4	20	27718	846.85	1.621	8.0159
Present	3	4.4	40	84322	846.26	1.621	8.0183
Present	3	4.4	80	269304	846.12	1.621	8.0185
Kuhlmann (2008)	3	4.4			844.9 ± 3.3	1.618 ± 0.010	8.010 ± 0.002
Present	3	13.9	20	27718	893.86	0.949	3.444
Present	3	13.9	40	84322	882.64	0.946	3.445
Present	3	13.9	80	269304	882.26	0.946	3.445
Kuhlmann (2008)	3	13.9			861 ± 65	0.957 ± 0.004	3.451 ± 0.057

for the temperature (see Chapter 3). The mesh is generated using a tensor grid $N \times N\Gamma/2$ which is refined in two steps. First, the elements which are closer than $\delta y = 0.1$ from the free surface and $\delta = 0.05$ from the wall are refined using the Plaza–Carey algorithm [127]. Then, elements touching the free surface are refined two more times to ensure that the high shear stresses, especially close to the corners, are well captured. In the end the smallest length of the side of an element is seven times smaller than the side length of a non-refined element. The number of degrees of freedom denoted N_{DF} correspond to the number of basis functions used to discretize the perturbation mode. It depends on the mesh and on whether the perturbation is two- or three-dimensional.

5.4.2 Code Verification

To test our implementation, we compare our the critical Reynolds number Re_c and oscillation frequency ω_c with those obtained by Kuhlmann & Albensoeder [83] for specfic sets of parameters. This is shown in table 5.1. To find critical pairs, we proceed in two steps. First, we use a cubic interpolation of the eigenvalue with the largest real part to find the neutral Reynolds numbers for a given wavenumber k, as in Chapter 3. The Reynolds number is considered to be a neutral Reynolds number if $|\sigma_1| < 10^{-6}$. Second, the Reynolds number is fixed and we explore the wavenumber vicinity: the eigenvalues at $k - \delta k$, k and $k + \delta k$ are probed and the maximum is approximated using a quadratic interpolant. This is repeated using 4 times smaller δk around the

TABLE 5.2 – Thermal and kinetic perturabtion energy budgets for different Prandtl numbers and $\Gamma = 3$. The main contribution to the kinetic and thermal energy budget are written in boldface.

Pr	Re_c	k_c	I_1 J_1	I_2 J_2	I_3	I_4	M_1	M_2
0.1	5497	2.13	0.0371 0.2664	**0.5215** **0.7335**	−0.0069	0.0850	0.0723	**0.2911**
4.4	846.26	1.621	0.0010 **0.7617**	0.0466 0.2382	0.0059	0.0136	**0.3373**	**0.5865**
13.9	882.64	0.946	−0.001 **0.8274**	0.0100 0.1722	0.0006	−0.0041	**0.4795**	**0.4957**

newly approximated maximum, until the difference between two successive values of k is smaller than 10^{-3}. These two steps are sequentially repeated until the sum of the variation in Reynolds δRe and wavenumber δk satisfies the tolerance condition $|\delta \mathrm{Re}| + |\delta k| < 10^{-3}$.

In table 5.1, we see that for both two-dimensional and three-dimensional perturbations, the critical Reynolds numbers and oscillation frequencies fall within the margins provided by Kuhlmann & Albensoeder [83] as soon as the grid parameter $N \geq 40$. Therefore, all the following simulations are made using $N = 40$.

5.5 Sensitivities at Criticality

In this section, we recall the different instability mechanisms at representative Prandtl numbers $\mathrm{Pr} = 0.1$, and $\mathrm{Pr} = 13.9$, which correspond to molten metals like iron and n-decane, respectively. For both these cases, the basic flow at the critical Reynolds number will be discussed as well as the eigenmode and the instability mechanism. After that, the sensitivity to changes in the heat flux and in the shear stress at the free surface will be presented.

5.5.1 Low Prandtl Number $\mathrm{Pr} = 0.1$

Basic Flow and Instability Mechanism

At low Prandtl number and low Reynolds number (*i.e.* Marangoni number $\mathrm{Re}\,\mathrm{Pr} = \mathrm{Ma} \to 0$), thermal diffusion effects are preponderant and the temperature profile at the free surface is linear, see fig. 5.4(a). Since there is no source term in the heat equation and the transport terms are negligible, the temperature field varies linearly in the whole domain as both the free surface and the bottom wall are considered adiabatic. Increasing the Reynolds number, deviations from the linear profile appear. At the critical Reynolds number $\mathrm{Re}_c = 5497$, they are visible in fig. 5.4(a) near the cold wall $x = -1.5$ and are due to the locally high velocity magnitude. In fact, the velocity

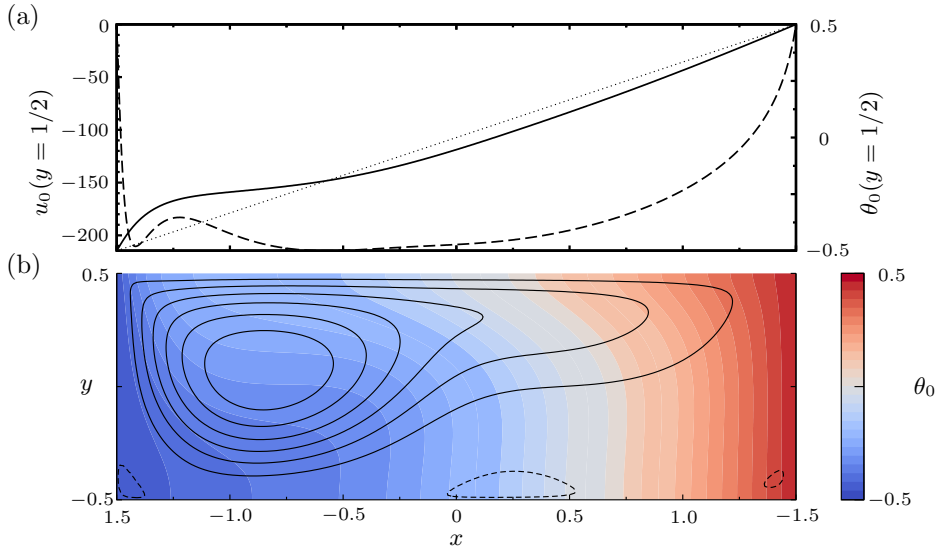

FIGURE 5.4 – Basic flow at Re = 5497, Pr = 0.1, Γ = 3. (a) Tangential velocity (dashed line, left scale) and temperature (full line, right scale). Conducting temperature profile for Ma → 0 is indicated by a dotted line. (b) Basic flow streamlines are shown with full lines, while the basic flow temperature field is shown by colors.

magnitude at the free surface gradually increases as the flow leaves the hot corner, and reaches a plateau near the center of the surface where its value varies around $u_0 \approx -210$. As the flow approaches the cold corner, the surface velocity decreases after passing a small peak at $x = -1.42$. The fluid is then transported downwards at a velocity magnitude comparable to the surface velocity and due to the presence of the lower wall a vortex is formed. Because of this strong surface velocity, warmer fluid gets closer to the cold corner resulting in the deviation from the linear profile at the free surface. In the bulk of the flow, the strong core vortex, whose center is located close to the cold wall, is responsible for the transport of cold fluid towards the center of the cavity, as can be seen in fig. 5.4(b). On the other hand, in the slow region of the flow in the lower half of the cavity close to the hot wall, thermal diffusion still dominates and the iso-temperature curves are nearly vertical.

Qualitatively, the streamlines of the flow are similar to those of a lid-driven cavity, see for instance fig. 4.13 (on page 64) or fig. 8 of Albensoeder *et al.* [5]. Indeed, the main part of the production rate of the perturbation energy is I_2 which indicates that the inertial effects are important in the destabilization mechanism. The second post in the energy budgets is M_2 which corresponds to the work done by thermocapillary stresses in the z-direction at the free surface through the Marangoni effect. The local production rate of perturbation kinetic energy corresponding to the inertial effects $i = \sum i_n$ is displayed in fig. 5.5(a). Unlike the lid-driven case, the maximum is located along the wall downstream of the cold corner and not above a recirculation zone. In the limit of vanishing Prandtl numbers, the thermal budget must be passive since the thermal perturbation are immediately dissipated. At Pr = 0.1, this is not the case, and

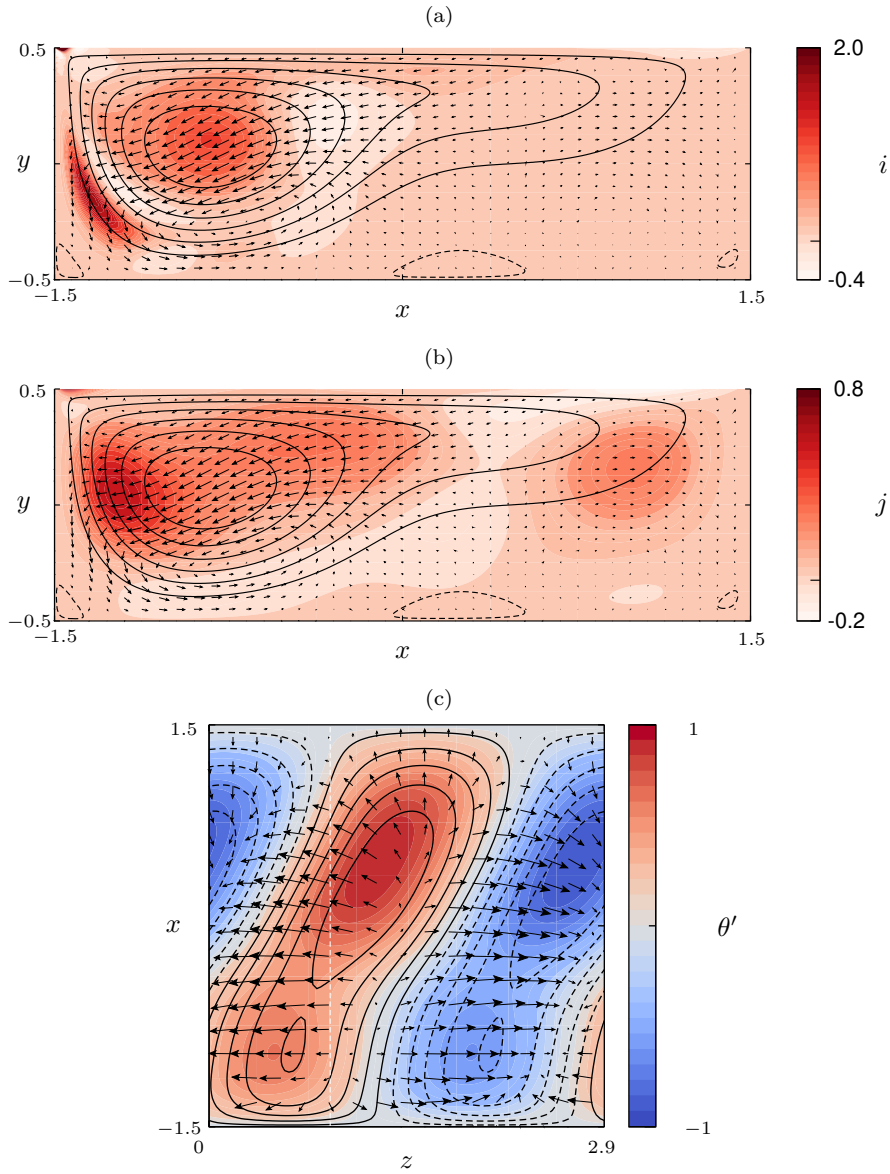

FIGURE 5.5 – (a,b) Color indicates the local rate of production of (a) perturbation kinetic energy $i = \sum i_n$ and (b) perturbation thermal energy $j = \sum j_n$ in the same plane where they take their maximum. Arrows indicate the x-, y- component of the perturbation velocity while the full lines show the basic flow streamlines. (c) Color represents the arbitrarily scaled perturbation temperature at the plane $y = 0.09$ where it takes its maximum, lines and arrows indicate the perturbation temperature isovalues and velocity at the free surface. The white dashed line indicates the plane in which (a) and (b) are shown. The wave propagates in the negative z direction.

we can only suspect that the mechanical part of the energy budget is of importance. Following the argument of Albensoeder *et al.* [5], if the streamline of the basic flow is curved, if in the region where i_2 is high the momentum of the basic flow decays radially outwards from the vortex center, then the instability is centrifugal. Here inertial effects work in conjunction with the thermocapillary stresses. The temperature perturbation produced by the velocity perturbation affects almost directly the free surface temperature distribution. The perturbation temperature profile on the plane $y = 0.09$ where it takes its maximum and at the free surface are very similar. They are respectively indicated by colors and isolines in fig. 5.5(c) and superpose almost perfectly. The surface temperature perturbations engender mainly spanwise velocity perturbation as can be seen in fig. 5.5(c). This provides a feedback mechanism for the I_2 term in the bulk. The wave propagates in the negative z direction and the maximum of the temperature perturbation lags behind the plane of maximum of thermal energy production rate.

Sensitivity with Respect to Changes of the Basic Flow

The growth-rate sensitivity to basic flow variations $\Re\nabla_{\boldsymbol{q}_0}\gamma_1$ is plotted in fig. 5.6. In (a) and (b), the sensitivity of the variation to x- and y-components of the basic flow velocity are shown. They take their minimum close to the cold wall and the free surface, respectively. Their maximum is located in the inner part of the main vortex. Note that in the case of the y-component $\nabla_{v_0}\gamma$, the sensitivity values at the free surface are the largest by magnitude, although variations of the y-component of the basic flow velocity are not allowed at the surface by the boundary conditions and previous assumptions (no surface deformation, and no flow through the surface). This is not an implementation error, but rather information that is irrelevant in our case.

On the other hand, small variations of the basic flow velocity have an impact which is two orders of magnitude smaller than variation of the temperature field. This can be seen comparing the scales of (a), (b) and (c). The sensitivity to basic temperature variations takes its maximum around $\boldsymbol{x} = (-0.5, 0.375)^{\mathrm{T}}$, and its minimum at the free surface $\boldsymbol{x} = (-1.456, 1)^{\mathrm{T}}$. It seems then that the stability of the flow depends greatly on the basic flow temperature at the surface, and that small changes there could dramatically change the critical Reynolds number.

Sensitivity with Respect to External Forces

The sensitivities of the leading eigenvalue with respect to a steady force directed in x-, y-direction and to a steady heat source are shown in fig. 5.7(a,b,c), respectively. The region where a steady force will affect the growth rate the most coincides with the region of the vortex where the flow is directed upwards. While the maximum of the sensitivity with respect to a steady force is located in the bulk of the flow, the sensitivity with respect to a steady heat source is greater along the free surface where both its maximum and minimum arise. Again the same difference in the order of magnitude appears between the adjoint basic flow components and the structural sensitivity components. This is not very surprising, since the latter is the right-hand

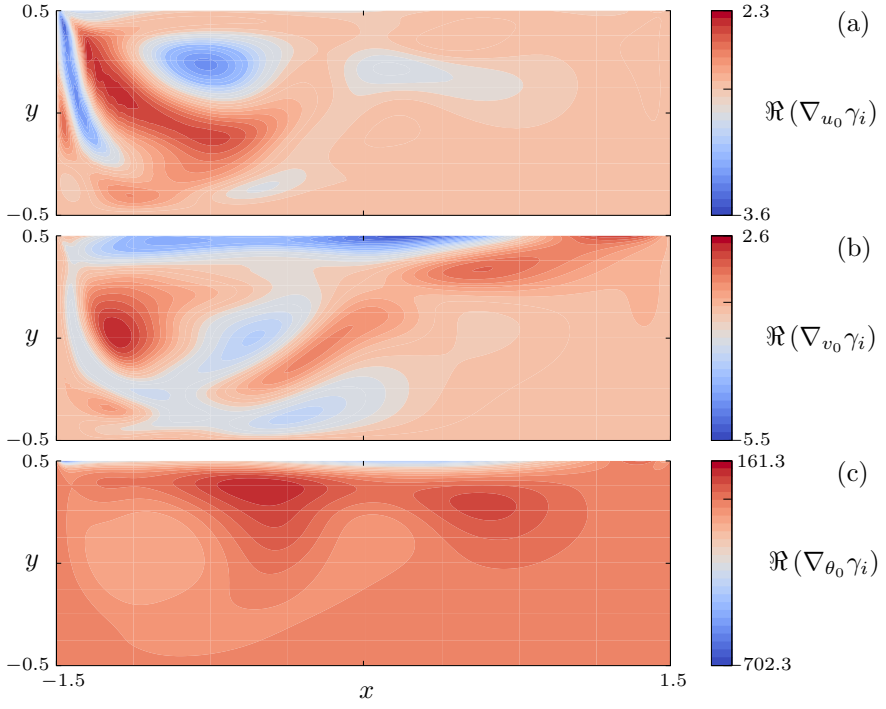

FIGURE 5.6 – Real part of the leading eigenvalue sensitivity with respect to changes in the basic flow (a) x-component velocity $\Re(\nabla_{u_0}\gamma)$, (b) y-component velocity $\Re(\nabla_{v_0}\gamma)$ and (c) temperature $\Re(\nabla_{\theta_0}\gamma)$ for $\Gamma = 3$, $\mathrm{Pr} = 0.1$, $\mathrm{Re} = 5497$, $k = 2.13$.

side in (5.11).

Sensitivity with Respect to Changes in the Heat Flux and Shear Stress

The evaluation of the sensitivity with respect to shear stress and heat flux variations at the free surface are plotted in fig. 5.8. Both of them oscillate around the zero line. Thus, if an extra positive shear stress is applied in a region where $\Re(\nabla_\tau\gamma)$ is positive, the growth rate will increase, and ,conversely it will decrease where the sensitivity to shear-stress variation is negative.

One can clearly see from the scales that four orders of magnitude separate the shear-stress sensitivity and heat-flux sensitivity. If one assumes an external gas flow in the streamwise direction $\boldsymbol{u}_{\mathrm{ext}} = u_{\mathrm{ext}}\boldsymbol{e}_x$ causes the external shear stress, the interface condition for the basic flow would read:

$$\frac{\partial u_0}{\partial y} = -\mathrm{Re}\frac{\partial \theta_0}{\partial x} + \underbrace{\frac{\mu_{\mathrm{ext}}}{\mu}\frac{\partial u_{\mathrm{ext}}}{\partial y}}_{\delta\tau},$$

where the subscript "ext" denotes the quantities of the external flow. Typically the external fluid has a dynamic viscosity two or three orders of magnitude lower than

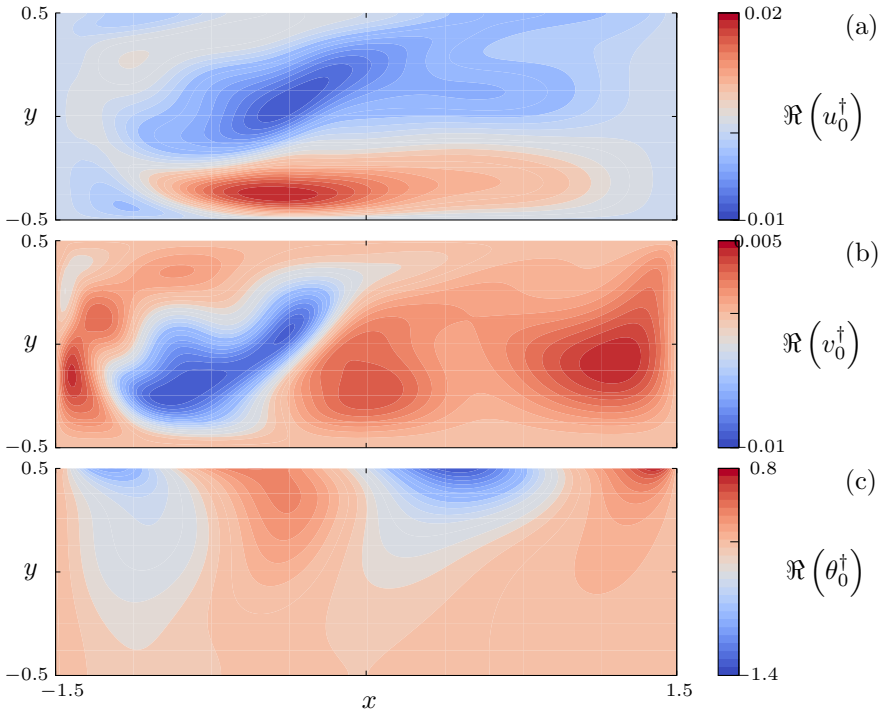

FIGURE 5.7 – Real part of the adjoint basic flow or real part of the sensitivity to a steady momentum heat or source term. (a) x-component $\Re\left(u_0^\dagger\right)$, (b) y-component $\Re\left(v_0^\dagger\right)$ and (c) temperature $\Re\left(\theta_0^\dagger\right)$ of the adjoint basic flow for $\Gamma = 3$, $\mathrm{Pr} = 0.1$, $\mathrm{Re} = 5497$, $k = 2.13$.

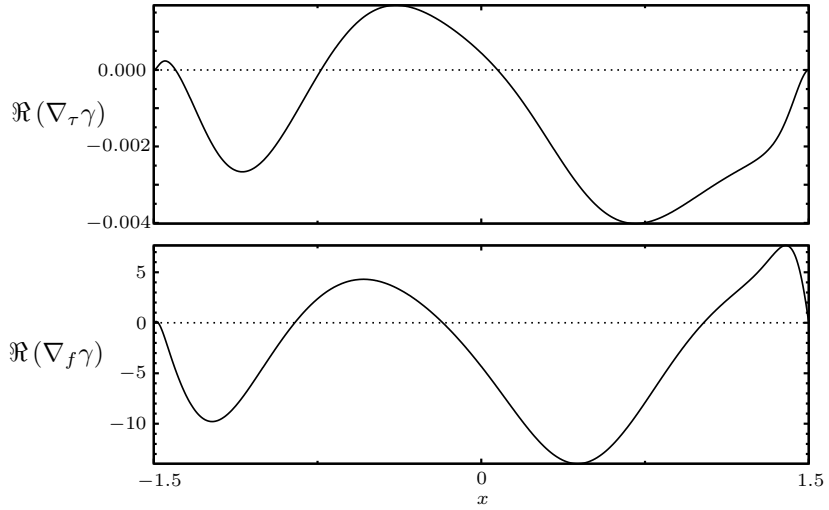

FIGURE 5.8 – Sensitivity of the leading eigenvalue with respect to surface shear-stress (a) and to surface heat-flux variations (b) for $\Gamma = 3$, $\mathrm{Pr} = 0.1$, $\mathrm{Re} = 5497$, $k = 2.13$.

that of the liquid in the cavity. The variation of shear stress $\delta\tau$ of the liquid in the cavity due to the external flow shear on the free surface is then already small. This diminishes even more the potential impact the shear stress of the external flow could have on the stability of the basic flow.

Therefore, at $\mathrm{Pr} = 0.1$, the temperature of the external flow has a much stronger impact on the stability of the basic flow than the external shear. However, the external flow velocity itself can impact the stability of the internal flow in that the faster the external flow is, the larger the heat transfer at the free surface can be.

Let us now focus on the sensitivity with respect to heat flux variations. In the linear approximation, a flux having locally the same sign as the sensitivity would solely destabilize the flow. Here the sign of the heat-flux sensitivity alternates along the surface. Starting from the hot corner at $x = 1.5$, a positive heat flux would destabilize the basic flow for $x \in [1.02, 1.5]$ followed by a negative flux for $x = [-0.18, 1.02]$. Such heat flux would locally increase the temperature near the hot corner and decrease it downstream from it, resulting in an increased driving shear stress downstream from the location of the positve heat flux. A second similar pattern but of lower magnitude is met along the second half of the surface. We can anticipate that the additional thermocapillary stress produced by this destabilizing heat flux would be similar in shape with the one depicted in fig. 5.8(a) with a change of sign since the addition stress would be in the $-x$ direction.

5.5.2 High Prandtl Number $\mathrm{Pr} = 13.9$

Basic Flow Description

Consistent with the observations made by Riley & Neitzel [135], Kuhlmann & Albensoeder [83], the basic flow show in fig. 5.9(b) is composed of a strong vortex close to the hot wall and a weaker vortex close to the cold wall. Both vortices are rotating counterclockwise, carrying the hot fluid along the surface and the cold fluid at the bottom of the cavity. One can see in fig. 5.9(a) that the temperature along the free surface (full lines) rapidly decays as the fluid is transported away from the hot corner. The temperature stays nearly constant along a large portion of the surface before dramatically dropping to reach the minimal temperature imposed at the cold wall. Correspondingly, the dashed line in fig. 5.9(a) indicates that the flow is accelerated as it leaves the hot corner and the surface velocity magnitude reaches a peak at $x = 1.39$. This can also be seen from the crowding of the streamlines in fig. 5.9(b). As the temperature profile flattens, the driving force is reduced and the flow decelerates progressively and its magnitude is about 30% of the previous peak. Close to the cold corner, the magnitude of flow velocity greatly increases in an extremely sharp peak.

Due to the flow being stronger close to the hot wall than at the cold wall (except for the cold-corner peak), the thermal boundary layer on the hot wall at $x = 1.5$ is thinner than on the cold wall at $x = -1.5$, resulting in larger wall normal temperature gradient along the hot wall. Close to the hyperbolic point between the two vortices the temperature gradient increases slightly in magnitude as warmer fluid is dragged from the free surface by the strong vortex and colder fluid is carried upwards by the

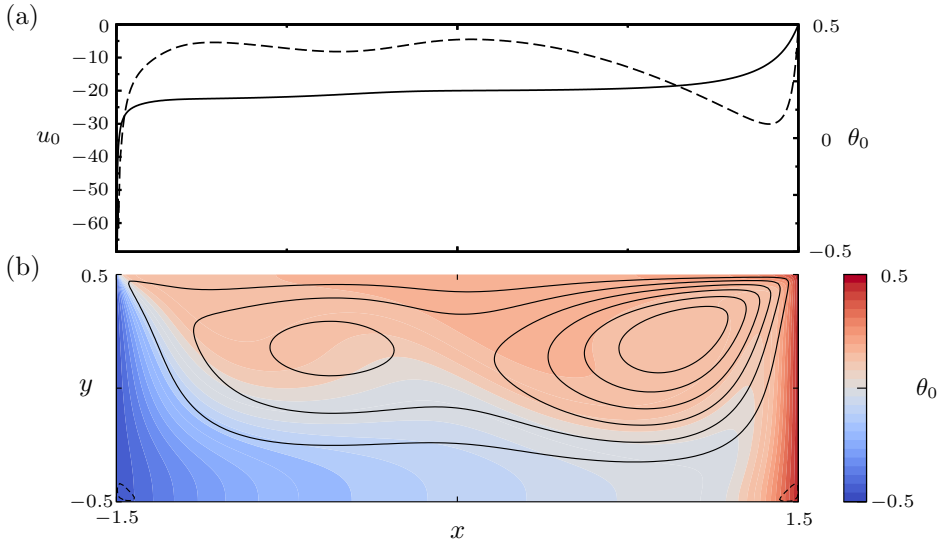

FIGURE 5.9 – Basic flow at Re = 882.64, Pr = 13.9, Γ = 3. (a) Tangential surface velocity (dashed line, left scale) and surface temperature (full line, right scale). (b) Basic flow streamlines are shown as full lines, while the basic flow temperature field is shown in color.

other vortex.

Instability Mechanism

As indicated in table 5.2, the energy production done by the work of the thermocapillary forces M_1 and M_2 is readily dissipated and balanced by the dissipation (normalized to 1). Therefore, inertial effects have almost no role in the growth of the perturbation energy. The velocity perturbation in the bulk only transports the basic temperature and, therefore, produces the temperature perturbation which in turn feeds the thermocapillary stresses when reaching the free surface.

In fig. 5.10(a), the local production rates of thermal perturbation energy has a wide peak around the hyperbolic point of the basic flow streamlines, where the perturbation velocity meets the locally higher basic flow temperature gradient. The mode shown in fig. 5.10 is propagating in the positive z direction. The perturbation temperature reaches an extremum in the vicinity of the maximum of the rate of production (see 5.10(b)) and is transported to the surface by the vortices of the basic flow. This triggers the Marangoni effect and drives the perturbation velocity, which forms vortices. At least three perturbation vortices are formed: the main one is located in the colder part of the cavity ($x < 0$). It is rotating counterclockwise in fig. 5.10(a). In addition a weaker clockwise vortex arises close to the cold corner. The third vortex is located in the warmer half of the flow ($x > 0$) and rotates clockwise in fig. 5.10(a). From fig. 5.10(b) one can see that these vortices stay confined in their respective halves.

Interestingly, the temperature at the free surface (shown by contour lines in fig.

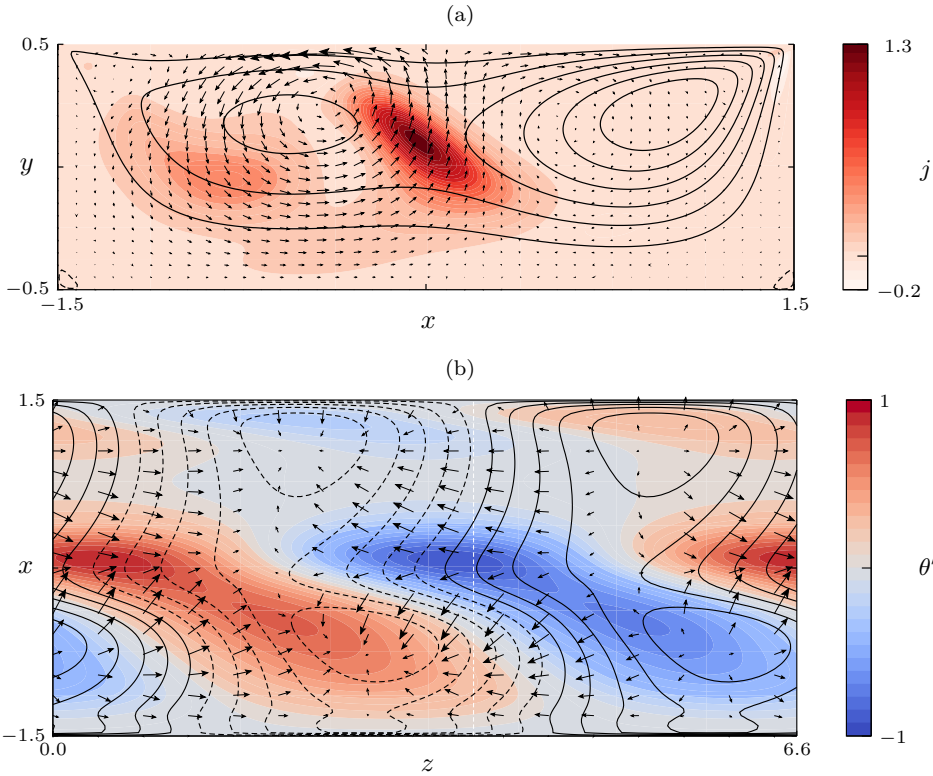

FIGURE 5.10 – (a) The local thermal perturbation energy production j in the plane $z = 3.75$ where it takes its maximum is shown by color while arrows denote the perturbation velocity on that plane. Full lines are the streamlines of the basic flow. (b) The perturbation temperature over one wavelength is shown by color on the plane $y = 0.007$ where it takes its maximum and by black contour lines at the free surface. Full lines denote positive values while dashed lines denote negative values. The perturbation velocity at the free surface is shown by arrows. The plane plotted in (a) in shown in (b) by the white dashed line. The wave propagates in the positive z direction.

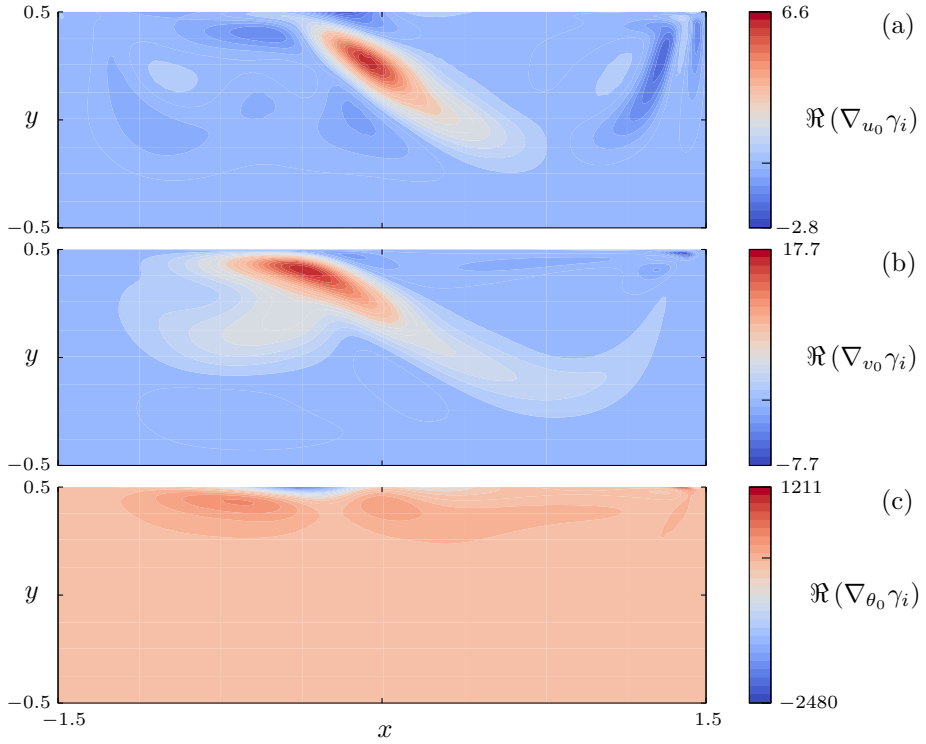

FIGURE 5.11 – Real part of the leading eigenvalue sensitivity with respect to changes of the basic flow (a) x-component velocity $\nabla_{u_0}\gamma$, (b) z-component velocity $\nabla_{v_0}\gamma$ and (c) temperature $\nabla_{\theta_0}\gamma$.

5.10(b)) is shifted in comparison with the temperature on the plane $y = -0.007$ where the maximum perturbation temperature is reached. Besides, the temperature perturbation close to the midplane, shown in color in fig. 5.10(b), indicates that the a hydrothermal wave is propagating obliquely. For the aspect ratio considered here, the hydrothermal wave is confined to the colder half of the cavity. This mode is then representative of the hydrothermal waves, observed in shallower containers in for instance Kuhlmann & Albensoeder [83]($\Gamma = 8$, in their fig. 17), as well as in infinitely long layers [167, 166].

Sensitivitity with Respect to Changes in the Basic Flow

The sensitivity of the growth rate with respect to changes of the basic flow is displayed in fig. 5.11. The location where the sensitivity is the largest corresponds to the weaker basic-state vortex close to the free surface. In particular, an increase of the x-component of the basic flow velocity (opposite to the basic flow) in the rightmost part of the weaker vortex would increase the growth rate of the mode (see fig.5.11b). Accelerating the flow in the vertical direction in this weaker vortex would also destabilize the system as the flow gets closer to the free surface. Indeed that would result in a cooler flow reaching the free surface, exactly where the growth sensitivity with respect

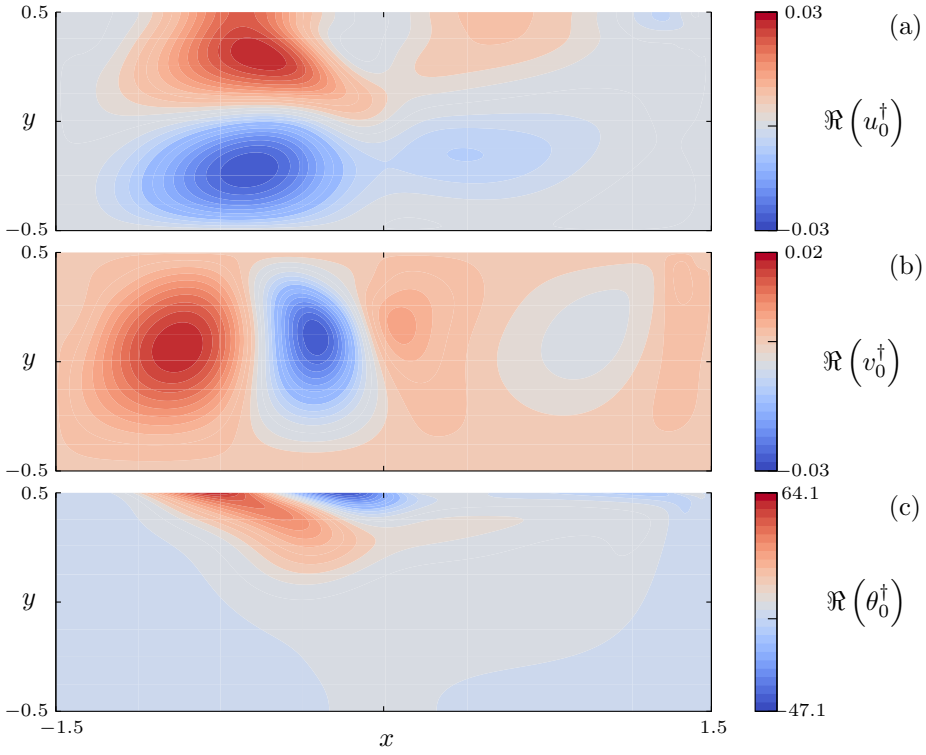

FIGURE 5.12 – Real part of the adjoint basic flow or real part of the leading eigenvalue sensitivity to a steady momentum or heat source term. (a) x-component $u_0^\dagger$, (b) y-component $v_0^\dagger$ and (c) temperature $\theta_0^\dagger$ of the adjoint basic flow.

to a cooling is the largest (fig. 5.11(c)). Again, the sensitivity of the growth rate with respect to changes in the basic-state temperature is two to three orders of magnitude larger than the sensitivity with respect to changes in the basic-state velocity.

Sensitivity with Respect to Steady Source Terms

The growth-rate sensitivities with respect to steady forces and steady heat sources are depicted in fig. 5.12. The zone with the greater sensitivity to a small steady force corresponds to the zone occupied by the hydrothermal wave (colder half of the cavity). Moreover, forces opposing the motion of the basic flow in the weaker vortex have a large destabilizing effect. Apparently, a weaker vortex in the colder half would lead to higher temperature gradients of the basic state in the bulk. This could in fact profoundly change the structure of the flow, as we shall see later in section 5.6.4.

The growth-rate sensitivity with respect to a heat source is displayed in fig. 5.12(c). One can clearly see that the growth rate is mainly affected by source terms close to the free surface, in the half $x < 0$. The distribution of $\theta_0^\dagger$ again indicates an increased growth rate if the weak vortex is suppressed (the thermocapillary forces corresponding

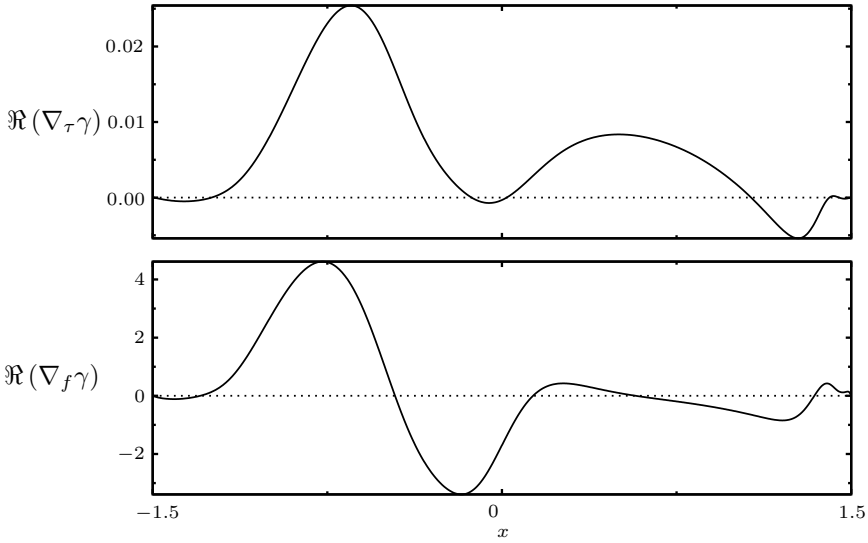

FIGURE 5.13 – Growth-rate sensitivity with respect to shear (a) and the heat flux variations (b) at $\mathrm{Pr} = 13.9$

to $\theta_0^\dagger$ act against it). In contrast, the effect of heat flux through the free surface above the stronger vortex seems to be rather low. The growth-rate sensitivity with respect to variations of the heat flux is four times smaller above the main vortex (warmer half) than on the weak vortex (colder half).

In this part, we have found that the impact of the heat flux through the free surface on the stability of the flow depends largely on the spatial distribution of the surface heat flux. The growth-rate sensitivity with respect to small heat flux variations naturally depends on the type of the instability. This was found to be true for both the high and low Prandtl numbers investigated. For the hydrothermal waves observed at high Prandtl number, surface heat flux variations on the cooler half of the surface are the most effective. At low Prandtl number, the sensitivity magnitude is of the same order of magnitude over both halves of the free surface.

For both low and high Prandtl numbers, we found that the sensitivity of the leading eigenvalue with respect to small heat flux variations oscillates along the free surface. Therefore control the stability of the flow can be controlled using a dedicated flux, regardless of its sign, since both positive and negative heat flux can have a stabilizing or destabilizing effect, depending on the location at which the flux is imposed. The following section provides an example for such a control strategy.

5.6 Sensitivity-Based Control

In order to illustrate the importance of the distribution of an imposed heat flux along the free surface, we shall develop in this section a framework to generate several heat

fluxes that modify the basic flow in a way that the growth rate of the most dangerous mode changes its sign.

First, we formulate the search for the heat flux distribution as a minimization problem and detail the optimization work flow. Then, we will find fluxes that change the onset of time-dependent flows for the configurations investigated above.

While a technical realization of these heat fluxes is beyond the scope of this work, the results demonstrate the importance of the thermal conditions at the free surface for the critical onset.

5.6.1 Formulation

Primarily, we are interested in stabilizing or destabilizing the basic flow using a tailored flux imposed at the free surface. To that end, we define a target growth rate σ_T whose sign depends on the desired stability of the system. Then, we want the *state* variables γ, $\hat{\boldsymbol{q}}$, $\boldsymbol{q}_0$ to be the solution of the state equations which are the steady Navier–Stokes equation and the eigenvalue problem. These *state* variables can be controlled through a *control variable*, in our case the heat flux $f(x)$ through the boundary. To find a flux such that $\sigma = \sigma_T$, one can minimize a cost function, for instance

$$\mathcal{J}(f) = (\sigma_1 - \sigma_T)^2 . \tag{5.13}$$

Note that this function does not depend explicitly on the control variable f, but only implicitly through the most dangerous perturbation growth rate σ_1. Eventually one could add some terms depending on f. Then $\mathcal{J}$ would depend both implicitly and explicitly on f. In the end, this problem can be formulated as a non-linear optimization problem:

$$\text{Find } f_T = \arg\min \left[\mathcal{J}(f)\right] \tag{5.14}$$

$$\text{such that } \begin{cases} \mathcal{F}(\boldsymbol{q}_0) = 0, , & \text{(5.15a)} \\ \nabla\theta_0 \cdot \boldsymbol{n} - f = 0, & \text{(5.15b)} \\ \mathcal{A}(\boldsymbol{q}_0) \cdot \hat{\boldsymbol{q}} + \gamma \mathcal{M} \hat{\boldsymbol{q}} = 0, & \text{(5.15c)} \end{cases}$$

where $f_T(x)$ is a (perhaps non-unique) heat flux, and (5.15b) corresponds to the boundary condition at the free surface of the heat equation. The Lagrangian function $\mathcal{L}$ associated to this constrained optimization problem is

$$\begin{aligned} \mathcal{L}(f, \boldsymbol{q}_0, \gamma, \hat{\boldsymbol{q}}, \boldsymbol{q}_0^\dagger, f^\dagger, \hat{\boldsymbol{q}}^\dagger) = \mathcal{J}(f) &- \left\langle \mathcal{F}(\boldsymbol{q}_0), \boldsymbol{q}_0^\dagger \right\rangle_V \\ &- \left\langle \mathcal{A}(\boldsymbol{q}_0) \cdot \hat{\boldsymbol{q}} + \gamma \mathcal{M} \hat{\boldsymbol{q}}, \hat{\boldsymbol{q}}^\dagger \right\rangle_V \\ &- \left\langle \nabla\theta_0 \cdot \boldsymbol{n} - f, f^\dagger \right\rangle_S , \end{aligned} \tag{5.16}$$

where the $\boldsymbol{q}_0^\dagger$, $f^\dagger$, $\hat{\boldsymbol{q}}^\dagger$ are the Lagrangian multipliers corresponding of the constraints on the basic flow (5.15a), the heat flux (5.15b) and the eigenvalue problem (5.15c),

respectively. The scalar products on the volume $\langle a, b\rangle_V$ and on the free surface $\langle a, b\rangle_S$ are defined by

$$\langle \boldsymbol{a}, \boldsymbol{b}\rangle_V = \int_V \boldsymbol{a}^* \cdot \boldsymbol{b}\, \mathrm{d}V \quad \text{and} \quad \langle \boldsymbol{a}, \boldsymbol{b}\rangle_S = \int_V \boldsymbol{a}^* \cdot \boldsymbol{b}\, \mathrm{d}S \quad .$$

Taking the Fréchet derivative of $\mathcal{L}$ with respect to all state and control variables and canceling all the derivatives with respect to the state variables allows us to identify the derivative with respect to f as

$$\nabla_f \mathcal{J}(f) = \frac{2}{\mathrm{Pr}} \left(\sigma_1 - \sigma_T\right) \theta_0^\dagger, \tag{5.17}$$

where σ_1 is the growth rate of the mode and $\theta_0\dagger$ is computed using the adjoint basic flow equations (5.11). The proof is essentially [1] the same as for the sensitivity analysis in Appendix B. Indeed, an equivalent approach would be to use the real part of the heat flux sensitivity $\Re(\nabla_f \gamma_i)$(5.12) while directly differentiating the cost function (5.13).

5.6.2 Optimization Procedure

Now that the gradient of the cost function with respect to changes in the heat flux at the free surface is know, it can be used in a minimzation algorithm, which contains the following steps

1. Compute the basic flow $\boldsymbol{q}_0$ associated with the current estimate of the heat flux $f(x)$,
2. Evaluate the direct eigenvalues and eigenmodes γ, $\hat{\boldsymbol{q}}$ by solving (5.2),
3. Evaluate the adjoint eigenvalues and eigenmodes $\gamma^\dagger$, $\hat{\boldsymbol{q}}^\dagger$ by solving (5.7),
4. Normalize the direct and adjoint modes using (5.8),
5. Evaluate the sensitivity to changes in the basic flow $\nabla_{\boldsymbol{q}_0}\gamma$ using (5.9),
6. Compute the adjoint basic flow $\boldsymbol{q}_0^\dagger$ using (5.11),
7. Evaluate the gradient $\nabla_f \mathcal{J}$ using (5.17),
8. Perform a step from the BFGS algorithm (see Chapter 3) using the gradient of step 7 and evaluation of the cost function $\mathcal{J}$ to update the heat flux distribution,
9. Depending on a tolerance on the cost function, the target flux f_T is obtained or return to 1.

1. The only difference comes in the rescaling of the modes: $\langle \hat{\boldsymbol{q}}_i \mathcal{M} \hat{\boldsymbol{q}}_i^\dagger \rangle = 2(\sigma_1 - \sigma_T)$ instead of (5.8). This amounts to rescaling $\theta_0^\dagger$ with this new factor since the equations (5.11) are linear.

In the following, we shall find (among potentially many other candidates) a heat flux that either stabilizes or destabilizes the flow for a low- or a high-Prandtl-number fluid. In each case, a first optimization (Opti_1) will be carried without any additional constraints on the flux, starting from an initial first guess of the surface heat flux $f_{\text{FG}}(x) = 0$. Follows a second optimization (Opti_2) in which the condition $f(x) \geq 0$ is imposed, since heat can be supplied technically (e.g. by a laser), but not easily removed. In order to probe the dependency of the result on the initial guess for $f(x)$, we repeat the previous procedure (Opti_3 and Opti_4) with another arbitrarily chosen starting flux $f_{\text{FG}}(x) = (\Gamma/2 - x)(x + \Gamma/2)/30$. The energy budgets of the leading eigenmode after each of the optimizations are reported in table. 5.3.

Note that these optimized heat fluxes do not change the average shear of the basic flow along the free surface since

$$\int_S \frac{\partial u_0}{\partial y} \, \mathrm{d}S = -\mathrm{Re} \int_S \frac{\partial \theta_0}{\partial x} \, \mathrm{d}S = -\mathrm{Re} \, .$$

Therefore the flux is only changing the distribution of the thermocapillary shear stresses along the surface, not their average value.

5.6.3 Low Prandtl Number

The fluxes and the basic flows presented in this subsection were all obtained by the algorithm in 5 to 7 iterations, and the cost function was always such that $\mathcal{J}(f) < 10^{-14}$ after minimization. This means that the target growth rates were obtained up to the 7th digit.

Flow Destabilization

We consider a subcritical basic flow with an adiabatic free surface at $\mathrm{Pr} = 0.1$ and $\mathrm{Re} = 4500 < \mathrm{Re}_c = 5497$ so a Reynolds number 18% below the critical one and $\sigma(f(x) = 0) = -2.74$. The basic flows obtained when the surface is adiabatic, with a flux as obtained after Opti_1 and Opti_2 are shown in fig. 5.14. If we consider the results from Opti_1 (no particular constraint on the heat flux), we can see from fig. 5.14(a) that the profile of the optimal flux (dotted line) is strikingly similar to the growth-rate sensitivity at the critical Reynolds number (see fig. 5.8(b) on page 93). This means that the sensitivity with respect to heat flux of the growth rate of the least stable mode do not change much with the Reynolds number. Comparing the velocity profiles (fig. 5.14(c)) for the adiabatic (full line) and optimized flux (dotted line) reveals that the optimized flow is slightly accelerated in the upstream part of the free surface and decelerated in the downstream half. This is also reflected by the temperature decaying faster as the flow leaves the hot corner, and being flatter in the downstream half, resulting in a locally lower shear. Consistently, the peak close to the cold corner $x = -1.5$ has almost vanished. In fig. 5.14(d,e), one can appreciate the global cooling of the fluid, and the streamlines plotted for the same isovalues. The basic flow changes only slightly such that the basic vortex is stronger and extends further towards the hot wall.

TABLE 5.3 – Kinetic and thermal perturbation energy budgets for an adiabatic surface $f(x) = 0$ and after the optimizations for subcritical (a,c) and supercritical conditions (b,d) for low (a,b) and high (c,d) Prandtl numbers. In Opti_1 and Opti_3, the sign of the flux is not constrained. In Opti_2 and Opti_4 the flux is positive. The initial guess for Opti_1 and Opti_2 is $f_{\text{guess}}(x) = 0$, while for Opti_3 and Opti_4 $f_{\text{guess}}(x) = (\Gamma/2 - x)(x + \Gamma/2)/30$.

(a)

$\text{Pr} = 0.1$, $\text{Re} = 4500 < \text{Re}_c$, $k = 2.166$, $\sigma_T = 0.1$

state	I_1	I_2	I_3	I_4	M_1	M_2	J_1	J_2
$f(x) = 0$	0.0376	0.4693	-0.0033	0.0949	0.0719	0.2806	0.2482	0.7198
Opti_1	0.0446	0.5204	-0.0026	0.1090	0.0586	0.2720	0.2388	0.7623
Opti_2	0.0398	0.4864	-0.0179	0.1079	0.0821	0.3037	0.3066	0.6945
Opti_3	0.0431	0.5036	-0.0091	0.1109	0.0651	0.2883	0.2772	0.7240
Opti_4	0.0378	0.4816	-0.0163	0.1055	0.0836	0.3096	0.3236	0.6775

(b)

$\text{Pr} = 0.1$, $\text{Re} = 6500 > \text{Re}_c$, $k = 2.166$, $\sigma_T = -0.1$

state	I_1	I_2	I_3	I_4	M_1	M_2	J_1	J_2
$f(x) = 0$	0.0325	0.5516	-0.0019	0.0845	0.0694	0.2996	0.2774	0.7489
Opti_1	0.0293	0.4992	0.0017	0.0842	0.0800	0.3043	0.3060	0.6929
Opti_2	0.0290	0.4932	0.0012	0.0836	0.0828	0.3089	0.3178	0.6811
Opti_3	0.0286	0.4684	-0.0023	0.0893	0.0940	0.3207	0.3447	0.6543
Opti_4	0.0284	0.4676	-0.0018	0.0895	0.0947	0.3203	0.3484	0.6505

(c)

$\text{Pr} = 13.9$, $\text{Re} = 700 < \text{Re}_c$, $k = 0.957$, , $\sigma_T = 0.1$

state	I_1	I_2	I_3	I_4	M_1	M_2	J_1	J_2
$f(x) = 0$	-0.0002	0.0079	0.0002	-0.0027	0.4918	0.4917	0.7756	0.1601
Opti_1	-0.0009	0.0112	0.0003	-0.0043	0.6260	0.3683	0.8599	0.1923
Opti_2	-0.0013	0.0095	0.0003	-0.0004	0.6233	0.3689	0.8905	0.1649
Opti_3	-0.0008	0.0105	0.0002	-0.0033	0.6224	0.3714	0.8669	0.1870
Opti_4	-0.0012	0.0097	0.0004	-0.0015	0.6240	0.3689	0.8717	0.1820

(d)

$\text{Pr} = 13.9$, $\text{Re} = 1000 > \text{Re}_c$, $k = 0.957$, $\sigma_T = -0.1$

state	I_1	I_2	I_3	I_4	M_1	M_2	J_1	J_2
$f(x) = 0$	-0.0008	0.0112	0.0009	-0.0049	0.5053	0.4889	0.8470	0.1829
Opti_1	-0.0003	0.0152	0.0011	-0.0102	0.4786	0.4822	0.7458	0.2079
Opti_2	-0.0003	0.0163	0.0010	-0.0122	0.4874	0.4777	0.7444	0.2114
Opti_3	-0.0005	0.0146	0.0006	-0.0092	0.4736	0.4936	0.7646	0.1878
Opti_4	-0.0005	0.0146	0.0006	-0.0092	0.4736	0.4936	0.7646	0.1878

The term in the energy budget that has grown the most is I_2, which, after optimization, represents more than half of the total production rate of perturbation energy, whereas the terms representing the suplly of mechanical of energy by thermocapillary effect slightly decrease, as displayed in table 5.3. This means that the heat flux imposed at the surface favored the inertial mechanism in the bulk rather than the surface mechanisms.

If we impose the positivity constraint ($f > 0$, Opti_2), the optimized flow differs slightly. Two distinct zones are heated, one close to the hot corner, and the other downstream from the middle of the free surface. These two zones correspond to the regions where the growth-rate sensitivity is positive (fig. 5.8b), suggesting that the sensitivity barely changed with the addition of the heat flux. Logically, the surface temperature is higher all along the free surface (fig. 5.14(a)), and the temperature difference with the uncontrolled case increases only in the vicinity of the region where the flux is imposed, as the Prandtl number is low.

The peak values of the imposed flux to obtain $\sigma_T = 0.1$ is nearly more than seven times higher than the one from Opti_1 close to the hot corner. Due to this large incoming heat flux, two local temperature maxima arise along the free surface. Therefore, the wall is even colder than a portion of the free surface and a counter flow forms close to the hot corner, as shown in fig. 5.15(f). Downstream from this first heated region, the flow is rapidly accelerating until $x = 0.95$. The velocity stays then nearly constant for roughly one third of the cavity length up to $x = -0.23$, before slowing down due to the local increase of temperature in the second zone of non-zero heat flux. The second increase of the temperature results in an increase shear stress close to the cold corner, since the gradient of temperature is higher. The velocity peak close to the cold wall is then more pronounced than in the uncontrolled case with a velocity magnitude of $|u_0| = 243$ compared to $|u_0| = 185$ in the adiabatic case.

While the terms related to the work done by the thermocapillary stresses M_1 and M_2 were decreasing in Opti_1, they are the terms in the energy budget which increased the most in Opti_2. In fact the contribution in the energy budget from the inertial terms decreased slightly. Therefore, the positive flux favored the thermocapillary effects over the inertial effects.

The third and fourth optimizations, using a different initial condition for $f(x)$ yielded similar results. In particular, the case Opti_4 ($f > 0$), has the same energy budget as Opti_2 up to the third digit.

Basic Flow Stabilization

In a similar way as for the flow destabilization, we consider a Reynolds number 18% larger than the critical Reynolds number, $\text{Re} = 6500 > \text{Re}_c = 5497$, and target a growth rate of $\sigma_T = -0.1$. The basic flows obtained when the surface is adiabatic ($\sigma = 2.39$), with a flux as obtained after Opti_1 and Opti_2 are shown in fig. 5.15.

Considering the first optimization Opti_1 in which the flux sign is not constrained, we find an optimal flux (fig. 5.15(a), dotted line) having a similar shape as the heat flux sensitivity but with an opposite sign. If the flux sign is constrained to be positive

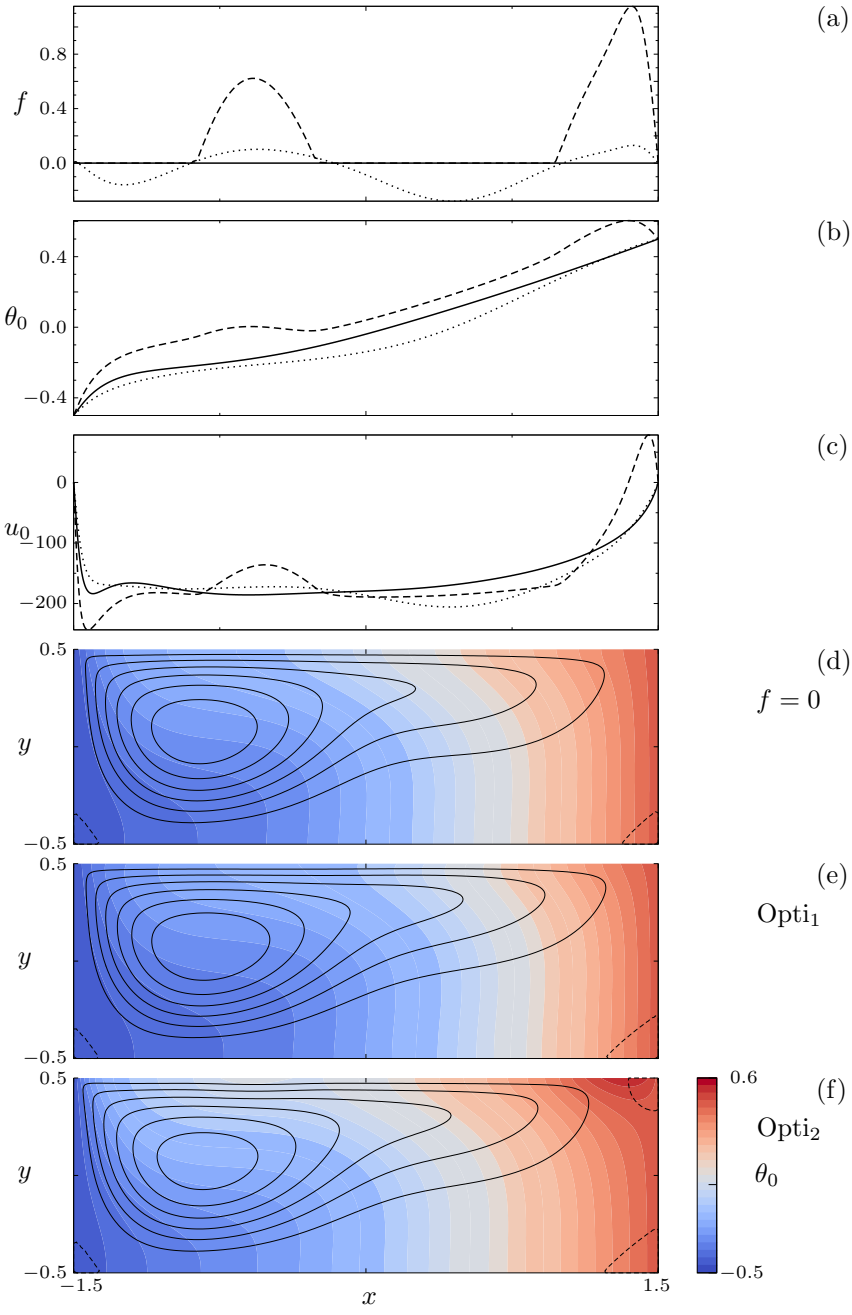

FIGURE 5.14 – Basic flows at different optimization stages for Pr = 0.1, Re = 4500 < Re_c. Surface heat flux (a), basic surface temperature (b) and basic surface velocity (c) with $f = 0$ and $\sigma = -2.74$ (solid line), and after Opti_1 (dotted line) and Opti_2 (dashed line) both for $\sigma_T = 0.1$. (d,e,f) show the basic temperature field (color) and streamlines (solid and dashed lines) for an adiabatic free surface, and for the flux after Opti_1 and Opti_2, respectively.

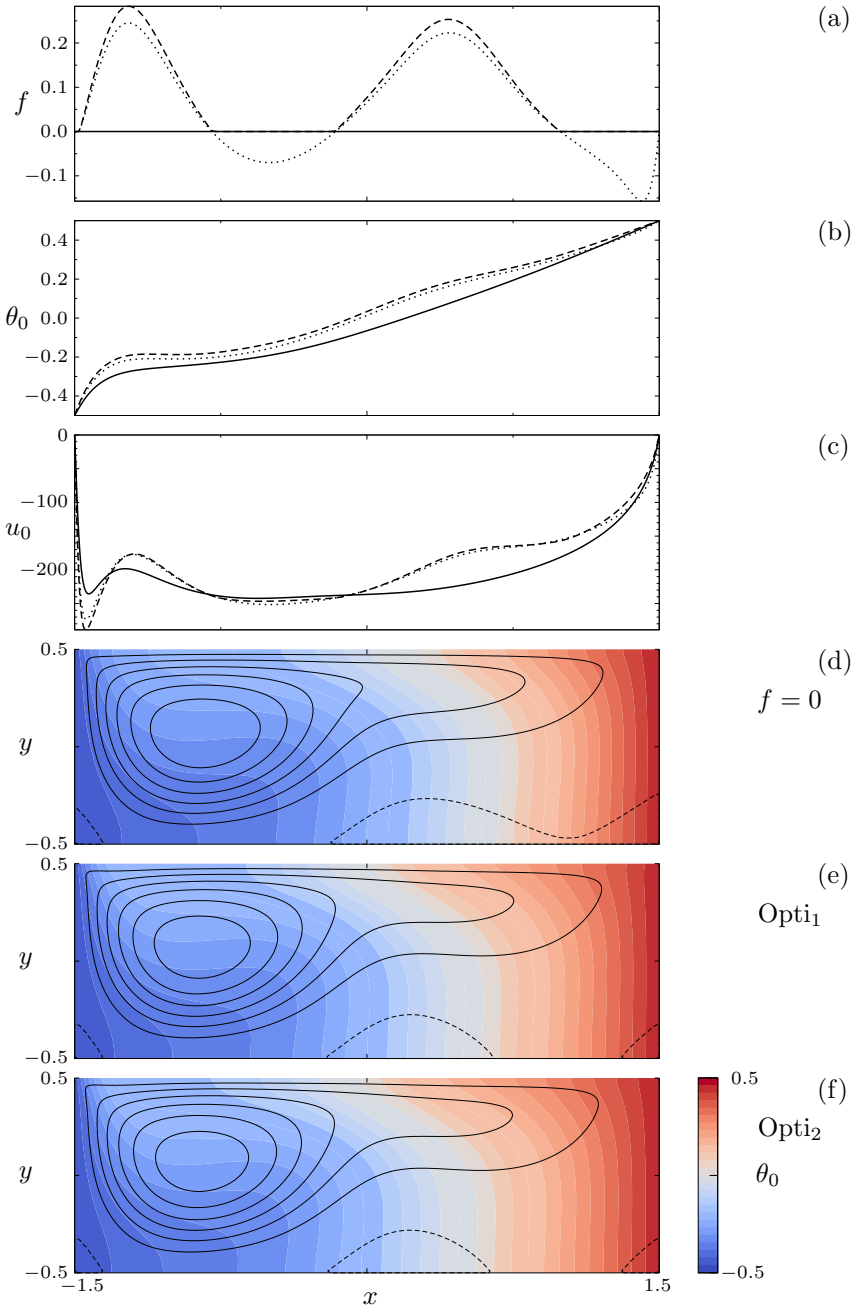

FIGURE 5.15 – Basic flows at different optimization stages with $\mathrm{Pr} = 0.1$, $\mathrm{Re} = 6500 > \mathrm{Re}_c$. Surface heat flux (a), basic surface temperature (b) and basic surface velocity (c) with $f = 0$ and $\sigma = 2.39$ (solid line), and after Opti_1 (dotted line) and Opti_2 (dashed line) both for $\sigma_T = -0.1$. (d,e,f) show the basic temperature field (color) and streamlines (solid and dashed lines) for an adiabatic free surface, and for the flux after Opti_1 and Opti_2, respectively.

(Opti_2), the flux is only slightly increased in the regions where the flux for Opti_1 was already positive. In both cases, the temperature at the free surface is increased. This results in a higher shear rate close to the cold corned, and slows down the flow along the hot part of the free surface (fig. 5.15(c)), where the surface velocity is almost 25% smaller as compared to the uncontrolled case. The velocity at the free surface after both optimizations is nearly identical.

As the temperature gradient along the free surface are reduced, one observes a weaker vortex in the hot half of the cavity. A consequence of this weaker flow is that the strong recirculation present at the bottom of the cavity in the adiabatic case (fig. 5.15(d)) splits in two parts in the controlled cases (e) and (f).

In table 5.3, one can see that on one hand the production rates of perturbation energy linked to the Marangoni effects have slightly increased. On the other hand, this is largely compensated by the decrease of the inertial posts in the budget, and in particular I_2. Therefore, this mechanism is less efficiently extracting the perturbation energy from the basic flow close to the cold wall (not shown).

For the present small Prandtl number, the heat flux required to stabilize the flow for $\text{Re} > \text{Re}_c$ is smaller in magnitude than the one needed to destabilize the flow for $\text{Re} < \text{Re}_c$. In case of only positive fluxes, the maximum of the optimal flux is about 1 for the destabilization while it is about 0.3 for the stabilization.

A variation of the first guess given to the optimization algorithm significantly affects the profile of the optimal solution f found by the BFGS algorithm. In Opti_3 and Opti_4 the initial flux is defined by $f_{\text{FG}}(x) = (\Gamma/2 - x)(x - \Gamma/2)/30$, with a maximum at $x = 0$ and $f(0) = 0.025$. The optimized basic flows are shown in fig. 5.16. The heat fluxes obtained are greater than zero for $x < 1.10$, and no changes of the sign of f is observed between the two maxima. The upstream maximum has now the largest magnitude whereas the downstream peak is lower as compared to Opti_1 and Opti_2 (fig. 5.15). The perturbation temperature at the free surface is then slightly higher and the velocity mismatch with the adiabatic case are also accentuated. The structure of the flow in the bulk does not change visibly, but one can see in the energy budget that the thermocapillary effects increased, while the inertial effects decreased even more. This underlines the dependence of the obtained flux to the initial guess, indicating the existence of multiple optima for this non-linear problem.

5.6.4 High Prandtl Number

To compute the fluxes and basic flows presented in this subsection for $\text{Pr} = 13.9$, the BFGS algorithm needed up to 13 iterations to decrease the cost function $\mathcal{J}(f)$ to less than 10^{-8}, in the case of flow destabilization. Equivalently, the target growth rate was achieved up to 4 digits. The number of iterations suggests that the structure of the flow at high Prandtl numbers depends more on the surface heat flux than at low Prandtl numbers. However, for flow stabilization, the algorithm needed only up to 6 steps to reduces the cost function to 10^{-12}, similar as for small Prandtl numbers, so the target growth rate was approached up to the 6th digit.

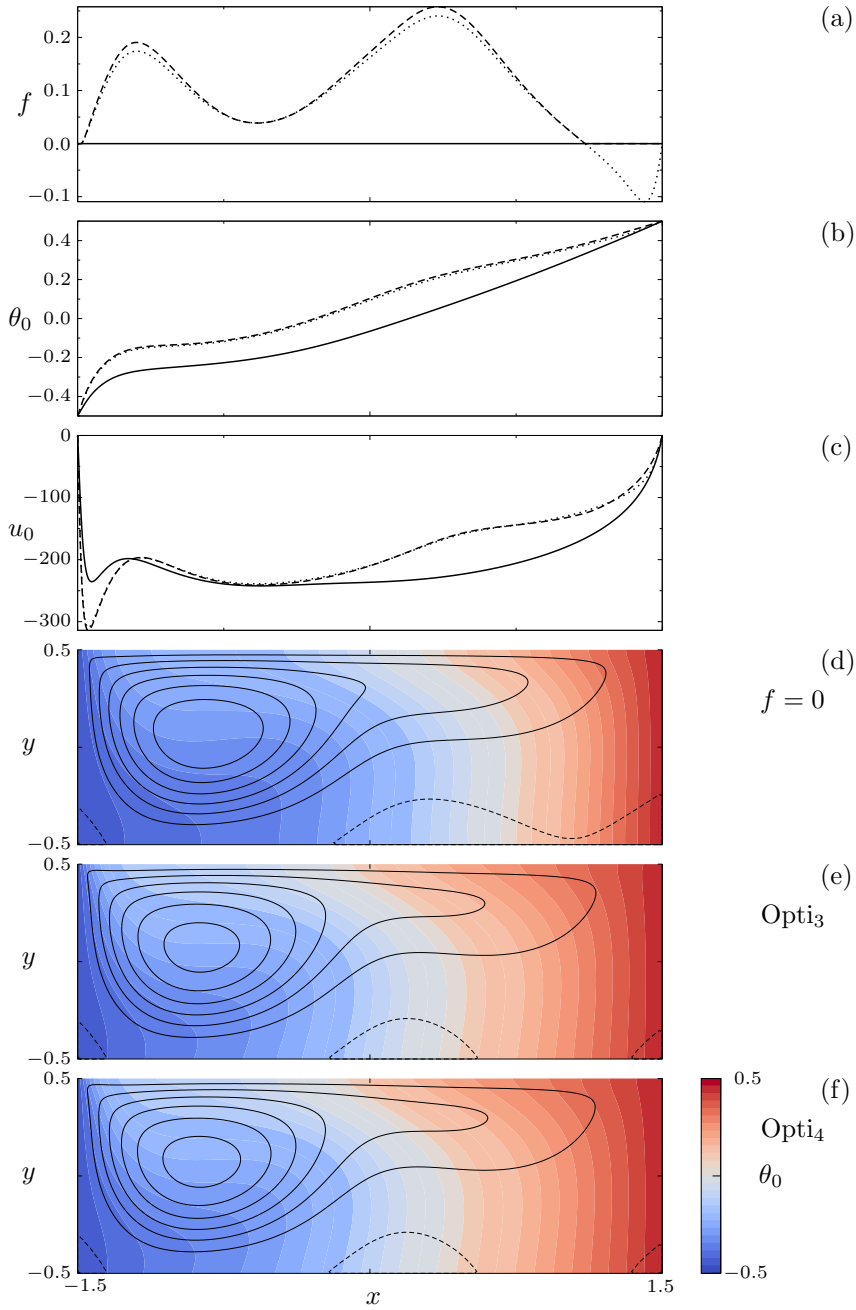

FIGURE 5.16 – Same as in fig. 5.15, but for Opti$_3$ and Opti$_4$ instead of Opti$_1$ and Opti$_2$.

Flow Destabilization

We consider now the flow for a higher Prandtl number Pr = 13.9, at a subcritical Reynolds number Re = 700 < Re_c = 882, which is 20% belowe the linear stability boundary. The basic flows obtained when the surface is adiabatic ($\sigma(f = 0) = -0.105$), with a flux as obtained after Opti_1 and after Opti_2 are shown in fig. 5.17. If we consider the results from Opti_1 (no particular constraint on the heat flux), we can see from fig. 5.17(a) that the heat flux obtained (dotted line) does *not* have the same profile as the flux sensitivity from fig. 5.13(b) (on page 99). Apparently the sign of the surface heat flux oscillates once more than the sign of sensitivity.

In fact, this is consistent with the appearance of a third co-rotating vortex in the basic flow which can be seen in fig. 5.17(e). The alternation of positive and negative flux close to the hot corner slightly accelerates the flow at the free surface. Afterward, the flux is positive again from $x = 0.77$ to $x = -0.03$ and the temperature increases, resulting into a thermocapillary shear in the positive direction opposing the basic flow. As a result, the main vortex near the hot wall shrinks. The same flux alternation repeats itself twice and two other smaller vortices are formed, visible in fig. 5.17 by the waviness of the streamlines. This leads to the existence of two hyperbolic points between the three vortices, and, therefore, higher temperature gradients around these points as explained earlier.

This change of the structure of the basic flow naturally affects the leading eigenvalue, albeit the general shape of the mode remains unchanged. The vortices of the most dangerous mode (subcritically unstable) are very similar to those shown in fig. 5.10. However, the angle made by the isotherms of the perturbations with respect to the cold wall diminishes and the mode becomes more oblique (not shown). This can also be seen from the energy budget: in the adiabatic case, M_1 and M_2 are almost equal. However, with the imposed heat flux, $M_1 > 0.60$ and $M_2 < 0.4$. M_2 represent the kinetic energy production due to the work done by the spanwise thermocapillary forces. Therefore the spanwise component of the perturbation is weaker at the free surface.

If one constrains the flux to be positive, a very large flux close to the hot corner appears, about ten times larger than the flux magnitude obtained by Opti_1. It is positive until $x = 1.34$, and the velocity magnitude grows until that same point. The velocity peak is slightly shifted in the negative direction in comparison to the adiabatic case. A after Opti_1, a stronger vortex but smaller in size is created near the hot wall, and two other co-rotating vortices are also created in the colder half of the cavity. Along the free surface, the temperature locally increases slightly due to the heat fluxes. Even though the controlling heat flux does not create opposing thermocapillary forces, the abrupt acceleration and deceleration of the flow at the free surface results in a waviness of the streamlines in fig. 5.17(f), similar as for Opti_1. Despite these differences, the energy budget stays the same as for Opti_1, and the durection of propagation of the most unstable mode is also a bit more oblique than in the adiabatic case.

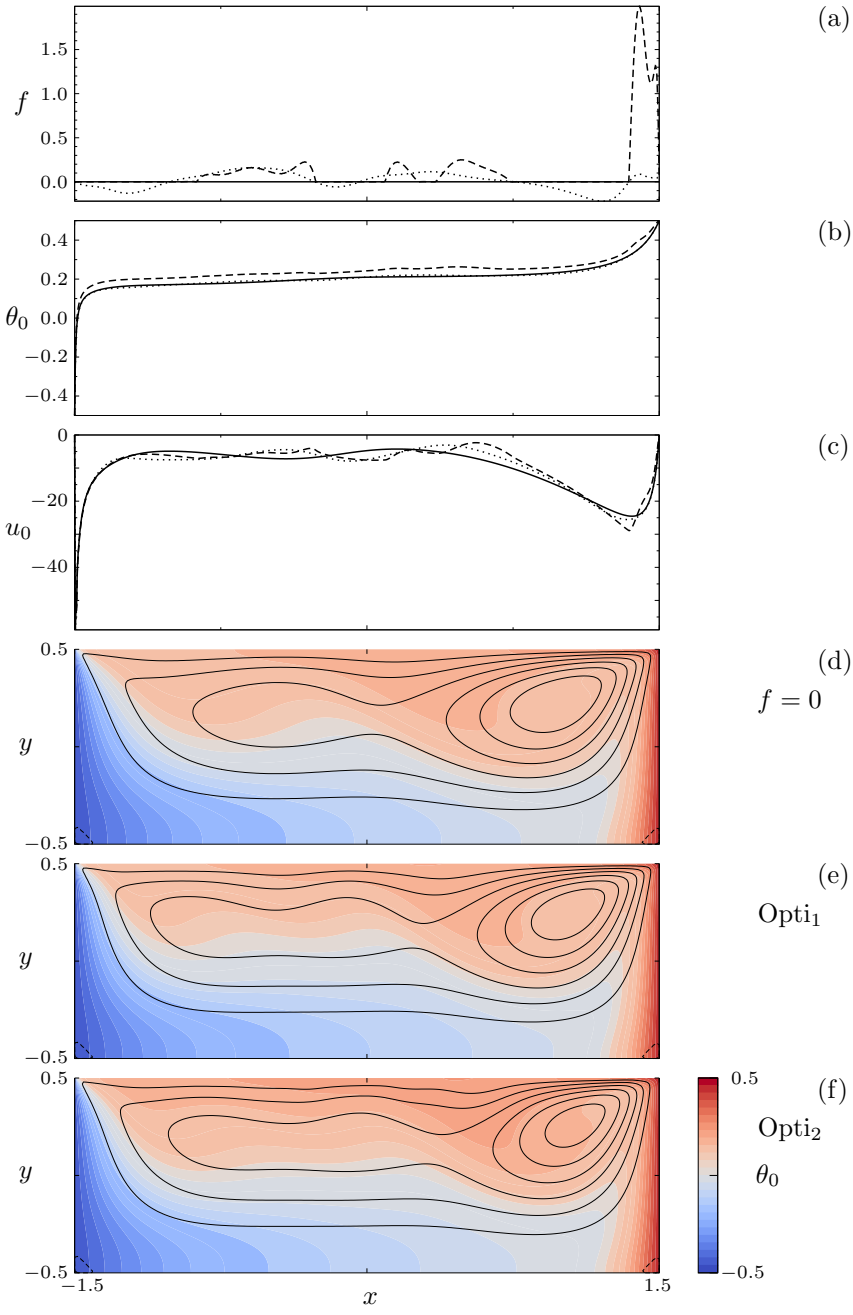

FIGURE 5.17 – Basic flows at different optimization stages with Pr = 13.9, Re = 700 < Re_c. Surface heat flux (a), basic surface temperature (b) and basic surface velocity (c) with $f = 0$ and $\sigma = -0.105$ (solid line), and after Opti_1 (dotted line) and Opti_2 (dashed line) both for $\sigma_T = 0.1$. (d,e,f) show the basic temperature field (color) and streamlines (solid and dashed lines) for an adiabatic free surface, and for the flux after Opti_1 and Opti_2, respectively.

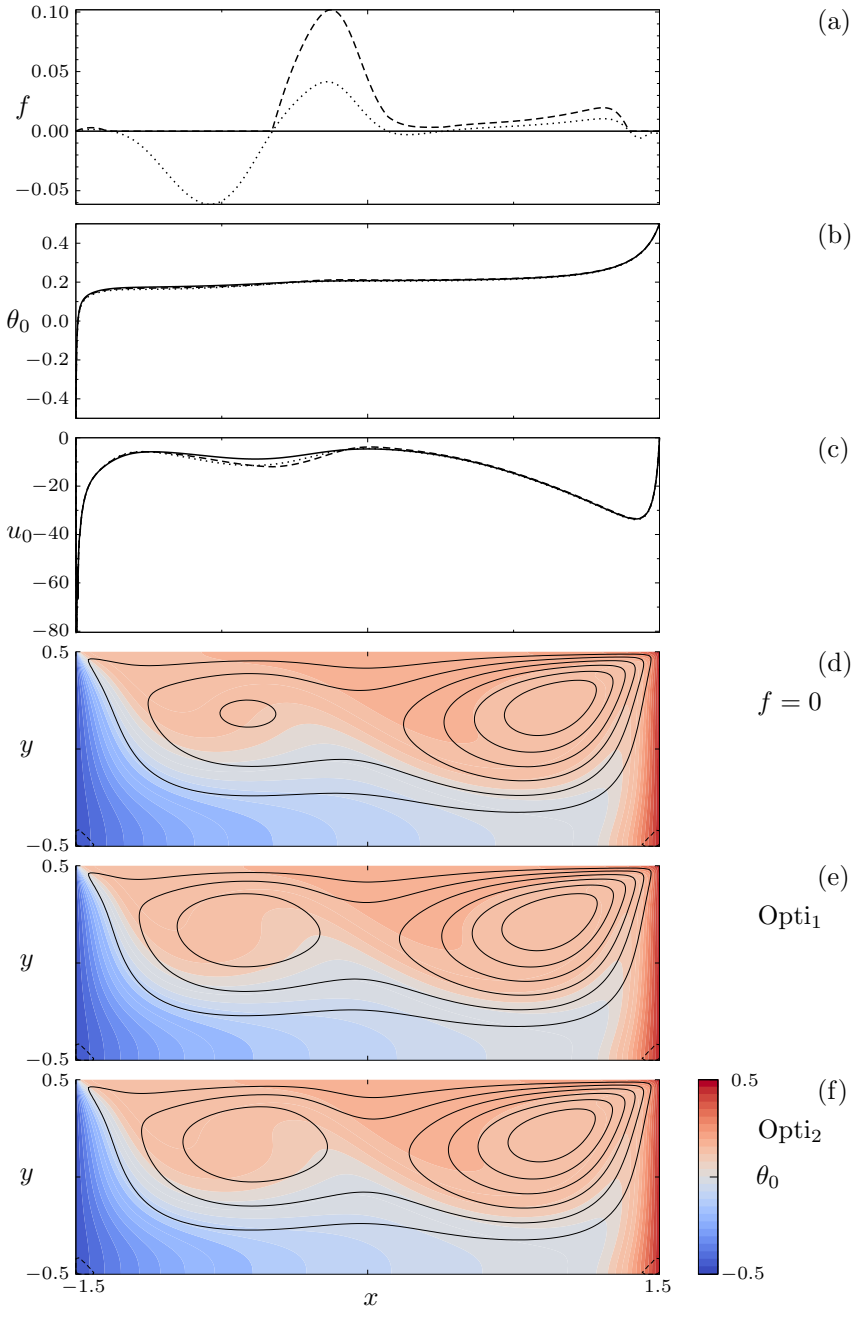

FIGURE 5.18 – Basic flows at different optimization stages with Pr = 13.9, Re = 1000 > Re_c. B. Surface heat flux (a), basic surface temperature (b) and basic surface velocity (c) with $f = 0$ and $\sigma = 0.053$ (solid line), and after $Opti_1$ (dotted line) and $Opti_2$ (dashed line) both for $\sigma_T - = 0.1$. (d,e,f) show the basic temperature field (color) and streamlines (solid and dashed lines) for an adiabatic free surface, and for the flux after $Opti_1$ and $Opti_2$, respectively.

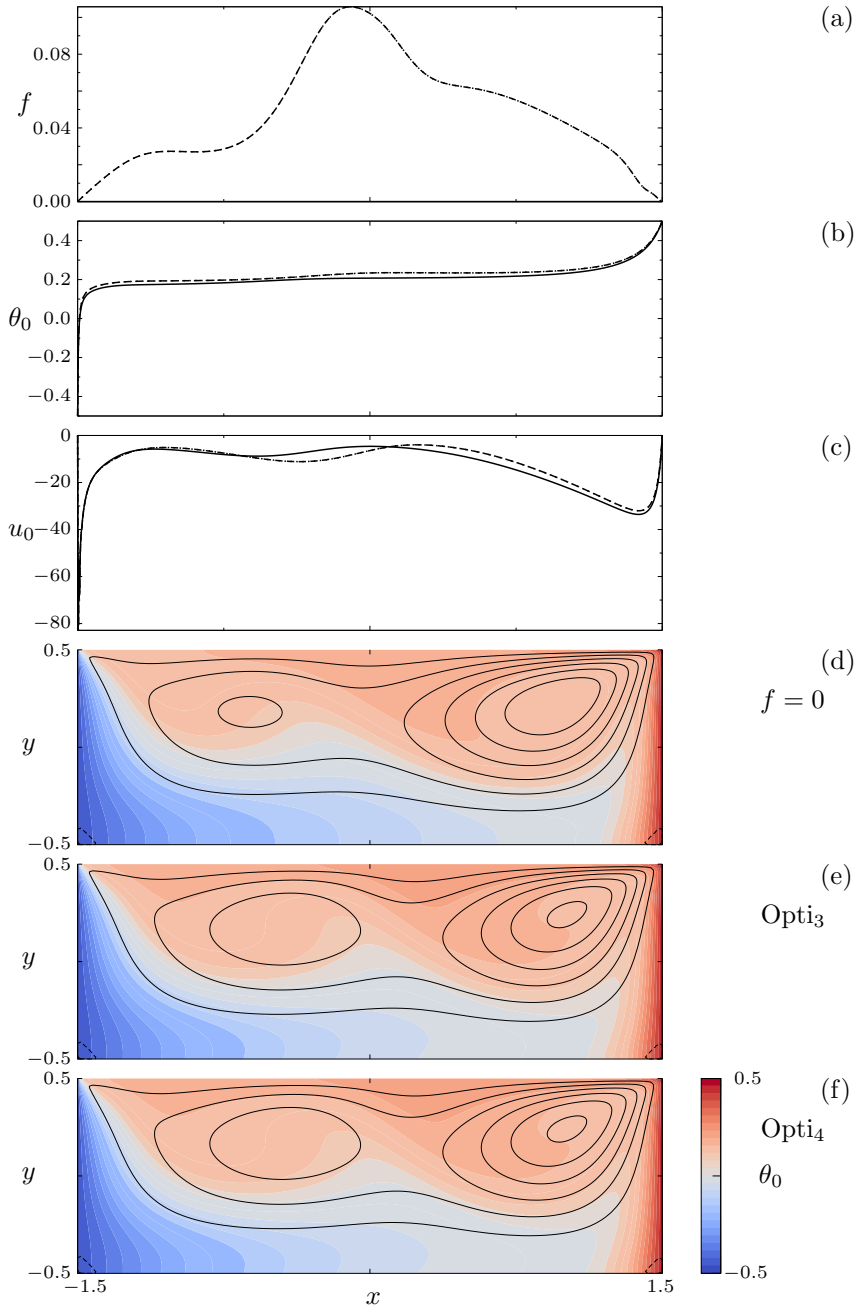

FIGURE 5.19 – Same as in fig. 5.18, but for Opti_3 and Opti_4 instead of Opti_1 and Opti_2.

Flow Stabilization

In a similar way as for the flow destabilization, we now consider a Reynolds number 13% larger than the critical Reynolds number, $\mathrm{Re} = 1000 > \mathrm{Re}_c = 882$, and a target growth rate of $\sigma_T = -0.1$. The basic flows obtained when the surface is adiabatic ($\sigma(f = 0) = -0.053$), with a flux as obtained after Opti_1 and after Opti_2 are shown in fig. 5.18.

Unlike in the destabilization case, the heat flux at the free surface (fig. 5.18) resembles very much the growth-rate sensitivity shown in fig. 5.13(b), and the controlled basic flow resembles the uncontrolled one. In particular the temperature at the free surface is nearly the same, see fig. 5.18(a). The same holds for the surface velocity, albeit the controlled flows accelerate slightly more above the weaker vortex in the cold half of the cavity. This vortex is then stronger in the controlled flow case. Looking at the energy budget in table 5.3 shows that the terms linked to the thermocapillary effect decreased slightly, and that the perturbation velocity is less efficient in producing the temperature perturbation *via* J_1.

When starting the optimization with a non-zero flux, we can obtain a substantially different flux. Although it still exhibits a peak of similar amplitude slightly downstream of the center of the surface ($x = 0$), the flux depicted in fig. 5.19(a) is only positive. In that case the temperature gradients along the free surface are lower in the hot half of the cavity, and the corresponding main vortex is weaker. On the other hand, the second vortex is slightly stronger and has grown in size.

5.7 Summary and Discussion

In this chapter, we first presented sensitivities of the growth rate of the most unstable mode for thermocapillary-driven flows in a shallow container at a low and a high Prandtl number. The instability mechanisms for both cases are different: at low Prandtl number a conjunction of inertial and surface mechanisms is responsible for the instability with the inertia effect dominating. At high Prandtl number only the thermocapillary effects are necessary to produce the hydrothermal wave, in which the temperature perturbations in the bulk are generated by a weak perturbation flow - driven by thermocapillarity. The growth-rate sensitivity of each of these modes with respect to small variation of the basic flow, small additional source terms, shear stresses and heat flux variation have been presented. We found that in both cases the sign of the sensitivity to small variations of the heat transfer changes along the surface.

Then we applied a sensitivity-based gradient descent method in order to obtain a surface flux that leads to a target growth rate of the most unstable mode, thereby shifting the linear stability boundary of the system. In a similar approach, Muldoon & Kuhlmann [114], Muldoon [112, 113] controlled the decay of two-dimensional oscillations in a cavity with aspect ratio $\Gamma = 8$, using an adjoint-based minimization method. They showed that two-dimensional perturbations could be suppressed using a time-dependent localized positive heat flux through an otherwise adiabatic free surface. However, the observable used in their minimization function consists of the tempo-

ral variation of the total kinetic energy, averaged over a given time horizon. Here, we directly controlled the linear stability of the two-dimensional flow with respect to three-dimensional perturbations and, therefore, do not need observables varying in time to quantify whether the system is destabilized or not. Besides, the cost function used to monitor the stability of the flow is much simpler in our case. However, a limitation of our approach is that it cannot cope with finite amplitude perturbations. However, for thermocapillary-driven cavities, the general stability problem including finite amplitude perturbations has not yet been addressed.

The present analysis has demonstrated the complexity and importance of the heat transfer on the stability of the basic flow. In particular, it was shown that there is no one-to-one correspondence between a positive heat flux and a destabilization or stabilization of the flow, since both can be achieved with a positive heat flux. Note that, although they are possible in principle, modal changes were not observed within this study. The least stable mode before and after the optimzation was always the same mode, although it was distorted by the changes of heat flux.

The impact of an imposed surface heat flux on a thermocapillary-driven cavity has not yet been comprehensively investigated. On the contrary numerous studies investigated the effect of heat transfer on the basic flow for the liquid bridge configuration and, eventually, some parallels can be drawn. To name only a few, Wang *et al.* [180] investigated the influence of a nearby heat source/sink on the structure of the basic flow and the onset of flow oscillations. Yasnou *et al.* [184] studied the impact of a co-axial gas flow for different gas temperatures on a liquid bridge made by a liquid of $\mathrm{Pr} = 13.9$. Both observed the formation of an additional vortex in the bulk of the flow when the free surface is heated, just like in fig. 5.17(e,f). This confirms the idea that, at high Prandtl numbers, the topology of the basic flow itself can be altered by heat transfer between the liquid and the external environment.

Concerning the stability of the liquid bridge under different heat-transfer condition, Yano *et al.* [183] reported a change of modes in the LB depending on the average heat flux through the free surface for very high Prandtl numbers. The hydrothermal wave seems to switch from propagating in the same direction as the surface flow when the heat flux is negative (heat loss) to an opposing direction when the heat flux is positive (heat gain). Moreover, linear stability analyses carried out by Shevtsova *et al.* [156] and, more recently, by Stojanovic & Kuhlmann [171] revealed dramatic changes of the flow stability in a liquid bridge under variations of the magnitude and direction of the velocity of a coaxial gas. The critical curve exhibit a very stiff slope as the axial flow changes direction, thereby passing from a overall positive to negative heat flux. Examining the sensitivity of the liquid bridge in theses condition could shed some light on the reasons of this abrupt changes of the stability of the system.

In general, heat transfer across the free surface is usually higher at the corners due to the thermal boundary layers present there. They can be very well seen for instance in Wang *et al.* [180], in their fig. 10, or in fig. 2 of Romanò & Kuhlmann [136]. The an importance fact is confirmed by our results: In the optimization process for high Prandtl, fluxes close to the corners were shown to be particularly important in the destabilization of the flow. This behavior would need to be confirmed for liquid bridges, although a similar behavior can be anticipated. If one simulates only the

liquid phase and not the surrounding gas, it is particularly important to take the high heat transfer near the corners into account, since they can dramatically affect the stability of the basic flow.

In this regard, our results confirm the importance of an accurate modeling of the heat transfer accross the free surface in order to be able to compare with experiments. Therefore, the attempt of modeling the heat flux though fits of a flux function obtained from two-phase simulations of a liquid bridge in a cooling chamber by Romanò & Kuhlmann [136] is a significant step forward. A possible extension of this modeling approach could be to identify the regions of importance for the flow dynamics through a sensitivity analysis, and weight the error of the fit with the sensitivity magnitude.

6

Stability Analysis of a Cubic Shear-Driven Cavity

6.1 Introduction

In this chapter, we will study the progressive destabilization of the incompressible flow in a cubic cavity, driven at its top by a constant shear stress. Although this setup has barely been considered in the literature, we will first comment on the its similarities with various problems, depicted in fig. 6.1: thermocapillary driven cavity for low-Prandtl-number fluids, liquid filled cavity driven by an external flow, the flow over an open cavity, and finally the lid-driven cavity. The progressive destabilization of the flow in a cubic lid-driven cavity has been investigated extensively and therefore we shall mainly compare with this last setup.

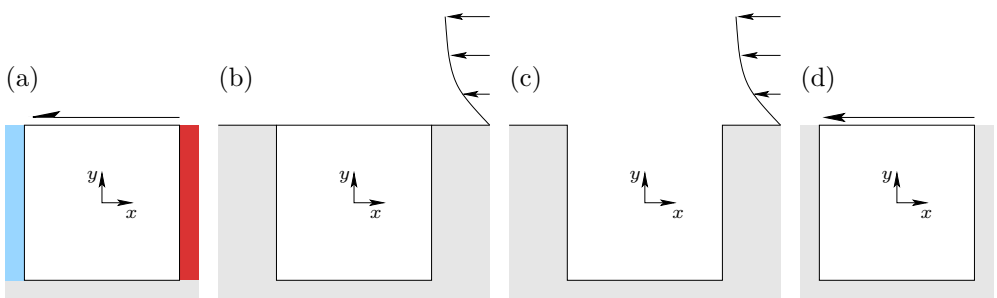

FIGURE 6.1 – Setups similar to the shear driven cavity: thermocapillary driven flow in a cavity (a), flow over a filled cavity (b), flow over an open cavity (c) and flow in a lid-driven cavity (d).

6.1.1 Similar Setups

Thermocapillary-Driven Flows at Low Prandtl Numbers

A thermocapillary-driven flow in a cavity filled by a liquid with a Prandtl number tending to zero and where the free surface is adiabatic, is equivalent to a cavity driven by a constant shear. In fact the temperature is linearly distributed between the hot and cold wall and the temperature gradient is then constant. Assuming that the surface tension varies linearly with the temperature, the shear stress generated by the temperature gradient is then constant along the surface (see Chapter 5, subsection 5.5.1). Consistent with this analysis, Hadid & Roux [65] investigated shallow cavities and layers for low Prandtl number and found that the two-dimensional basic flow was stable to two-dimensional perturbations at $\mathrm{Re} = 3 \times 10^4$ for $\mathrm{Pr} = 0$. Later Schimmel *et al.* [146] provided the critical curves for a cavity infinitely extended in its spanwise direction, driven by a constant shear stress and draw a parallel between this case and the lid-driven cavity. In both cases, for cavities of square cross sections, the flow is unstable to centrifugal instabilities with a high wave number.

Although Cartesian geometries were rarely investigated, axisymmetric setups received much more attention. For liquid bridges (already presented in Chapter 5), the top and bottom walls are heated and cooled, respectively. A nearly cylindrical geometry is maintained due to a high surface tension, and variations of surface tension along the free surface drive the flow. Wanschura *et al.* [181] found that the flow becomes unstable to a mechanical instability at vanishing Prandtl numbers, and would re-stabilize as the Prandtl number is increased. Levenstam *et al.* [91] performed both linear stability analysis and three-dimensional simulations and found that for $\mathrm{Pr} < 0.585$ the flow axisymmetric flow becomes three-dimensional at $\mathrm{Re} \approx 2000$ and oscillates at $\mathrm{Re} = 6000$. Motegi *et al.* [111] further investigated the secondary oscillatory flow by means of a Floquet analysis.

Flow over a Liquid-Filled Open Cavity

The liquid flow in a cavity driven by a gas stream is a comparable problem, provided that interface is non-deformable. The liquid in the cavity is then put in motion by the shear exerted by the gas on the liquid at the surface. In the context of Stokes flows, Schönecker & Hardt [151] derived an analytical solution for transverse and longitudinal flow over a cavity filled with an immiscible fluid. Interested by crystal growth applications Kalaev [72] investigated the gas stream over a cubic cavity filled with a liquid. Kalaev [72] was interested in the temporal behavior of the flow and in roughly quantifying the transition to turbulence. They quantified their results with a dimensionless number DN which will turn out to be our definition of the Reynolds number. Considering higher Reynolds numbers, van Eckeveld *et al.* [48] studied experimentally cavities partially filled with water in pipe subject to a dry air flow. The main focus was to to reduce the acoustic noise (pipe whistling) linked to vortex shedding from the downstream edge of the cavity.

Flow over an Open Cavity

The flow over an open cavity has first received attention in the 60's in the context of compressible flows and its acoustic properties. Experimentally Rossiter [139] showed that there was an acoustic mechanism resulting from the interaction of a shear layer with the downstream corner of the cavity. A two-dimensional Kelvin-Helmholtz instability is initiated at shear layer at the top of the cavity and vortices are shed from the downstream edge. He gave an empirical formula to predict the frequency of resonance. Depending on the boundary layer momentum thickness, the aspect ratio and the Reynolds number, and at low Mach number, different modes can be unstable. We refer to Brés & Colonius [27] who performed a linear stability analysis study at Ma = 0.3 and 0.8 for the system infinitely extended in the spanwise direction and is probably the most complete study on that subject. In particular they found that for a square cavity, the basic flow is unstable to modes with a high wave number. These modes are formed by vortices, similar to the Taylor Görtler vortices from the lid-driven cavity. This result could be reproduced numerically for instance by Alizard *et al.* [7] or Citro *et al.* [38] for incompressible flows.

Faure *et al.* [52, 51] investigated this instability experimentally in a cavity of various streamwise aspect ratios and of spanwise aspect ratio 6. They observed mushroom-like structures corresponding to these modes. Later Picella *et al.* [126] reproduced numerically the flow in the same cavity configuration. They observed the same patterns and spanwise recirculation structures and studied the successive Hopf bifurcations in this setup. In the context of urban canyons, [140] investigated a cubic cavity with spatially constant flow imposed at its to boundaries with a RANS turbulence model. They observed a mean flow symmetric with respect to its midplane and focused on the flow structure in view of pollutant dispersion in the canyon.

Flow in a Cubic Lid-Driven Cavity

In the previous chapters, we stressed the importance of the *lid-driven cavity* in fluid mechanics as it serves as a canonical benchmark for computational codes, exhibits complex flow patterns and shows a non-trivial dynamical evolution to turbulence. To avoid too many repetitions we refer to Chap. 4 for the historical perspective and the linear stability analysis of the infinitely extended systems. Of interest for this chapter is the cubic lid-driven cavity. The onset of linear instability has first been investigated by Feldman & Gelfgat [55] who found that the basic flow becomes unstable to oscillating perturbations at $Re \approx 1920$. The perturbations saturate and the system settles on a limit cycle. In other words, the systems loses its stability through a Hopf bifurcation. However, the scenario turned out to be more complicated as Kuhlmann & Albensoeder [85] pointed out that the Hopf bifurcation was slightly subcritical and subject to non-linear bursts when a sufficiently long time integration was performed (several viscous time units). Loiseau *et al.* [100] reproduced this result and showed that a second limit cycle was approached during the non-linear bursts. Using the fact that the oscillations and the basic flow are satisfying a mirror symmetry, Lopez *et al.* [101] could identify the complete bifurcation scenario for $\mathrm{Re} < 2100$ including the unstable limit cycles using edge state tracking [148, 68]. First, the flow bifurcates with a subcritical Hopf

bifurcation and saturates in a limit cycle. This limit cycle also bifurcates with an even more subcritical Neimark-Sacker bifurcation. The complex dynamics between these two limit cycle is characterized by bursts that break the mirror symmetry. The transition to turbulence is characterized by these intermittent bursts and follows a Pomeau–Manneville scenario [130].

6.1.2 Objectives

In this chapter, we will study the incompressible flow in a cubic cavity, driven at its top surface with a constant shear. We can expect that the flow will be destabilized by a similar mechanism as in the lid-driven cavity due to the similar structure of the basic flow, and because similar modes are obtained for the different setups discussed earlier.

The aim of this chapter is to obtain the sequence of bifurcations the flow undergoes by combining linear stability analysis and non-linear simulations. Of interest are the characteristics of the unstable modes and their relations to their lid-driven counterparts. Moreover, we want to state whether or not the scenario of transition to turbulence is the same as for the cubic lid-driven cavity, and whether we should expect other cavity setups to follow similar scenarii.

In a first section, we will define the setup and the mathematical models that we will be using. In a second section, we will validate the solvers against the results available for the cubic lid-driven cavity. Then the three-dimensional linear stability results will be presented and discussed in terms of symmetries. Finally, we will carry out a detailed analysis of the non-linear evolution upon increasing the strength of the driving.

6.2 Mathematical Formulation

6.2.1 Problem Definition

We consider the flow of an incompressible Newtonian fluid with density ρ and kinematic viscosity ν in a cubical cavity of side length L (fig. 6.2). The flow is driven by a constant stress $\tau > 0$ imposed on one face of the cube and aligned with the cube's edges, while the remaining boundaries are rigid.

Using the scales L, ν/L, L^2/ν and $\rho\nu^2/L^2$ for length, velocity, time and pressure, and a cartesian coordinate system with origin in the centre of the cavity, the domain occupied by the fluid is $V = [-1/2, 1/2]^3$ and the Navier–Stokes and continuity equations are

$$(\partial_t + \boldsymbol{u} \cdot \nabla)\, \boldsymbol{u} = -\nabla p + \nabla^2 \boldsymbol{u}, \tag{6.1a}$$

$$\nabla \cdot \boldsymbol{u} = 0. \tag{6.1b}$$

A constant stress acting in negative x direction is imposed on the boundary at $y = 1/2$

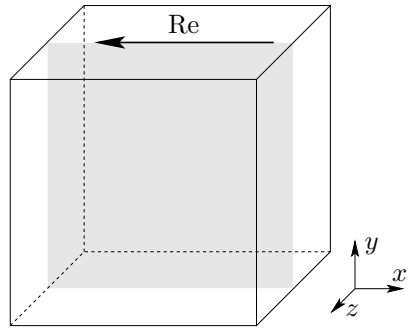

FIGURE 6.2 – Schematic of the cubical cavity. The grey square indicates the mirror-symmetry plane $z = 0$.

such that

$$\left.\begin{aligned} \partial_y u &= -\mathrm{Re} \\ v &= 0 \\ \partial_y w &= 0 \end{aligned}\right\} \quad \text{on } y = 1/2, \tag{6.2a}$$

while no-slip and no-penetration conditions are imposed on the remaining boundaries of the cavity

$$\boldsymbol{u} = \boldsymbol{0} \quad \text{on } x = \pm 1/2,\ y = -1/2,\ \text{and } z = \pm 1/2. \tag{6.2b}$$

The Reynolds number directly proportional to the strength of the stress is defined as

$$\mathrm{Re} = \frac{\tau L^2}{\rho \nu^2}. \tag{6.3}$$

It is the square of the conventional shear-stress Reynolds number $\mathrm{Re}_\tau = \sqrt{\tau/\rho} L/\nu$ based on the friction velocity $\sqrt{\tau/\rho}$.

The problem is invariant in time and mirror-symmetric with respect to the plane $z = 0$. Thus, the basic flow at low Reynolds number is expected to be steady and mirror-symmetric. We are interested in the linear stability of this basic flow and the nonlinear flow above the threshold Re_c at which the symmetry will be broken spontaneously.

6.2.2 Linear Stability Analysis of the Steady Basic Flow

The classical road to quantify the linear stability of a dynamical system is to first solve for the basic flow $\boldsymbol{q}_0 = (\boldsymbol{u}_0, p_0)$ which satisfies the steady Navier–Stokes equations

$$\boldsymbol{u}_0 \cdot \nabla \boldsymbol{u}_0 = -\nabla p_0 + \nabla^2 \boldsymbol{u}_0, \tag{6.4a}$$

$$\nabla \cdot \boldsymbol{u}_0 = 0, \tag{6.4b}$$

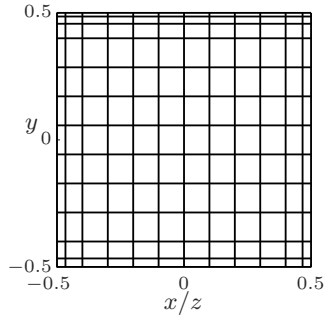

FIGURE 6.3 – $12 \times 12 \times 12$ tensor-grid mesh employed, with refined surface elements at the boundaries.

subject to the boundary conditions (6.2). However, one can eventually be interested in the subspace of mirror-symmetric basic flows and impose a symmetry condition on the midplane

$$\frac{\partial u_0}{\partial z} = 0, \quad \frac{\partial v_0}{\partial z} = 0, \quad w_0 = 0, \quad \text{at } z = 0. \tag{6.5}$$

Once $\boldsymbol{q}_0 = (\boldsymbol{u}_0, p_0)$ has been obtained, small perturbations $\boldsymbol{q}' = (\boldsymbol{u}', p')$ are considered. They are solutions of the linearized Navier–Stokes equations

$$(\partial_t + \boldsymbol{u}_0 \cdot \nabla) + (\boldsymbol{u}' \cdot \nabla)\, \boldsymbol{u}_0 = -\nabla p + \Delta \boldsymbol{u}, \tag{6.6a}$$

$$\nabla \cdot \boldsymbol{u}' = 0, \tag{6.6b}$$

and they must satisfy the boundary conditions

$$\partial_y u' = v' = \partial_y w' = 0 \quad \text{on } y = 1/2, \tag{6.7a}$$

$$\boldsymbol{u}' = 0 \quad \text{else.} \tag{6.7b}$$

Using the normal mode ansatz one obtains the eigenvalue problem described in section 2.3.2. For the perturbation modes, we never enforce symmetries.

6.3 Numerical Methods

6.3.1 Time-Dependent Flow

The time-dependent flow is computed using the spectral-element solver `Nek5000`, with an *ad-hoc* refinement of the elements close to the edges of the cavity as shown in Fig. 6.3. The elements at the free surface have been refined in order to better capture the strong variations of the velocity at the surface as a result of the imposed shear stress. The discontinuities in the first derivative at the top edges due to the jump in the boundary condition naturally slow down the convergence of the unsteady solver. For the spatial discretization, the $\mathbb{P}_N/\mathbb{P}_{N-2}$ formulation for the velocity/pressure is used employing Lagrange polynomials defined on the Gauss-Lobatto-Legendre quadrature

TABLE 6.1 – Critical Reynolds and frequencies for the flow in a cubic lid-driven cavity reported in literature.

Ref.	Method	$\mathrm{Re}_{\mathrm{lid},c}$	ω_c
Feldman *et al.* [55]		1914	1100.55
Kuhlmann *et al.* [85]		1919.5	1124.83
Gelfgat [61]		1919.4	1124.96
Lopez *et al.* [101]		1928.9	1124.93
Loiseau *et al.* [100]		$\mathrm{Re}_{\mathrm{lid},c} \in [1900, 1930]$	1123.2
Present	time marching	$\mathrm{Re}_{\mathrm{lid},c} \in [1918.5, 1919]$	1125.59
Present	eigenvalue solver	1918.75	1125.56

points of degree $N = 6$, on a tensor grid mesh of $12 \times 12 \times 12$ elements (fig. 6.3). Time integration is accomplished using the BDF3/EXT3 scheme, see Chapter 3 for more details. The time step was selected in order to keep at all times the Courant number $C \leq 0.5$. This leads, for $\mathrm{Re} = 57300$, to a time step $\Delta t \approx 1.2 \times 10^{-6}$.

To verify the solver the shear-boundary condition on $y = 1/2$ is replaced by a lid moving with constant velocity U_{lid} and we consider the Reynolds number of the lid-driven cavity $\mathrm{Re}_{\mathrm{lid}} = U_{\mathrm{lid}} L/\nu$. The critical Reynolds number is compared with literature. The critical Reynolds number is bracketed by running the solver to obtain the largest Reynolds number for which the flow remains steady and the lowest Reynolds number for which the flow is oscillatory. In a first step, the flow is computed for $\mathrm{Re}_{\mathrm{lid}} = 1900$ at which only one steady solution exists. Then the Reynolds number is gradually increased with a small increment $\Delta Re = 1$ using the `BoostConv` algorithm with a $\mathrm{BDF}_2/\mathrm{EXT}_2$ time-integration scheme until the time derivative of the total kinetic energy drops below 10^{-4}. In this way, the systems approaches the steady equilibrium, but does not completely remove the oscillations. In a second step, we run the unsteady solver with a $\mathrm{BDF}_3/\mathrm{EXT}_3$ time-integration scheme: as the time-integration scheme is different and the residual not too small, small perturbations in the flow are triggered. The evolution of this perturbation is monitored *via* the kinetic energy of the total flow during one time unit. Depending on the growth or decay of the oscillations, an estimation of the critical Reynolds number is obtained.

The reason why we used the second-order time integration scheme for the steady computations, is that we noted a numerical instability of the algorithm for third order time integration. The solution blows up less than 10 iterations after the flow corrections from the `BoostConv` algorithm. Therefore, we used only second-order time-scheme for finding the steady solution, which avoids low order dissipation errors and the numerical instability. The reason of this instability is not clear, but we note as well that in the original paper [39], only second-order time-integration is successfully tested. However, for lower Reynolds numbers, the third-order time-integration scheme seems to be stable (see Chapter 3).

The results obtained are compared in Table 6.1 with data for the critical Reynolds number available in the literature. The present results agree very well with the results of Kuhlmann & Albensoeder [85] and Gelfgat [61]. These studies are also the most

accurate, since they used a spectral method with a 128^3 tensor grid combined with a singularity subtraction method and a finite volume method with 256^3 grid points, respectively.

6.3.2 Steady Flow

To obtain the basic steady flow $(\boldsymbol{u}_0^{\mathrm{T}}, p_0)^{\mathrm{T}}$, the governing non-linear system of equations is solved using the `BoostConv` algorithm, recently proposed by Citro *et al.* [39], presented in Chapter 3. The `BoostConv` algorithm can be implemented on the basis of the time-dependent solver with minor changes only. It allows to track three-dimensional steady flow states, regardless of their stability. For all calculations we use a Krylov space dimension of $\dim(\mathcal{K}) = 10$ and a second-order time-integration scheme.

Although we found the `BoostConv` algorithm to be able to also track steady states unstable to non-oscillating perturbations, we enforce a mirror-symmetry boundary condition on the midplane in order to track the steady mirror-symmetric solution which first destabilizes as we will see later. Therefore, we enforce the additional boundary condition (6.5). Equations (6.4) are only solved for half of the domain and the flow is reconstructed by mirror symmetry. In that case, the `BoostConv` algorithm is not used and this enables us to use a third-order time integration scheme and bypass the numerical instability issue. When this approach is not possible, *i.e.* if the symmetric basic flow is found to be unstable, the `BoostConv` algorithm is employed.

6.3.3 Linear Stability

In the classical approach to linear stability, the generalized eigenvalue problem (2.12) is solved. However, the size of the discretized eigenvalue problem is usually too large to be solved directly by assembling the matrix of the discretized linearized problem. In this case, we solve the eigenvalue problem using a time marching technique, described in Chapter 3.

To verify the implementation of the linear stability analysis we consider again the lid-driven cube. The basic flow is obtained using the `BoostConv` algorithm with a time step between two iterates of $\Delta t = 7 \times 10^{-4}$ and a Krylov space dimension of 10. For the eigenvalue solver, we use a Krylov space of dimension $dim(\mathcal{K}) = 400$. To define the propagation operator, we use $\Delta t = 3.5 \times 10^{-4}$. As this Krylov space dimension is already large enough, no restart is needed from the implicitly restarted Arnoldi-method which is then equivalent to the classical Arnoldi method. The leading eigenvalues for three Reynolds numbers are reported in table 6.2. Quadratic interpolation to zero yields the critical Reynolds number indicated at the last line of table 6.1. As the critical Reynolds number is agreeing very well with the results from literature and, in particular, with those of [85] and [61], the steady solver and the eigenvalue solver can be considered verified.

TABLE 6.2 – Eigenvalues for specific Reynolds numbers.

$\mathrm{Re}_{\mathrm{lid}}$	σ_1	ω_1
1915	-0.891073	1123.81876
1918	-0.178565	1125.21944
1920	0.296443	1126.15033

6.4 Results

The basic state $\boldsymbol{q}_0 = (\boldsymbol{u}_0, p_0)^{\mathrm{T}}$, denoted S1 in fig. 6.4, is steady with symmetry $\boldsymbol{q}_0(\boldsymbol{x}, t) = \boldsymbol{q}_0(\boldsymbol{x}, t + t')$ with t' arbitrary. It also satisfies the spatial (mirror) symmetry, and we define the mirror symmetry map $\mathcal{M}$

$$\mathcal{M} : (u_0, v_0, w_0, p_0)\,(x, y, z) \to (u_0, v_0, -w_0, p_0)\,(x, y, -z)\,. \tag{6.8}$$

When the mirror symmetry is preserved, the spanwise velocity on the midplane should be identically zero: $w(z = 0) = 0$.

The basic flow can lose its stability by breaking of either the translational invariance in t, the spatial symmetry (6.8), or both. From the linear stability equations, perturbations of the symmetric basic state must either be mirror-symmetric, satisfying the same spatial symmetry $\mathcal{M}$ as the basic flow, or they are antisymmetric, satisfying

$$(\hat{u}, \hat{v}, \hat{w})\,(x, y, z) = (-\hat{u}, -\hat{v}, \hat{w})\,(x, y, -z)\,. \tag{6.9}$$

In order to quantify symmetry breaking we measure the deviation from the mirror symmetry by

$$\mathcal{S} = \frac{1}{2E} \int_V |\mathcal{M}(\boldsymbol{u}) - \boldsymbol{u}|^2 \mathrm{d}V, \tag{6.10}$$

where the total kinetic E energy is defined by

$$E = \frac{1}{2} \int_V |\boldsymbol{u}|^2 \mathrm{d}V. \tag{6.11}$$

The criterion $\mathcal{S}$ is the ratio of the kinetic energy which corresponds to the asymmetry over the total kinetic energy. This criterion is the same as defined by Lopez *et al.* [101]. However, they used a spectral method with Chebishev polynomials. These polynomials can be sorted into even and odd polynomials. Using the fact that the even polynomials are symmetric by design, one can consider only the odd polynomials to evaluate the integral in (6.10) and readily obtain $\mathcal{S}$. In SEM with Nek5000, we used a symmetric tensor grid and created a new communication map for the MPI processes to get the symmetrically opposed elements. This is, in comparison to the spectral method, not so straightforward to implement.

As the Reynolds number is increased, the basic flow becomes unstable and a sequence of instabilities can be identified. The relation and naming convention of the different bifurcation points and solutions found are sketched qualitatively in fig. 6.4.

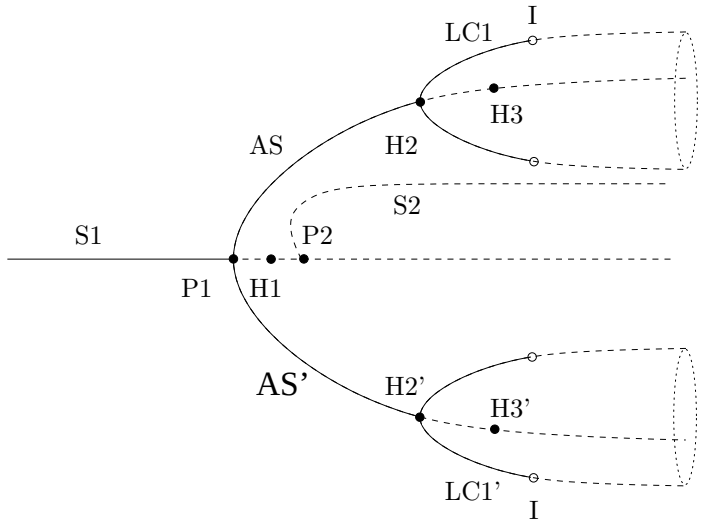

FIGURE 6.4 – Sketch of critical points and bifurcating solutions. Linearly stable solutions are indicated by full lines, unstable ones by dashed lines. S1 is the mirror-symmetric steady state, stable until a pitchfork bifurcation P1 where it becomes unstable to a non-oscillating anti-symmetric mode $\hat{\boldsymbol{q}}_{\mathrm{P1}}$. After saturation of the mode, the system reaches an asymmetric steady state AS or its anti-symmetric counterpart AS'. Upon increase of the Reynolds number, S1 loses its stability with respect to an oscillating mode $\hat{\boldsymbol{q}}_{\mathrm{H1}}$ at the Hopf Bifurcation H1. S2 is a mirror-symmetric steady state, originating from the pitchfork bifurcation P2. S2 is stable only in the subspace of mirror-symmetric solutions. The asymmetric steady state AS (resp. AS') is stable until a Hopf bifurcation H2 (resp. H2') where it becomes unstable to an oscillating mode $\hat{\boldsymbol{q}}_{\mathrm{H2}}$ (resp. $\hat{\boldsymbol{q}}_{\mathrm{H2'}}$). As the oscillations saturated, the system settles on a limit cycle LC1 (resp. LC1'). Upon increasing the Reynolds number AS (resp. AS') becomes unstable to a second oscillating mode $\hat{\boldsymbol{q}}_{\mathrm{H3}}$ in a Hopf bifurcation H3 (resp. H3'). The limit cycles LC1 and LC1' destabilize in I and a complex dynamics between the two limit cycles arises.

6.4.1 Stability of the Symmetric Basic Flow

Basic Flow Structure at Re = 53450

The basic flow structure before loss of symmetry is very similar to the one observed in the cubic cavity [55]. At Re = 53450, the flow at the top accelerates as it leaves the upstream edge, reaching maxima of velocity magnitude of $\max|\boldsymbol{u}_0| = 1863.9$ at $(x, y, z) = (-0.380, 0.5, \pm 0.449)$. The maxima are located close to the downstream top edge. The average free-surface velocity is $\boldsymbol{u}_{\mathrm{avg}} = (-1278.8, 0, 0)^{\mathrm{T}}$. The main characteristic of the flow is a core vortex aligned with the spanwise direction, best seen in fig. 6.5(c). As in the cubic lid-driven cavity, in the vicinity of the end walls the swirling motion is suppressed and two co-rotating eddies are formed in the bulk of cavity 6.5(a,b). The product of the vertical component of the velocity and the vertical component of the vorticity $v\,\omega_y$ takes its maximum and minimum at the points indicated by the pink circles. At these points, both the vortical structures and the y-component of the velocity are strong, and they will be useful in a comparison later. Between these eddies, the spanwise component of the flow is weaker and cancels in the midplane $z = 0$ forming then two distinct cells from which the fluid elements

cannot escape. These two cells can be seen in fig. 6.5(a,b) with the purple line denoting the isovalues $w_0 = 0$ crossing the cavity along the line $z = 0$ (*i.e.* in the symmetry plane). Close to the plane $z = 0$, at the bottom of the cavity ($y \in [-0.5, -0.4]$ in fig. 6.5(a)) and at the wall upstream to the top surface ($x \in [0.4, 0.5]$ in fig. 6.5(b)), one can observe changes in the sign of w_0 indicating another pair of vortices, which, however, have a very small amplitude.

Pitchfork Bifurcation

Linear Stability Analysis As the Reynolds number is increased, the mirror symmetry is lost first. The spectrum of eigenvalues of the linear stability problem slightly above the critical Reynolds number shows that the first eigenvalue crossing the imaginary axis has $\omega = 0$ (fig. 6.6). The critical Reynolds number obtained by interpolation of the growth rates obtained near the critical point P1 yields a critical Reynolds number of $\mathrm{Re}_{\mathrm{P1}} = 53\,495$. From the distribution of the spanwise velocity $w(x, y, z = 0)$ of the slightly supercritical eigenmode on $z = 0$, shown in fig. 6.7(a), this mode breaks the mirror symmetry (6.8) (*i.e.* $w(z = 0) \neq 0$), but is antisymmetric. The result of the linear stability analysis is confirmed by the full numerical simulation. The deviation of non-linear steady state AS at $\mathrm{Re} = 54\,000$ from the symmetric steady state S1 has essentially the same structure (apart from small non-linear corrections) as the linear mode on the midplane. This is demonstrated in fig. 6.7b which shows the spanwise velocity on the plane $z = 0$. The distribution of w_{AS} is almost indistinguishable from those of the eigenfunction $\hat{w}_{\mathrm{P1}}$ shown in fig. 6.7a. As a convention, we define AS the steady state in which $w(\boldsymbol{x}_p) > 0$, and AS′ its mirror symmetric (*i.e.* $w(\boldsymbol{x}_p) < 0$), where $\boldsymbol{x}_p = (-0.4, 0., 0.)^{\mathrm{T}}$ is an arbitrarily chosen point, shown by a cross $\times$ in fig. 6.7.

The global structure of the steady anti-symmetric mode P1 is illustrated in fig. 6.8 at slightly supercritical conditions at $\mathrm{Re} = 53\,700$. The anti-symmetric mode is breaking the mirror symmetry, this can be easily identified by w being particularly strong on $z = 0$ (fig. 6.8c). The perturbation velocity fields is primarily located near the upstream wall at $x = 0.5$ and extends upstream of the basic flow. Furthermore, the perturbation exhibits a strong velocity components in the streamwise direction, parallel to the basic flow. From the two major regions (yellow and purple) of u and v the perturbation flow primarily consists of a single slender vortex located in midplane $z = 0$ and extending over the solid walls. This structure can be clearly seen from fig. 6.8d which shows the structure of the vortex in the horizontal plane $y = -0.3$ in the upper half of the cavity. The structure of the perturbation flow corresponds to a single Taylor–Görtler vortex. While a single Taylor–Görtler vortex has not been reported before, the vortex structure is similar to the periodic Taylor–Görtler vortices known from the spanwise extended lid-driven cavity [81, 78, 5].

Finite-amplitude steady asymmetric flow At the critical Reynolds number $\mathrm{Re}_{\mathrm{P1}}$ the asymmetric steady flows AS and its counterpart AS' (fig. 6.4) bifurcate supercritically from the symmetric basic state S1. We find the steady asymmetric mode to grow to finite amplitude and saturate for $t \to \infty$. To compute the saturated

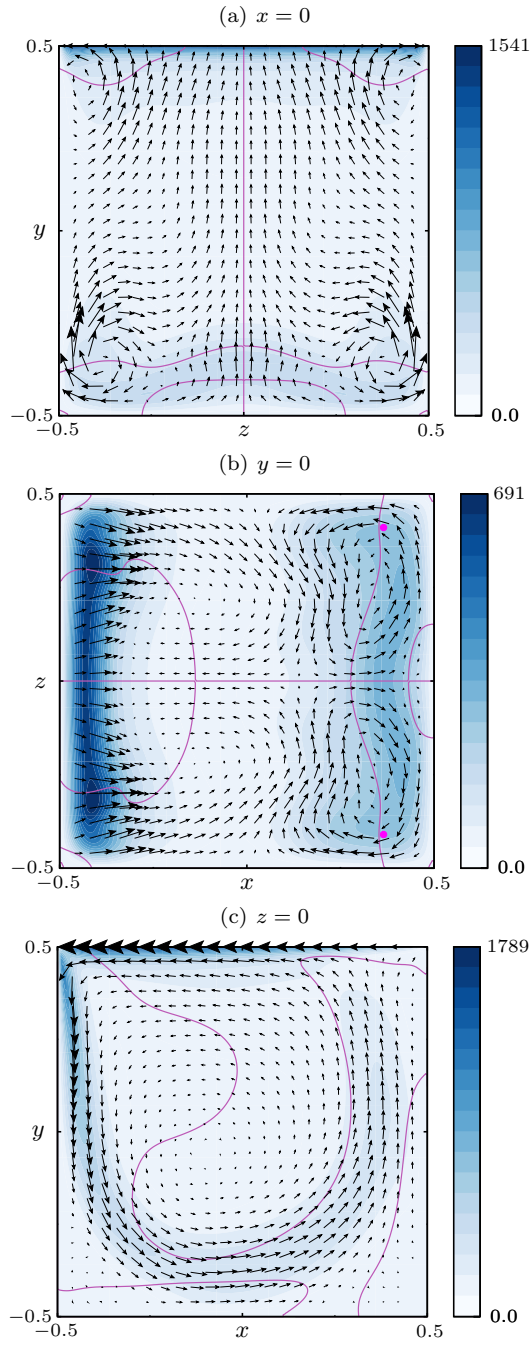

FIGURE 6.5 – Basic flow at $\mathrm{Re} = 53450 < \mathrm{Re}_c$ in the $x = 0$ plane (a), $y = 0$ plane (b) and $z = 0$ plane (c). Arrows denote the in-plane components of the velocity vector while the shades of blue indicate the velocity magnitude $|\boldsymbol{u}_0|$. Purple lines denote $w_0 = 0$ isovalues. Global extrema of $v\,\omega_y$ are indicated by the pink filled circles.

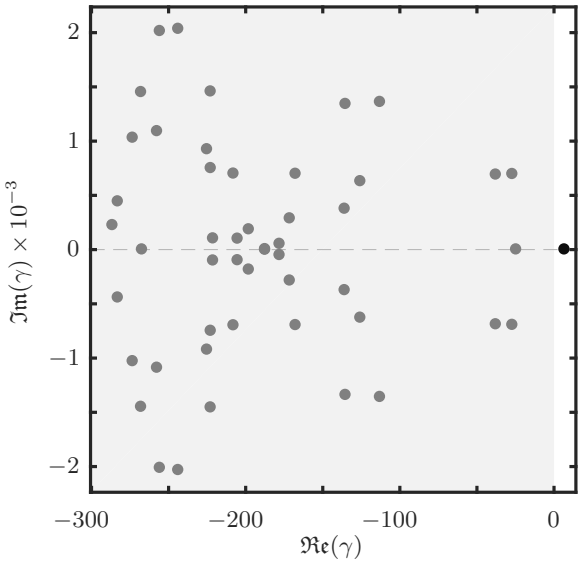

FIGURE 6.6 – Eigenvalue spectrum for the linear stability problem of the basic flow at the supercritical Reynolds number $\mathrm{Re} = 53\,700$. Grey shade indicates the region of negative growth rates.

flow state AS we run the unsteady solver until the time derivative of the total kinetic energy $\partial E/\partial t$ is less than 10^{-5}. The flow was first obtained for $\mathrm{Re} = 54000$ and then decreased in order to determine whether or not the bifurcation is supercritical. To measure the amplitude of the asymmetric steady flow, we consider the symmetry criterion $\mathcal{S}$ presented earlier. It is evaluated at different Reynolds numbers beyond criticality and a three parameter fit is performed (fig. 6.9). The fitting function is in the shape

$$f(\mathrm{Re}) = a_1(\mathrm{Re} - a_2)^{a_3} \ . \tag{6.12}$$

Parameter a_2 gives an estimate of the critical Reynolds number, parameter a_3 should be close to unity if the bifurcation is a supercritical pitchfork bifurcation. Since $\mathcal{S}$ takes the square of the deviation in the integral, it should vary linearly with the distance to the critical Reynolds number. The second estimate for the critical Reynolds number is $a_2 = 53490 = \mathrm{Re}_{P1}$ and $a_3 = 0.9612$. This is in perfect agreement with the result obtained from the linear stability analysis, since the relative difference is less than 0.01%.

Further Destabilization of S1

Hopf Bifurcation At slightly higher Reynolds number $\mathrm{Re}_{\mathrm{H1}} = 54\,107$, the already unstable steady state S1 loses its stability to a second mode: A complex conjugate pair of eigenvalues crosses the imaginary axis with $\omega_{\mathrm{H1}} = 689.68$. The index H1 refers to Hopf bifurcation point H1 in fig. 6.4. The oscillating eigenmode shown in fig. 6.10 is anti-symmetric (6.9), just like the stationary mode P1.

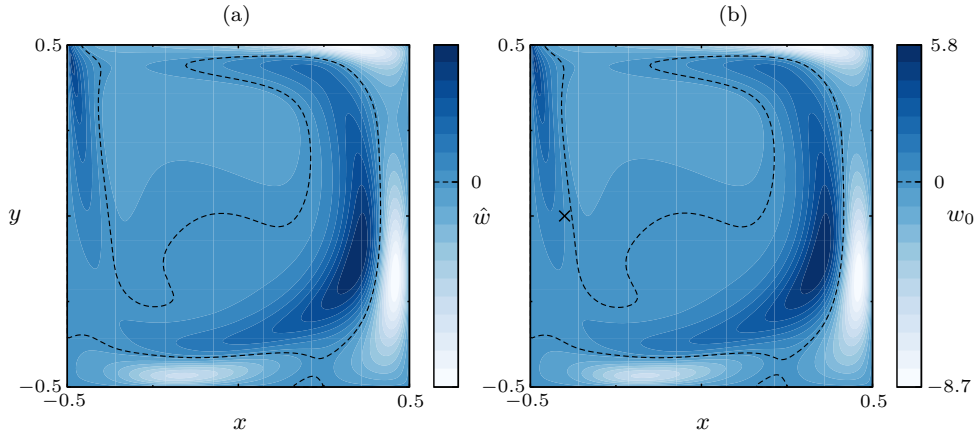

FIGURE 6.7 – Spanwise velocity fields on the plane $z = 0$ (a) of the slightly supercritical eigenmode $\hat{w}_{P1}(x, y)$ for Re = 53 700 and (b) of the velocity field $w_0(x, y, z = 0)$ of the slightly supercritical non-linear steady-state AS obtained by numerical simulation for Re = 54 000. The dashed lines correspond to $\hat{w} = 0$ (a) and $w_0 = 0$ (b). The marker (×) in (b) indicates the monitoring point $\boldsymbol{x}_p = (-0.4, 0., 0.)^{\mathrm{T}}$.

The time-dependent anti-symmetric mode also consists of a single Taylor-Görtler vortex. The vortex centerline is in the mid plane $z = 0$ and the vortex is stronger near the solid wall of the cavity upstream to the free surface. Besides, the vortex periodically changes its sense of rotation. The sense of rotation also varies along the apparent centerline of the Taylor–Görtler vortex. This is illustrated by the temporal evolution of the isosurfaces of u, v and w in fig. 6.10 and also supported by the structure of the perturbation flow in the plane $y = -0.3$ shown in fig. 6.11 at the same instants of time.

The realization of a flow in which the oscillating perturbation is initially growing and saturates in form of a limit cycle for long times is very unlikely: The faster growth of the stationary anti-symmetric mode prevents a further development of this oscillating mode. We did not find any stable limit cycle related to the secondary destabilization of the flow and thus did not determine the character of the bifurcating solution (sub/super-critical).

Second pitchfork bifurcation For a Reynolds number slightly larger than $\mathrm{Re}_{\mathrm{H1}}$, the mirror-symmetric basic state S1 experiences a second pitchfork bifurcation at $\mathrm{Re}_{P2} = 54130$, the corresponding mode is not oscillating, but is symmetric. The eigenmode is composed of two vortices which are symmetric to each other (not shown). This leads to a second branch of symmetric steady flows S2 when the space of solution is restricted to symmetric flows. In this subspace of solutions, the perturbation saturates and the vortices grow to a finite amplitude. Although it is not shown, we found that this bifurcation is subcritical and the folding point of the bifurcation is below Re = 53800. While this branch of symmetric solutions is stable to symmetric perturbations, it is, however, unstable to non-symmetric perturbations. In fact, the

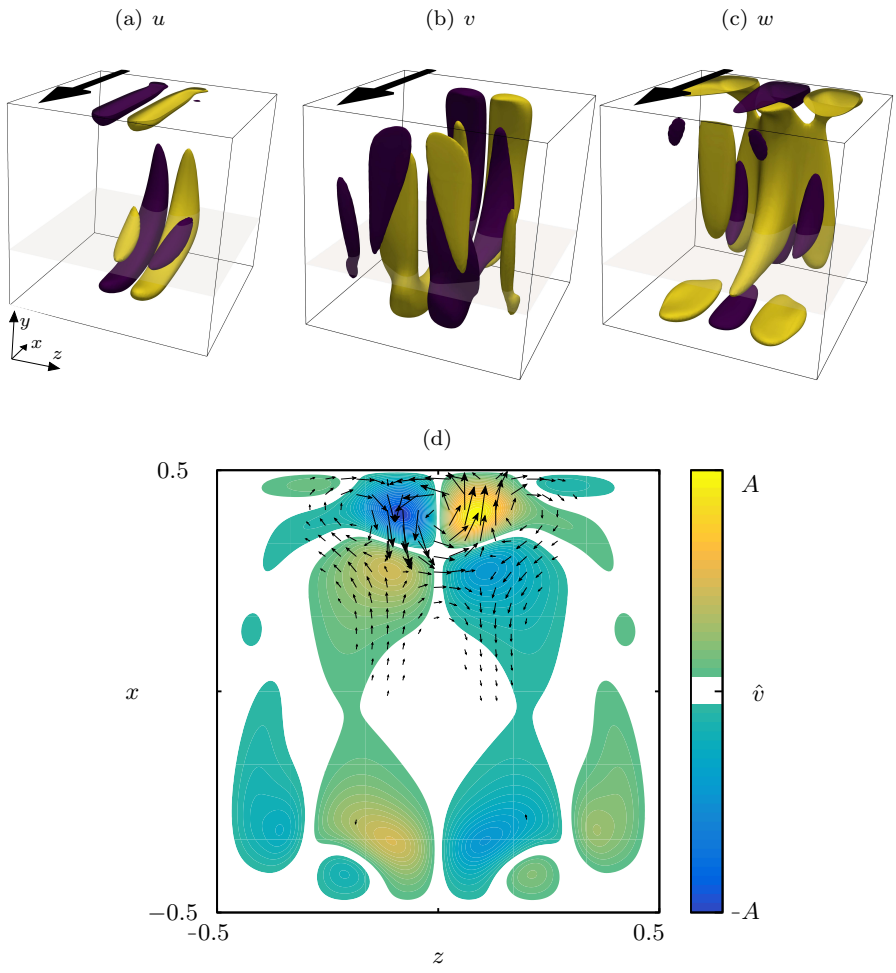

FIGURE 6.8 – Isosurfaces of the velocity components $\hat{u}$ (a), $\hat{v}$ (b) and $\hat{w}$ (c) of the most dangerous non-oscillating eigenmode $\boldsymbol{u}(\hat{\boldsymbol{x}})_{\mathrm{P1}}$ at $\mathrm{Re} = 53\,700$ at $\pm 20\%$ of their respective maxima. The arrow indicates the direction of the surface stress. (d) Structure of the most dangerous stationary eigenmode at $\mathrm{Re} = 53\,700$ shown in the plane $y = -0.3$. Arrows indicate the cross stream velocity field (u, w), while color indicates the velocity component v.

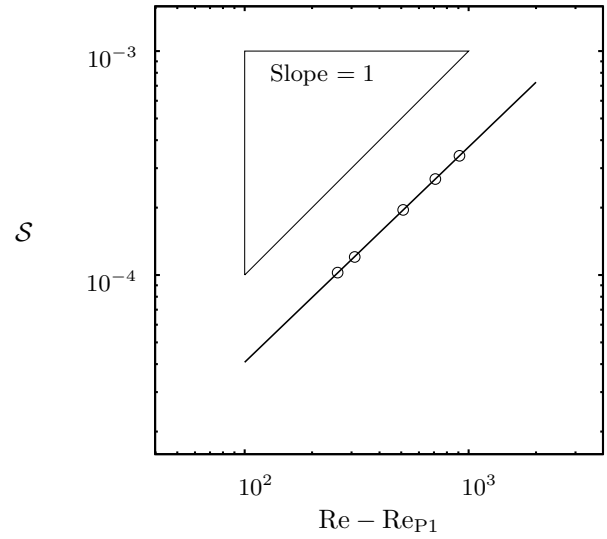

FIGURE 6.9 – Asymmetry measure $\mathcal{S}$ as a function of the Reynolds number. Open symbols represent numerical simulations, the fit of shape $a_1(\mathrm{Re} - a_2)^{a_3}$ is represented with a full line. The slope of a linear function is represented by the line of the triangle almost parallel to the fit.

TABLE 6.3 – Asymmetry parameters, leading eigenvalues and energy budget close to the bifurcation points. All modes energy budget have similar proportion for all modes, and are thus destabilized by the same mechanism.

	Re	$\mathcal{S}$	γ_i	I_1	I_2	I_3	I_4
P1	53500	0	0.13075	0.030	0.789	0.142	0.039
H1	54100	0	$-1.10422 \pm \mathrm{i}689.68$	0.042	0.782	0.141	0.035
P2	54100	0	-4.12442	0.061	0.763	0.119	0.053
H2	55700	7.6×10^{-4}	$-0.19771 \pm \mathrm{i}764.16$	0.036	0.789	0.131	0.044
H3	56200	9.0×10^{-4}	$0.26699 \pm \mathrm{i}82.559$	0.040	0.781	0.128	0.052

leading eigenvalues are very large $\sigma_{1,2} > 50$. Therefore the steady bifurcating solutions were not observed when simulating the problem without imposing a mirror symmetry in the midplane.

Instability mechanism The normalized energy budget is displayed in table 6.3 for several Reynold numbers. It can be seen that the magnitude of the different terms I_n (time averaged) for the three modes mentioned earlier are almost the same. Therefore the first non-oscillating symmetry breaking mode P1, the second oscillating symmetry breaking mode H1 and the third non-oscillating symmetric mode P2 are then destabilized by a similar process. The similarity is due to the very similar structure of the three modes. Since the contribution I_2 dominates, all these modes are destabilized primarily through to the lift-up mechanism i_2 by which the streamwise perturbation flow $u_{\parallel}$ is amplified by transport of basic state momentum in the cross-stream direction

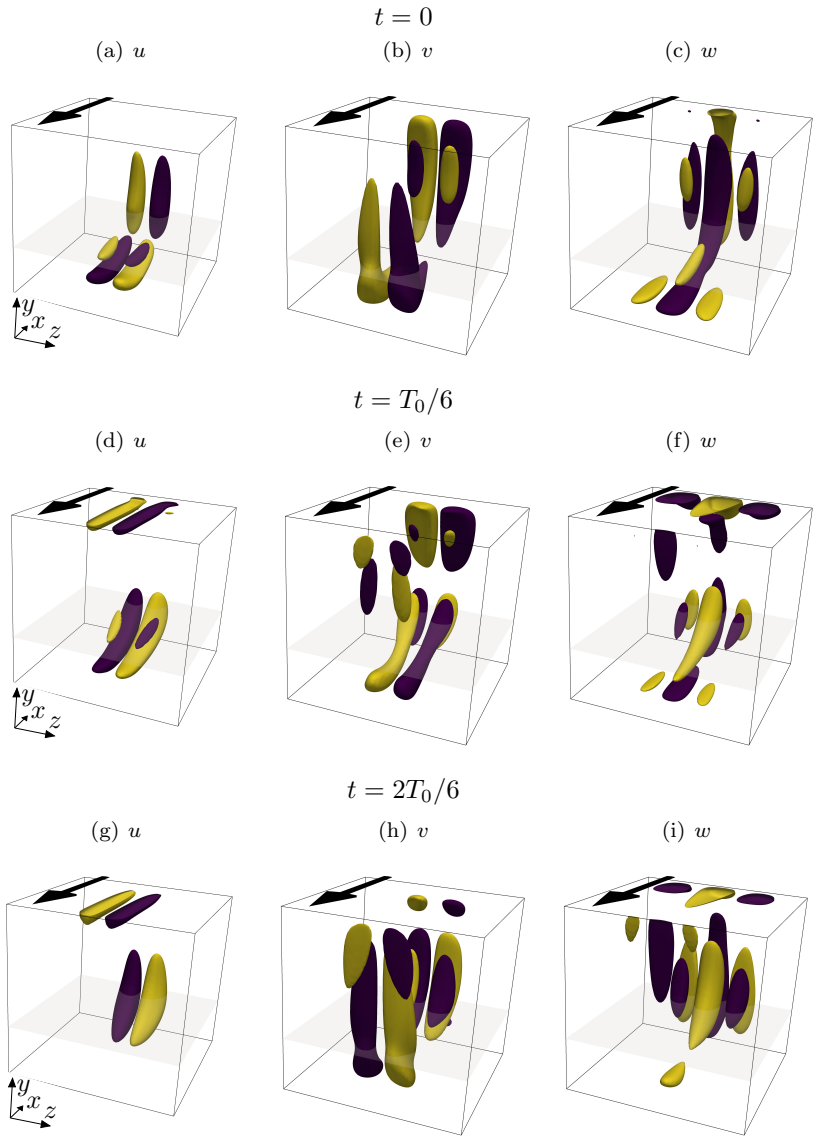

FIGURE 6.10 – Evolution of the time-dependent anti-symmetric eigenmode at $\mathrm{Re} = 54\,100 < \mathrm{Re}_{\mathrm{H1}}$. Shown are isosurfaces of u, v and w at three instants of time over half a period, $t = 0$, $t = T_0/6$ and $t = 2T_0/6$. Each isosurface correspond to $\pm 0.2 \times \max_{\boldsymbol{x}} |\boldsymbol{u}|$. Positive and negative values are coded in color. The arrow indicates the direction of the surface stress and grey shows the cut on which the flow is illustrated in fig. 6.11.

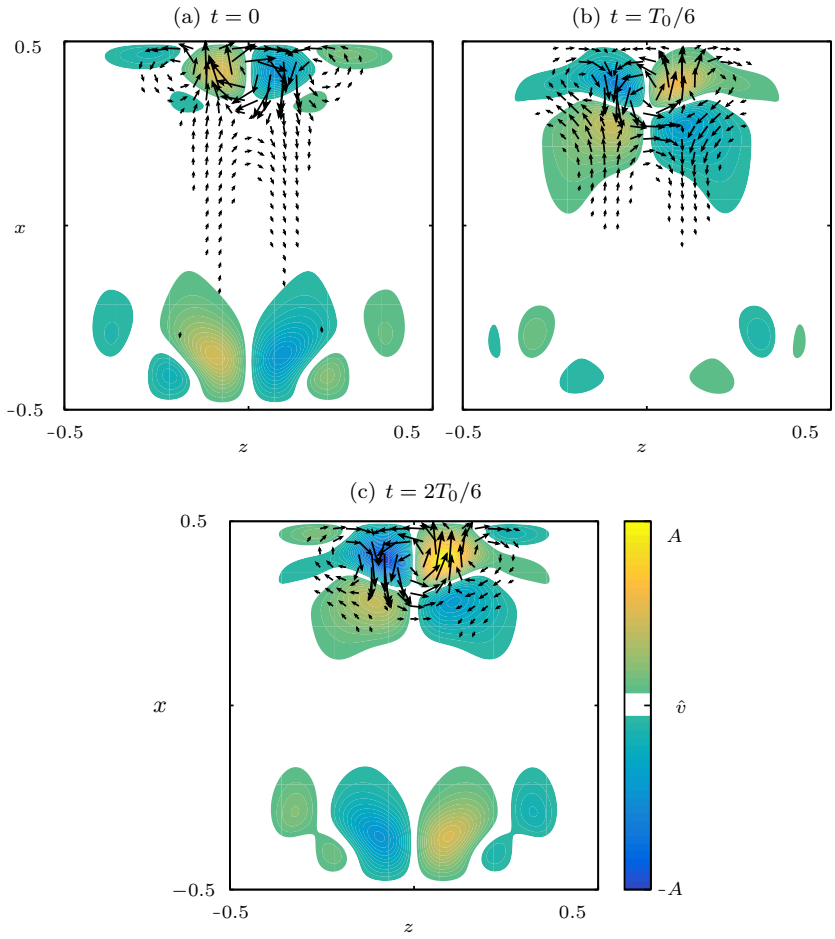

FIGURE 6.11 – Evolution of the time-dependent anti-symmetric eigenmode at $\mathrm{Re}_{\mathrm{H1}} = 54\,100$ in the plane $y = -0.3$ shown at $t = 0$, $t = T_0/6$ and $t = 2T_0/6$ corresponding to fig. 6.10. Arrows show the velocity vectors (u, w) in the plane while the velocity component v is shown by color.

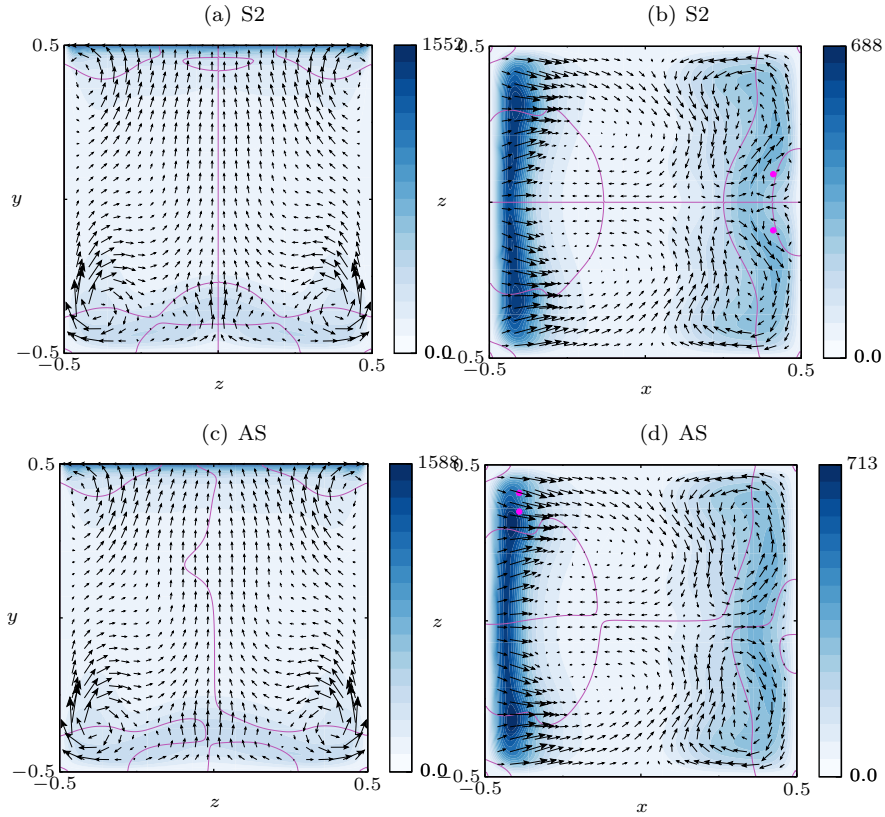

FIGURE 6.12 – Total flow on the plane $x = 0$ (a,c), $y = 0$ (b,d) on the symmetric branch S2 at $\mathrm{Re} = 54\,150$ (a,b) and on the asymmetric branch AS at $\mathrm{Re} = 55\,700$ (c,d). Arrows show the in-plane velocity components. Purple lines denote $w_0 = 0$ isovalues in all figures. The velocity magnitude is shown by shades of blue. Global extrema of $v\,\omega_y$ are indicated by the pink filled circles.

due to $u_\perp$. Furthermore, the distribution of the energy production terms (not shown) is very similar as those for periodic Taylor–Görtler vortices in an extended lid-driven square cavity (fig. 12 of [5]) which underlines the interpretation of the three modes as stationary and time-dependent Taylor-Görtler vortices.

Comparison of Steady Flows

In order to qualitatively compare the changes of the total flow induced by the two pitchfork bifurcations, the symmetric flow S2 at $\mathrm{Re} = 54\,150$ (unstable to non symmetric perturbation), and the non-symmetric flow AS at $\mathrm{Re} = 55\,700$ are shown in fig. 6.12. The flow in the $z = 0$ plane resembles very much the flow depicted in fig. 6.5c and no qualitative change has been noticed.

On the symmetric branch S2, after the second pitchfork bifurcation, the two unstable symmetric vortices have saturated and are clearly visible. In fact, the extrema of

the product of the y-component of the velocity and y-component of vorticity indicated by the pink dots in fig.6.12(b), are located within these Taylor-Görtler vortices. They are much stronger than the very weak vortices observed at $\mathrm{Re} = 53\,450$ in fig. 6.5, and they can be seen at the bottom of the cavity ($z = 0$, $y \in [-0.5, -0.4]$) and at the wall upstream to the sheared surface ($z \in [-0.1, 0.1]$, $x \in [0.4, 0.5]$) in fig. 6.12(a) and (b), respectively. The maximum value of the velocity magnitude is still located at the top surface with $\max|\boldsymbol{u}_0| = 1863.9$ at $\boldsymbol{x} = (-0.381, 0.5, 0.4487)^{\mathrm{T}}$, and the average velocity at the surface is $\boldsymbol{u}_{\mathrm{avg}} = (-1287.8, 0, 0)^{T}$.

On the asymmetric branch AS, however, the saturated perturbation does not seem to have such a visible effect on the total flow. In fact, the magnitude of the vortex centered on the midplane is so small that it can barely be seen in comparison with the end-walls vortices. The maximum value of the magnitude of the velocity is $\max|\boldsymbol{u}_0| = 1909.3$ at $\boldsymbol{x} = (-0.383, 0.5, 0.4494)^{\mathrm{T}}$ and the average flow at the surface is $\boldsymbol{u}_{\mathrm{avg}} = (-1316.1, 0, 0.37137)^{\mathrm{T}}$ reflecting the broken symmetry with a net spanwise flow on the top surface. This weak symmetry breaking is also visible by the purple lines in fig. 6.12(c,d) representing the $w_0 = 0$ isolines. In particular, the spanwise velocity on the midplane $w(z = 0)$ is not zero, and distinct cells are no longer present.

6.4.2 Time-Dependent Asymmetric Flow - Hopf Bifurcation

Linear Stability Analysis

A linear stability analysis of the steady asymmetric flow AS reveals a Hopf bifurcation at $\mathrm{Re}_{\mathrm{H2}} = 55\,718$. The `BoostConv` algorithm in combination with the second-order time-integration scheme is used to find the steady asymmetric flow AS. The critical frequency is $\omega_{\mathrm{H2}} = 764.16$, which is only about 10% larger than ω_{H1}. Since the basic flow is no longer symmetric, one cannot expect any symmetry of the perturbation variables.

Figure 6.13 shows the components of the velocity field of the eigenmode H2 at the slightly subcritical Reynolds number $\mathrm{Re} = 55\,700$. The mode resembles the oscillatory mode H1 destabilizing the symmetric basic state at $\mathrm{Re}_{\mathrm{H1}}$ (fig. 6.10). While mode H1 is anti-symmetric and like a standing wave, the modes H2 and H2' appear to travel in negative and positive z direction, respectively. The traveling direction is dictated by the particular asymmetric flow state (AS or AS') being destabilized and the Taylor–Görtler vortices involved are oriented slightly obliquely. Mode H2 traveling in the negative z direction is illustrated in fig. 6.13. The instabilities of the asymmetric steady flows AS and AS' also arise in form of one or two (at a time) Taylor-Götler vortices and are located in the vicinity of the midplane of the cavity. The relatively small amplitude of the deviation of the steady asymmetric flows states AS and AS' from the symmetric basic state (fig. 6.9 and fig. 6.12(c,d)) suggests that the onset of asymmetric oscillations is not caused by the asymmetry of the flow, but is rather a similar instability as for mode H1. The asymmetric part of the three-dimensional steady flow seems to *merely* suppress the onset of oscillations for a small range of Reynolds numbers $\mathrm{Re} \in [\mathrm{Re}_{\mathrm{H1}}, \mathrm{Re}_{\mathrm{H2}}]$. This interpretation is confirmed by the mean energy budget. From table 6.3 we notice that also the critical mode H2 is destabilized

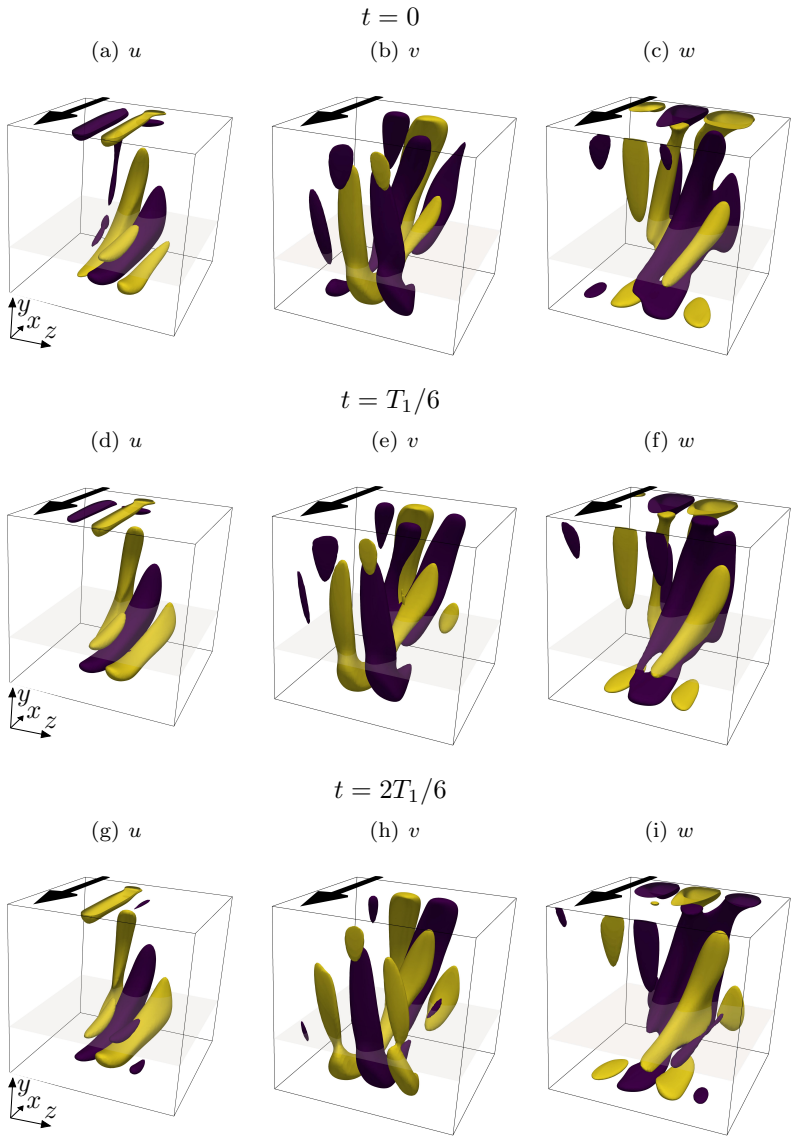

FIGURE 6.13 – Evolution of the time-dependent asymmetric eigenmode H2 at Re = 55 700. Shown are isosurfaces of u, v and w at three instants of time over half a period, $t = 0$, $t = T_1/6$ and $t = 2T_1/6$. Yellow and purple isosurfaces correspond to $\pm 20\%$ of the extrema of the velocity component, respectively. The arrow indicates the direction of the surface stress and grey shows the cut on which the flow is illustrated in fig. 6.14.

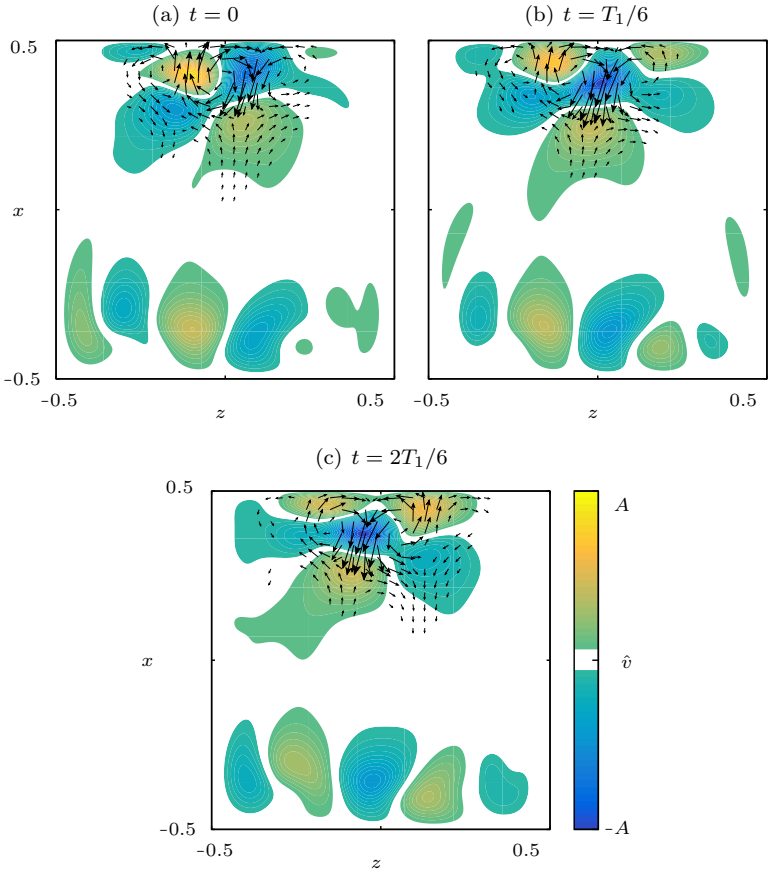

FIGURE 6.14 – Evolution of the time-dependent asymmetric eigenmode H2 at Re = 55 700 in the plane $y = -0.3$ shown at $t = 0$, $t = T_1/6$ and $t = 2T_1/6$ corresponding to fig. 6.13. Arrows show the velocity vectors (u, w) in the plane while the velocity component v is shown by color.

by the same mechanism as modes P1 and H1, because of the similar modal structure and the similar energy budget with again I_2 being dominant.

Finite Amplitude Oscillations

For $\mathrm{Re} > \mathrm{Re}_{\mathrm{H2}}$ the amplitude of the asymmetric oscillation saturates and reaches the limit cycle LC1. To investigate the saturation, the third-order time-integration scheme has been used. Let us introduce the peak to peak amplitude of the asymmetry measure $\mathcal{S}$ of the fully developed non-linear periodic flow with constant oscillation amplitude $\Delta\mathcal{S}$. To see whether the bifurcation is supercritical or not, we consider $\Delta\mathcal{S}^2$ as a function of the Reynolds number, and we use a fit function of the same shape as for the pitchfork bifurcation: $a_1(\mathrm{Re} - a_2)^{a_3}$. The results from the non-linear simulations and the best fit from a least square problem are shown in (fig. 6.15(a)) We find the

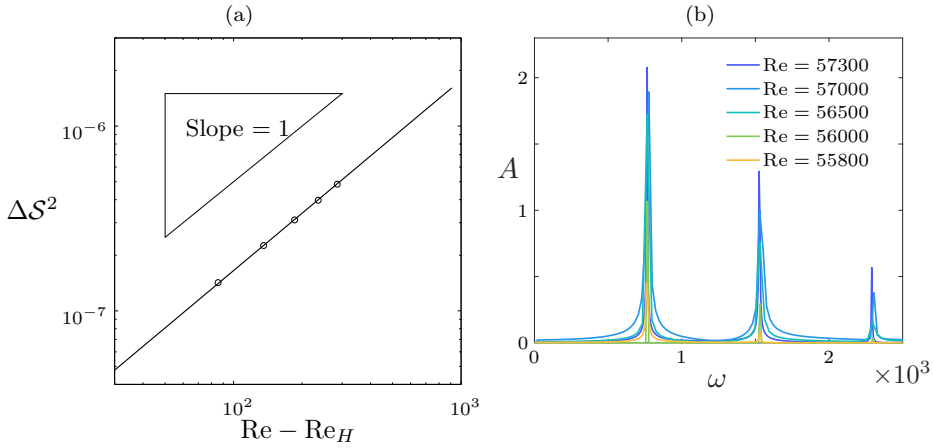

FIGURE 6.15 – (a) Squared peak to peak amplitude $\Delta\mathcal{S}^2$ of the saturated oscillatory asymmetric flow LC1. The straight line is a fit with shape function of the form $a_1\,(\mathrm{Re} - a_2)^{a_3}$. (b) Evolution of the spectral amplitudes A of the saturated asymmetric non-linear oscillations (LC1).

critical Reynolds $a_2 = \mathrm{Re}_{\mathrm{H2}} = 55\,715$ and $a_3 = 1.0307$. This means that $\Delta\mathcal{S}$ scales almost like the square root of the distance from the $\mathrm{Re}_{\mathrm{H2}}$, and indicates a supercritical Hopf bifurcation. The estimations of H2 from the linear stability analysis and from the fit agree almost perfectly.

As the Reynolds number increases, higher harmonics are generated whose amplitudes are shown in fig. 6.15(b). At $\mathrm{Re} = 57\,300$, the second and third harmonics have already grown to an appreciable amplitude of $0.65A_1$, and $0.18A_1$, where A_1 is the amplitude of the fundamental harmonic, and the fundamental frequency is $\omega_{\mathrm{LC1}} = 764.5$. Due to the two asymmetric steady solutions AS and AS' there also exists another limit cycle LC1' which is created near the other asymmetric flow state.

Further Destabilization of the Steady Asymmetric Flow

As one continues increasing the Reynolds number on the asymmetric branch AS, a second oscillating mode is destabilized at $\mathrm{Re}_{\mathrm{H3}} \approx 56\,200$. The associated frequency is $\omega_{\mathrm{H3}} = 82.55$, which is approximatively ten times less than the frequency ω_{H2} of the limit cycle LC1. Again, the energy budgets are extremely similar to the ones of all previous modes, indicating that the steady state AS is destabilized by the same centrifugal mechanism. This mode H3 (resp. H3') consists of three vortices that are travelling in the negative (resp. positive) z direction. In fig. 6.16 and fig. 6.17, vortices travelling in the $-z$ direction are shown. Qualitatively, the vortices of mode H3 seem to be more aligned with the streamwise component of the basic flow than those of mode H2, which are more in a spiral form. This is particularly visible for the x-component of the perturbation velocity in figs. 6.13(a,d,g) and 6.16 (a,d,g).

The bifurcation diagram is represented in terms of the asymmetry measure, together with the sign of the spanwise velocity at the probing point $\boldsymbol{x}_p$ from fig. 6.7(b),

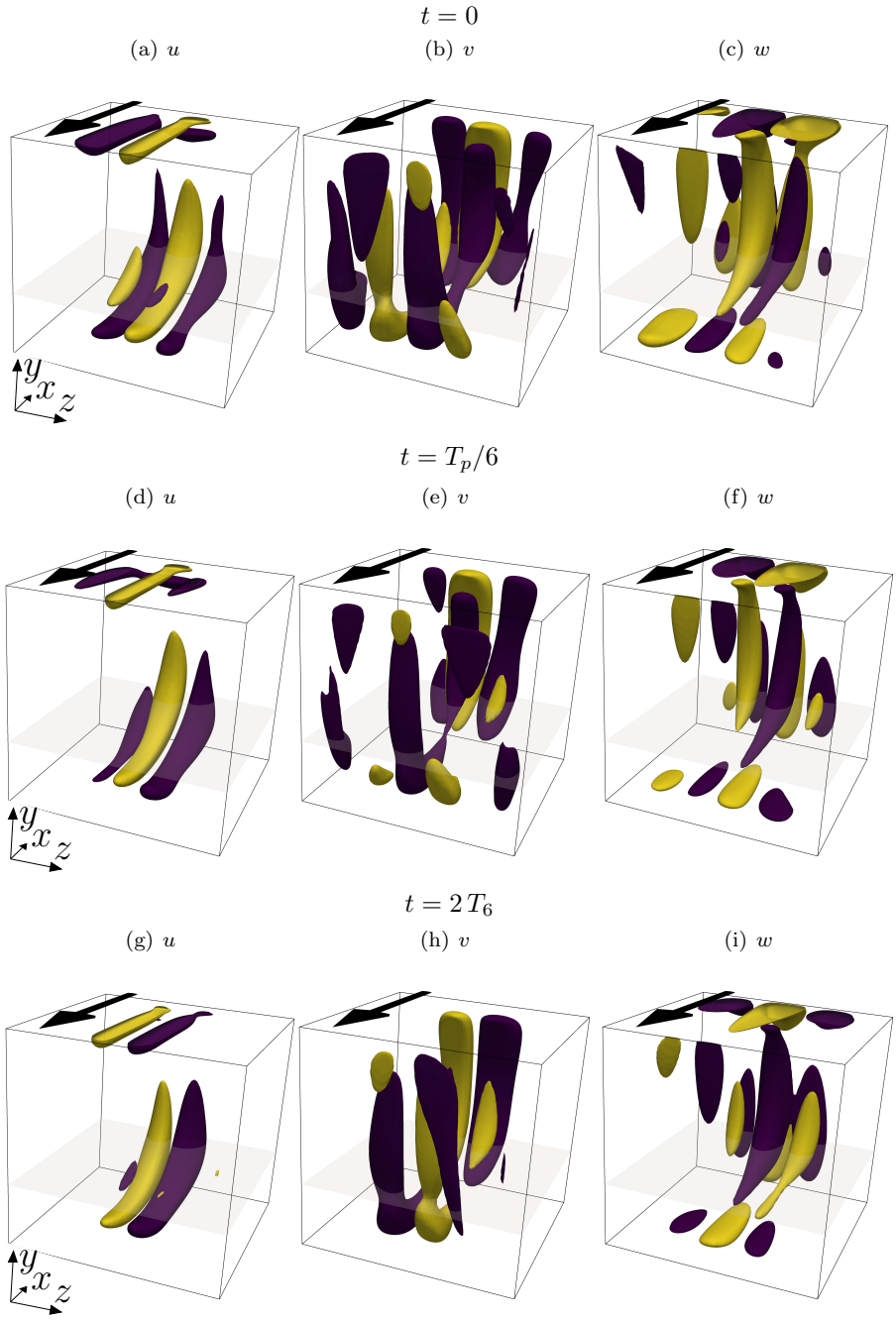

FIGURE 6.16 – Evolution of the time-dependent asymmetric eigenmode H3 at $\mathrm{Re} = 56\,200$. Shown are isosurfaces of u, v and w at three instants of time over half a period, $t = 0$, $t = T_1/6$ and $t = 2T_1/6$. Yellow and purple isosurfaces correspond to $\pm 20\%$ of the extrema of the velocity component, respectively. The arrow indicates the direction of the surface stress and grey shows the cut on which the flow is illustrated in fig. 6.14.

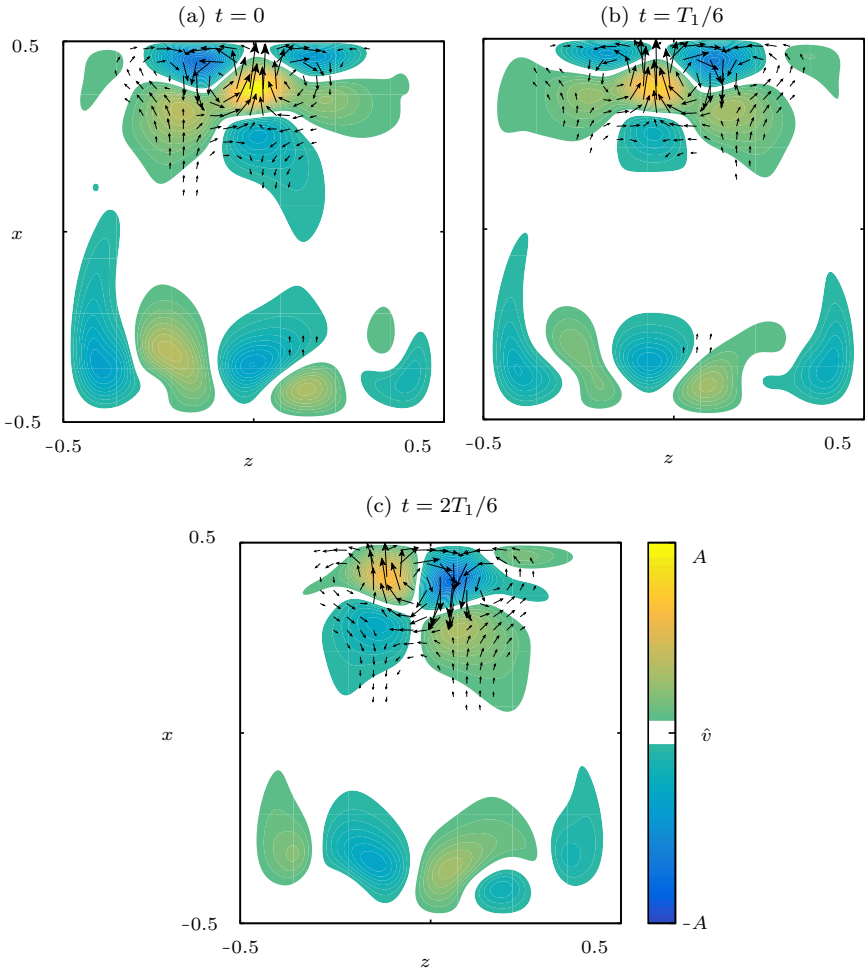

FIGURE 6.17 – Evolution of the second most instable mode H3 at Re = 56 200 on the asymmetric branch in the plane $y = -0.3$ shown at $t = 0$, $t = T_p/6$ and $t = 2T_p/6$ corresponding to fig. 6.16. Arrows show the velocity vectors (u,w) in the plane, while the velocity component v is shown by color.

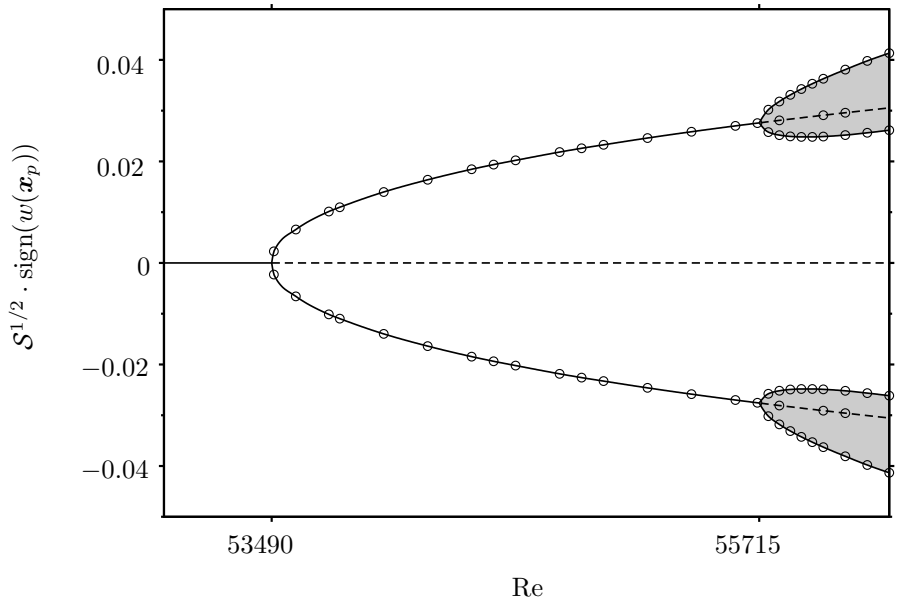

FIGURE 6.18 – Bifurcation diagram, symbols show the simulations results, the amplitude of the oscillations after the Hopf bifurcation is represented with a grey shading. Unstable branches are shown by dashed lines.

is shown in fig. 6.18. Only the estimates of the critical Reynolds numbers from the saturated steady state or limit cycle are shown.

6.4.3 Destabilization of the Limit Cycle

For even higher Reynolds numbers, $\mathrm{Re} \in [57\,000, 58\,000]$, the limit cycles LC1 and LC1' become unstable. Long periods of oscillations with constant amplitude are interrupted by non-linear bursts in an intermittent fashion leading to a complex dynamics.

The dynamics is illustrated by the evolution of $w(\boldsymbol{x}_p, t)$ shown in fig. 6.19 (middle). After a burst, the dynamical system may return to the same limit cycle or to the limit cycle which exists near the other asymmetric steady state. The switch between the two limit cycles LC1 and LC1' can be seen in fig. 6.19 (middle) at about $t = 48.5$ when the mean value $\overline{w(\boldsymbol{x}_p, t)}$ during the phases of regular oscillation changes from negative before the burst to positive after the burst (white dashed lines). The timespan during which the burst happens is not the same for all bursts and the durations of the regular oscillations differ as well.

When the system is locked on one of the limit cycles its spectrum contains only harmonics of the fundamental frequency as discussed above (fig. 6.19, bottom). During a bursting event, however, the power density spreads on a broad bandwidth. This spreading happens in the form of peaks (almost) regularly spaced around the harmonics of the limit cycle.

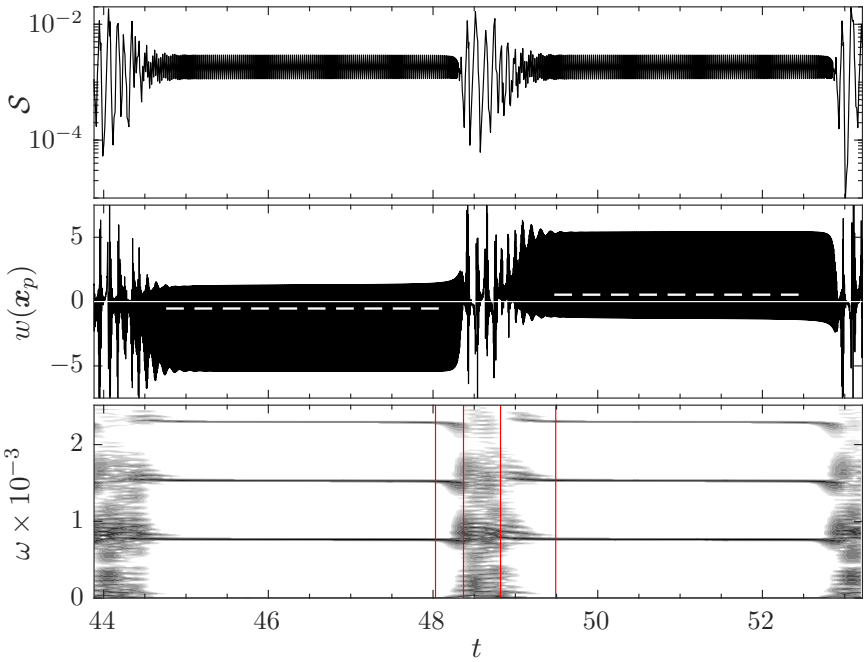

FIGURE 6.19 – The two upper panels show the time evolution of $\mathcal{S}(t)$ (top) and $w(\boldsymbol{x}_p, t)$ (middle) at $\mathrm{Re} = 57\,300$. The mean values of $w(\boldsymbol{x}_p, t)$ corresponding to LC1 and LC1' are indicated by horizontal white dashed lines and the full line indicates the zero. A Short-time Fourier transform of $w(\boldsymbol{x}_p, t)$ with sliding window of width of 0.6 time units is shown in the lower panel. The gray shading represents the spectral amplitude of the signal, only amplitudes larger than 10^{-4} are plotted. The red vertical lines qualitatively delimit the three phases mentioned in the text.

These bursting events can be subdivided in three distinct phases. In the first phase, the oscillation frequency of the limit cycle decreases, and frequencies below the harmonics start invading the spectrum in a continuous manner. The mechanism triggering this first step is, however, not very clear.

In a second phase, the flow undergoes strong oscillations. The beat frequency is about $\omega_{\mathrm{beat},1} = 50 \pm 5$. Due to the strong non-linear interactions, the beating is strongly anharmonic which results in the multiple peaks at $\omega = n\omega_{LC1} \pm m\omega_{\mathrm{beat}}$ in the short-time spectrum in the lower panel of fig. 6.19. During this second step, the symmetry of the flow varies significantly. In fact, $\mathcal{S}$ varies from 10^{-6} to 10^{-2} in the last burst of fig. 6.19. This indicates that the flow is repeatedly nearly symmetric. In accordance, the value of $w(\boldsymbol{x}_p)$ is getting close to zero.

In the last phase, the beat frequency of the signal during the return to regular oscillations is $\omega_{\mathrm{beat}} \approx 75 \pm 5$ which is close to the frequency of the unstable low-frequency limit cycle which is created by the secondary bifurcation H3 from the unstable asymmetric steady solution, $\omega_{H3} = 82$. The limit cycle LC1 is apparently a saddle limit cycle attracting from one orthogonal direction and repelling in the other. To formally prove this, one would need to perform a Floquet analysis, see e.g. [57, 17, 153], if the destabilization mechanism is linear.

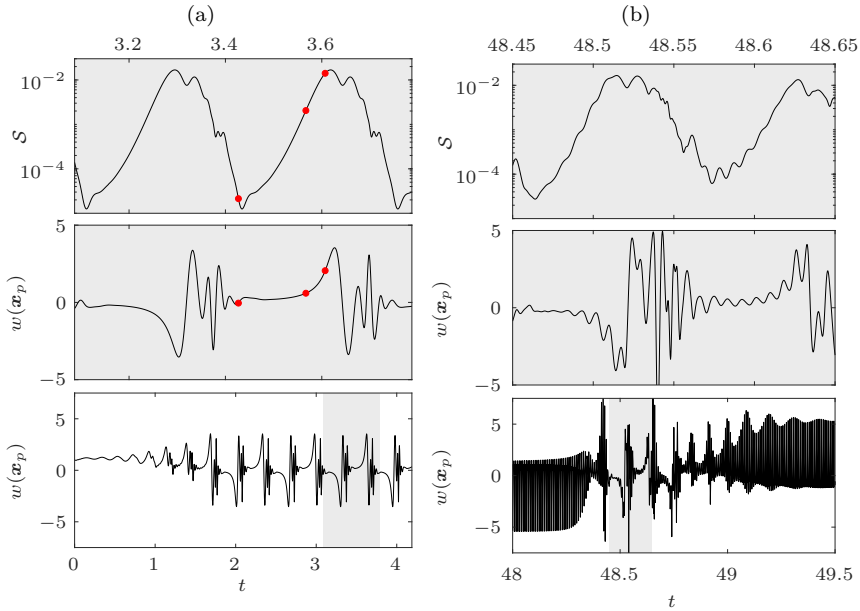

FIGURE 6.20 – Temporal evolution of $w(\boldsymbol{x}_p, t)$ at Re = 57300 with (a) and without employing a low-pass filter (b). The two upper panels show zooms into the signal as indicated by the gray shading in the bottom panel. The red dots in the top and middle panels of (a) indicates the times as which the total flow is shown in fig. 6.21.

To probe the existence of another unstable limit cycle in the second step, one may take advantage of the frequency of LC1 being ten times higher than the hypothesized limit cycle at this Reynolds number. This allows to design a low pass filter to obtain only the dynamics associated with the slowly evolving mode. To that end selective frequency damping (SFD) is used, not to seek the basic flow as usual [2], but to eventually find the low-frequency limit cycle. Following the notation of [2] the parameters $\chi = 3000$ and $\Delta = 0.0007$ are selected, corresponding to a cut-off frequency $\omega_c = 227$ which is more than twice as small as ω_{H2} of the limit cycle LC1, but still large enough not to damp oscillations with frequencies of $\omega \approx 50$ and its second harmonic. This approach is much more economic computationally than other methods to find unstable manifolds, e.g. tracking of edge states [101, 148, 68], due to a relatively long period of the hypothetical limit cycle.

Initiating the flow with $\boldsymbol{q} = \boldsymbol{q}_{0,\mathrm{AS}} + a\hat{\boldsymbol{q}}_{H3}$ with a small constant a the flow initially oscillates with a low frequency of $\omega \approx 30$ and a growing amplitude (fig. 6.20a). At about $t = 1.2$ higher-frequency oscillations of low amplitude develop on the low-frequency signal until the signal $w(\boldsymbol{x}_p, t)$ settles on a periodic flow with fundamental frequency $\omega \approx 10$ and higher harmonics for $t > 1.8$. These frequencies do not match the ones of the flow which is not damped. This is due to the low pass filter apparently further slowing down already slow dynamics. That side effect most likely depends on the strength of the damping χ.

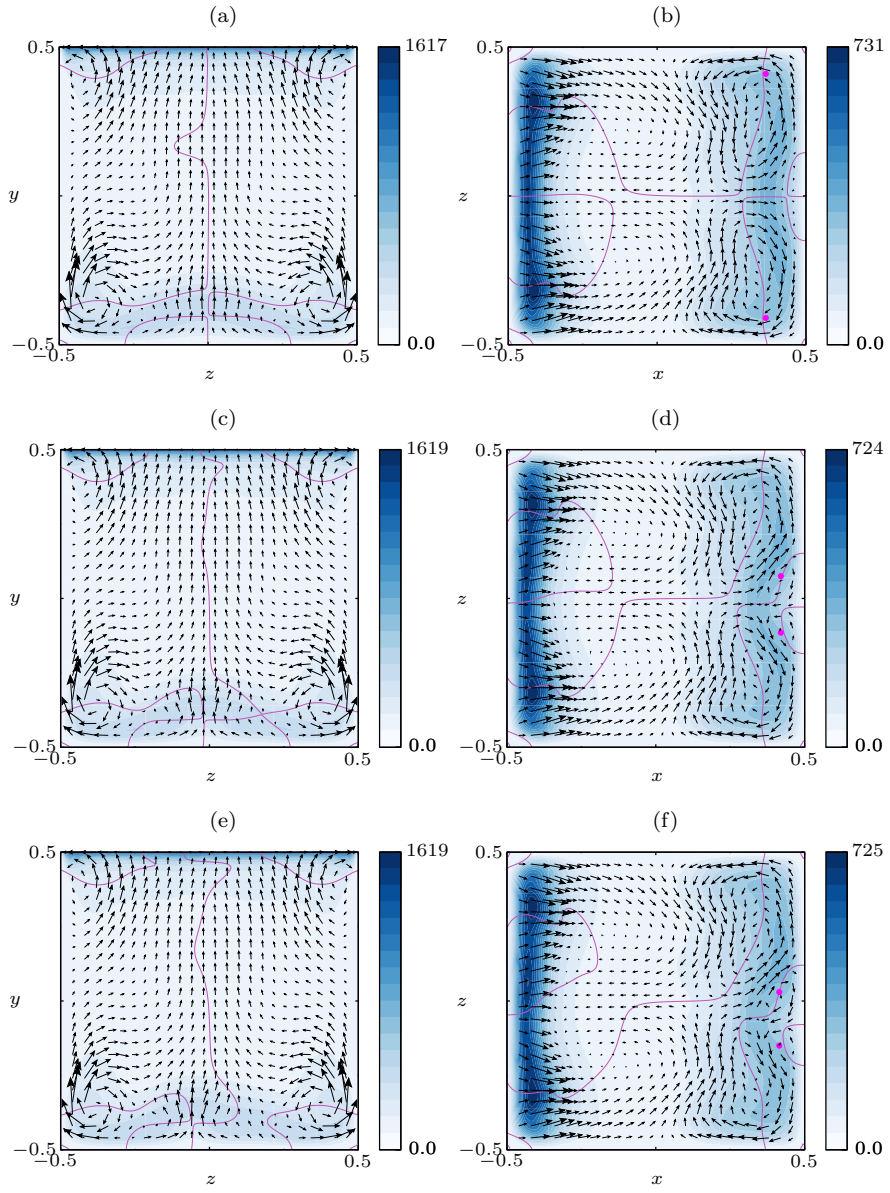

FIGURE 6.21 – Instantaneous snapshots of the damped velocity in the $x = 0$ plane (a,c,e) and in the $y = 0$ plane (b,d,f), at the times indicated in fig. 6.20(a) by the red dots: at $t = 3.427$ (a,b), at $t = 3.567$ (c,d) and at $t = 3.607$ (e,f). The color denotes the flow velocity magnitude while the arrows denote the in-plane components of the velocity field.

However, from fig. 6.20 one can see that the dynamics are similar (up to a time scale). In both cases, the system passes by a nearly symmetric state with $\mathcal{S} \in [10^{-5}, 10^{-4}]$ and then the asymmetry measure $\mathcal{S}$ increases in an exponential fashion before oscillations with a frequency close to ω_{LC1} start appearing. Eventually the oscillations are damped before the system settles again in a nearly symmetric state. Apparently, the direction in which the symmetry is breaking alternates, see fig. 6.20 (middle). To understand the flow states during these periodic patterns, we look at the damped velocity field shown in fig. 6.21, at the times marked by red dots in fig. 6.20 (top,middle). We see that in (a,b) that the flow is nearly symmetric but also resembles the basic flow S1 (6.5)(a,b). In particular the extrema of the product of the y-component of the velocity and the y-component of the vorticity $v\,\omega_y$ are also located near the spanwise wall in the large almost mirror-symmetric eddies. Then in (c,d), two nearly symmetric vortices have grown close to the plane $z = 0$, $x \in [0.4, 0.5]$. These are very much similar to those of the symmetric flow stemming from P2 and visible in fig. 6.12(a,b). Similarly, the extrema of $v\,\omega_y$ are located in the Taylor–Görtler vortices. In the mean time, symmetry breaking modes are growing and the two centered vortices are transported in the spanwise direction, as shown in fig. 6.21(e,f). It is perhaps better visible by comparing the location of the extrema of $v\,\omega_y$. This triggers the shedding of 5 vortices in this damped case (not shown). These vortices eventually weaken, and the symmetric flow is approached again, completing the loop. We have not been able to quantify the distances of the flow from both saddles S1 and S2, for the reason that even in the mirror symmetric subspace of solutions, the saddle S1 is not reachable (or at least not trivially). We tried increasing the Reynolds number gradually with a step $\Delta Re = 10$ together with the `BoostConv` algorithm, but even then the solution always settled on S2.

From these observation we anticipate that the evolution of the shear-driven cavity exhibits a Pomeau–Manneville scenario [130] where the limit cycle LC1 becomes unstable in only a single direction in phase space which caused the system to deviate from the limit cycle and initiate the burst. After a short exploration of the phase space, potentially visiting neighboring saddles like S1 and S2 the system may again settle on either LC1 and LC1' before the next burst event. The scenario on an increase of the Reynolds number is symbolically sketched in fig. 6.22. Further increasing the Reynolds number, the duration of the oscillations near LC1 becomes shorter and shorter and the system becomes more chaotic. The system is still characterized by the shedding of Taylor-Görler vortices, but their structure and spanwise direction of propagation becomes irregular. A similar route is also reported by Kalaev [72] for a filled cavity driven by an external gas stream.

6.5 Discussion and Conclusion

In general the flow in a cubic shear driven cavity shares characteristics with its lid-driven and open cavity counterparts. In both lid-driven and open cavity, the basic flow becomes unstable to spanwise periodic Taylor-Görler vortices with a high wave number, in both infinitely extended [5, 27] and finite-size cavities [55, 52].

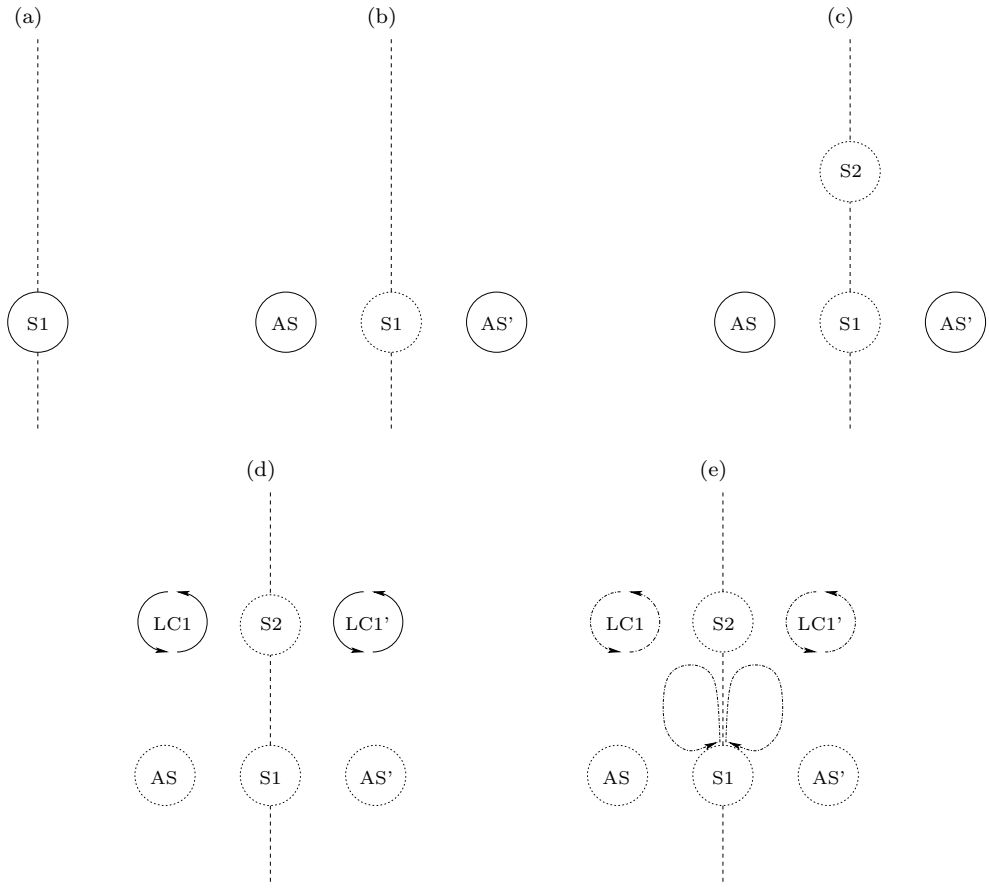

FIGURE 6.22 – The dashed line represents the subspace of mirror-symmetric solutions. Steady stable and unstable states are shown with full and dotted line circles, respectively. Stable limit cycle is shown with full line arrows, while unstable limit cycles are shown with dot-dashed arrows. (a) For $\mathrm{Re} < 53490$ the steady symmetric flow S1 is unique and stable. (b) S1 loses its stability to non oscillating perturbation and two non symmetric steady states AS and AS' that are antisymmetric with respect to each other appear. (c) S1 loses its stability to non-oscillating perturbation and a steady state S2 can be approached, S2 is stable in the symmetric subspace but unstable in the whole space of solutions. (d) At $\mathrm{Re} = 55\,715$, AS and AS' undergo Hopf bifurcations which lead to two limit cycles LC1 and LC1'. (e) Both LC1 and LC1' lose their stability in the long term, leading to a complex dynamic between the two limit cycles and the symmetric saddle states S1 and S2.

In particular, cubic cavities have been studied in different configurations. Kalaev [72] found that a flow in a cavity filled with a liquid and driven by a gas stream at its top surface becomes unsteady at $\mathrm{Re} \approx 55\,555$, and that a turbulent flow is achieved at $\mathrm{Re} = 10^5$. This agrees qualitatively well with our observation.

The instability mechanism is similar to the one reported in the lid-driven and open cavities. In the shear-driven cavity, using the terminology of Albensoeder *et al.* [5], the modes consists mainly of *stationnary* Taylor-Görtler vortices, whose centers are following the streamlines of the basic flow. The second component of the energy budget I_2 accounting for the transfer of kinetic energy extracted by the vortical structures and transfered to the streamwise velocity component of the perturbation flow is the main contributor to the perturbation energy production: $I_2 = 79\%$. This is consistent with the results of Loiseau *et al.* [100] who found for the cubic lid-driven cavity $I_2 = 81$ at slightly supercritical conditions. Loiseau *et al.* [100] linked it to the lift-up effect in boundary layer flows in which velocity streaks (i.e. $\boldsymbol{u}_{\parallel}$) are promoted by streamwise counter-rotating vortices (i.e. $\boldsymbol{u}_{\perp}$). Albensoeder *et al.* [5] draw the complementary conclusion that I_2 was also a footprint of centrifugal instabilities in this context. More elaborated criteria of Bayly *et al.* [19] and Sipp & Jacquin [163] cannot be used here as indicators for centrifugal instability, because the basic flow is three-dimensional, whereas the necessary condition to apply those criteria is that the basic flow should be two-dimensional.

Symmetry breaking was also observed numerically by Picella *et al.* [126] in the open cavity. They found modes breaking the symmetry being unstable slightly after symmetric modes became unstable. They, however, insisted that these mode have never been triggered in transient simulations. Loiseau [98] also found symmetry breaking modes in the lid-driven cavity, but they would become unstable only at higher Reynolds numbers.

The bifurcation scenario seems somehow similar to the one observed for axisymmetric liquid bridges for low Prandtl numbers [91], and for much lower Reynolds numbers. In a first destabilization step the axisymmetry is lost at $\mathrm{Re} = 1793$ [181] and the flow becomes thee-dimensional. Upon further increasing the Reynolds number to $\mathrm{Re} = 5960$, the three-dimensional flow becomes unstable to three-dimensional oscillating perturbations [94]. To the authors' best knowledge, no experimental nor numerical study on thermocapillary driven flow at low Prandtl number in a cubic cavity has ever been carried for Reynolds numbers of comparable magnitude. Although, with a similar code we recovered for $\mathrm{Pr} = 0.01$ the same symmetry breaking at a higher Reynolds numbers $\mathrm{Re}_{\mathrm{P1}} \in [68\,000, 70, 000]$, followed by oscillations upon increasing the driving strength $\mathrm{Re}_{\mathrm{H2}} \in [75\,000, 80\,000]$.

In previous studies [55, 100, 85, 101, 61], the cubic lid-driven cavity flow loses its time invariance through a slightly subcritical Hopf bifurcation leading to a limit cycle. Loiseau *et al.* [100]and Lopez *et al.* [101] noted that a second limit cycle is present and that through the bursts observed by Kuhlmann & Albensoeder [85] the system was visiting this second limit cycle. Here the situation is different: the two limit cycles are anti-symmetric to each other and through bursts and exploration of the phase space the system can settle on the opposite limit cycle, or come back to the same limit cycle. The burts may be related and due to the existence of some other limit cycle, which

we could not pinpoint, though. The existence of LC1 and LC1' adds another feature to the dynamics, not present in the lid-driven cavity, which further complicates the transition scenario.

It seems then that, although the setups are similar, with similar destabilization mechanisms, the bifurcation pattern is different and the path to turbulence changed. It would be of interest to test if changing the direction of the lid motion by a small yaw angle would also change the bifurcation pattern, by, e.g., giving preference to one of the limit cycles LC1.

7

General Conclusion

In this dissertation, we studied the flow in rectangular containers, driven by the tangential motion of one of the boundaries. We used the framework of the linear stability analysis to study the onset of instability in three different configurations.

Obliquely-Driven Cavity

In Chapter 4, we studied the incompressible steady two-dimensional flow in a square, a shallow and a deep cavities driven by a moving lid. The lid motion is tangential to the surface, but not aligned with the cross section: there is a yaw angle α. For all aspect ratios studied, we found that the critical Reynolds number of the linear theory is lower at moderate angles than in the limiting cases $\alpha = 0, \pi/4$. This is at odd with results reported in literature, but supported by non-linear transient simulations, carried out with an independent solver.

When the lid velocity is aligned with the cross section, we recovered the classical results from the lid-driven cavity. When the lid velocity moves nearly perpendicularly to the cross section the basic two-dimensional flow is strongly stabilized. The spanwise perturbation velocity component $\hat{w}$ is promoted by the cross-section components $\hat{u}$ and $\hat{v}$. This is the classical lift-up mechanism. However, the mechanisms promoting of the x- and y-components of the perturbation velocity drastically weaken as the lid motion angle increases to $\pi/4$. Therefore, the lack of feedback for the lift-up mechanism is responsible for the strong stabilization of the system for large angles.

Even though the critical Reynolds number from linear stability increases in the limit of large yaw angles, the system might become unstable to finite-amplitude perturbations for lower Reynolds numbers. Classically, the plane Couette flow is stable for all Reynolds numbers [47] but the onset of instability to finite-amplitude perturbations is about $\mathrm{Re} = 125$ [147]. Although the onset of three-dimensional flow due to finite-amplitude perturbations for laterally-bounded Couette flow has received less attention, we anticipate that, similarly, the bounded flow would also be unstable to finite-amplitude perturbations.

Thermocapillary-Driven Cavity

In Chapter 5, we investigated the thermocapillary-driven flow of a low- and a high-Prandtl-number fluid in a shallow cavity. In particular, we investigated the sensitivity of the growth rate of the three-dimensional perturbation for both Prandtl numbers.

To demonstrate the importance of the spatial distribution of the heat-flux along the free surface, we formulated a non-linear optimization problem in order to obtain heat-fluxes that efficiently shift the onset of flow oscillations. In particular, we showed that it is possible to both stabilize and destabilize the flow by a suitable imposed heat flux for both high- and low-Prandtl number fluids. Therefore, there is no one-to-one correspondence between the sign of the average heat flux along the surface and its effect on the stability of the system. It is rather the spatial distribution that dictates the effect on the onset of oscillatory flow.

The results demonstrate the need for an accurate modeling of the heat transfer in thermocapillary-driven flows when considering the liquid phase only. As most research has dealt with a cylindrical configuration, it would be of interest to extend the present analysis to cylindrical geometries.

The heat flux across the free surface in such geometries is often similar: the heat-flux profile exhibits sharp peaks close to the hot and cold corners due to the presence of thermal boundary layers. As the global shape of the flux is often known, it would also be of interest to apply a second-order sensitivity analysis as introduced by Boujo *et al.* [25]. This would allow a more accurate prediction of the variation of the growth rate of the most unstable mode for particular heat-flux profiles.

Finally, an extension of this work could be to investigate the effect of a heat source placed in the environment near the interface on the growth rate of the perturbation. To this end, one would need to simulate the gas phase as well and perform a similar sensitivity analysis. One could then obtain optimal positions of the heater to quench or promote the instability.

Cubic Shear-Driven Cavity

In Chapter 6, we considered the progressive loss of symmetries of the three-dimensional flow in a cubic cavity, driven by a constant shear. In a first step, the flow loses its mirror symmetry, as the basic flow becomes unstable to a Taylor–Görtler vortex, whose centerline lies in the midplane. By analyzing the finite-amplitude saturation of the mode, we could interpret this first destabilization as a supercritical pitchfork bifurcation. The system settles on one of two equilibria antisymmetric to each other. Upon further increasing the shear stress, the equilibria become unstable to oscillating perturbations, leading to two antisymmetric limit cycles. These Hopf bifurcations are also supercritical.

Upon further increasing the Reynolds number, the limit cycles also destabilize in some direction in phase space. The weak destabilization leads to bursting events during which the system visits the vicinity of several saddle points. Through these bursting

events the system can pass from one limit cycle to its antisymmetric counterpart. This constitutes an interesting dynamics between the limit cycles which is absent in the configuration of the lid-driven cubic cavity.

A natural extension of this work is to understand the mechanisms of destabilization of the limit cycles. This would involve a Floquet analysis, which could be implemented by minor changes in the solver used. In case the destabilization happens through a non-linear mechanism, a dynamic-mode decomposition can also be considered.

A

Sensitivity of the Eigenvalues to Variation of the Wavenumber

Based on the eigenvalue equation (2.9) of the form $[\gamma_i \boldsymbol{M} + \boldsymbol{A}(k)]\,\hat{\boldsymbol{q}}_i = 0$ where $\hat{\boldsymbol{q}}_i = (\hat{\boldsymbol{u}}_i, \hat{p}_i)^{\mathrm{T}}$ is the vector of the mode variables, we use the classical approach of [104] who considered the sensitivity of the eigenvalue γ_i and eigenvector $\hat{\boldsymbol{q}}_i$ with respect to a variation of the basic flow. As in [104], we treat like in an optimal control framework and define $\hat{\boldsymbol{q}}_i$ and γ_i being state variables and k being a control parameter. The Lagrangian is defined as

$$\mathcal{L}\left(\gamma_i, k, \hat{\boldsymbol{q}}_i, \hat{\boldsymbol{q}}_i^\dagger\right) = \gamma_i - \left\langle [\gamma_i \boldsymbol{M} + \boldsymbol{A}(k)]\,\hat{\boldsymbol{q}}_i, \hat{\boldsymbol{q}}_i^\dagger \right\rangle, \tag{A.1}$$

where $\hat{\boldsymbol{q}}_i^\dagger = \left(\hat{\boldsymbol{u}}_i^\dagger, \hat{p}_i^\dagger\right)^{\mathrm{T}}$ are the adjoint variables. Formally the first term of the right hand side is the cost function of the problem and the second term is enforcing the constraint through the lagrangian multipliers. Cancelling the derivative with respect to the lagrangian multiplier $\hat{\boldsymbol{q}}_i^\dagger$ is equivalent to enforcing the state equation *i.e.* the eigenvalue problem. Cancelling the derivative with respect to the state variables $\hat{\boldsymbol{q}}_i$ and γ_i is equivalent to solving the adjoint problem and enforcing a normalisation condition on $\hat{\boldsymbol{q}}_i$ and $\hat{\boldsymbol{q}}_i^\dagger$. Evaluating the derivative of the Lagrangian with respect to the parameter k will give us the gradient of the cost function and by construction the sensitivity of the eigenvalue with respect to variations of k.

Differentiating $\mathcal{L}$ with Respect to γ_i

Evaluating the differential of the Lagrangian functional (A.1) with respect to $\delta\gamma_i$ and requiring $\delta_{\gamma_i}\mathcal{L} = 0$ yields

$$\left\langle \nabla_{\gamma_i}\mathcal{L}\left(\gamma_i, k, \hat{\boldsymbol{q}}_i, \hat{\boldsymbol{q}}_i^\dagger\right), \delta\gamma_i \right\rangle = \delta\gamma_i - \gamma_i \left\langle \boldsymbol{M}\delta\hat{\boldsymbol{q}}_i, \hat{\boldsymbol{q}}_i^\dagger \right\rangle = 0. \tag{A.2}$$

This leads to the normalization condition

$$\left\langle \boldsymbol{M}\hat{\boldsymbol{q}}_i, \hat{\boldsymbol{q}}_i^\dagger \right\rangle = 1\ . \tag{A.3}$$

Differentiating $\mathcal{L}$ with Respect to any Eigenvector $\hat{\boldsymbol{q}}_i$

Setting the differential of the Lagrangian in the direction $\delta\hat{\boldsymbol{q}}_i$ to zero, $\delta_{\hat{\boldsymbol{q}}_i}\mathcal{L} = 0$, we obtain

$$\left\langle \nabla_{\hat{\boldsymbol{q}}_i}\mathcal{L}\left(\gamma_i, k, \hat{\boldsymbol{q}}_i, \hat{\boldsymbol{q}}_i^\dagger\right), \delta\hat{\boldsymbol{q}}_i \right\rangle = -\left\langle \left[\gamma_i \boldsymbol{M} + \boldsymbol{A}\left(k\right)\right]\delta\hat{\boldsymbol{q}}_i, \hat{\boldsymbol{q}}_i^\dagger \right\rangle = 0, \tag{A.4}$$

which leads to the adjoint eigenvalue problem

$$\left[\gamma_i^\dagger \boldsymbol{M} + \boldsymbol{A}^\dagger\right]\hat{\boldsymbol{q}}_i^\dagger = 0. \tag{A.5}$$

A.0.1 Differentiating $\mathcal{L}$ with Respect to k

Considering $\delta_k\mathcal{L} = 0$ we obtain

$$\left\langle \nabla_k\mathcal{L}\left(\gamma_i, k, \hat{\boldsymbol{q}}_i, \hat{\boldsymbol{q}}_i^\dagger\right), \delta k \right\rangle = -\left\langle \frac{\partial \boldsymbol{A}\left(k\right)}{\partial k}\delta k\hat{\boldsymbol{q}}_i, \hat{\boldsymbol{q}}_i^\dagger \right\rangle. \tag{A.6}$$

In the present formulation $\boldsymbol{A}$ is the right hand side of (4.8). Taking the derivative of the vectorial form of these equations with respect to k we obtain

$$\left\langle \frac{\partial \boldsymbol{A}(k)\hat{\boldsymbol{q}}_i}{\partial k}\delta k, \hat{\boldsymbol{q}}_i^\dagger \right\rangle = \left\langle 2k\,\delta k\,\hat{\boldsymbol{u}}_i, \hat{\boldsymbol{u}}_i^\dagger \right\rangle + \mathrm{i}\left\langle w_0\hat{\boldsymbol{u}}_i\,\delta k, \hat{\boldsymbol{u}}_i^\dagger \right\rangle + \mathrm{i}\left\langle \hat{p}_i\,\delta k, \hat{w}_i^\dagger \right\rangle + \mathrm{i}\left\langle \hat{w}_i\,\delta k, \hat{p}_i^\dagger \right\rangle. \tag{A.7}$$

The first term on the right hand side derives from the viscous diffusion. The following terms derive from the transport of perturbation momentum in the spanwise direction, the pressure gradient and the continuity equation. Finally we obtain the sensitivity of the eigenvalue γ_i with respect to wave number changes

$$\frac{\partial\gamma_i}{\partial k}\delta k = \langle \nabla_k\mathcal{L}, \delta k\rangle = -2k\,\delta k - \mathrm{i}\left\langle w_0\hat{\boldsymbol{u}}_i, \hat{\boldsymbol{u}}_i^\dagger \right\rangle \delta k - \mathrm{i}\left\langle \hat{p}_i, \hat{w}_i^\dagger \right\rangle \delta k - \mathrm{i}\left\langle \hat{w}_i, \hat{p}_i^\dagger \right\rangle \delta k, \tag{A.8}$$

where we used the normalisation $\left\langle \hat{\boldsymbol{u}}_i, \hat{\boldsymbol{u}}_i^\dagger \right\rangle = 1$ which derives from (A.3).

B

Sensitivities

In this appendix, the sensitivity of an eigenvalue to small variations in the basic flow variables, to a small source term in momentum and heat equation, and to changes in the boundary condition will be derived, that were used in Chapter 5. Therefore we keep the same setup and notations.

The equations will be derived for an incompressible fluid driven by surface tension but also by buoyancy forces. We also consider Newton's cooling law for the heat flux at the free surface. We will see that these two variations from the problem studied in Chapter 5 do not affect the final expressions.

First we will focus on the derivation of the adjoint equations, needed afterward. Then we will follow the steps of Marquet *et al.* [104] and derive the structural sensitivity (or sensitivity to changes in the basic flow), and then the heat flux sensitivity. In this appendix, we will use the denomination from the thermocapillary-driven cavity of Chapter 5.

B.0.1 Notations

First let us define some notation: the scalar product on the the volume is defined as

$$\langle \boldsymbol{a}, \boldsymbol{b} \rangle = \int_V \boldsymbol{a}^* \cdot \boldsymbol{b} \, \mathrm{d}V,$$

and the scalar product on the free surface S as

$$\langle \boldsymbol{a}, \boldsymbol{b} \rangle_S = \int_S \boldsymbol{a}^* \cdot \boldsymbol{b} \, \mathrm{d}S \ .$$

Let us denote $\mathcal{A}$ a linear application. The adjoint of $\mathcal{A}$, denoted $\mathcal{A}^\dagger$ is defined by the relation

$$\langle \boldsymbol{a}, \mathcal{A}\boldsymbol{b} \rangle = \left\langle \mathcal{A}^\dagger \boldsymbol{a}, \boldsymbol{b} \right\rangle \ .$$

B.1 Equations for the Linear Stability Analysis

B.1.1 Basic Flow

Let us consider the non-dimensional Navier–Stokes equations in the framework of the Boussinesq approximation

$$(\partial_t + \boldsymbol{u}\cdot\nabla)\boldsymbol{u} = -\nabla p + \Delta\boldsymbol{u} + \mathrm{Gr}\,\theta\boldsymbol{e}_g + \boldsymbol{F}, \tag{B.1a}$$

$$\nabla\cdot\boldsymbol{u} = 0, \tag{B.1b}$$

$$(\partial_t + \boldsymbol{u}\cdot\nabla)\theta = \frac{1}{\mathrm{Pr}}\Delta\theta + q, \tag{B.1c}$$

subject to the boundary conditions for the velocity $\boldsymbol{u}$

$$\boldsymbol{u} = 0 \qquad \text{at all walls}, \tag{B.2a}$$

$$\boldsymbol{u}\cdot\boldsymbol{n} = 0 \qquad \text{at } y = 1/2, \tag{B.2b}$$

$$\left[\left(\nabla\boldsymbol{u} + \nabla\boldsymbol{u}^T\right)\cdot\boldsymbol{n}\right]\cdot\boldsymbol{t}_i + \mathrm{Re}\nabla_{\boldsymbol{t}_i}\theta = 0 \qquad , \tag{B.2c}$$

and for the temperature θ

$$\theta = \pm 1/2 \qquad \text{at } x = \pm\Gamma/2, \tag{B.2d}$$

$$\nabla\theta\cdot\boldsymbol{n} + \mathrm{Bi}(\theta - \theta_a) = f \qquad \text{at } y = 1/2, \tag{B.2e}$$

$$\nabla\theta\cdot\boldsymbol{n} = 0 \qquad \text{at } y = -1/2. \tag{B.2f}$$

We made use of the Reynolds, Grashof, Prandtl and Biot numbers which we define as

$$\mathrm{Re} = \frac{\Sigma_1\Delta T h}{\rho\nu}; \quad \mathrm{Gr} = \frac{g\beta\Delta T h^3}{\nu^2}; \quad \mathrm{Pr} = \frac{\nu}{\kappa}; \quad \mathrm{Bi} = \frac{lh}{k}, \tag{B.3}$$

where h is a typical length of the system, ρ is the fluid density, ν is the kinematic viscosity, Σ_1 is opposite of the rate of change of the surface tension upon changing temperature, g is the gravitational acceleration and β is the thermal expansion coefficient.

One particular solution of this equation is the solution of the steady Navier–Stokes equation

$$\boldsymbol{u}_0\cdot\nabla\boldsymbol{u}_0 = -\nabla p_0 + \Delta\boldsymbol{u}_0 + \mathrm{Gr}\,\theta_0\boldsymbol{e}_g, \tag{B.4a}$$

$$\nabla\cdot\boldsymbol{u}_0 = 0, \tag{B.4b}$$

$$\boldsymbol{u}_0\cdot\nabla\theta_0 = \frac{1}{\mathrm{Pr}}\Delta\theta_0, \tag{B.4c}$$

together with the same boundary conditions (B.2a).

Remark In the last section, one will denote the basic flow equations and boundary condition as

$$\mathcal{F}(\boldsymbol{q}_0) = \boldsymbol{f}, \tag{B.5}$$

where $\boldsymbol{q}_0 = (\boldsymbol{u}_0, p_0, \theta_0)^T$, $\boldsymbol{f}$ denotes a potential external forcing through an volume force $\boldsymbol{F}$ or volume heat source q or a heat flux at the free surface f. In this case, it will be assumed to be zero.

B.1.2 Perturbation Equation : An Eigenvalue Problem

As in Chapter 2, linearizing (B.1a) around the basic state $\boldsymbol{q}_0$ and taking a normal mode ansatz, we obtain the generalized eigenvalue problem

$$(\gamma_i + \boldsymbol{u}_0 \cdot \nabla)\,\hat{\boldsymbol{u}}_i + \hat{\boldsymbol{u}}_i \cdot \nabla \boldsymbol{u}_0 = -\nabla \hat{p}_i + \Delta \hat{\boldsymbol{u}}_i + \mathrm{Gr}\,\hat{\theta}_i \boldsymbol{e}_g, \tag{B.6a}$$

$$\nabla \cdot \hat{\boldsymbol{u}}_i = 0, \tag{B.6b}$$

$$(\gamma_i + \boldsymbol{u}_0 \cdot \nabla)\,\hat{\theta}_i + \hat{\boldsymbol{u}}_i \cdot \nabla \theta_0 = \frac{1}{\mathrm{Pr}}\,\Delta \hat{\theta}_i, \tag{B.6c}$$

subject to the boundary conditions for the velocity $\hat{\boldsymbol{u}}_i$

$$\hat{\boldsymbol{u}}_i = 0 \qquad \text{at all walls,} \tag{B.7a}$$

$$\hat{\boldsymbol{u}}_i \cdot \boldsymbol{n} = 0 \qquad \text{at the free surface } y = 1/2, \tag{B.7b}$$

$$\left[\left(\nabla \hat{\boldsymbol{u}} + \nabla \hat{\boldsymbol{u}}^T\right) \cdot \boldsymbol{n}\right] \cdot \boldsymbol{t}_i + \mathrm{Re} \nabla_{\boldsymbol{t}_i} \hat{\theta} = 0, \tag{B.7c}$$

and for the temperature $\hat{\theta}_i$

$$\hat{\theta}_i = 0 \qquad \text{at the lateral walls } x = \pm \Gamma/2, \tag{B.7d}$$

$$\nabla \hat{\theta}_i \cdot \boldsymbol{n} - \mathrm{Bi}\,\hat{\theta}_i = 0 \qquad \text{at } y = 1/2, y = -1/2. \tag{B.7e}$$

This is an eigenvalue problem which can be written

$$\gamma \mathbf{B} \hat{\boldsymbol{q}} + \mathcal{A} \hat{\boldsymbol{q}} = 0, \tag{B.8}$$

where $\mathcal{A}$ is a linear application that depends on $\boldsymbol{q}_0$.

B.1.3 Derivation of the Adjoint Eigenvalue Problem

Let us derive then the Adjoint perturbation equation, which will show to be of use by the next sections.

By definition of the adjoint, one searches $\mathcal{A}^\dagger$ such that

$$\left\langle \mathcal{A} \hat{\boldsymbol{q}}, \hat{\boldsymbol{q}}^\dagger \right\rangle = \left\langle \mathcal{A}^\dagger \hat{\boldsymbol{q}}^\dagger, \hat{\boldsymbol{q}} \right\rangle. \tag{B.9}$$

Expliciting the integrals

$$\begin{aligned}\left\langle \hat{\boldsymbol{q}}^\dagger, \mathcal{A}\hat{\boldsymbol{q}} \right\rangle = &\int_V \gamma \hat{\boldsymbol{u}}^\dagger \cdot \hat{\boldsymbol{u}}^* \,\mathrm{d}V + \int_V \hat{\boldsymbol{u}}^\dagger \cdot \boldsymbol{u}_0 \cdot \nabla \hat{\boldsymbol{u}}^* \,\mathrm{d}V + \int_V \hat{\boldsymbol{u}}^\dagger \cdot \hat{\boldsymbol{u}}^* \cdot \nabla \boldsymbol{u}_0 \,\mathrm{d}V \\ &- \int_V \hat{\boldsymbol{u}}^\dagger \cdot \nabla \hat{p}^* \,\mathrm{d}V - \int_V \hat{\boldsymbol{u}}^\dagger \Delta \hat{\boldsymbol{u}}^* \,\mathrm{d}V + \mathrm{Gr} \int_V \hat{\theta}^* \, \hat{\boldsymbol{u}}^\dagger \cdot \boldsymbol{e}_g \,\mathrm{d}V \\ &+ \int_V \hat{p}^\dagger \nabla \cdot \hat{\boldsymbol{u}}^* \\ &+ \int_V \gamma \hat{\theta}^\dagger \hat{\theta}^* \,\mathrm{d}V + \int_V \hat{\theta}^\dagger \boldsymbol{u}_0 \cdot \nabla \hat{\theta}^* \,\mathrm{d}V + \int_V \hat{\theta}^\dagger \hat{\boldsymbol{u}}^* \cdot \nabla \theta_0 \,\mathrm{d}V \\ &- \frac{1}{\mathrm{Pr}} \int_V \hat{\theta}^\dagger \Delta \hat{\theta}^* \,\mathrm{d}V. \end{aligned} \tag{B.10}$$

The two first lines of the latter equation come from the momentum equations, the third line is the continuity constraint, and the two last lines come from the heat equation. One wants to isolate the perturbation variables *i.e.* not having the differentiation terms applying on $\hat{\boldsymbol{u}}$, $\hat{p}$ and $\hat{\theta}$ but rather on their respective adjoints $\hat{\boldsymbol{u}}^\dagger$,$\hat{p}^\dagger$ and $\hat{\theta}^\dagger$. Integrating by parts the terms differentiating the pertubation variables, and using the fact that $\boldsymbol{u}'$ is a solenoidal vectorfield, yields

$$\begin{aligned}\left\langle \hat{\boldsymbol{q}}, \mathcal{A}^\dagger \hat{\boldsymbol{q}}^\dagger \right\rangle = &\int_V \gamma \hat{\boldsymbol{u}}^* \cdot \hat{\boldsymbol{u}}^\dagger \,\mathrm{d}V - \int_V \hat{\boldsymbol{u}}^* \cdot \boldsymbol{u}_0 \cdot \nabla \hat{\boldsymbol{u}}^\dagger \,\mathrm{d}V + \int_V \hat{\boldsymbol{u}}^* \cdot \hat{\boldsymbol{u}}^\dagger \cdot (\nabla \boldsymbol{u}_0)^T \,\mathrm{d}V \\ &+ \int_V \hat{p}^* \nabla \cdot \hat{\boldsymbol{u}}^\dagger \,\mathrm{d}V - \int_V \hat{\boldsymbol{u}}^* \Delta \hat{\boldsymbol{u}}^\dagger \,\mathrm{d}V + \mathrm{Gr} \int_V \hat{\theta}^* \hat{\boldsymbol{u}}^\dagger \cdot \boldsymbol{e}_g \,\mathrm{d}V \\ &+ \int_S \hat{\boldsymbol{u}}^\dagger \cdot \boldsymbol{u}_0 \underbrace{\hat{\boldsymbol{u}}^* \cdot \boldsymbol{n}}_{=0} \,\mathrm{d}S + \int_S \hat{p}^* \hat{\boldsymbol{u}}^\dagger \cdot \boldsymbol{n} \,\mathrm{d}S \\ &- \int_S \hat{\boldsymbol{u}}^\dagger \cdot \nabla \hat{\boldsymbol{u}}^* \cdot \boldsymbol{n} \,\mathrm{d}S + \int_S \hat{\boldsymbol{u}}^* \cdot \nabla \hat{\boldsymbol{u}}^\dagger \cdot \boldsymbol{n} \,\mathrm{d}S \\ &- \int_V \hat{\boldsymbol{u}}^* \cdot \nabla \hat{p}^\dagger \,\mathrm{d}V + \int_S \hat{p}^* \hat{\boldsymbol{u}}^\dagger \cdot \boldsymbol{n} \,\mathrm{d}S \\ &+ \int_V \gamma \hat{\theta}^* \hat{\theta}^\dagger \,\mathrm{d}V - \int_V \hat{\theta}^* \boldsymbol{u}_0 \cdot \nabla \hat{\theta}^\dagger \,\mathrm{d}V + \int_V \hat{\theta}^\dagger \hat{\boldsymbol{u}}^* \cdot \nabla \theta_0 \,\mathrm{d}V \\ &- \frac{1}{\mathrm{Pr}} \int_V \hat{\theta}^* \Delta \hat{\theta}^\dagger \,\mathrm{d}V \\ &+ \int_S \hat{\theta}^* \hat{\theta}^\dagger \boldsymbol{u}_0 \cdot \boldsymbol{n} \,\mathrm{d}S - \frac{1}{\mathrm{Pr}} \int_S \hat{\theta}^\dagger \underbrace{\nabla \hat{\theta}^* \cdot \boldsymbol{n}}_{=-\mathrm{Bi}\,\hat{\theta}^*} \,\mathrm{d}S + \frac{1}{\mathrm{Pr}} \int_S \hat{\theta}^* \nabla \hat{\theta}^\dagger \cdot \boldsymbol{n} \,\mathrm{d}S. \end{aligned}$$

From this we can deduce that the adjoint problem is defined as

$$\begin{aligned} &\gamma^\dagger \hat{\boldsymbol{u}}^\dagger - \boldsymbol{u}_0 \cdot \nabla \hat{\boldsymbol{u}}^\dagger + \hat{\boldsymbol{u}}^\dagger \cdot (\nabla \boldsymbol{u}_0)^T + \hat{\theta}^\dagger \nabla \theta_0 = \nabla \hat{p}^\dagger + \Delta \hat{\boldsymbol{u}}^\dagger, \\ &\nabla \cdot \hat{\boldsymbol{u}}^\dagger = 0, \\ &\gamma^\dagger \hat{\theta}^\dagger - \boldsymbol{u}_0 \cdot \nabla \hat{\theta}^\dagger = \frac{1}{\mathrm{Pr}} \Delta \hat{\theta}^\dagger + \mathrm{Gr}\, \hat{\boldsymbol{u}}^\dagger \cdot \boldsymbol{e}_g, \end{aligned} \tag{B.11}$$

combined with the boundary conditions on the adjoint velocity mode $\hat{\boldsymbol{u}}_i^\dagger$

$$\hat{\boldsymbol{u}}_i^\dagger = 0 \qquad \text{at all walls,} \tag{B.12a}$$

$$\hat{\boldsymbol{u}}_i^\dagger \cdot \boldsymbol{n} = 0 \qquad \text{at } y = 1/2, \tag{B.12b}$$

$$\left[\left(\nabla\hat{\boldsymbol{u}}^\dagger + \nabla\hat{\boldsymbol{u}}^{\dagger\,T}\right)\cdot\boldsymbol{n}\right]\cdot\boldsymbol{t}_k = 0, \tag{B.12c}$$

and for the temperature $\hat{\theta}_i^\dagger$

$$\hat{\theta}_i^\dagger = 0 \qquad \text{at } x = \pm\Gamma/2, \tag{B.12d}$$

$$\nabla\hat{\theta}_i^\dagger \cdot \boldsymbol{n} = 0 \qquad \text{at } y = -1/2, \tag{B.12e}$$

$$\nabla\hat{\theta}_i \cdot \boldsymbol{n} - \mathrm{Bi}\,\hat{\theta}_i - \mathrm{Pr}\,\mathrm{Re}\nabla_{\boldsymbol{t}}\cdot\hat{\boldsymbol{u}}_i^\dagger = 0 \qquad \text{at } y = 1/2, \tag{B.12f}$$

where $\nabla_{\boldsymbol{t}}\hat{\boldsymbol{u}}_i^\dagger$ the divergence of the tangential component (see below).

We note the apparition of a Marangoni number at the temperature boundary condition (Ma = RePr). One notices that the production of temperature adjoint perturbation is now in the momentum equation, the gravity term are now in the heat equation. These adjoint equation are in agreement with what can be found in the literature, *e.g.* [24].

The boundary at the free surface for the temperature is, however, far from being evident: stress free boundary condition at the free surface for the adjoint velocity and a flux of the adjoint temperature through the free surface that is proportional to the tangential part of the velocity's divergence. Follows its derivation.

Adjoint thermal boundary condition at the free surface

$$\int_{S_F} \hat{\boldsymbol{u}}^\dagger \cdot \nabla\hat{\boldsymbol{u}} \cdot \boldsymbol{n}\,\mathrm{d}S = \int_{S_F} \Big(\underbrace{(\hat{\boldsymbol{u}}^\dagger \cdot \boldsymbol{n})}_{=0}\boldsymbol{n} + (\hat{\boldsymbol{u}}^\dagger \cdot \boldsymbol{t}_1)\boldsymbol{t}_1 + (\hat{\boldsymbol{u}}^\dagger \cdot \boldsymbol{t}_2)\boldsymbol{t}_2 \Big) \cdot \nabla\hat{\boldsymbol{u}} \cdot \boldsymbol{n}\,\mathrm{d}S \tag{B.13}$$

$$\begin{aligned}\nabla\hat{\boldsymbol{u}}\cdot\boldsymbol{n} &= ((\nabla\hat{\boldsymbol{u}}\cdot\boldsymbol{n})\cdot\boldsymbol{n})\boldsymbol{n} + ((\nabla\hat{\boldsymbol{u}}\cdot\boldsymbol{n})\cdot\boldsymbol{t}_1)\boldsymbol{t}_1 + ((\nabla\hat{\boldsymbol{u}}\cdot\boldsymbol{n})\cdot\boldsymbol{t}_2)\boldsymbol{t}_2 \\ &= ((\nabla\hat{\boldsymbol{u}}\cdot\boldsymbol{n})\cdot\boldsymbol{n})\boldsymbol{n} - \mathrm{Re}(\nabla\hat{\theta}\cdot\boldsymbol{t}_1)\boldsymbol{t}_1 - \mathrm{Re}(\nabla\hat{\theta}\cdot\boldsymbol{t}_2)\boldsymbol{t}_2. \end{aligned} \tag{B.14}$$

Inserting the result in the previous equation, gives

$$\begin{aligned}\int_{S_F} \hat{\boldsymbol{u}}^\dagger \cdot \nabla\hat{\boldsymbol{u}} \cdot \boldsymbol{n}\,\mathrm{d}S &= -\mathrm{Re}\int_{S_F} \Big[(\hat{\boldsymbol{u}}^\dagger \cdot \boldsymbol{t}_1)\boldsymbol{t}_1 + (\hat{\boldsymbol{u}}^\dagger \cdot \boldsymbol{t}_2)\boldsymbol{t}_2\Big] \cdot \Big[(\nabla\hat{\theta}\cdot\boldsymbol{t}_1)\boldsymbol{t}_1 + (\nabla\hat{\theta}\cdot\boldsymbol{t}_2)\boldsymbol{t}_2\Big]\,\mathrm{d}S \\ &= -\mathrm{Re}\int_{S_F} (\hat{\boldsymbol{u}}^\dagger \cdot \boldsymbol{t}_1)(\nabla\hat{\theta}\cdot\boldsymbol{t}_1) + (\hat{\boldsymbol{u}}^\dagger \cdot \boldsymbol{t}_2)(\nabla\hat{\theta}\cdot\boldsymbol{t}_2)\,\mathrm{d}S. \end{aligned}$$

Integrating by part gives

$$\int_{S_F} \hat{\boldsymbol{u}}^\dagger \cdot \nabla\hat{\boldsymbol{u}} \cdot \boldsymbol{n}\,\mathrm{d}S = \mathrm{Re}\int_{S_F} \partial_{\boldsymbol{t}_1}(\hat{\boldsymbol{u}}^\dagger \cdot \boldsymbol{t}_1)\hat{\theta} + \partial_{\boldsymbol{t}_2}(\hat{\boldsymbol{u}}^\dagger \cdot \boldsymbol{t}_2)\hat{\theta}\,\mathrm{d}S.$$

Then one can deduce the thermal boundary condition at the free surface

$$\nabla\hat{\theta}^\dagger \cdot \boldsymbol{n} = -\mathrm{Bi}\,\hat{\theta}^\dagger + \mathrm{PrRe}\nabla_{\boldsymbol{t}} \cdot \hat{\boldsymbol{u}}^\dagger, \tag{B.15}$$

where $\nabla_{\boldsymbol{t}} \cdot \bullet = \sum_{i=1}^{2} \partial_{\boldsymbol{t}_i} \bullet \cdot \boldsymbol{t}_i$, which can be thought as "the tangential part of the divergence".

B.2 Sensitivity of γ to Changes in the Basic Flow

One is interested in the changes of stability that can be induced to variation of the basic flow variables. It can be useful for instance if one wants to quantify the error on the eigenvalue when one knows that a region of the flow is subject to computational error *e.g.* in the thermocapillary driven cavity, close to the free surface cold corner where the gradients are particularly strong. The derivation is similar to what Marquet *et al.* [104], or [108] for a compressible fluid. To that end, let us introduce a Lagrangian functional

$$\mathcal{L}(\gamma, \hat{\boldsymbol{q}}, \boldsymbol{q}_0, \hat{\boldsymbol{q}}^\dagger) = \gamma - \left\langle \hat{\boldsymbol{q}}^\dagger, \gamma\mathbf{B}\hat{\boldsymbol{q}} + \mathcal{A}(\boldsymbol{q}_0)\hat{\boldsymbol{q}} \right\rangle, \tag{B.16}$$

where $\hat{\boldsymbol{q}}^\dagger$ is the Lagrangian multiplier enforcing the constraint $\gamma\mathbf{B}\hat{\boldsymbol{q}} + \mathcal{A}(\boldsymbol{q}_0)\hat{\boldsymbol{q}} = 0$. Note that when the latter constraint is satisfied, a small variation of this Lagrangian functional $\delta\mathcal{L}$ is equal to a small variation of the growth rate $\delta\gamma$. Therefore, when the constraint on the eigenvalue problem is satisfied, one has

$$\begin{aligned}\delta\gamma &= \left\langle \nabla_{\boldsymbol{q}_0}\gamma, \delta\boldsymbol{q}_0 \right\rangle \\ &= \left\langle \nabla_{\boldsymbol{q}_0}\mathcal{L}, \delta\boldsymbol{q}_0 \right\rangle.\end{aligned}$$

To get this sensitivity to changes in the basic flow $\nabla_{\boldsymbol{q}_0}\gamma$, one has to cancel all the other derivatives of the Lagrangian function with respect to $\gamma, \hat{\boldsymbol{q}}, \hat{\boldsymbol{q}}^\dagger$.

with respect to γ

$$\frac{\partial}{\partial\gamma}\mathcal{L} \cdot \delta\gamma = \delta\gamma - \left\langle \hat{\boldsymbol{q}}^\dagger, \delta\gamma\,\mathbf{B}\hat{\boldsymbol{q}} \right\rangle,$$

which brings the normalisation condition

$$\left\langle \hat{\boldsymbol{q}}^\dagger, \mathbf{B}\hat{\boldsymbol{q}} \right\rangle = 1. \tag{B.17}$$

with respect to $\hat{\boldsymbol{q}}^\dagger$ As the eigenvalue problem is supposed to be fulfilled, one trivially has that $\frac{\partial}{\partial\hat{\boldsymbol{q}}^\dagger}\mathcal{L} \cdot \delta\hat{\boldsymbol{q}}^\dagger = 0$.

with respect to $\hat{q}$

$$\frac{\partial}{\partial \hat{\boldsymbol{q}}}\mathcal{L}\cdot\delta\hat{\boldsymbol{q}} = \left\langle \hat{\boldsymbol{q}}^\dagger, \gamma\mathbf{B}\hat{\boldsymbol{q}} + \mathcal{A}\hat{\boldsymbol{q}}\right\rangle \tag{B.18}$$

$$= \left\langle \gamma^\dagger\mathbf{B}\hat{\boldsymbol{q}}^\dagger + \mathcal{A}\hat{\boldsymbol{q}}^\dagger, \delta\hat{\boldsymbol{q}}\right\rangle \tag{B.19}$$

$$= 0 \tag{B.20}$$

where $\mathcal{A}^\dagger$ is the adjoint of $\mathcal{A}$ which has been derived in the previous section. It defines the adjoint eigenvalue problem.

with respect to $\boldsymbol{q}_0$

$$\frac{\partial}{\partial \boldsymbol{q}_0}\mathcal{L}\cdot\delta\boldsymbol{q}_0 = -\left\langle \hat{\boldsymbol{q}}^\dagger, \left[\frac{\partial}{\partial \boldsymbol{q}_0}\mathcal{A}(\boldsymbol{q}_0)\right]\cdot\delta\boldsymbol{q}_0\cdot\hat{\boldsymbol{q}}\right\rangle \tag{B.21}$$

where

$$\left[\frac{\partial}{\partial \boldsymbol{q}_0}\mathcal{A}(\boldsymbol{q}_0)\right]\cdot\delta\boldsymbol{q}_0\cdot\hat{\boldsymbol{q}} = \begin{pmatrix} \delta\boldsymbol{u}_0\cdot\nabla\hat{\boldsymbol{u}} + \hat{\boldsymbol{u}}\cdot\nabla\delta\boldsymbol{u}_0 \\ 0 \\ \delta\boldsymbol{u}_0\cdot\nabla\hat{\theta} + \hat{\boldsymbol{u}}\cdot\nabla\delta\theta_0 \end{pmatrix}, \tag{B.22}$$

in which the second line is to remind that the perturbation continuity equation does not depends on the basic flow, actually only the terms of transport and production of perturbation variables are kept. Now the integral reads

$$\left\langle \left[\frac{\partial}{\partial \boldsymbol{q}_0}\mathcal{A}(\boldsymbol{q}_0)\right]\cdot\delta\boldsymbol{q}_0\cdot\hat{\boldsymbol{q}}, \hat{\boldsymbol{q}}^\dagger\right\rangle = \int_V \hat{\boldsymbol{u}}^\dagger\delta\boldsymbol{u}_0\cdot\nabla\hat{\boldsymbol{u}}^* + \hat{\boldsymbol{u}}^\dagger\hat{\boldsymbol{u}}^*\cdot\nabla\delta\boldsymbol{u}_0\ \mathrm{d}V,$$
$$+\int_V \hat{\theta}^\dagger\delta\boldsymbol{u}_0\nabla\hat{\theta}^* + \hat{\theta}^\dagger\hat{\boldsymbol{u}}^*\cdot\nabla\delta\theta_0\ \mathrm{d}V. \tag{B.23}$$

Integrating by part the terms related to production (using that $\nabla\cdot\hat{\boldsymbol{u}}$), and using the transpose of the gradients in the term related to transport

$$\left\langle \left[\frac{\partial}{\partial \boldsymbol{q}_0}\mathcal{A}(\boldsymbol{q}_0)\right]\cdot\hat{\boldsymbol{q}}^\dagger\cdot\hat{\boldsymbol{q}}, \delta\boldsymbol{q}_0\right\rangle = \int_V \delta\boldsymbol{u}_0\cdot\hat{\boldsymbol{u}}^\dagger\cdot\nabla\hat{\boldsymbol{u}}^H - \delta\boldsymbol{u}_0\cdot\hat{\boldsymbol{u}}^*\cdot\nabla\hat{\boldsymbol{u}}^\dagger\ \mathrm{d}V$$
$$+\int_V \delta\boldsymbol{u}_0\cdot\nabla\hat{\theta}^*\hat{\theta}^\dagger - \delta\theta_0\hat{\boldsymbol{u}}^*\cdot\nabla\hat{\theta}^\dagger\ \mathrm{d}V. \tag{B.24}$$

All the boundary terms vanish, because $\hat{\boldsymbol{u}}\cdot\boldsymbol{n} = \hat{\boldsymbol{u}}^\dagger\cdot\boldsymbol{n} = 0$. One can identify the gradient

$$\nabla_{\boldsymbol{q}_0}\gamma = \left[\frac{\partial}{\partial \boldsymbol{q}_0}\mathcal{A}(\boldsymbol{q}_0)\right]^\dagger\cdot\hat{\boldsymbol{q}}^\dagger\hat{\boldsymbol{q}}, \tag{B.25}$$

and explicitly

$$\nabla_{\boldsymbol{q}_0}\gamma = \begin{pmatrix} -\hat{\boldsymbol{u}}^\dagger\cdot\nabla\hat{\boldsymbol{u}}^H + \hat{\boldsymbol{u}}^*\cdot\nabla\hat{\boldsymbol{u}}^\dagger - \hat{\theta}^\dagger\nabla\hat{\theta}^* \\ 0 \\ \hat{\boldsymbol{u}}^*\cdot\nabla\hat{\theta}^\dagger \end{pmatrix}. \tag{B.26}$$

where the superscript H denotes the transpose of the conjugate. Besides, one can identify the terms related to production (where gradient of adjoint variables appears) and the terms related to transport (the others).

B.3 Sensitivity of γ to a Heat Flux Variation at the Free Surface

To derive the sensitivity of γ to a heat flux variation at the free surface, one can use the a similar approach as in the previous section. Knowing the sensitivity to heat flux can be of interest when one wants to control the flow with the heat flux, or to find the flux at the boundary, given experimental data.

We refer to Marquet *et al.* [104] for the derivation of the sensitivity to steady forces. Tchoufag *et al.* [172] used a similar method to study the eigenvalue sensitivity of the wake after a bubble to changes in tangential stress or normal velocity at the bubble interface and what follows is mainly small changes to this, in order to obtain the heat flux sensitivity. Recently Boujo *et al.* [25] extended this framework to second order sensitivity.

B.3.1 Derivation

The problem that we will consider is the following

$$\mathcal{F}(\boldsymbol{q}_0) = \boldsymbol{0}, \tag{B.27}$$
$$\gamma \mathbf{B}\hat{\boldsymbol{q}} + \mathcal{A}(\boldsymbol{q}_0)\cdot\hat{\boldsymbol{q}} = 0, \tag{B.28}$$
$$\nabla\theta_0 \cdot \boldsymbol{n} + \mathrm{Bi}\theta 0 = f. \tag{B.29}$$

The term $\mathcal{F}(\boldsymbol{q}_0)$ encompasses the Steady Navier–Stokes (B.1a), together with the appropriate boundary conditions described in (B.2a). The second line represent the eigenvalue problem from the linear stability analysis. The third line correspond to the boundary condition at the free surface with the control flux f. As before let us use a Lagrangian functional

$$\begin{aligned}\mathcal{L}(\gamma, \boldsymbol{q}, \boldsymbol{q}_0, \boldsymbol{q}_0^\dagger, \hat{\boldsymbol{q}}^\dagger, f, f^\dagger) = \gamma &- \left\langle \hat{\boldsymbol{q}}^\dagger, \gamma\mathbf{B}\hat{\boldsymbol{q}} + \mathcal{A}(\boldsymbol{q}_0)\hat{\boldsymbol{q}} \right\rangle \\ &- \left\langle \boldsymbol{q}_0^\dagger, \mathcal{F}(\boldsymbol{q}_0) \right\rangle \\ &- \left\langle f^\dagger, \nabla\theta_0\cdot\boldsymbol{n} + \mathrm{Bi}\theta_0 - f \right\rangle_S .\end{aligned} \tag{B.30}$$

For the same reason as in the previous section, we want to cancel the derivative of $\mathcal{L}$ with respect to $\gamma, \boldsymbol{q}, \boldsymbol{q}_0, \boldsymbol{q}_0^\dagger, \hat{\boldsymbol{q}}^\dagger, f^\dagger$. The derivative with respect to adjoint quantities are trivially obtained. Canceling the derivative with respect to gamma will give the normalization condition (B.17). Canceling the derivative with respect to $\hat{\boldsymbol{q}}$ will lead to the adjoint perturbation eigenvalue problem (B.18).

Differentiation with Respect to $\boldsymbol{q}_0$

The differentiation with respect to the basic flow variables gives three term:

$$\left\langle \nabla_{\boldsymbol{q}_0}\mathcal{L}, \delta\boldsymbol{q}_0 \right\rangle = -\left\langle \hat{\boldsymbol{q}}^\dagger, \left[\partial_{\boldsymbol{q}_0}\mathcal{A}(\boldsymbol{q}_0)\right]\delta\boldsymbol{q_0}\hat{\boldsymbol{q}} \right\rangle \tag{B.31}$$

$$-\left\langle \boldsymbol{q}_0^\dagger, \left[\partial_{\boldsymbol{q}_0}\mathcal{F}(\boldsymbol{q}_0)\right]\delta\boldsymbol{q}_0 \right\rangle \tag{B.32}$$

$$-\left\langle f^\dagger, \nabla\delta\theta_0\cdot\boldsymbol{n} + \mathrm{Bi}\delta\theta_0 \right\rangle_S . \tag{B.33}$$

We can notice that first term of the right hand side of (B.31) is already know from the previous section and corresponds to the sensitivity to changes in the basic flow. The second term (B.32) is essentially the linearized Navier-Stokes operator around $\boldsymbol{q}_0$, except that the boundary conditions are not fixed yet since we allow variations of the basic flow also in the boundary condition. They will notably appear in the double integration by part of the Laplacians. Here we only look at the temperature diffusion, but the same is done for the viscous terms.

$$\begin{aligned}\frac{1}{\mathrm{Pr}}\int_V \Delta\delta\theta_0\theta_0^\dagger \,\mathrm{d}V = \frac{1}{Pr}\int_V \delta\theta_0\Delta\theta_0^\dagger \,\mathrm{d}V \\ + \frac{1}{\mathrm{Pr}}\int_S \left(\nabla\delta\theta_0\cdot\boldsymbol{n} + \mathrm{Bi}\,\delta\theta_0\right)\theta_0^\dagger \,\mathrm{d}S \\ - \frac{1}{\mathrm{Pr}}\int_S \left(\nabla\theta_0^\dagger\cdot\boldsymbol{n} + \mathrm{Bi}\,\theta_0^\dagger\right)\delta\theta_0 \,\mathrm{d}S\end{aligned}$$

where we added and subtracted the term with the Biot number in second and third line, respectively. The third line corresponds to the boundary conditions of the adjoint problem, while the second line are extra terms coming from the integration. One can then notice that the operator $[\partial_{\boldsymbol{q_0}}\mathcal{B}(\boldsymbol{q}_0)]^\dagger$ is in fact $\mathcal{A}(\boldsymbol{q}_0)^\dagger$. Then the equation (B.31) reads

$$\left\langle \nabla_{\boldsymbol{q}_0}\mathcal{L}, \delta\boldsymbol{q}_0 \right\rangle = \left\langle \nabla_{\boldsymbol{q}_0}\gamma, \delta_{\boldsymbol{q}_0} \right\rangle - \left\langle \mathcal{A}(\boldsymbol{q}_0)^\dagger\boldsymbol{q}_0^\dagger, \delta\boldsymbol{q}_0 \right\rangle \tag{B.34}$$

$$+\left\langle \frac{\theta_0^\dagger}{\mathrm{Pr}}, \nabla\delta\theta_0 + \mathrm{Bi}\,\delta\theta_0 \right\rangle_S - \left\langle f^\dagger, \nabla\delta\theta_0 + \mathrm{Bi}\,\delta\theta_0 \right\rangle_S , \tag{B.35}$$

where the first line corresponds to the volume terms and the second line to the surface terms. To cancel this gradient component, one needs to cancel volume terms and surface terms separately. Then come the equalities

$$\mathcal{A}(\boldsymbol{q}_0)\boldsymbol{q}_0^\dagger = \nabla_{\boldsymbol{q}_0}\gamma \tag{B.36}$$

$$\frac{\theta_0^\dagger}{\mathrm{Pr}} = f^\dagger. \tag{B.37}$$

From (B.36), we obtain a linear system of equations, which allows use to find the adjoint basic flow $\boldsymbol{q}_0^\dagger$, provided that one already computed the structural sensitivity using the eigenmode and its adjoint. The second equation (B.37) gives a relation between the adjoint flux variable and the adjoint basic temperature.

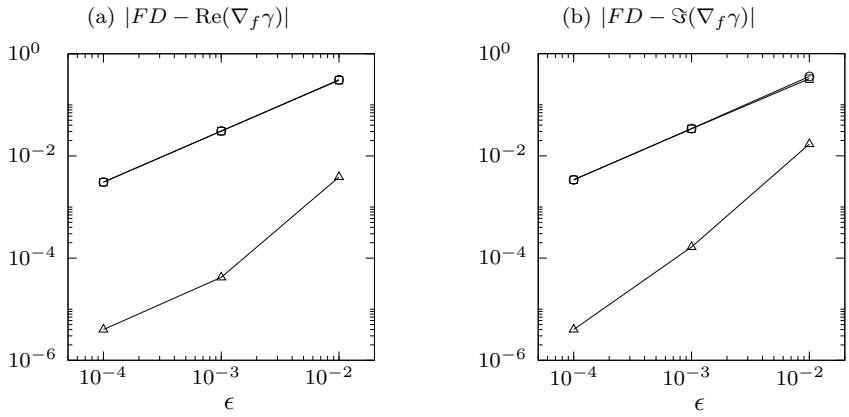

FIGURE B.1 – Evolution of the relative difference between the finite difference estimation and the sensitivity, (a) real part, (b) imaginary part. Circles and squares denote finite difference of first order forward and backward, respectively, triangles denote centered finite difference of second order.

Differentiation with Respect to f

Differentiating with respect to flux gives

$$\langle \nabla_f \mathcal{L}, \delta f \rangle = \left\langle f^\dagger, \delta f \right\rangle_S . \tag{B.38}$$

Using then the relation (B.37), one gets

$$\langle \nabla_f \mathcal{L}, \delta f \rangle = \left\langle \frac{\theta_0^\dagger}{\mathrm{Pr}}, \delta f \right\rangle_S . \tag{B.39}$$

Finally, one can conclude that the eigenvalue sensitivity to changes in the flux reads

$$\nabla_f \gamma = \frac{\theta_0^\dagger}{\mathrm{Pr}}. \tag{B.40}$$

This expression can be numerical verified, as in the next subsection.

B.3.2 Numerical Validation

To validate numerically both the implementation and the previous derivation, we check the evolution of the difference estimation between finite difference and the sensitivity as the finite difference results get more accurate. To that end, we consider the setup $\mathrm{Re} = 844.9$, $\mathrm{Pr} = 4.4$, $\Gamma = 3$, $k = 1.618$, polynomial order $N = 3$, on a mesh adapted using the variational adaptive mesh solver implemented in FEniCS in order to have the norm of the stress tensor converged for this particular setup.

Practically, we evaluate the largest eigenvalue $\gamma_1(f_0)$) with an adiabatic free surface so $f_0(x) = 0$ and with a perturbation flux scaled with a parameter epsilon $\gamma_1(f_0 + \epsilon f)$,

where $f = x$ is chosen arbitrarily. Estimation of the sensitivity of the eigenvalue to fluxes of that shape f can be obtained with first order finite difference, forward and backward, and with a centered scheme, that read

$$FD_F = \frac{\gamma_1(f_0 + \epsilon f) - \gamma_1(f_0)}{\epsilon} + \mathcal{O}(\epsilon),$$
$$FD_B = \frac{\gamma_1(f) - \gamma_1(f_0 - \epsilon f)}{\epsilon} + \mathcal{O}(\epsilon),$$
$$FD_C = \frac{\gamma_1(f_0 + \epsilon f) - \gamma_1(f_0 - \epsilon f)}{2\epsilon} + \mathcal{O}(\epsilon^2),$$

respectively. The evolution of $|\gamma_f \gamma_0 - FD|$ for both real and imaginary part is shown in fig. B.1, the convergence toward the same number validates the implementation and theory.

Bibliography

[1] Aidun, C. K., Triantafillopoulos, N. G. & Benson, J. D. 1991 Global stability of a lid-driven cavity with throughflow: Flow visualization studies. *Phys. Fluids A* **3**, 2081–2091.

[2] Åkervik, E., Brandt, L., Henningson, D. S., Hopffner, J., Marxen, O. & Schlatter, P. 2006 Steady solutions of the Navier–Stokes equations by selective frequency damping. *Phys. Fluids* **18**, 068102–1–068102–4.

[3] Albensoeder, S. & Kuhlmann, H. C. 2005 Accurate three-dimensional lid-driven cavity flow. *J. Comput. Phys.* **206**, 536–558.

[4] Albensoeder, S. & Kuhlmann, H. C. 2006 Nonlinear three-dimensional flow in the lid-driven square cavity. *J. Fluid Mech.* **569**, 465–480.

[5] Albensoeder, S., Kuhlmann, H. C. & Rath, H. J. 2001 Three-dimensional centrifugal-flow instabilities in the lid-driven cavity problem. *Phys. Fluids* **13**, 121–135.

[6] Alekseenko, S. V., Kuibin, P. A., Okulov, V. L. & Shtork, S. I. 1999 Helical vortices in swirl flow. *J. Fluid Mech.* **382**, 195–243.

[7] Alizard, F., Robinet, J.-C. & Gloerfelt, X. 2012 A domain decomposition matrix-free method for global linear stability. *Computers & Fluids* **66**, 63–84.

[8] Alnaes, M., Blechta, J., Hake, J., Johansson, A., Kehlet, B., Logg, A., Richardson, C., Ring, J., Rognes, M. E. & Wells, G. N. 2015 The fenics project version 1.5. *Arch. Num. Soft.* **3**.

[9] Amestoy, P., Buttari, A., L'Excellent, J.-Y. & Mary, T. 2019 Performance and Scalability of the Block Low-Rank Multifrontal Factorization on Multicore Architectures. *ACM Trans. Math. Software* **45**, 2:1–2:26.

[10] Amestoy, P., Duff, I. S., Koster, J. & L'Excellent, J.-Y. 2001 A fully asynchronous multifrontal solver using distributed dynamic scheduling. *SIAM J. Matrix Anal. Appl.* **23**, 15–41.

[11] Anderson, J. D. 2016 *Some Reflections on the History of Fluid Dynamics*, 2nd edn.

[12] Antoulas, A. C. 2005 *Approximation of Large-Scale Dynamical Systems*. Society for Industrial and Applied Mathematics.

[13] Arnoldi, W. E. 1951 The principle of minimized iterations in the solution of the matrix eigenvalue problem. *Quart. Appl. Math.* **9**, 17–29.

[14] Auteri, F., Quartapelle, L. & Vigevano, L. 2002 Accurate ω-ψ spectral solution of the singular driven cavity problem. *J. Comput. Phys.* **180**, 597–615.

[15] Avriel, M. 2012 *Nonlinear Programming : Analysis and Methods*. Dover Publications.

[16] Bagheri, S., Åkervik, E., Brandt, L. & Hennignson, D. S. 2009 Matrix-free methods for the stability and control of boundary layers. *AIAA J.* **47**, 1057–1068.

[17] Barkley, D. & Henderson, R. D. 1996 Three-dimensional Floquet stability analysis of the wake of a circular cylinder. *J. Fluid Mech.* **322**, 215–241.

[18] Batchelor, G. K. 1967 *An Introduction to Fluid Dynamics*. Cambridge University Press.

[19] Bayly, B. J., Orszag, S. A. & Herbert, T. 1988 Instability mechanisms in shear flow transition. *Annu. Rev. Fluid Mech.* **20**, 359–391.

[20] Benz, S., Hintz, P., Riley, R. J. & Neitzel, G. P. 1998 Instability of thermocapillary-buoyancy convection in shallow layers. part 2. suppression of hydrothermal waves. *J. Fluid Mech.* **359**, 165–180.

[21] Biswas, S. & Kalita, J. C. 2020 Topology of corner vortices in the lid-driven cavity flow: 2d vis a vis 3d **90**, 2201–2216.

[22] Botella, O. & Peyret, R. 1998 Benchmark spectral results on the lid-driven cavity flow. *Comp. Fluids* **27**, 421–433.

[23] Botella, O. & Peyret, R. 2001 Computing singular solutions of the Navier–Stokes equations with the Chebyshev-collocation method. *Int. J. Num. Meth. Fluids* **36**, 125–163.

[24] Bouizi, O. & Delcarte, C. 2006 Adjoint approach of the spatial sensitivity to disturbances of internal flows with free surface. *Int. J. Numer. Methods Fluids* **50**, 947–972.

[25] Boujo, E., Fani, A. & Gallaire, F. 2019 Second-order sensitivity in the cylinder wake: Optimal spanwise-periodic wall actuation and wall deformation. *Physical Review Fluids* **4**.

[26] Brandt, L. 2014 The lift-up effect: The linear mechanism behind transition and turbulence in shear flows. *Eur. J. Mech. B. Fluids* **47**, 80 – 96.

[27] Brés, G. A. & Colonius, T. 2008 Three-dimensional instabilities in compressible flow over open cavities. *J. Fluid Mech.* **599**, 309–339.

[28] Bruneau, C.-H. & Saad, M. 2006 The 2d lid-driven cavity problem revisited. *Comp. Fluids* **35**, 326–348.

[29] Bucci, M. A. 2017 Subcritical and supercritical dynamics of incompressible flow over miniaturized roughness elements. PhD thesis, École nationale supérieure d'arts et métiers - ENSAM.

[30] Bucci, M. A., Puckert, D. K., Andriano, C., Loiseau, J.-C., Cherubini, S., Robinet, J.-C. & Rist, U. 2018 Roughness-induced transition by quasi-resonance of a varicose global mode. *J. Fluid Mech.* **836**, 167–191.

[31] Burggraf, O. R. 1966 Analytical and numerical studies of the structure of steady separated flows. *J. Fluid Mech.* **24**, 113–151.

[32] Burguete, J., Mukolobwiez, N., Daviaud, F., Garnier, N. & Chiffaudel, A. 2001 Buoyant-thermocapillary instabilities in extended liquid layers subjected to a horizontal temperature gradient. *Phys. Fluids* **13**, 2773–2787.

[33] Carpenter, B. M. & Homsy, G. M. 1989 Combined buoyant-thermocapillary flow in a cavity. *J. Fluid Mech.* **207**, 121–132.

[34] Carpenter, B. M. & Homsy, G. M. 1990 High Marangoni number convection in a square cavity: Part II. *Phys. Fluids A* **2**, 137–149.

[35] Charru, F. & de Forcrand-Millard, P. 2009 *Hydrodynamic Instabilities*. Cambridge University Press.

[36] Chernyshenko, S. & Baig, M. 2005 Streaks and vortices in near-wall turbulence. *Philosophical Transactions of the Royal Society A: Mathematical, Physical and Engineering Sciences* **363**, 1097–1107.

[37] Chomaz, J.-M. 2005 Global instabilities in spatially developing flows: Non-normality and nonlinearity. *Annu. Rev. Fluid Mech.* **37**, 357–392.

[38] Citro, V., Giannetti, F., Brandt, L. & Luchini, P. 2015 Linear three-dimensional global and asymptotic stability analysis of incompressible open cavity flow. *J. Fluid Mech.* **768**, 113–140.

[39] Citro, V., Luchini, P., Giannetti, F. & Auteri, F. 2017 Efficient stabilization and acceleration of numerical simulation of fluid flows by residual recombination. *J. Comput. Phys.* **344**, 234–246.

[40] Cunha, G., Passaggia, P.-Y. & Lazareff, M. 2015 Optimization of the selective frequency damping parameters using model reduction. *Phys. Fluids* **27**, 094103.

[41] Daviaud, F. & Vince, J. M. 1993 Travelling waves in a fluid layer subjected to a horizontal temperature gradient. *Phys. Rev. E* **48**, 4432–4436.

[42] De Vahl Davis, G. & Mallinson, G. D. 1976 An evaluation of upwind and central difference approximations by a study of recirculating flow. *Comp. Fluids* **4**, 29–43.

[43] Deville, M. O., Fischer, P. F. & Mund, E. H. 2002 *High-Order Methods for Incompressible Fluid Flow*. Cambridge University Press.

[44] Ding, Y. & Kawahara, M. 1998 Linear stability of incompressible fluid flow in a cavity using finite element method. *Int. J. Num. Meth. Fluids* **27**, 139–157.

[45] Ding, Y. & Kawahara, M. 1999 Three-dimensional linear stability analysis of incompressible viscous flows using the finite element method. *Int. J. Num. Meth. Fluids* **31**, 451–479.

[46] Drazin, P. G. 2002 *Introduction to hydrodynamic stability*. Cambridge: Cambridge University Press.

[47] Drazin, P. G. & Reid, W. H. 1981 *Hydrodynamic Stability*. Cambridge: Cambridge University Press.

[48] van Eckeveld, A. C., Westerweel, J. & Poelma, C. 2017 Mitigation of whistling in vertical corrugated pipes by liquid addition. *Exp. Fluids* **58**.

[49] Edwards, W. S., Tuckerman, L. S., Friesner, R. A. & Sorensen, D. C. 1994 Krylov methods for the incompressible Navier–Stokes equations. *J. Comput. Phys.* **110**, 82–102.

[50] Ellingsen, T. & Palm, E. 1975 Stability of linear flow. *Phys. Fluids* **18**, 487–488.

[51] Faure, T., Pastur, L., Lusseyran, F., Fraigneau, Y. & Bisch, D. 2009 Three-dimensional centrifugal instabilities development inside a parallelepipedic open cavity of various shape. *Exp. Fluids* **47**, 395–410.

[52] Faure, T. M., Adrianos, P., Lusseyran, F. & Pastur, L. 2007 Visualizations of the flow inside an open cavity at medium range Reynolds numbers. *Exp. Fluids* **42**, 169–184.

[53] Fefferman, C. L. 2000 Existence and smoothness of the Navier–Stokes equation.

[54] Feldman, Y. 2015 Theoretical analysis of three-dimensional bifurcated flow inside a diagonally lid-driven cavity. *Theor. Comput. Fluid Dyn.* **29**, 245–261.

[55] Feldman, Y. & Gelfgat, A. Y. 2010 Oscillatory instability of a three-dimensional lid-driven flow in a cube. *Phys. Fluids* **22**, 093602–1–093602–9.

[56] Finlayson, B. A. 1972 *The Method of Weighted Residuals and Variational Principles*. Academic Press.

[57] Floquet, G. 1883 Sur les équations différentielles linéaires à coefficients périodiques. *Annales scientifiques de l'École normale supérieure* **12**, 47–88.

[58] Fortin, A., Jardak, M., Gervais, J. & Pierre, R. 1997 Localization of Hopf bifurcation in fluid flow problems. *Int. J. Numer. Methods Fluids* **24**, 1185–1210.

[59] Gallaire, F. & Chomaz, J.-M. 2003 Instability mechanisms in swirling flows. *Phys. Fluids* **15**, 2622–2639.

[60] Gelfgat, A., ed. 2019 *Computational Modelling of Bifurcations and Instabilities in Fluid Dynamics*. Springer International Publishing.

[61] Gelfgat, A. Y. 2019 Linear instability of the lid-driven flow in a cubic cavity. *Theor. Comput. Fluid Dyn.* .

[62] Gelfgat, A. Y. & Molokov, S. 2011 Quasi-two-dimensional convection in a three-dimensional laterally heated box in a strong magnetic field normal to main circulation. *Physics of Fluids* **23**, 034101.

[63] Ghia, U., Ghia, K. N. & Shin, C. T. 1982 High-Re solutions for incompressible flow using the Navier-Stokes equations and a multigrid method. *J. Comput. Phys.* **48**, 387–411.

[64] Godrèche, C. & Manneville, P. 1998 *Hydrodynamics and Nonlinear Instabilities*. Cambridge: Cambridge University Press.

[65] Hadid, H. B. & Roux, B. 1992 Buoyancy- and thermocapillary-driven flows in differentially heated cavities for low-prandtl-number fluids. *J. Fluid Mech.* **235**, 1–36.

[66] Hill, D. C. 1992 A theoretical approach for analyzing the restabilization of wakes. In *30th Aerospace Sciences Meeting and Exhibit*. American Institute of Aeronautics and Astronautics.

[67] Hurle, D. T. J. & Series, R. W. 1994 Use of a magnetic field in melt growth. In *Handbook of Crystal Growth* (ed. D. T. J. Hurle), , vol. 2a, p. 259. North Holland.

[68] Itano, T. & Toh, S. 2001 The dynamics of bursting process in wall turbulence. *J. Phys. Soc. Japan* **70**, 703–716.

[69] Jeong, J. & Hussain, F. 1995 On the identification of a vortex. *J. Fluid Mech.* **285**, 69–94.

[70] Jordi, B. E., Cotter, C. J. & Sherwin, S. J. 2015 An adaptive selective frequency damping method. *Phys. Fluids* **27**, 094104–1–094104–8.

[71] Joseph, D. D. 1976 *Stability of Fluid motions I*, *Springer Tracts in Natural Philosophy*, vol. 27. Berlin, Heidelberg: Springer.

[72] Kalaev, V. V. 2012 Liquid flow in a cubic cavity generated by gas motion along the free surface. *Int. J. Heat and Mass Tran.* **55**, 5214–5221.

[73] Kamotani, Y., Wang, L., Hatta, S., Wang, A. & Yoda, S. 2003 Free surface heat loss effect on oscillatory thermocapillary flow in liquid bridges of high Prandtl number fluids. *Intl J. Heat Mass Transfer* **46**, 3211–3220.

[74] Karniadakis, G. & Sherwin, S. 2005 *Spectral/hp Element Methods for Computational Fluid Dynamics*. Oxford University Press.

[75] Kawaguti, M. 1961 Numerical solution of the Navier–Stokes equations for the flow in a two-dimensional cavity. *J. Phys. Soc. Jap.* **16**, 2307–2315.

[76] Keller, J. B. & Miksis, M. J. 1983 Surface tension driven flows. *SIAM Journal on Applied Mathematics* **43**, 268–277.

[77] Knoll, D. A. & Keyes, D. E. 2004 Jacobian-free Newton–Krylov methods: a survey of approaches and applications. *J. Comput. Phys.* **193**, 357–397.

[78] Koseff, J. R. & Street, R. L. 1984 The lid-driven cavity flow: A synthesis of qualitative and quantitative observations. *J. Fluids Eng.* **106**, 390–398.

[79] Koseff, J. R. & Street, R. L. 1984 On endwall effects in a lid-driven cavity flow. *J. Fluids Eng.* **106**, 385–389.

[80] Koseff, J. R. & Street, R. L. 1984 Visualization studies of a shear driven three-dimensional recirculating flow. *J. Fluids Eng.* **106**, 21–29.

[81] Koseff, J. R., Street, R. L., Gresho, P. M., Upson, C. D., Humphrey, J. A. C. & To, W.-M. 1983 A three-dimensional lid-driven cavity flow: Experiment and simulation. In *Proceedings of the 3rd International Conference on Numerical Methods in Laminar and Turbulent Flow* (ed. C. Taylor), pp. 564–581. Swansea: Pineridge Press.

[82] Ku, H. C., Hirsh, R. S. & Taylor, T. D. 1987 A pseudospectral method for solution of the three-dimensional incompressible Navier–Stokes equations. *J. Comput. Phys.* **70**, 439–462.

[83] Kuhlmann, H. & Albensoeder, S. 2008 Three-dimensional flow instabilities in a thermocapillary-driven cavity. *Phys. Rev. E* **77**, 036303–1–036303–15.

[84] Kuhlmann, H. C. 1999 *Thermocapillary Convection in Models of Crystal Growth*, *Springer Tracts in Modern Physics*, vol. 152. Berlin, Heidelberg: Springer.

[85] Kuhlmann, H. C. & Albensoeder, S. 2014 Stability of the steady three-dimensional lid-driven flow in a cube and the supercritical flow dynamics. *Phys. Fluids* **26**, 024104–1–024104–11.

[86] Kuhlmann, H. C. & Nienhüser, C. 2002 Dynamic free-surface deformations in thermocapillary liquid bridges. *Fluid Dyn. Res.* **31**, 103–127.

[87] Kuhlmann, H. C. & Romanò, F. 2018 *The Lid-Driven Cavity*, *Computational Methods in Applied Sciences*, vol. 50, pp. 233–309. Berlin, Heidelberg: Springer.

[88] Lanczos, C. 1950 An iteration method for the solution of the eigenvalue problem of linear differential and integral operators. *J. Res. Natl. Bur. Stand. (U. S.)* **45**, 255–282.

[89] Lehoucq, R. B. & Sorensen, D. C. 1996 Deflation techniques for an implicitly restarted arnoldi iteration. *SIAM Journal on Matrix Analysis and Applications* **17**, 789–821.

[90] Levenstam, M. 1994 Thermocapillary convection in floatzones. PhD thesis, Royal Institute of Technology, Stockholm.

[91] Levenstam, M., Amberg, G. & Winkler, C. 2001 Instabilities of thermocapillary convection in a half-zone at intermediate Prandtl numbers. *Phys. Fluids* **13**, 807–816.

[92] Levich, V. G. & Krylov, V. S. 1969 Surface tension-driven phenomena. *Annu. Rev. Fluid Mech.* **1**, 293–316.

[93] Leypoldt, J. 1999 Dreidimensionale numerische Simulation thermokapillarer Strömungen in zylindrischen flüssigkeitsbrücken. PhD thesis, Universität Bremen.

[94] Leypoldt, J., Kuhlmann, H. C. & Rath, H. J. 2000 Three-dimensional numerical simulation of thermocapillary flows in cylindrical liquid bridges. *J. Fluid Mech.* **414**, 285–314.

[95] Liberzon, A., Feldman, Y. & Gelfgat, A. Y. 2011 Experimental observation of the steady-oscillatory transition in a cubic lid-driven cavity. *Phys. Fluids* **23**, 084106–1–084106–7.

[96] Lifschitz, A. & Hameiri, E. 1991 Local stability conditions in fluid dynamics. *Phys. Fluids A* **3**, 2644–2651.

[97] Logg, A., Mardal, K.-A. & Wells, G. 2012 *Automated Solution of Differential Equations by the Finite Element Method*. Springer Berlin Heidelberg.

[98] Loiseau, J.-C. 2014 Dynamics and global stability of three-dimensional flows. PhD thesis, École nationale supérieure d'arts et métiers - ENSAM.

[99] Loiseau, J.-C., Bucci, M., Cherubini, S. & Robinet, J.-C. 2019 *Time-Stepping and Krylov Methods for Large-Scale Instability Problems*, pp. 33–73. Cham: Springer International Publishing.

[100] Loiseau, J.-C., Robinet, J.-C. & Leriche, E. 2016 Intermittency and transition to chaos in the cubical lid-driven cavity flow. *Fluid Dyn. Res.* **48**, 061421–1–061421–11.

[101] Lopez, J. M., Welfert, B. D., Wu, K. & Yalim, J. 2017 Transition to complex dynamics in the cubic lid-driven cavity. *Phys. Rev. Fluids* **2**, 074401–1–074401–23.

[102] Marangoni, C. 1865 Sull'espansione delle goccie d'un liquido galleggianti sulla superfice di altro liquido. PhD thesis, Università di Pavia.

[103] Marcus, P. S. & Tuckerman, L. S. 1987 Simulation of flow between concentric rotating spheres. part 2. transitions. *J. Fluid Mech.* **185**, 31–65.

[104] Marquet, O., Sipp, D. & Jacquin, L. 2008 Sensitivity analysis and passive control of cylinder flow. *J. Fluid Mech.* **615**, 221–252.

[105] Mathur, M., Ortiz, S., Dubos, T. & Chomaz, J.-M. 2014 Effects of an axial flow on the centrifugal, elliptic and hyperbolic instabilities in stuart vortices. *J. Fluid Mech.* **758**, 565–585.

[106] Maxwell, J. C. 1890 Capillary action. In *The Scientific Papers of James Clerk Maxwell* (ed. W. D. Niven), pp. 541–591. Cambridge University Press.

[107] Mayer, E. W. & Powell, K. G. 1992 Viscous and inviscid instabilities of a trailing vortex. *J. Fluid Mech.* **245**, 91–114.

[108] Meliga, P. & Chomaz, J. 2010 Global modes in a confined impinging jet: application to heat transfer and control. *Theor. Comput. Fluid Dyn.* **25**, 179–193.

[109] Meliga, P., Sipp, D. & Chomaz, J.-M. 2010 Open-loop control of compressible afterbody flows using adjoint methods. *Phys. Fluids* **22**, 054109.

[110] Mialdun, A. & Shevtsova, V. 2006 Influence of interfacial heat exchange on the flow organization in liquid bridge. *Microgravity Sci. Technol.* **18**, 146–149.

[111] Motegi, K., Fujimura, K. & Ueno, I. 2017 Floquet analysis of spatially periodic thermocapillary convection in a low-Prandtl-number liquid bridge. *Phys. Fluids* **29**, 074104.

[112] Muldoon, F. H. 2012 Control of hydrothermal waves in a thermocapillary flow using a gradient-based control strategy. *Int. J. Num. Meth. Fluids* .

[113] Muldoon, F. H. 2018 Numerical study of hydrothermal wave suppression in thermocapillary flow using a predictive control method. *Comp. Math. Math. Phys.* **58**, 493–507.

[114] Muldoon, F. H. & Kuhlmann, H. C. 2015 Objective function choice for control of a thermocapillary flow using an adjoint-based control strategy. *Int. J. Heat Fluid Flow* **56**, 28–42.

[115] Nakabayashi, K., Tsuchida, Y. & Zheng, Z. 2002 Characteristics of disturbances in the laminar–turbulent transition of spherical Couette flow. 1. spiral Taylor–Görtler vortices and traveling waves for narrow gaps. *Phys. Fluids* **14**, 3963–3972.

[116] Neitzel, G. P., Chang, K.-T., Jankowski, D. F. & Mittelmann, H. D. 1993 Linear-stability theory of thermocapillary convection in a model of the float-zone crystal-growth process. *Phys. Fluids A* **5**, 108–114.

[117] Nienhüser, C. & Kuhlmann, H. C. 2002 Stability of thermocapillary flows in non-cylindrical liquid bridges. *J. Fluid Mech.* **458**, 35–73.

[118] Olendraru, C. & Sellier, A. 2002 Viscous effects in the absolute–convective instability of the Batchelor vortex. *J. Fluid Mech.* **459**, 371–396.

[119] Pan, F. & Acrivos, A. 1967 Steady flows in rectangular cavities. *J. Fluid Mech.* **28**, 643–655.

[120] Patera, A. T. 1984 A spectral element method for fluid dynamics: Laminar flow in a channel expansion. *J. Comput. Phys.* **54**, 468–488.

[121] Peng, Y.-F., Shiau, Y.-H. & Hwang, R. R. 2003 Transition in a 2-D lid-driven cavity flow. *Comp. Fluids* **32**, 337–352.

[122] Peplinski, A., Schlatter, P., Fischer, P. F. & Henningson, D. S. 2014 Stability tools for the spectral-element code Nek5000: Application to jet-in-crossflow. In *Spectral and High Order Methods for Partial Differential Equations-ICOSAHOM 2012*, pp. 349–359. Springer.

[123] Peplinski, A., Schlatter, P. & Henningson, D. S. 2015 Global stability and optimal perturbation for a jet in cross-flow. *Eur. J. Mech. B/Fluids* **49**, 438–447.

[124] Petrov, V., Haaning, A., Muehlner, K. A., VanHook, S. J. & Swinney, H. L. 1998 Model-independent nonlinear control algorithm with application to a liquid bridge experiment. *Phys. Rev. E* **58**, 427–431.

[125] Petrov, V., Schatz, M. F., Muehlner, K. A., VanHook, S. J., McCormick, W. D., Swift, J. B. & Swinney, H. L. 1996 Nonlinear control of remote unstable states in a liquid bridge convection experiment. *Phys. Rev. Lett.* **77**, 3779.

[126] Picella, F., Loiseau, J.-C., Lusseyran, F., Robinet, J.-C., Cherubini, S. & Pastur, L. 2018 Successive bifurcations in a fully three-dimensional open cavity flow. *J. Fluid Mech.* **844**, 855–877.

[127] Plaza, A. & Carey, G. 2000 Local refinement of simplicial grids based on the skeleton. *Appl. Num. Math.* **32**, 195–218.

[128] Poliashenko, M. & Aidun, C. K. 1995 A direct method for computation of simple bifurcations. *J. Comput. Phys.* **121**, 246–260.

[129] Pomeau, Y. 2014 Surface tension: From fundamental principles to applications in liquids and in solids. In *5th Warsaw School of Statistical Physics*. Warsaw University Press.

[130] Pomeau, Y. & Manneville, P. 1980 Intermittent transition to turbulence in dissipative dynamical systems. *Commun. Math. Phys.* **74**, 189–197.

[131] Povitsky, A. 2001 Three-dimensional flow in cavity at yaw. *Tech. Rep.* NASA/CR-2001-211232, ICASE Report No. 2001-31,. ICASE, NASA Langley Research Center,, ICASE, Hampton, Virginia.

[132] Povitsky, A. 2005 Three-dimensional flow in cavity at yaw. *Nonlinear Analysis* **63**, e1573–e1584.

[133] Prasad, A. K. & Koseff, J. R. 1989 Reynolds number and end-wall effects on a lid-driven cavity flow. *Phys. Fluids A* **1**, 208–218.

[134] Ramanan, N. & Homsy, G. M. 1994 Linear stability of lid-driven cavity flow. *Phys. Fluids* **6**, 2690–2701.

[135] Riley, R. J. & Neitzel, G. P. 1998 Instability of thermocapillary-buoyancy convection in shallow layers. part 1. characterization of steady and oscillatory instabilities. *J. Fluid Mech.* **359**, 143.

[136] Romanò, F. & Kuhlmann, H. C. 2019 Heat transfer across the free surface of a thermocapillary liquid bridge. *Tech. Mech.* **39**, 72–84.

[137] Romanò, F., Türkbay, T. & Kuhlmann, H. C. 2020 Lagrangian chaos in steady three-dimensional lid-driven cavity flow **30**, 073121.

[138] Romanò, F., Wu, H. & Kuhlmann, H. C. 2019 A generic mechanism for finite-size coherent particle structures. *Int. J. Multiphase Flow* **111**, 42–52.

[139] Rossiter, J. E. 1964 Wind tunnel experiments on the flow over rectangular cavities at subsonic and transonic speeds. techreport 64037. Royal Aircraft Establishment.

[140] Ryu, Y.-H. & Baik, J.-J. 2009 Flow and dispersion in an urban cubical cavity. *Atmos. Environ.* **43**, 1721–1729.

[141] Saad, Y. 2011 *Numerical Methods for Large Eigenvalue Problems*. Society for Industrial and Applied Mathematics.

[142] Sahin, M. & Owens, R. G. 2003 A novel fully-implicit finite volume method applied to the lid-driven cavity problem—part ii: Linear stability analysis. *Int. J. Num. Meth. Fluids* **42**, 79–88.

[143] Sakurai, M., Kuhlmann, H. C. & Rath, H. J. 2000 Marangoni convection in an open boat. *Z. Angew. Math. Mech.* **80**, 701–702.

[144] Sakurai, M., Kuhlmann, H. C. & Rath, H. J. 2001 Instability of Marangoni convection in open rectangular containers. *Z. Angew. Math. Mech.* **81**, 953–954.

[145] Sampath, R. & Zabaras, N. 2001 Adjoint variable method for the thermal desgin of eutectic directional solidification processes in an open-boat configuration. *Numerical Heat Transfer, Part A: Applications* **39**, 655–683.

[146] Schimmel, F., Albensoeder, S. & Kuhlmann, H. 2005 Stability of thermocapillary-driven flow in rectangular cavities. *Proc. Appl. Math. Mech.* **5**, 583–584.

[147] Schmid, P. J. & Henningson, D. S. 2001 *Stability and Transition in Shear Flows*, *Appl. Math. Sci.*, vol. 142. New York, Berlin: Springer.

[148] Schneider, T. M., Gibson, J. F., Lagha, M., Lillo, F. D. & Eckhardt, B. 2008 Laminar-turbulent boundary in plane Couette flow. *Phys. Rev. E* **78**, 037301–1–037301–4.

[149] Schreiber, R. & Keller, H. B. 1983 Driven cavity flows by efficient numerical techniques. *J. Comput. Phys.* **49**, 310–333.

[150] Schwabe, D. 1981 Marangoni effects in crystal growth melts. *Physicochem. Hydrodyn.* **2**, 263–280.

[151] Schönecker, C. & Hardt, S. 2013 Longitudinal and transverse flow over a cavity containing a second immiscible fluid. *J. Fluid Mech.* **717**, 376–394.

[152] Sha, W. & Nakabayashi, K. 2001 On the structure and formation of spiral Taylor–Görtler vortices in spherical Couette flow. *J. Fluid Mech.* **431**, 323–345.

[153] Shaabani-Ardali, L. 2018 Stability and optimal control of time-periodic flows - application to a pulsed jet. PhD thesis, Université Paris Saclay.

[154] Shankar, P. N. & Deshpande, M. D. 2000 Fluid mechanics in the driven cavity. *Annu. Rev. Fluid Mech.* **32**, 93–136.

[155] Shen, J. 1991 Hopf bifurcation of the unsteady regularized driven cavity flow. *J. Comput. Phys.* **95**, 228–245.

[156] Shevtsova, V., Gaponenko, Y., Kuhlmann, H. C., Lappa, M., Lukasser, M., Matsumoto, S., Mialdun, A., Montanero, J. M., Nishino, K. & Ueno, I. 2014 The JEREMI-project on thermocapillary convection in liquid bridges. Part B: Overview on impact of co-axial gas flow. *Fluid Dyn. Mat. Proc.* **10**, 197–240.

[157] Shevtsova, V. M., Ermakov, M. K., Ryabitskii, E. & Legros, J. C. 1997 Oscillations of a liquid bridge free surface due to the thermal convection. *Acta Astronaut.* **41**, 471–479.

[158] Shiomi, J. & Amberg, G. 2002 Active control of a global thermocapillary instability. *Phys. Fluids* **14**, 3039–3045.

[159] Shiomi, J., Amberg, G. & Alfredsson, H. 2001 Active control of oscillatory thermocapillary convection. *Phys. Rev. E* **64**, 031205–1–031205–7.

[160] Shiomi, J., Kudo, M., Ueno, I., Kawamura, H. & Amberg, G. 2003 Feedback control of oscillatory thermocapillary convection in a half-zone liquid bridge. *J. Fluid Mech.* **496**, 193–211.

[161] Siegmann-Hegerfeld, T., Albensoeder, S. & Kuhlmann, H. C. 2008 Two- and three-dimensional flows in nearly rectangular cavities driven by collinear motion of two facing walls. *Exp. Fluids* **45**, 781–796.

[162] Siegmann-Hegerfeld, T., Albensoeder, S. & Kuhlmann, H. C. 2013 Three-dimensional flow in a lid-driven cavity with width-to-height ratio of 1.6. *Exp. Fluids* **54**, 1526–1–1526–10.

[163] Sipp, D. & Jacquin, L. 2000 Three-dimensional centrifugal-type instabilities of two-dimensional flows in rotating systems. *Phys. Fluids* **12**, 1740–1748.

[164] Sipp, D., Marquet, O., Meliga, P. & Barbagallo, A. 2010 Dynamics and control of global instabilities in open-flows: A linearized approach. *Appl. Mech. Rev.* **63**.

[165] Sipp, D. & Schmid, P. J. 2016 Review article closed-loop control of fluid flow: a review of approaches and tools. *Appl. Mech. Rev.* .

[166] Smith, M. K. 1986 Instability mechanisms in dynamic thermocapillary liquid layers. *Phys. Fluids* **29**, 3182–3186.

[167] Smith, M. K. & Davis, S. H. 1983 Instabilities of dynamic thermocapillary liquid layers. Part 1. Convective instabilities. *J. Fluid Mech.* **132**, 119–144.

[168] Solin, P., Segeth, K. & Dolezel, I. 2003 *Higher-Order Finite Element Methods*. Taylor & Francis Inc.

[169] Soulhac, L., Perkins, R. J. & Salizzoni, P. 2008 Flow in a street canyon for any external wind direction. *Bound.-Layer Met.* **126**, 365–388.

[170] Stewart, G. W. 2002 A krylov–schur algorithm for large eigenproblems. *SIAM Journal on Matrix Analysis and Applications* **23**, 601–614.

[171] Stojanovic, M. & Kuhlmann, H. C. 2020 Stability of thermocapillary flow in high-Prandtl-number liquid bridges exposed to a coaxial gas stream. *Microgravity Sci. Technol.* .

[172] Tchoufag, J., Magnaudet, J. & Fabre, D. 2013 Linear stability and sensitivity of the flow past a fixed oblate spheroidal bubble. *Phys. Fluids* **vol. 25**.

[173] Temprano-Coleto, F., Peaudecerf, F. J., Landel, J. R., Gibou, F. & Luzzatto-Fegiz, P. 2018 Soap opera in the maze: Geometry matters in marangoni flows. *Phys. Rev. Fluids* **3**.

[174] Theofilis, V. 2003 Advances in global linear instability analysis of nonparallel and three-dimensional flows. *Prog. Aerospace Sci.* **39**, 249–315.

[175] Theofilis, V., Duck, P. W. & Owen, J. 2004 Viscous linear stability analysis of rectangular duct and cavity flows. *J. Fluid Mech.* **505**, 249–286.

[176] Trefethen, L. N. & Embree, M. 2005 *Spectra and Psoeudospectra*.

[177] Tuann, S.-Y. & Olson, M. D. 1978 Review of computing methods for recirculating flows. *J. Comput. Phys.* **29**, 1–19.

[178] Tuckerman, L. S., Langham, J. & Willis, A. 2019 *Order-of-Magnitude Speedup for Steady States and Traveling Waves via Stokes Preconditioning in Channelflow and Openpipeflow*.

[179] Velten, R., Schwabe, D. & Scharmann, A. 1991 The periodic instability of thermocapillary convection in cylindrical liquid bridges. *Phys. Fluids A* **3**, 267–279.

[180] Wang, A., Kamotani, Y. & Yoda, S. 2007 Oscillatory thermocapillary flow in liquid bridges of high Prandtl number fluid with free surface heat gain. *Int. J. Heat Mass Transfer* **50**, 4195–4205.

[181] Wanschura, M., Shevtsova, V. S., Kuhlmann, H. C. & Rath, H. J. 1995 Convective instability mechanisms in thermocapillary liquid bridges. *Phys. Fluids* **7**, 912–925.

[182] Xu, J. & Zebib, A. 1998 Oscillatory two- and three-dimensional thermocapillary convection. *J. Fluid Mech.* **364**, 187–209.

[183] Yano, T., Nishino, K., Ueno, I., Matsumoto, S. & Kamotani, Y. 2017 Sensitivity of hydrothermal wave instability of Marangoni convection to the interfacial heat transfer in long liquid bridges of high Prandtl number fluids. *Phys. Fluids* **29**, 044105.

[184] Yasnou, V., Gaponenko, Y., Mialdun, A. & Shevtsova, V. 2018 Influence of a coaxial gas flow on the evolution of oscillatory states in a liquid bridge. *Int. J. Heat Mass Transfer* **123**, 747 – 759.

[185] Zajic, D., Fernando, H. J. S., Calhoun, R., Princevac, M., Brown, M. J. & Pardyjak, E. R. 2011 Flow and turbulence in an urban canyon. *J. Appl. Meteorol. and Climatol.* **50**, 203–223.

[186] Zebib, A., Homsy, G. M. & Meiburg, E. 1985 High Marangoni number convection in a square cavity. *Phys. Fluids* **28**, 3467–3476.